The Pennsylvania State University
The Graduate School
College of Engineering

THE PREDICTION OF VIBRATORY STRESSES IN WALL-BOUNDED JETS DUE TO UNSTEADY AEROACOUSTIC LOADING

A Thesis in
Acoustics
by
Claudio Notarangelo

Submitted in Partial Fulfillment
of the Requirements
for the Degree of

Master of Science

December 2017

The thesis of Claudio Notarangelo was reviewed and approved* by the following:

Phillip J. Morris
Professor of Aerospace Engineering
Thesis Adviser

Kenneth S. Brentner
Professor of Aerospace Engineering

Victor W. Sparrow
Professor of Acoustics
Head of the Department of Acoustics

*Signatures are on file in the Graduate School.

Abstract

A coordinated project has been underway at the Pennsylvania State University in an effort to improve CFD predictions of unsteady aerodynamic loading generated by the exhaust of a rectangular jet on a deck downstream of the nozzle exit. Numerical simulations are conducted using Wind-US, a computational platform developed by the NASA Glenn Research Center and the Arnold Engineering Development Center.

Parametric studies are carried out to investigate the effects of several numerical parameters, including time discretization, grid density, upstream forcing, turbulence dissipation and numerical schemes on the computed turbulent flow. The impact of a boundary layer shield on the Large-Eddy Simulation (LES) solution is also investigated. The numerical models included a boundary layer stability preservation technique which combined a time accurate solution with a constant CFL solution in the boundary layer to maintain numerical stability, independent of the boundary layer spacing. Results from the LES running with the boundary layer preservation scheme showed a 20-fold decrease in wall-clock time compared to the fully time-accurate simulations. Numerical predictions characterizing the structural loading on the deck surface are compared to experimental values measured at the United Technology Research Center (UTRC). A proper orthogonal decomposition (POD) method is applied to several of the CFD solutions to provide further insight into some of the non-physical behaviors found in the LES simulations running with the boundary layer stability preservation algorithm.

Sub-scale experiments of wall bounded jets are designed and run in the Penn State high speed noise facility with the purpose of furthering the understanding of the unsteady pressures on a plate over which a turbulent jet is exhausting. A patch-and-scan nearfield acoustic holography technique (NAH) is attempted to reconstruct the cross-spectra and cross-correlations of the wall-pressure fluctuations on the flight deck.

Table of Contents

List of Figures

List of Tables

List of Symbols

Symbol	Property
M_e	exit Mach number
P_0	stagnation pressure
P_a	ambient static pressure
NPR	nozzle pressure ratio
U_e	jet exit velocity
M_∞	freestream Mach number
P_∞	freestream pressure
M_c	convective Mach number
M_j	fully expanded jet Mach number
M_d	design Mach number
U_j	fully expanded jet velocity
U_∞	freestream velocity
a_j	speed of sound of the jet
a_∞	freestream speed of sound
ρ	density
p	pressure
e	energy per unit mass
τ_{ij}	viscous stress tensor
t	time
u	flow velocity
q	heat flux
P_r	Prandtl number

h	enthalpy
κ	thermal conductivity
C_p	heat capacity at constant pressure
μ	dynamic viscosity
δ_{ij}	Kronicher delta
$\tau_{ij,turb}$	Reynolds stress tensor
μ_T	dynamic eddy viscosity
k	turbulent kinetic energy
ε	turbulence dissipation
α	angle of attack
β	sideslip angle
γ	ratio of specific heats
n	numerical scheme order
Δx	grid spacing
CFL_{max}	CFL number threshold
BL_s	boundary layer shield
U_f	forcing function
C_b	turbulent kinetic energy dissipation limiter
μ_∞	free-stream dynamic viscosity
h_{nozzle}	nozzle height
$\emptyset_{inj}$	injection angle
T_{inj}	injection temperature
Δ_{LES}	LES grid length scale
C_{bls}	boundary layer shield offset multiplier

Acknowledgments

Firstly, I would like to express my sincere gratitude to my advisor, Dr. Philip J. Morris, for the continuous support during the course of my graduate studies. While writing this thesis, he gave me the support and freedom I needed to move on while working a full-time job. Besides my advisor, I would also like to thank Dr. Dennis K. McLaughlin for letting me use the anechoic wind tunnel to run the sub-scale experiments.

I would also like to thank the rest of my thesis committee: Dr. Kenneth Brentner and Dr. Victor Sparrow, for their insightful comments and encouragement. My sincere thanks also go to Dr. Bob Bush and Dr. Kerwin Low for their guidance throughout the development of this project.

Dozens of other people have helped and thought me immensely at Penn State. I would like to express my appreciation to Darryl Douglas, Darren Slotnick, Christopher Shemaker and Scott Hromisin who took time of out their work to help me set up and run the small-scale jet experiments. I would also like to thank my dear friends Umberto Saetti and Josh Hrisko without whom this thesis would have been completed a year earlier.

Finally, I would like to express my profound gratitude to my parents Luigi and Evelina, my brother Marco and my sister Giulia, for their unconditional love and care. They have cherished me with every great moment and always supported me during the most difficult times. Vi voglio bene!

Chapter 1
Introduction

1.1 Motivation

Aircraft noise emissions reduction has become a driving factor for competitive stealth aircraft design. One of the features of many stealth aircraft is a high aspect ratio rectangular nozzle that is mounted above the aircraft fuselage. This nozzle configuration allows the aircraft fuselage to shield the noise and other detectible properties generated by the jet engine. While this type of wall bounded jet produces a lower acoustic signature, it also introduces additional issues. Figure 1.1 shows a photograph of the Northrop Grumman X-47B UCAS stealth drone, which uses a high aspect ratio, wall bounded nozzle configuration (highlighted in red).

The jet stream exiting the nozzle can travel at supersonic speeds and potentially generate shocks and expansion waves that impinge on the aircraft fuselage. The impact of the shock structures on the boundary layer can produce unsteady pressures on the deck surface. Additionally, the interaction between ambient air and the high-speed jet stream causes a jet shear layer to form. The turbulent eddies from the jet shear layer can impinge on the flight deck and produce additional unsteady forces on the aircraft.

All of these forces can cause the deck to vibrate with a resulting decrease in the fatigue life of the structure. Understanding the aerodynamic loading generated by the turbulent jet exhausting on the deck will aid structural engineers in making the appropriate design decisions.

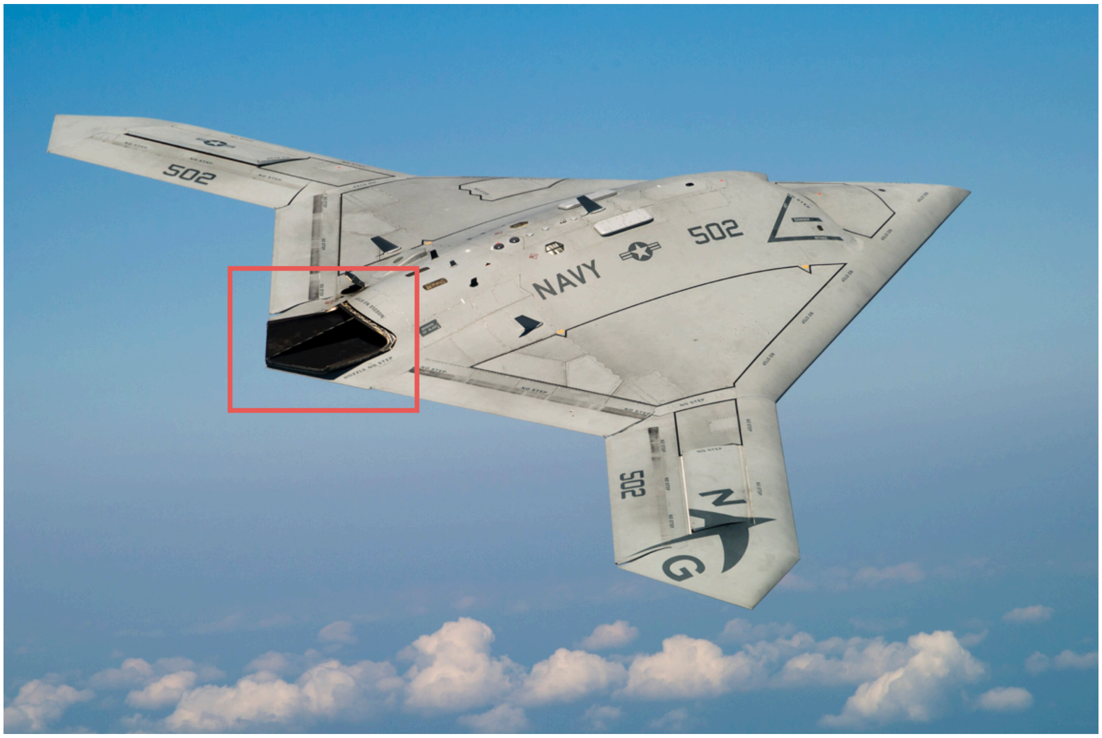

Figure 1.1 Photograph of the Northrop Grumman X-47B UCAS [18]

1.2 Background

The nozzle design plays an important role in the noise produced by the turbulent jet. A nozzle is designed to accelerate the fluid into a high-speed jet to achieve maximum thrust. The internal profiles of the nozzles employed in commercial and military aircraft are of two types: converging or converging-diverging. The converging nozzle is used to generate a jet with a subsonic exit Mach number. The exit Mach number (M_e) is a dimensionless quantity representing the ratio of the jet exit velocity to the local speed of sound. This Mach number can be determined through the use of the isentropic flow relations given in Eq. 1.1 as long as the ratio of the total stagnation pressure to the ambient static pressure (P_0/P_a) is below a critical value.

$$M_e = \left(\frac{2}{\gamma-1}\right)^{\frac{1}{2}}\left(\left(\frac{P_0}{P_a}\right)^{\frac{\gamma-1}{\gamma}} - 1\right)^{\frac{1}{2}} \tag{1.1}$$

For air with γ = 1.4 this critical pressure ratio, also referred as the nozzle pressure ratio (NPR), is P_0/P_a = 1.893 [1]. At this condition, the exit Mach number has reached unity and the nozzle is said to be choked. If the NPR is greater than the critical value, the exit Mach number will remain M_e = 1. However, the flow exiting the nozzle will tend to expand supersonically eventually adjusting to the ambient pressure through a system of expansion waves and shocks.

The converging-diverging nozzle has an internal profile that converges from the nozzle inlet to a throat and then diverges from the throat to the nozzle exit. In a converging-diverging nozzle, the nozzle pressure ratio determines the flow pattern downstream of the nozzle exit. If 1< P_0/P_a, the flow through the nozzle will be subsonic and isentropic and the pressure at the exit will match the ambient pressure. The nozzle becomes choked at a critical pressure ratio of P_0/P_a = 1.893. If the pressure is increased above P_0/P_a, a normal shock will form downstream of the throat and the exit Mach number will remain subsonic. As the NPR is increased, the shock moves downstream until it is situated at the nozzle exit. A schematic of this process is shown in Figure 1.2. The critical NPR required to produce this flow condition is found using (1.2). M_{bs} corresponds to the Mach number just ahead of the normal shock and A_{exit}/A_{throat} is the nozzle area ratio.

$$NPR_{critical} = \left(\frac{A_{exit}}{A_{throat}}\right)\left(\frac{\gamma+1}{2}\right)^{\frac{\gamma+1}{2(\gamma-1)}} M_{bs}\left(1+\frac{\gamma-1}{2}M_{bs}^2\right)^{\frac{1}{2}} \qquad (1.2)$$

Once the nozzle pressure ratio exceeds the critical value given in (1.2), there are three possible flow conditions. If $NPR_{critical}$ is below P_0/P_{bs}, where P_{bs} is the pressure just ahead of the normal shock, then the flow passes through an oblique shock at the nozzle exit. In this case the flow is called over-expanded. When $NPR_{critical}$ is equal to P_0/P_{bs}, then the flow is fully expanded and the jet exhausts smoothly. If $NPR_{critical}$ is above P_0/P_{bs}, then the nozzle flow must expand to reach P_{bs} and an expansion fan is generated from the nozzle edges. In this case the flow is called under-expanded. Military nozzles typically have a sharp throat so that expansion waves can form at the throat once the nozzle is choked.

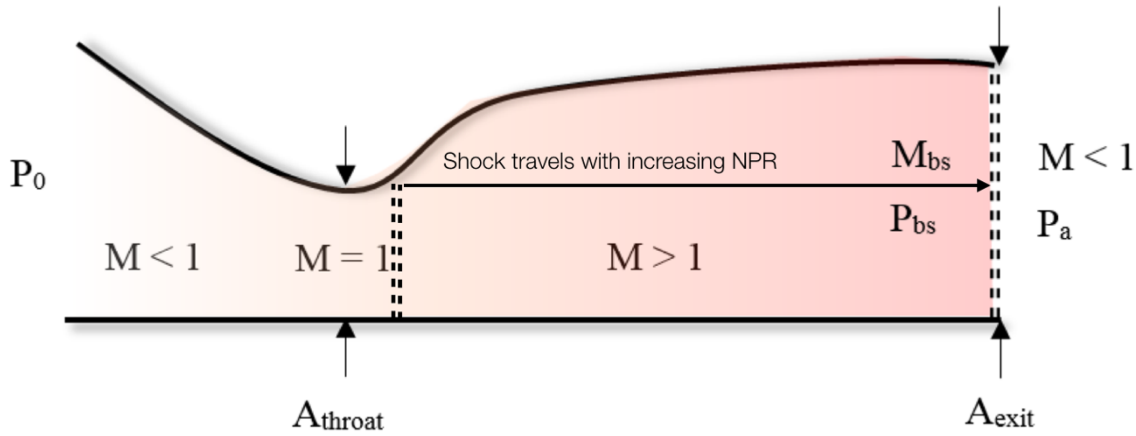

Figure 1.2 Example of a normal shock at the nozzle exit

The free jet consists of a potential core region, a transition region and a fully-developed region. The jet core is defined as the region where the jet velocity is 99% of the jet exit velocity, U_e. The end of the core is commonly assumed as the point where the jet velocity drops below 95% of U_e. Upon exiting the nozzle, the high-speed jet interacts with the ambient medium, resulting in the formation of the shear layer. The outer layer of the jet is subjected to strong turbulent fluctuations which cause the shear layer to grow continuously downstream. The turbulent shear layer enhances flow mixing by entraining the ambient fluid. In the transition region, the shear layers reach the jet centerline. The jet continues to spread as the velocity decays at a rate necessary to conserve axial momentum. Nearly all of the noise is generated in the potential and transition regions [2]. Within the fully-developed region, the velocity profile of the jet takes a self-similar shape. Figure 1.3 shows the general development of a turbulent free jet.

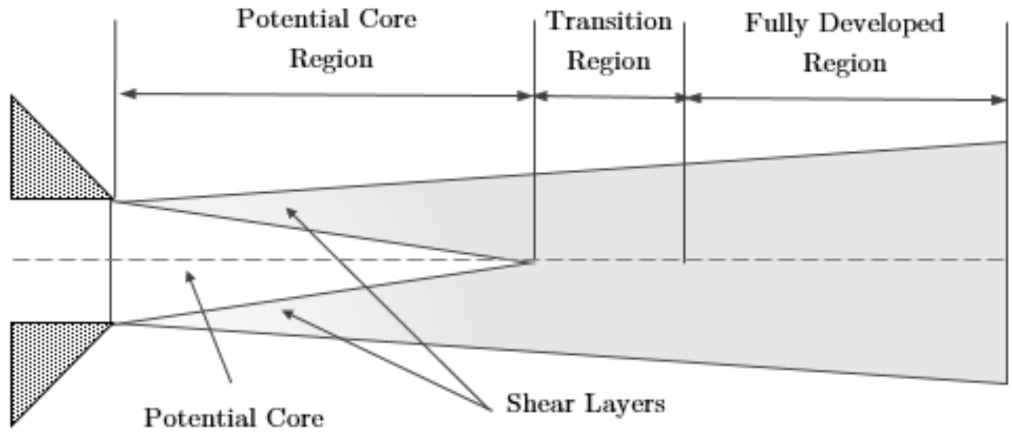

Figure 1.3 Schematic of the development of a free jet

Jet noise is a byproduct of the turbulence that is generated when the jet interacts with the ambient medium. The spectral content of jet noise is spread over a wide range of frequencies. This reflects the fact that the eddies that comprise the turbulent mixing process vary considerably, increasing in size progressively downstream of the exhaust nozzle and decaying in intensity as the average jet velocity falls. The noise spectrum generated by the high-speed jet is highly dependent on the jet Mach number, jet temperature and observer angle. When the jet is subsonic, the broadband noise is mainly due to turbulent mixing. If the jet is supersonic and perfectly expanded (on-design condition), the large-scale mixing noise manifests itself primarily as Mach wave radiation [11]. In a supersonic jet operating at an off-design condition, additional noise is generated in the form of broadband shock-associated noise (BBSAN) emanating from the shock-turbulence interaction as well as screech tones [12]. The peak frequency of the BBSAN varies inversely with the shock-cell spacing. Figure 1.4 shows a typical narrowband shock noise spectrum at an azimuthal angle of 0˚ from the experimental data that are presented later in this thesis. Table 1.1 shows the operating conditions used to obtain the spectrum shown below.

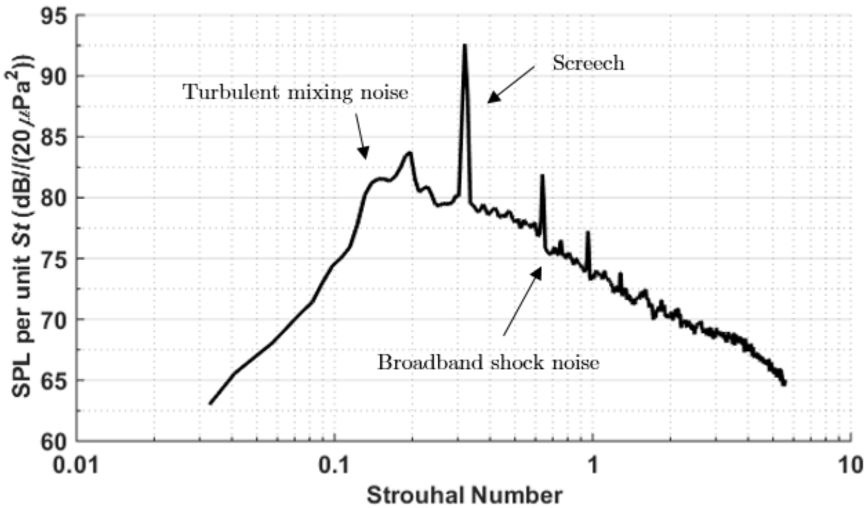

Figure 1.4 Typical jet noise spectrum.

Table 1.1 Run Conditions

NPR	M_j	M_d	TTR
3.5	1.47	1.26	1.0

The presence of the aft-deck changes the features of the jet flow emanating from the nozzle. In the transition region, the shear layer will converge with the potential layer only from one side. A turbulent boundary layer will develop along the wall on the bottom edge. As the jet becomes supersonic, a system of oblique shocks and expansion waves begins to form upstream and downstream of the nozzle exit. The interaction between the shock structures and the deck surface results in shock-boundary layer interactions (SBLI). A generic feature of such flows is that the incident shock alters the boundary layer developing along the deck. The changes can be local, but for sufficiently large pressure rises, the boundary layer separates and a separation bubble appears. This separation region can result in unsteady pressure fluctuations at the wall. The major parameters that influence the size of the separation bubble are the jet Mach number and the Reynolds number. Figure 1.5 shows a schlieren picture of an oblique shock impinging on a turbulent boundary layer at $M_\infty = 2.28$ with an incident shock-angle of 32.41˚. The image is based on the instantaneous density-gradient field, extracted from a Large-Eddy Simulation of SBLI over an adiabatic flat plate [3].

Previous experimental studies on supersonic boundary layer flows have shown that the SBL's motions have a frequency up to three orders of magnitude lower than the characteristic frequency of the turbulent boundary layer [4, 5]. The low-frequency unsteadiness associated with the intermittent flow separation near the foot of the reflected shock may lead to failure by structural fatigue. Hadjadj [3] performed several Large-Eddy Simulations to match experimental data from Dupont [6], and his simulations were in agreement with the experiments. His results confirmed that the LES model was able to accurately capture the frequency of the most energetic low-frequency unsteadiness and the bandwidth of the low-frequency content. Priebe [7] performed a Direct Numerical Simulation of a reflected shock-wave turbulent boundary layer interaction at Mach 2.9. From the wall-pressure signal in the interaction region and pressure measurements in the freestream, the characteristic low-frequency of the shock motion was inferred and found to agree with the scaling model proposed by Piponniau [8].

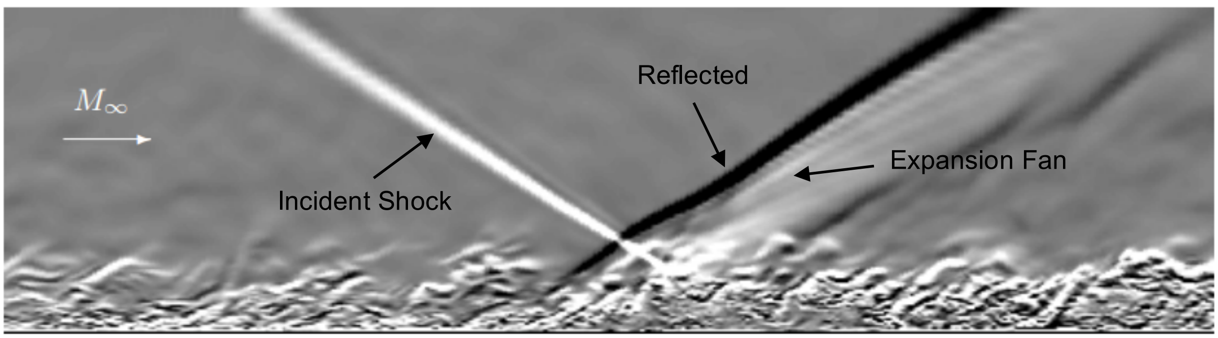

Figure 1.5 Instantaneous numerical schlieren of SBLI [3]

The shear layer is a region of high vorticity and intense turbulent activity. Since the impact of the shear layer onto the flight deck is a major cause of the unsteady loading, it is important to accurately predict its development and flow characteristics. A fully developed turbulent free shear layer is characterized by large-scale coherent structures in the form of span wise vortex rollers with a transverse length scale on the order of the shear layer thickness. Hussain [9] defines a coherent structure as a "connected turbulent fluid mass with instantaneously phase-correlated vorticity over its spatial extent". These turbulent structures begin to form when an initial disturbance causes the jet boundary to mix with the ambient air. As the vortices convect downstream, they interact with one another, thus forming larger vortices.

The linear growth rate of the shear layer is dependent on the velocity at which the structures convect downstream and the jet temperature ratio. The convective Mach number, M_c, is defined as:

$$M_c = \frac{U_j - U_\infty}{a_j + a_\infty} \tag{1.3}$$

where U_j is the fully expanded jet velocity, U_∞ is the velocity of the ambient medium, a_j is the speed of sound in the jet and a_∞ is the ambient speed of sound. For a supersonic jet, the shear layer grows at a much slower rate compared to a subsonic jet, thus increasing the length of the potential core. This is a result of the compressibility effects. A slower growth of the shear layer can also be achieved by decreasing the jet temperature, which leads to lower exhaust velocities and a change in the temperature profile.

In computational simulations, the initial shear layers stay laminar for a longer distance than what is typically observed in the experimental data. This behavior can be caused by the excessive level of dissipation in the turbulence model or by the lack of disturbances in the shear layer. In hybrid RANS-LES methods, the boundary layers upstream of the shear layer are typically resolved by a RANS model and therefore the development of turbulent modes in the shear layer is not forced by the turbulence coming from the boundary layers. Kok and Van der Horn [10] modified the sub-grid model in their hybrid Large-Eddy Simulations (X-LES) to include a stochastic diffusion model in order to better resolve the initial development of the shear layer. Stochastic sub grid-scale (SGS) models can be seen as random forcing of the resolved scales through non-linear interactions with the sub grid scales. The modified X-LES model consists of a composition of RANS k–ω turbulence model and a k-equation SGS mode. The X-LES model is used to study the free shear layer from the trailing edge of a flat plate using two different grids, G1 and G2, with 1.29 and 10.3 million cells. For grid G1, the mesh sizes, time step and grid filter width are all doubled compared to G2. As a reference, zonal RANS-LES computations are also performed on G2. In the zonal RANS-LES model, the boundary layers are set explicitly to RANS and the shear layers to LES. In this particular case, the free-stream velocities are set to $u_1 = 41.5$ m/s and $u_2 = 22.4$ m/s at the different sides of the flat plate and the Reynolds number based on the momentum thickness at the railing edge of the high-speed side is 2900. The results from the numerical calculations are compared to experimental data from Deville et al. [31].

Figure 1.6 compares the self-similar solutions using the similarity coordinate $\eta = (y-y_{1/2})/\theta$, with $y_{1/2}$ being the location where $u^+ = (u-u_2)/(u_1-u_2) = 1/2$ and θ being the shear-layer momentum thickness. The model with the higher spatial resolution (G2) produced much more accurate results than the coarser grid (G1), especially when comparing the resolved normal stresses. This suggests that failure to have enough grid resolution near the nozzle exit can lead to the shear layer growing incorrectly. Note that there is still a difference between the experimental and the numerical data which indicates that the finer grid resolution may not be entirely sufficient to properly resolve the shear layer.

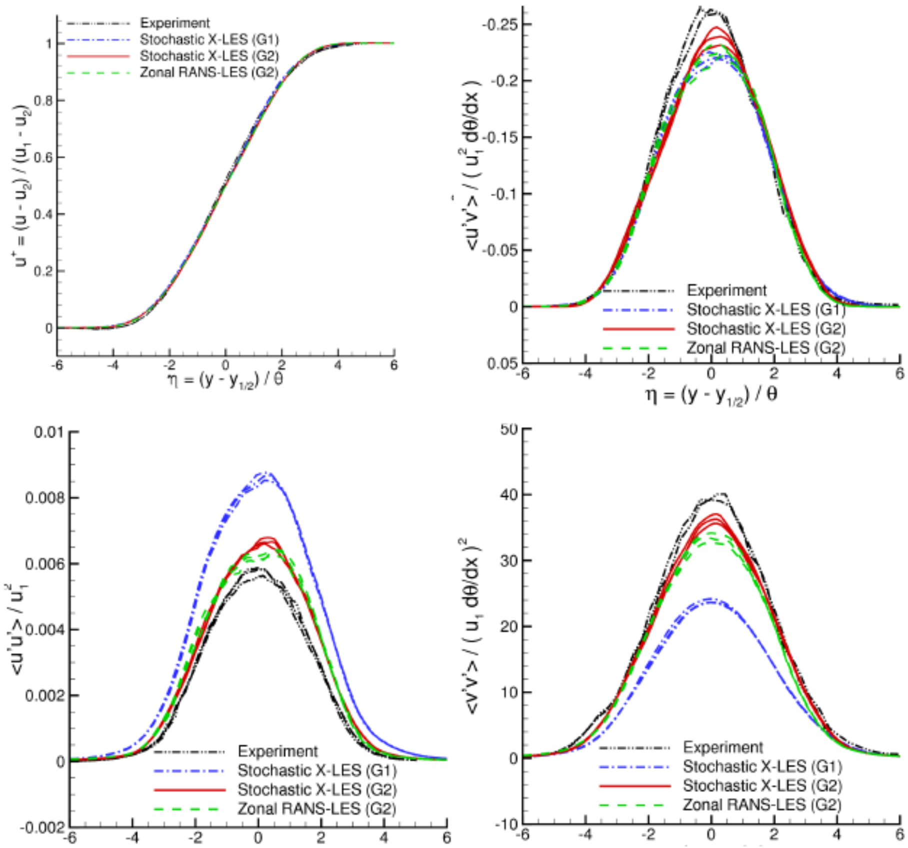

Figure 1.6 Top left: mean pressure. Top right: resolved shear stress <u'v'>. Bottom left: resolved normal stress <u'u'>. Bottom right: resolved normal stress <v'v'>. [10]

1.3 Previous Work

Prediction methods for jet noise were initially based on the power laws established by Lighthill [13]. Over the last decade, advances in computational fluid dynamics (CFD) have made it possible to improve predictions by replacing the parameters used in semi-empirical models with solutions obtained by solving the compressible unsteady Navier-Stokes equations. In the direct noise computation, the time-dependent aerodynamic field and the acoustic field are calculated simultaneously. Direct numerical simulations (DNS) of Poiseuille flows were performed by Hu et al. [14]. Figure 1.7 shows the power spectral density of the wall-pressure fluctuations. The spectral content is broadband with a mid-frequency peak. A very similar spectral shape can be observed for shear layer pressure spectra.

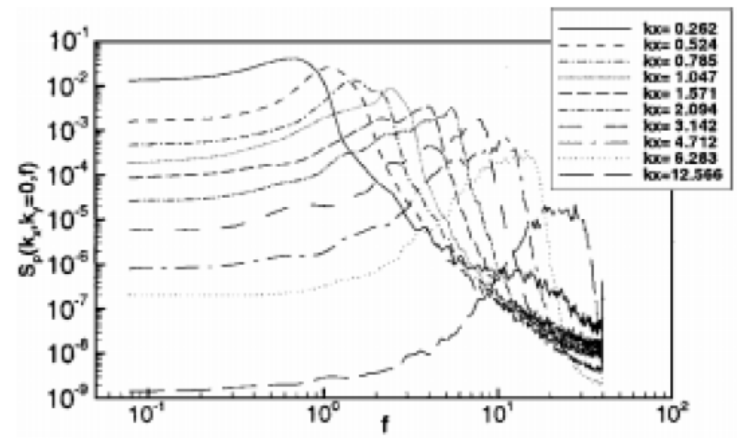

Figure 1.5 Spectral density of wall pressure for Poiseuille flow [14]

The accurate resolution of the mean velocity profiles near the wall for high Reynolds number wall bounded flows is still far from affordable due to the limitation of computational resources. Chen et al. [15] performed a numerical study on wall bounded flows using a Constrained Large-Eddy Simulation (CLES) method. The CLES approach computes the whole flow domain by solving the LES equations with a Reynolds-stress constrained subgrid-scale stress model in the near-wall regions. By imposing physical constraints on the subgrid-scale model, CLES removes the buffer layer mismatch that is often found in the hybrid RANS/LES method. The predicted mean velocity profile, turbulent stresses and skin friction coefficient show good agreement with the available experimental data.

Ahlman et al. [16] performed a direct numerical simulation (DNS) of a turbulent plane wall-jet at M = 0.5. From their numerical results, the inner part of the wall-jet was found to closely resemble a turbulent zero pressure gradient boundary-layer. On the other hand, the outer layer resembled a free plane jet. The downstream growth of the jet and the streamwise mean velocity decay (Fig. 1.8) were both found to be approximately linear, in correspondence to what was measured in the experiments conducted by Eriksson et al. [17]. U_{in} represents the jet inlet velocity, U_c is the coflow velocity which is set to 10% of the jet inlet velocity, U_m is the maximum velocity and *h* is the jet inlet height.

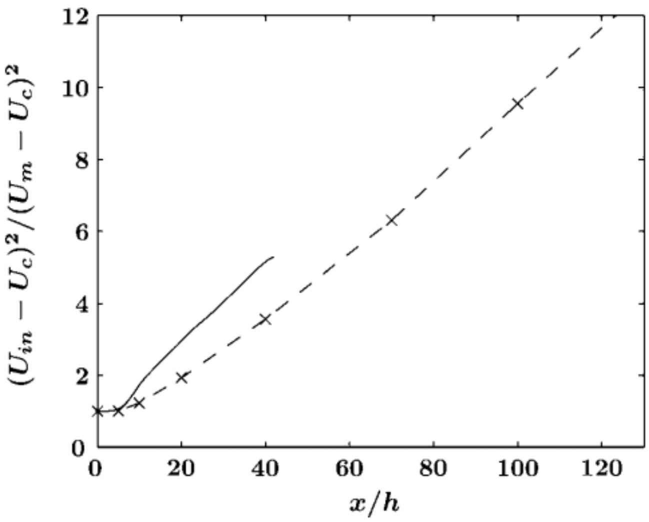

Figure 1.6 Decay of streamwise mean velocity with downstream distance. Simulation (solid) and experimental data (-x-).

1.4 Objectives

The objective of the present work is to predict the unsteady pressure loading on the aft deck of a high aspect ratio, wall bounded nozzle. Numerical simulations are conducted using Wind-US, a fully viscous, hybrid RANS/LES model. A constant CFL number approach is used in the vicinity of the wall to reduce the computational cost of the simulation and to improve the numerical stability of the boundary layer. This provides a good compromise between accuracy and computational efficiency. The effects of several numerical parameters such as physical time step, numerical scheme, upstream forcing, grid resolution and numerical dissipation are also included in the study.

In addition to the computational simulations, a small-scale experiment is conducted in a high speed anechoic wind tunnel to provide further insight into the physics of this problem. The experiments are carried out using two nozzle configurations and four different run conditions. Ultimately, the goal of this thesis is to provide the predicted pressure loads as a forcing function to determine the vibratory stresses on the deck.

1.5 Thesis Outline

Chapter 2 outlines the aft-deck geometry, the boundary conditions and the numerical methods used in the CFD simulations. The latter includes the numerical discretization techniques, the modifications made in the boundary layer stability preservation model, the governing equations and the turbulence models. Chapter 3 describes the computational results from the parametric studies at two different run conditions. A detailed comparison between the numerical predictions and the experimental data is included in this chapter. Chapter 4 presents the experimental methods used in the sub-scale experiments. These include the nozzle design, run conditions and instrumentation setup. Chapter 5 shows the results from the small-scale experiments. These results include power spectral density (PSD) plots at individual sensor positions, general trends in the behavior of the flow and the reconstruction of the wall-pressure cross-spectra and cross-correlations on the deck. Chapter 6 presents a summary of the research and some recommendations for future work.

Chapter 2
Numerical Methods

Numerical simulations of a wall-bounded high-aspect ratio supersonic nozzle are carried out on the Department of Aerospace Engineering's cluster Cocoa4 at Penn State. The cluster is comprised of 54 computational nodes over a 20 GB/s Infiniband Network Fabric. Each node contains 2 quad-core Xeons running at 2.66 GHz for a total of 8 cores per node. Each CFD simulation is solved using a total of 133 cores. The simulations are performed using Wind-US, a computational platform developed by the NASA Glenn Research Center and the Arnold Engineering Development Center. This chapter will provide details of the numerical methods, boundary conditions and nozzle geometry used in the Wind-US simulations. Numerical calculations of an under-expanded jet have been performed at a nozzle pressure ratio (NPR) of 4.0.

2.1 Governing Equations

Wind-US uses a second-order-accurate finite difference scheme to solve the Euler or the compressible Reynolds-averaged form of the Navier-Stokes equations. The partial differential equations are modeled in their full conservative form and solved at discrete time intervals and discrete locations in space. Explicit terms are computed using a mixed upwind/central differencing method while the implicit terms are computed using a four-stage Runge-Kutta scheme [20]. Tensor forms of the Euler and Navier-Stokes equations are shown in equations 2.1 and 2.2.

$$\begin{cases} \dfrac{\partial u_i}{\partial t} + u_j \dfrac{\partial u_i}{\partial x_j} = -\dfrac{\partial p}{\partial x_i} \\ \dfrac{\partial u_i}{\partial x_i} = 0 \\ \dfrac{\partial e_i}{\partial t} + u_i \dfrac{\partial e_i}{\partial x_i} + p \dfrac{\partial u_i}{\partial x_j} = 0 \end{cases} \tag{2.1}$$

$$
\begin{cases}
\dfrac{\partial \rho}{\partial t} + \dfrac{\partial}{\partial x_i}(\rho u_i) = 0 \\
\dfrac{\partial}{\partial t}(\rho u_j) + \dfrac{\partial}{\partial x_i}(\rho u_j u_i) = -\dfrac{\partial p}{\partial x_j} + \dfrac{\partial t_{ij}}{\partial x_i} \\
\dfrac{\partial}{\partial t}(\rho e) + \dfrac{\partial}{\partial x_i}\big((\rho e + p)u_i\big) = -\dfrac{\partial q_i}{\partial x_i} + \dfrac{\partial}{\partial x_i}(u_j \tau_{ij})
\end{cases} \tag{2.2}
$$

The i and j subscripts label the N-dimensional space coordinates, ρ is density, p is pressure, e is energy per unit mass and τ_{ij} is the viscous stress tensor. The convective heat flux q is given by Fourier's law:

$$
q_i = -\frac{\mu}{P_r}\frac{\partial h}{\partial x_i} \tag{2.3}
$$

where h is the enthalpy and P_r is the laminar Prandtl number, given by:

$$
P_r = \frac{C_p \mu}{\kappa} \tag{2.4}
$$

where κ is the coefficient of thermal conductivity.

The compressible Reynolds-Averaged Navier-Stokes (RANS) equations, similar to the Favre-Averaged Navier-Stokes equations, are time-averaged equations of fluid motion. The assumption behind the RANS equations is that the flow variables can be separated into their mean and fluctuating components (2.5).

$$
\begin{aligned}
u_i &= u_i' + \overline{u_i} \\
p &= p' + \bar{p} \\
\tau_{ij} &= \tau_{ij}' + \overline{\tau_{ij}}
\end{aligned} \tag{2.5}
$$

The Reynolds-time average of a generic flow variable φ is defined as:

$$
\bar{\varphi} = \lim_{T\to\infty} \frac{1}{T}\int_{t_0}^{t_0+T} \varphi \, dt \tag{2.6}
$$

Favre-averaging is used when the generic parameter φ is weighted by the density ρ as:

$$
\tilde{\varphi} = \frac{\overline{\rho\varphi}}{\bar{\rho}} \tag{2.7}
$$

where the fluctuating component of the Favre-averaged quantity is given by:

$$
\varphi'' = \varphi - \tilde{\varphi} \tag{2.8}
$$

One of the properties of the Favre and Reynold's time-average is that the mean of a fluctuating quantity is equal to zero.

$$\widetilde{\varphi''} = 0$$
$$\overline{\varphi'} = 0 \tag{2.9}$$
$$\overline{\rho\,\varphi''} = 0$$

The unsteady Reynolds-averaged Navier-Stokes equations are obtained by substituting the decomposed flow quantities into the Navier-Stokes equations and then taking the time average [19]. The process is performed on the continuity equations as:

$$\frac{\partial \bar{\rho}}{\partial t} + \frac{\partial}{\partial x_i}\overline{(\rho\widetilde{u_i} + \rho u_i'')} = 0 \tag{2.10}$$

Equation 2.9 is applied to eliminate the mean of the fluctuating velocity. The resulting equation is:

$$\frac{\partial \bar{\rho}}{\partial t} + \frac{\partial}{\partial x_i}(\bar{\rho}\widetilde{u_i}) = 0 \tag{2.11}$$

The same procedure is applied to the momentum equation:

$$\frac{\partial}{\partial t}(\bar{\rho}\widetilde{u_j}) + \frac{\partial}{\partial x_i}(\bar{\rho}\widetilde{u_j}\widetilde{u_i}) = -\frac{\partial \bar{p}}{\partial x_j} + \frac{\partial}{\partial x_i}(\overline{\tau_{ij}} - \overline{\rho u_i'' u_j''}) \tag{2.12}$$

where the viscous stress tensor τ_{ij} can be expressed in terms of the traceless viscous strain rate as:

$$\tau_{ij} = 2\mu S_{ij} = \mu\left(\frac{\partial u_i}{\partial x_j} + \frac{\partial u_j}{\partial x_i}\right) - \frac{2}{3}\mu\frac{\partial u_k}{\partial x_k}\,\delta_{ij} \tag{2.13}$$

The term μ represents the dynamic viscosity and δ_{ij} is the Kronicher delta. The same procedure is applied to the energy equation below.

$$\frac{\partial}{\partial t}(\bar{\rho}\tilde{e}) + \frac{\partial}{\partial x_i}\left((\bar{\rho}\tilde{e} + \bar{p})\widetilde{u_i}\right) = -\frac{\partial}{\partial x_i}\left(\overline{q_i} + \overline{\rho e'' u_i''}\right) + \frac{\partial}{\partial x_i}(\widetilde{u_j}(\overline{\tau_{ij}} - \overline{\rho u_i'' u_j''})) + \frac{\partial}{\partial x_i}(\overline{\tau_{ij} u_j''} - \overline{\rho u_j'' u_j'' u_i''}) \tag{2.14}$$

The last term in the time-averaged energy equation is very small unless the flow is hypersonic, and thus it is neglected. The quantity $\tau_{ij,turb} = -\overline{\rho u_i'' u_j''}$, known as the Reynolds stress tensor, describes the influence of the turbulent fluctuations on the mean flow field and the spread of momentum by turbulence. The Reynolds stresses introduced by the time averaging require a turbulence model to produce a closed system of solvable equations. RANS models are hence tasked with providing prescriptions for the Reynolds stress tensor in terms of known quantities such as the mean flow field or geometric parameters. In order to model the Reynolds stresses in equations 2.12 and 2.14, Wind-US uses the Boussinesq approximation, which relates the Reynolds stresses to the mean velocity gradients.

$$\tau_{ij,turb} = -\overline{\rho u_i'' u_j''} = 2\mu_T S_{ij} - \frac{2}{3}\rho k \delta_{ij} \tag{2.15}$$

where μ_T is the dynamic eddy-viscosity and k is the turbulence kinetic energy, defined as:

$$k = \frac{1}{2}\overline{u_i'' u_i''} \tag{2.16}$$

The entire stress tensor term can then be written as:

$$\overline{\tau_{ij}} + \tau_{ij,turb} = 2(\mu + \mu_T)\widetilde{S_{ij}} - \frac{2}{3}\rho k \delta_{ij} \tag{2.17}$$

The term $\overline{\rho e'' u_i''}$ in the time-averaged energy equations corresponds to the turbulent transport of heat and can be modeled using a gradient approximation for the turbulent heat-flux:

$$q_i = \overline{\rho e'' u_i''} = -\frac{\mu_t}{P_{r_t}}\frac{\partial h}{\partial x_i} \tag{2.18}$$

where P_{r_t} is the turbulent Prandtl number. The Prandtl number is often used to relate the turbulent heat flux to the turbulent momentum flux. By setting a constant P_{r_t} it is possible to compute the turbulent heat flux based on the turbulent eddy-viscosity predicted by the turbulence model.

2.2 Numerical Models

The mainstream approach used within computational fluid dynamics (CFD) simulations combines the RANS equations with the assumptions that enforce the conservation of mass and energy. CFD models break down the fluid domain into a mesh of discrete cells and then locally solve for the RANS and conservation laws. The accuracy of a time-dependent simulation is primarily determined by the mesh resolution, the turbulence model and the physical time step.

Direct Numerical Simulations (DNS) have been used to study the noise radiated by a low Reynolds number round jet [21]. Direct numerical simulations solve the time-dependent Navier-Stokes equations and resolve all of the relevant length scales in the turbulent flow field. The advantage of this approach is that no turbulence models are required since the whole range of spatial and temporal scales of the turbulence are resolved. However, the computational cost of DNS is very high, even at low Reynolds numbers. For the Reynolds numbers encountered in most industrial applications, the computational resources required by DNS would exceed the capacity of the most powerful computers currently available.

The most common numerical method for CFD is the RANS two-equation turbulence model. The two-equation model introduces two additional transport equations for k, the turbulent kinetic energy, and another turbulent quantity, e.g. the turbulence frequency ω, in order to calculate the eddy viscosity. The two equations require five model constants to be closed [22]. An important limitation of RANS is that these constants are found empirically for a given geometry, therefore reducing the versatility of the model. The eddy viscosity is calculated as a ratio of k and ω, as shown in equation 2.19.

$$\mu_T = \rho \frac{k}{\omega} \tag{2.19}$$

RANS simulations have the benefit of running on coarser grids and thus are computationally cheaper than other models. However, this comes at the cost of reduced information about the flow, as all variables are time averaged and all turbulent length scales are modeled.

Another approach, although computationally expensive, to resolving flows in which large-scale organized turbulence structures are influential is by means of Large-Eddy Simulations (LES). Large-Eddy Simulations also solve the time-dependent Navier-Stokes equations. However, a spatial filter is used to remove the small scales that are not being resolved by the grid. In the LES model, the large-scale motions containing most of the energy are resolved explicitly, and a sub-grid scale model is used to model the effects of the small scales. Lindner et al. [23] performed a numerical study on non-reacting turbulent jets using RANS and LES models. Figure 2.1 shows the impact of the two different models on the eddy resolution.

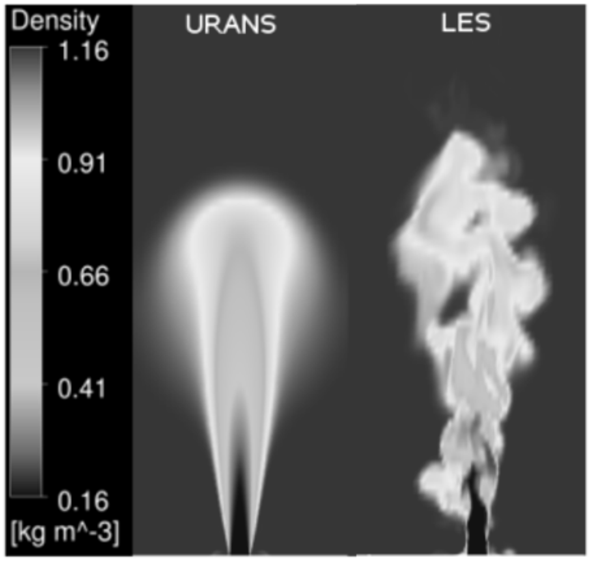

Figure 2.1 Density distribution in the transient regime of a free jet for different turbulence models: RANS and LES [23].

The Wind-US calculations presented in this thesis are executed using an hybrid LES method (LESb), where a standard RANS model is used in the boundary layer regions and smoothly transitions to a sub-grid scale formulation in regions where the grid resolution is fine enough to support the LES. The transfer from RANS to LES regions depends on the local grid spacing and turbulent flow properties. This combined model allows the use of the LES methods with grids typical of those used with traditional RANS simulations while retaining high resolution of the large eddies. The LESb model was initially developed by Bush and Mani [24] and it combines LES with a shear stress transport (SST) formulation. The SST closure is a two-equation eddy-viscosity model that uses a standard k-ω formulation in the inner parts of the boundary layer and switches to a k- ε formulation near the freestream. Many researchers such as Bardina et al. [25] have shown that this model provides high prediction accuracy for flows that include adverse pressure gradients, streamline curvature and separation.

In the LESb hybrid method, the turbulent kinetic energy dissipation rate ε is increased to enable the transition from RANS to LES. This is achieved through a limiter that is a function of the local turbulent length scale and the local grid dimensions. The model represents the turbulent viscosity as a function of the time-averaged density $\bar{\rho}$, the grid filter width Δ, the kinetic energy of the unresolved scales k and a characteristic length scale l_b, as shown in equation 2.20:

$$\mu_T = \bar{\rho} C_\mu l_b \sqrt{k} \tag{2.20}$$

where C_μ is a constant and l_b is defined as:

$$l_b = \min\,(l_\varepsilon, C_b\Delta) \tag{2.21}$$

The length scale l_ε characterizes the average eddy size and is defined as

$$l_\varepsilon = \frac{k^{\frac{1}{2}}}{C_\mu \omega} \tag{2.22}$$

where $l_\varepsilon \ll \Delta$ represents the unresolved length scales. For stretched grids, it is assumed that the smallest resolved eddies are roughly isotropic and so must be resolved in all three coordinate directions, and in time. Therefore, the grid filter width is set as

$$\Delta = \max\,(dx, dy, dz, u * dt, \sqrt{k} * dt) \tag{2.23}$$

. The floating coefficient C_b is used to calibrate the limiter on the turbulent kinetic energy dissipation as shown in equations 2.24-2.25. Essentially, the desired value of this floating coefficient should give a spectrum that avoids the build-up of the high-frequency oscillations and the suppression of resolvable eddies. Increasing C_b favors the growth of the region where the hybrid LES-RANS model reduces to a standard SST turbulence model. The LESb formulation compares the computed effective length scale with the grid scale, and limits the dissipation terms accordingly. The turbulent kinetic energy is reduced from that predicted by the traditional turbulence model such that length scales that are resolved do not contribute to the Reynolds stress terms.

$$\varepsilon_b = \max\left(\varepsilon, \frac{k^{\frac{3}{2}}}{C_b\Delta}\right) \tag{2.24}$$

$$\omega_b = \max\left(\omega, \frac{k^{\frac{1}{2}}}{C_\mu C_b\Delta}\right) \tag{2.25}$$

The Wind-US simulations are started from a steady-state simulation (RANS) in order to minimize the transient period. The unsteady runs are then performed using the hybrid LESb method. A compressibility correction [26] is also applied to the turbulence model to account for the decrease in growth rate in the mixing layer with increasing Mach number. The total variation diminishing flux limiter (TVD), which prevents overshooting of the flow-field properties in regions of high gradients, is set to a compression value of 1.0 to improve numerical stability when using high order discretization schemes.

For standard LES simulations of high Reynolds number wall bounded flows, the computational stability requirements in high shear regions lead to physical time steps smaller than those needed to resolve the large-scale motions in the shear layer, which are often of interest for engineering design. Because the upper limit of numerical stability is restricted by the Courant-Friedrichs-Lewy (CFL) condition (Eq. 2.26), the global time step must be obtained from the maximum CFL number and the smallest grid spacing in the field. Therefore, the stability of the calculations in regions of dense grid packing determines the time step for the entire flow-field.

$$CFL = \frac{u_i}{\Delta x_i}\Delta t \tag{2.26}$$

The CFL_{max} subroutine in Wind-US sets a CFL limiter for time accurate calculations (i.e. every point advances at the same global time step), allowing the local time step to vary based on a selected CFL number threshold (CFL_{max}). That is, the local time step formulation is recast as:

$$dt = min(dt_{LES}; dt_{CFL}) \tag{2.27}$$

where dt_{LES} is defined as the constant physical time step required to resolve the smallest scale of interest and dt_{CFL} is the spatially varying time step set by the specified, constant CFL number, the grid spacing and flow conditions. The local time step changes only in regions where the grid size is smaller than the smallest length scale we wish to resolve (e.g. in the boundary layer). An example of the dt_{CFL} formulation is shown in Equation 2.28.

$$dt_{CFL} = CFL_{max} * min\left(\frac{dx}{(u+a)}; \frac{dy}{(v+a)}; \frac{dz}{(w+a)}\right) \tag{2.28}$$

Due to the small grid spacing required to resolve high shear at the wall, using a constant time step optimized for shear layer resolution would result in very large CFL numbers near the wall. To circumvent this, imposing a constant CFL number threshold (CFL_{max}) will help to preserve stability in regions using smaller spatial dimension. Higher CFL_{max} values increase the number of regions with stability issues and the size of the spatial domain that is running time accurate. A CFL_{max} value of infinity would be equivalent to a simulation that is fully time accurate in all regions. With larger allowable time steps, the total CPU time required for the stretched-time method to reach a certain time-level will be significantly less than of the fully-time accurate method. A list of the speed-up times is given in Chapter 3.

2.3 Discretization Methods

In computational fluid dynamics, finite difference methods are used to discretize and solve hyperbolic partial differential equations. Wind-US offers a wide variety of explicit operators for evaluating the first-derivative terms of the convective terms of the Navier-Stokes equations. For structured grids, these include a central difference scheme, upwind Coakley and the upwind Roe scheme. Depending on the type of finite element scheme used, the accuracy can be specified as anywhere from first to fifth order, where a lower order of accuracy yields to faster convergence but less accurate results. The default scheme is Roe's second-order upwind-biased flux-difference splitting algorithm. The Roe solver determines the inter-cell numerical flux between two computational cells using a constant coefficient linear system instead of the original nonlinear system.

Upwind schemes can have several advantages over central differencing schemes, including numerical dissipation and better explicit stability. Conversely, upwind schemes have generally been more complicated and computationally intensive than central difference, which are also less diffusive than fully upwind numerical schemes. Upwind schemes are more suitable for simulations that involve supersonic and hypersonic flows in which there are very strong embedded shocks. The work presented in this thesis is performed using a 2nd order Roe upwind-biased algorithm that has been modified for stretched grids.

2.4 Aft-Deck Geometry

The rectangular nozzle used in the present numerical study has an aspect ratio of 8:1. The round inlet has an area of 0.42 in^2 and the deck extends downstream of the nozzle exit for a total of 33 nozzle heights. A septum located at the nozzle centerline divides the jet exhaust at the nozzle exit. The computational domain is split into 135 individual zones to allow appropriate parallel data partitioning. The nozzle and aft-deck geometries are shown in Figure 2.2.

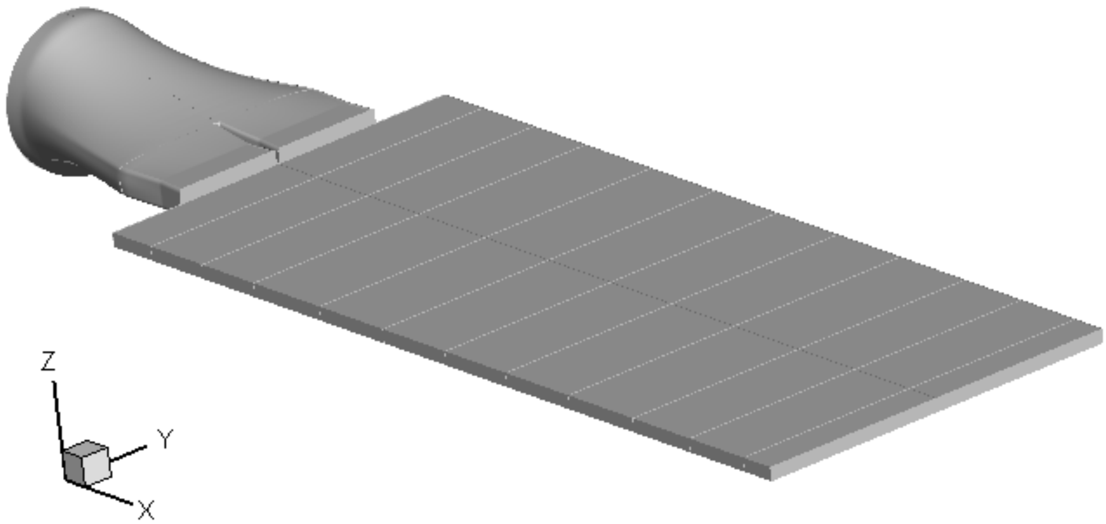

Figure 2.2 Aft-deck geometry

Figure 2.3 shows a two-dimensional slice of the geometry down the nozzle centerline, with each edge labeled with the type of boundary condition used. The outflow boundary condition is used to model the jet flow exiting the computational domain. The grid at the outflow boundaries is modeled using a single computational plane in a single zone. The viscous wall boundary is used to define the interior walls of the nozzle the surface of the deck. This boundary condition imposes a no-slip condition, a zero-pressure gradient and an adiabatic heat transfer condition at the zone boundary. The nozzle input flow is specified using an arbitrary inflow boundary condition. The inflow conditions are held constant for all zones inside the rectangular nozzle.

Table 2.1 shows the values used to define the arbitrary inflow conditions for the NPR = 4.0 case. *M* represents the Mach number, *P* and *T* are the total pressure and total temperature, α is the angle of attack and β is the sideslip angle. The freestream conditions listed in Table 2.2 are used to initialize the flow field at the start of the simulation. In addition, the same conditions are also applied to outflow and freestream boundaries during the course of the flow solution. *P* and *T* represent the static pressure and static temperature values. The fluid properties along with the laminar and turbulent Prandtl numbers are shown in Table 2.3.

Table 2.1 Arbitrary Inflow Conditions

	M	P (psi)	T (R)	α (˚)	β (˚)
NPR 4.0	0.5	58.8	777.0	0.0	0.0

Table 2.2 Freestream Conditions

	M	P (psi)	T (R)	α (˚)	β (˚)
NPR 4.0	0.1	14.7	530	0.0	0.0

Table 2.3 Gas Properties

γ	Pr_l	Pr_t	R ($ft^2/s^2\,R$)
1.4	0.72	0.5	1716

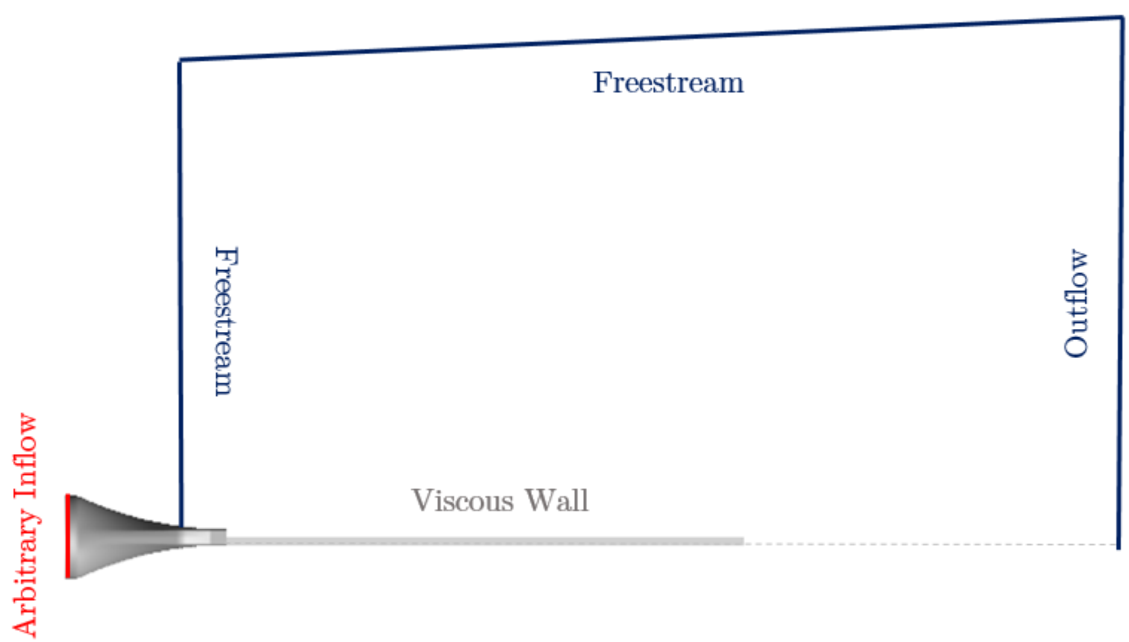

Figure 2.3 Boundary Conditions

A multi-block structured grid is used to mesh the aft-deck geometry. The minimum grid spacing at the nozzle exit is set as 0.0394 inches, and it is gradually stretched in the streamwise and radial directions using a stretching ratio of 1.01. In order to predict the correct growth of the shear layer, the grid spacing in the shear layer should be sized relative to the turbulent length scales, the smallest of which is the Kolmogorov scale η.

$$\eta = L/Re_L^{\frac{3}{4}} \tag{2.29}$$

Re_L represents the Reynolds number based on the largest turbulent length scale L [27]. In this case, it is convenient to use the nozzle height h as the characteristic length scale. However, it is often impractical to refine the grid down to the Kolmogorov length scale. It is more appropriate to limit the grid spacing in the shear layer to 10-100 η, where the smallest turbulent scales are still considered isotropic. Since the turbulent length scales in the shear layer increase in size as they travel downstream, it is reasonable for the grid to stretch as well. The modified LES solver uses wall models to resolve the flow near the deck, therefore the grid spacing does not have to be as refined as in the shear layer. Figure 2.4 shows the computational grid with high-density layers near the deck surface, in the shear layers and along the nozzle centerline. The location of the deck with respect to the nozzle exit has been highlighted in red.

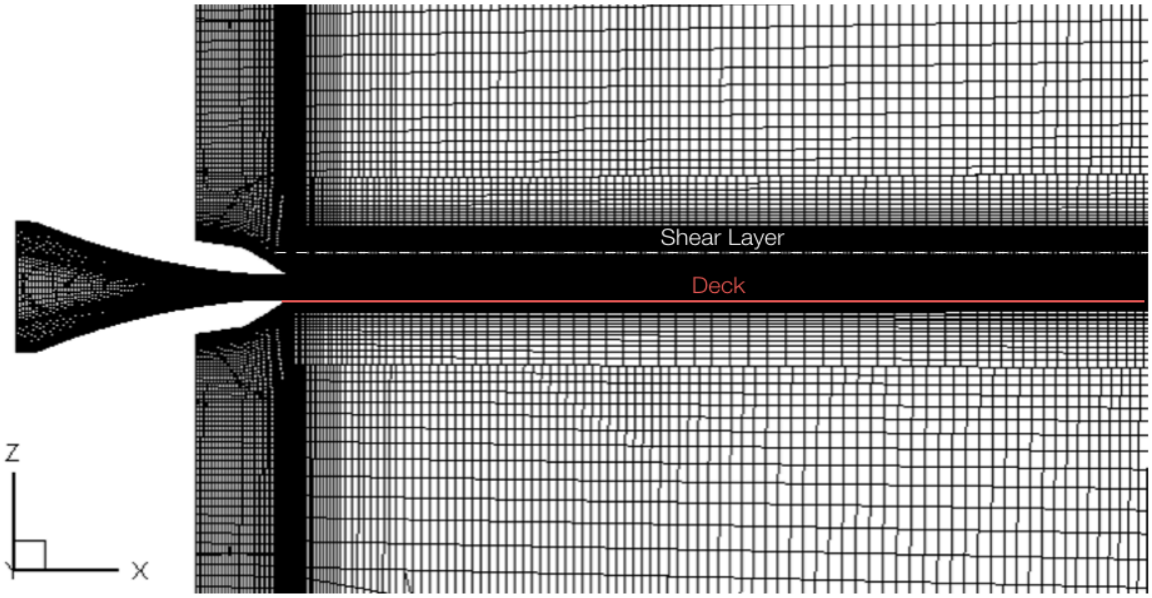

(a)

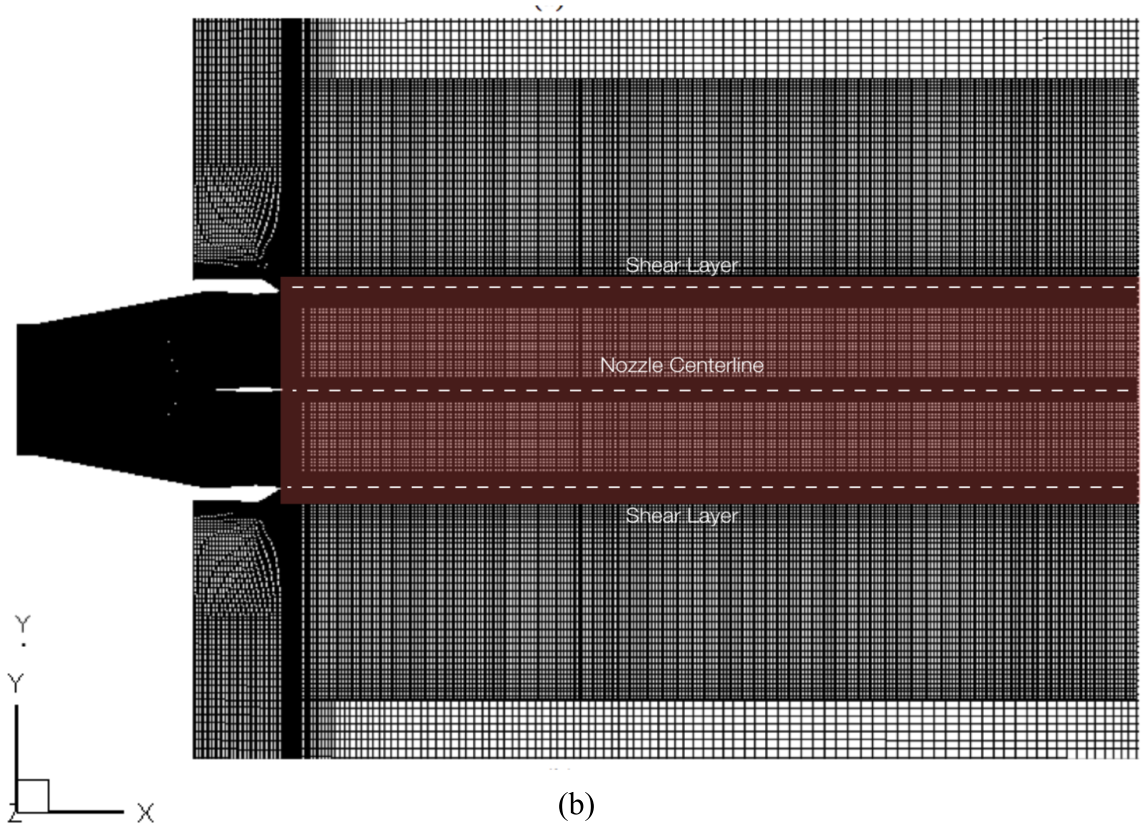

(b)

Figure 2.4 (a) Top view of grid on deck surface. (b) Side view of grid at nozzle center

2.5 Signal Processing

The default MATLAB PWELCH [28] function is used to perform the signal processing of the unsteady wall pressures. Welch's method splits the time-dependent signal of the wall pressure fluctuations into different segments which are then multiplied by a window function. The window function helps to decrease aliasing and leakage by minimizing the weight near the beginning and end of the signal. The window function being used in this thesis is the Hanning window (Fig. 2.5).

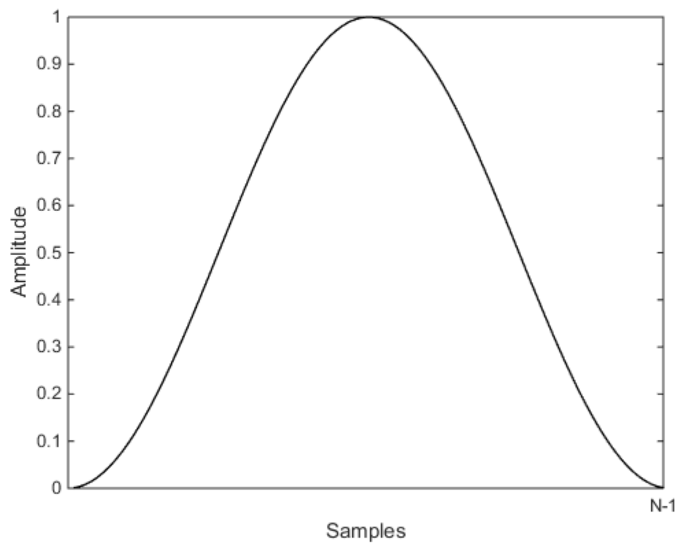

Figure 2.5 Coefficients of the Hanning window

Once the Hanning window is applied to each segment, the Fast Fourier Transform of the biased estimate of the autocorrelation sequence is used to compute the power spectral density (PSD). Assuming that X is a segment of the signal being analyzed, the above process for calculating the PSD is described by:

$$P(f) = \frac{\Delta t}{N}\left|\sum_{n=0}^{N-1} H_n X_n e^{-i2\pi f n}\right|^2 \qquad -\frac{1}{2}\Delta t < f \leq \frac{1}{2}\Delta t \tag{2.30}$$

where Δt is the sampling interval, H is the Hanning window and f is the frequency vector in Hz. The PSD segment are then averaged together to produce the estimate of the power spectral density. Because the process is wide-sense stationary and Welch's method uses PSD estimates of different segments of the time-dependent signal, *P(f)* represents the uncorrelated estimates of the true PSD which reduces variability due to the averaging. Note that the pressure has been non-dimensionalized as:

$$p^* = p\left(\frac{h_{nozzle}}{\overline{U_e}\mu_\infty}\right) \tag{2.31}$$

where h_{nozzle} represents the nozzle height, μ_∞ is the free-stream dynamic viscosity and $\overline{U_e}$ is the mean jet exit velocity. The Struhal number St is used to describe the non-dimensional frequency vector. A specific description of the scaling parameters has been omitted to preserve confidentiality.

$$St = f\left(\frac{h_{nozzle}}{\overline{U_e}}\right) \tag{2.32}$$

The cross-correlation *R* measures the similarity between two discrete-time sequences, x and y, as a function of the lag τ. The MATLAB XCORR function [38] is used to compute the cross-correlation between the unsteady wall pressure signals. By default, XCORR computes the raw correlation as:

$$R_k = \sum_{i=0}^{n-k-1} x_{i+k} * y_i^* \qquad k \geq 0 \tag{2.34}$$

where y^* is the complex conjugate of the signal y, $k = -n : n$ with n being the maximum length of the signals x and y. The sequence of the cross-correlation lags can be found by dividing the vector *k* by the sampling frequency of x and y.

$$\tau = \frac{k}{f_s} \tag{2.35}$$

The normalized cross-correlation is defined as the dimensional value of the cross-correlation divided by the product of the RMS surface pressure signals. The function handle *'coeff'* is used to normalize the sequence so that the auto-correlations at zero lag equal 1.

$$R_{norm} = \frac{R_k}{norm(x)*norm(y)} \tag{2.36}$$

where norm denotes the 2-norm of the vectors x and y. A copy of the MATLAB program used to generate the cross-correlations is included in Appendix A.

2.6 POD Analysis

The proper orthogonal decomposition (POD) is a statistical method that aims at obtaining a compact representation of the data and revealing relevant, but unexpected, structures hidden in the data. The fundamental idea behind POD is to decompose a time-dependent variable into a linear combination of spatial basis functions (POD modes) and a set of corresponding time-dependent coefficients. The POD modes are extracted using the "method of snapshots", initially introduced by Sirovich et al. [32] as a way to efficiently obtain a reduced-order model for unsteady aerodynamics applications containing large data sets.

The mathematical formulation presented here closely follows the one in reference [33]. Let p^i be a snapshot of the fluctuating pressure at time-step i. The vector p is arranged as an M x 1 column vector, where M is the total number of spatial points. The ensemble of all the snapshots N is defined as:

$$\phi = [p^1 \; p^2 \; \dots \; p^N] \qquad (2.33)$$

The sample auto-covariance matrix can be found by taking the inner product of the matrix ϕ with itself.

$$C = \phi^T \phi \qquad (2.34)$$

The mode information is obtained by solving for the eigenvalues, λ^i, and eigenvectors, A^i, of the auto-covariance matrix.

$$CA^i = \lambda^i A^i \qquad (2.35)$$

There are N eigenvalues, λ^i, that correspond to N eigenvectors, A^i. Since all covariance matrices are symmetric and positive semi-definite, each of the eigenvalues must be real and non-negative. The eigenvalues, and their corresponding eigenvectors, are arranged and numbered from largest to smallest:

$$\lambda^1 > \lambda^2 > \lambda^3 > \cdots > \lambda^N = 0 \qquad (2.36)$$

The POD modes, Θ^i, are found by performing an orthogonal transformation to the basis of the eigenvectors of the sample auto-covariance matrix, and then projecting the data onto a subspace spanned by eigenvectors corresponding to the largest eigenvalues as shown in Eq. 2.37. The eigenvalues represent the energy contribution for each mode Θ^i .

$$\theta^i = \frac{\sum_{n=1}^{N} A_n^i p^n}{\left\|\sum_{n=1}^{N} A_n^i p^n\right\|} \tag{2.37}$$

To perform the POD reconstruction, the matrix ℵ is formed from the mode shapes

$$\aleph = [\theta^1\ \theta^2\ \dots\ \theta^k] \tag{2.38}$$

Where k indicates the number of POD modes used in the reconstruction. The POD coefficient a_i can be found for the snapshot n as:

$$a_i = \aleph^T p^i \tag{2.39}$$

The ℵ matrix is then multiplied by the coefficient matrix to reconstruct the Mx1 pressure fluctuation vector p_r at time step i.

$$p_r^i = \aleph a_i \tag{2.40}$$

This process is repeated for every snapshot in time from $1 \leq i \leq N$ to produce the full reconstructed pressure field. A copy of the MATLAB script used to generate the POD plots is included in Appendix B. The POD visualization is based on the MATLAB code written by Michael Lurie [27]. The next chapter describes the simulation results obtained with Wind-US.

2.7 Summary

This chapter described the numerical methods necessary to carry out CFD calculations of the unsteady aeroacoustic loading generated by the exhaust of a rectangular jet on a deck downstream of the nozzle exit. Wind-US, a CFD code developed by the NASA Glenn Research Center and the Arnold Engineering Development Center, is used to perform the simulations. The Wind-US calculations presented in this thesis are executed using the LESb hybrid method, where a standard RANS model is used in the boundary layer regions and smoothly transitions to a sub-grid scale formulation in regions where the grid resolution is fine enough to support the LES

A multi-block structured grid is used to mesh the aft-deck geometry. A computational grid with high-density layers near the deck surface, shear layer and along the nozzle centerline is used to properly resolve the development of the jet shear layer and boundary layer.

The following chapter will detail the results of the numerical calculations and compare them to the experimental measurements.

Chapter 3
Simulation Results

This chapter outlines results of the numerical simulations performed with Wind-US. The approach used to simulate the wall-bounded jet flow has been described in Chapter 2. In this chapter comparisons with the wall pressure data provided by United Technology Research Center (UTRC) are made to study the effects of several numerical parameters on the computed jet flow. Each section describes the results from the numerical parametric studies. The calculations have been performed at a nozzle pressure ratio (NPR) of 4.0, simulating an under-expanded flow. All CFD calculations are performed using a total temperature ratio (TTR) of 1.5 and a sampling frequency f_s of 33.3 kHz. Table 3.1 below lists the various simulation parameters associated with each parametric study.

Table 3.1 Simulation parameters.

Parametric Study	Parameter
Boundary layer stability preservation	CFL_{max}
Turbulence dissipation	C_b
Time step	Δt
Grid sequencing	Δx
Numerical scheme	N
Upstream forcing	U_f
Boundary layer shield	BL_s

3.1 *Boundary Layer Stability Preservation*

A first set of calculations has been performed on an under-expanded case in order to investigate the impact of the boundary layer stability model (CFL_{max}) on the computed turbulent jet. The modification to the LESb model improves the boundary layer stability and enables the use of longer time steps. The input parameters used for the unsteady LESb calculations are shown in Table 3.2. Δt represents the physical time step used in the time accurate region, NPR is the nozzle pressure ratio, M is the inflow Mach number, T is the total temperature, P is the total pressure and C_b is a multiplier for the turbulence damping. CFD predictions from the time-accurate simulation (run 1) are compared to the results from the constant CFL simulations (runs 2, 3 and 4). All data has been non-dimensionalized for proprietary reasons.

The time accurate simulation is limited by a time step size of Δt = 0.3 μs in order to ensure numerical stability. For the Δt = 3 μs case, CFL_{max} values higher than 9.0 are found to make the LESb model unstable. It is possible that the strong shocks present in the under-expanded case generate sharp gradients near the boundary layer and the shear layer, thus imposing a limit on the maximum time step size required to capture the sudden changes in the local properties of the flow.

Table 3.2 Input conditions used for the boundary layer preservation parametric study.

Run	NPR	M	T (R)	P (psi)	Δt (μs)	CFL_{max}	C_b	t_{run} (s)
1	4.0	0.5	777	58.8	0.3	---	0.01	0.04
2	4.0	0.5	777	58.8	3	9.0	0.01	0.04
3	4.0	0.5	777	58.8	3	5.0	0.01	0.04
4	4.0	0.5	777	58.8	3	3.0	0.01	0.04

First a study is performed on the NPR = 4.0 case to investigate the impact of the total run time on the calculated surface pressure spectra. The input conditions used to initialize the LESb model are shown in Table 3.3. The time-dependent signal of the non-dimensional pressure fluctuations on the deck surface are converted into their power spectral density using the Welch PSD estimate. The Welch function uses a sliding Hanning window of 1024 samples with a 50% overlap. Two of the sampling locations along the nozzle ¼ span are used to generate the power spectral density plots are shown in Fig. 3.1. The PSD estimates show that a run length of 0.04 seconds is sufficient to accurately predict the wall-pressure spectrum (relative to the time accurate case). Therefore, a total run time of 0.04 seconds is used to accumulate the time history data from the LESb simulations. The first 0.002 seconds have been discarded in order to exclude any initial transient from the data post-processing. The length of the transient period corresponds to the time required by a large-scale eddy structure to travel the length of the deck with a convective speed equal to 65% of the jet exit velocity. This agrees well with the findings by Murakami and Papamoschou et al. [29].

Table 3.3 LESb input conditions

NPR	M	T (R)	P (psi)	Δt (μs)	CFL_{max}	C_b
4.0	0.5	777	58.8	6	11	0.1

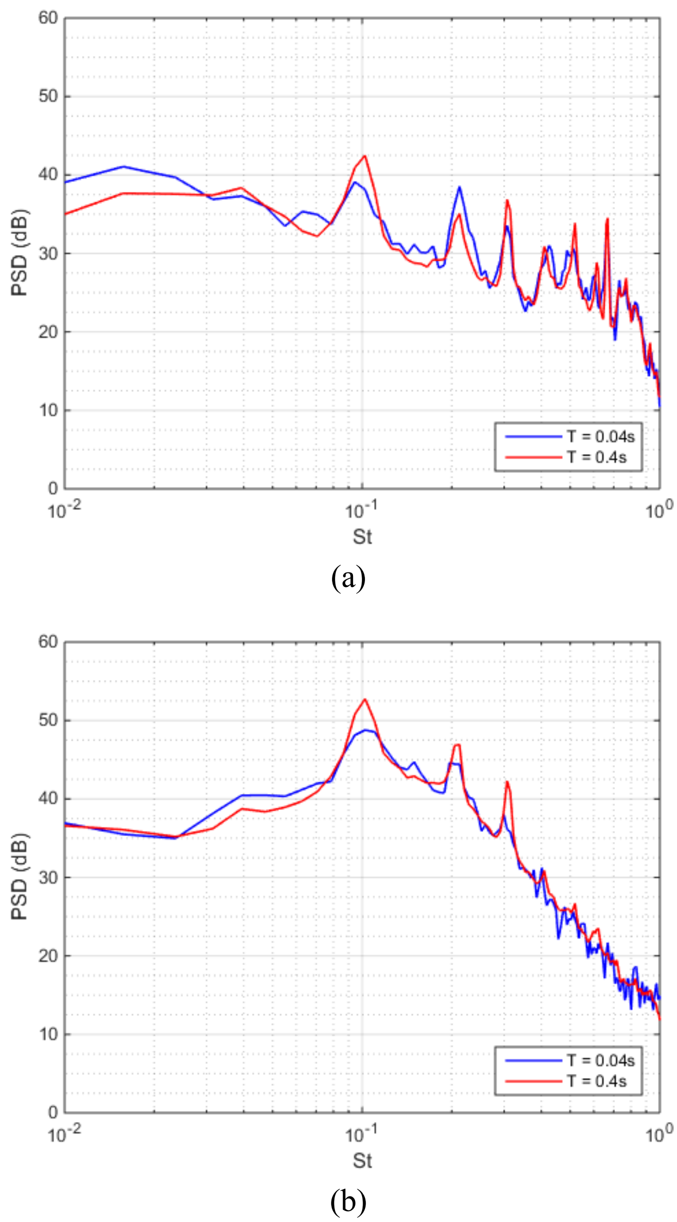

Figure 3.1 Welch power spectral densities of surface pressure fluctuations along the nozzle ¼-span at (a) x/h_{nozzle} =8.3; (b) x/h_{nozzle} =11.8.

The impact of the constant CFL region on the computed Welch power spectral densities along the nozzle ¼ span is presented in Fig. 3.3. The sensors used to generate the PSD plots are aligned along the nozzle ¼ span (Fig. 3.2). The gray scale contour of the mean surface pressure from the RANS simulation shows the evolution of the shock structure with downstream distance from the jet exit. The scale of the pressure contour has been removed from this plot and it is used for illustrative purposes. The x/h_{nozzle} = 2.4 and 7.1 sensor locations will be referred as "upstream" while the location for the x/h_{nozzle} = 11.8 sensor will be referred as "downstream".

The modified LESb model introduces artificial oscillations with peak frequencies that scale directly with CFL_{max}. However, this phenomenon is localized in regions where a strong laminar shock-boundary layer interaction occurs. The numerical mechanisms causing the periodic instabilities are not yet well understood. Figure 3.3c shows that less high-frequency unsteadiness is predicted for the LESb case that has the lowest CFL limit in the boundary layer (CFL_{max} = 3). Comparisons between the UTRC measurements and the Wind-US simulations show that the LESb models predict the PSD poorly at the upstream locations, where the simulations over-estimate the unsteady forces at St < 0.1. At the downstream locations, the time-accurate LESb model does an improved job at predicting the unsteadiness on the deck. However, all simulations over-estimate the frequency content above St = 0.1, which indicates that the solutions are under-damped.

The frequency range of interest for the analysis of potential structural modes on the deck surface is $St = 0.005 - 0.5$. Figure 3.3a shows that in simulations where CFL_{max} is greater than 3.0, the spurious oscillations are confined to frequencies higher than St = 0.5. Therefore, it can be concluded that the frequencies of interest are not affected by the non-physical unsteadiness as long as CFL_{max} is higher than 3.0.

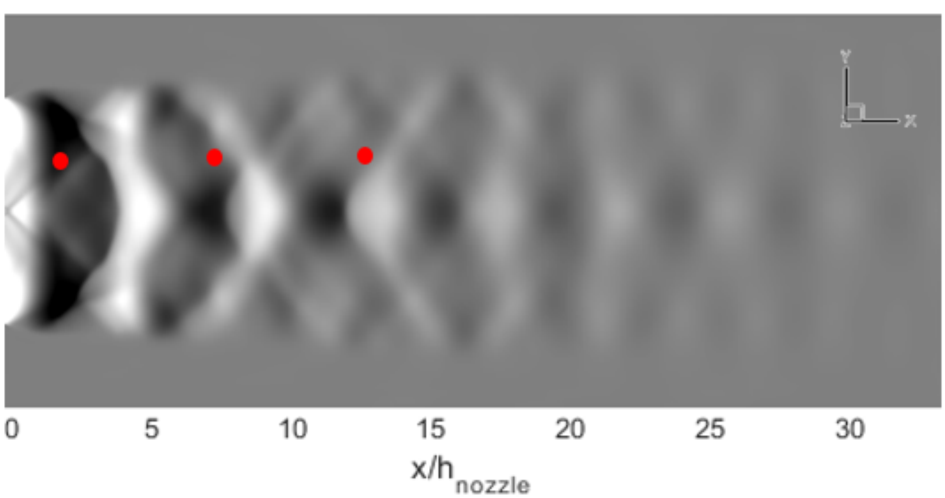

Figure 3.2 Surface sensor used to generate the power spectral density plots

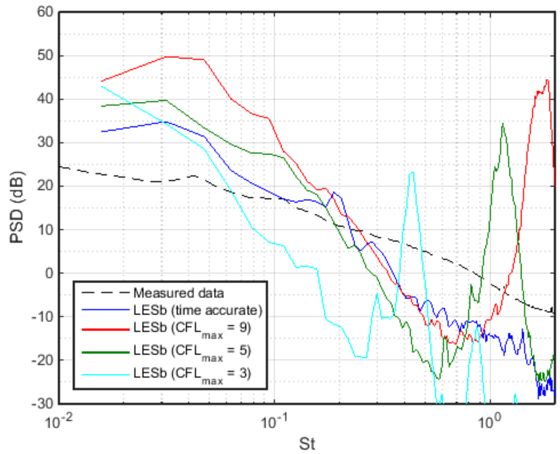

(a)

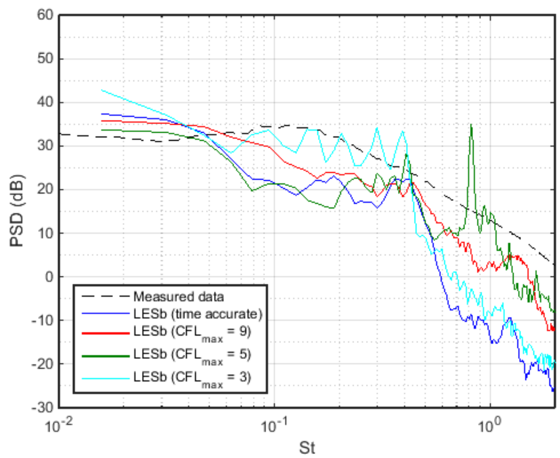

(b)

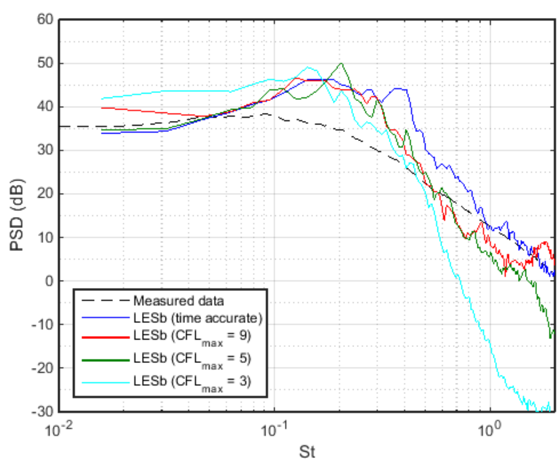

(c)

Figure 3.3 Welch power spectral densities of surface pressure fluctuations along the nozzle ¼-span at (a) x/h_{nozzle} = 2.4; (b) x/h_{nozzle} =7.1; (c) x/h_{nozzle} =11.8

Figure 3.4 shows the extent of the region with spatially varying time steps for the non-time accurate runs. The time step contours indicate that for CFL_{max} values greater than 3.0, the constant CFL region is confined to the outer edge of the boundary layer. When CFL_{max} is less than 3.0, the constant CFL region extends all the way to the shear layer (x/h_{nozzle} = 1). The subsequent numerical studies will be performed using a CFL_{max} higher than 3.0 in order to prevent the stretched-time region from influencing the flow in the potential core and the shear layer.

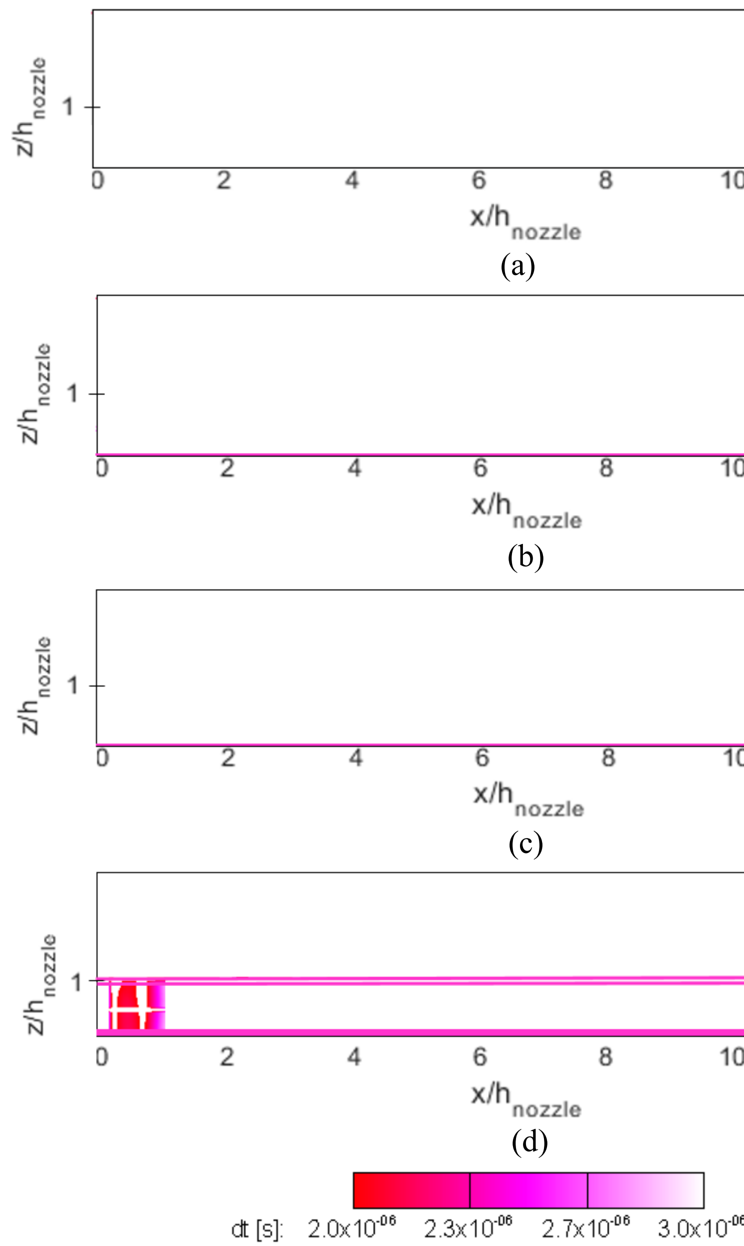

Figure 3.4 Time-step contours from LESb simulations. (a) Time-accurate; (b) CFL_{max} = 9; (c) CFL_{max} = 5; (d) CFL_{max} = 3

A cutting plane normal to the deck surface is used to generate the accumulated mean Mach number contours of the flow exiting the nozzle for the steady-state RANS and the LESb solutions. Figures 3.5 and 3.6 show the results along the nozzle centerline and the ¼ span. While the use of the boundary layer stability preservation scheme does not show any noticeable impact on the profile of the shear layer, there is a significant difference between the RANS and the LESb solutions, especially in the development of the initial shear layer along the nozzle ¼ span (Fig. 3.6). Large-Eddy Simulation, by definition, is a technique in which not all scales of motion are resolved. When performing LESb calculations to predict the development of shear layers and vortices whose scale is close the numerical filter, it is very important to retain the energy of the low-level perturbations during the initial stages of the shear layer transition from laminar to turbulent. Inadequate resolution of the turbulence structures in the nozzle boundary layer and at the nozzle exit may lead to a longer transitional behavior of the initial jet layers [30]. It can therefore be concluded that the azimuthal grid in the vicinity of the nozzle exit has inadequate resolution for the LESb model to correctly resolve the initial shear layer development. Additionally, the LESb solutions show an overly-damped shock train compared to the RANS solution.

The RANS model under-predicts the level of turbulence in the potential core region, thus reducing the amount of turbulent mixing and slowing the shear layer growth rate throughout the flow field. This is because RANS models are based upon a time average of the unsteady Navier-Stokes equations, which inherently contain less information. Since the three-dimensional structures play a key role in the development of turbulent jet flows, it is difficult for RANS-based models to accurately replicate the physics even in an average sense. The LESb predicts the start of the transition region at $x/h_{nozzle} = 28$, while the RANS model shows a potential core that extends beyond $x/h_{nozzle} = 35$ (Fig. 3.6).

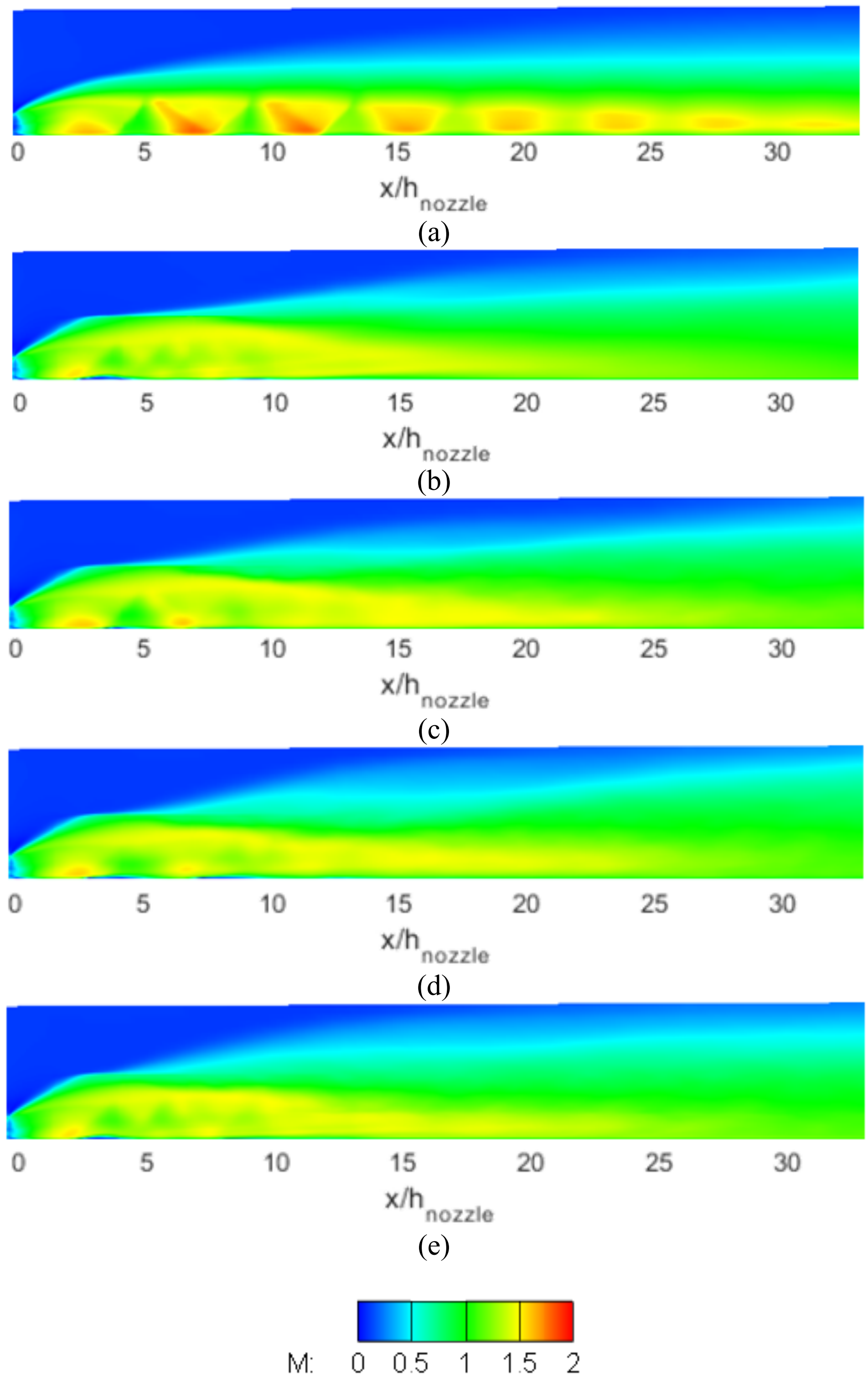

Figure 3.5 Mean Mach number contours along the nozzle centerline for (a) SSRANS; (b) Time-accurate; (c) $CFL_{max} = 9$; (d) $CFL_{max} = 5$; (e) $CFL_{max} = 3$.

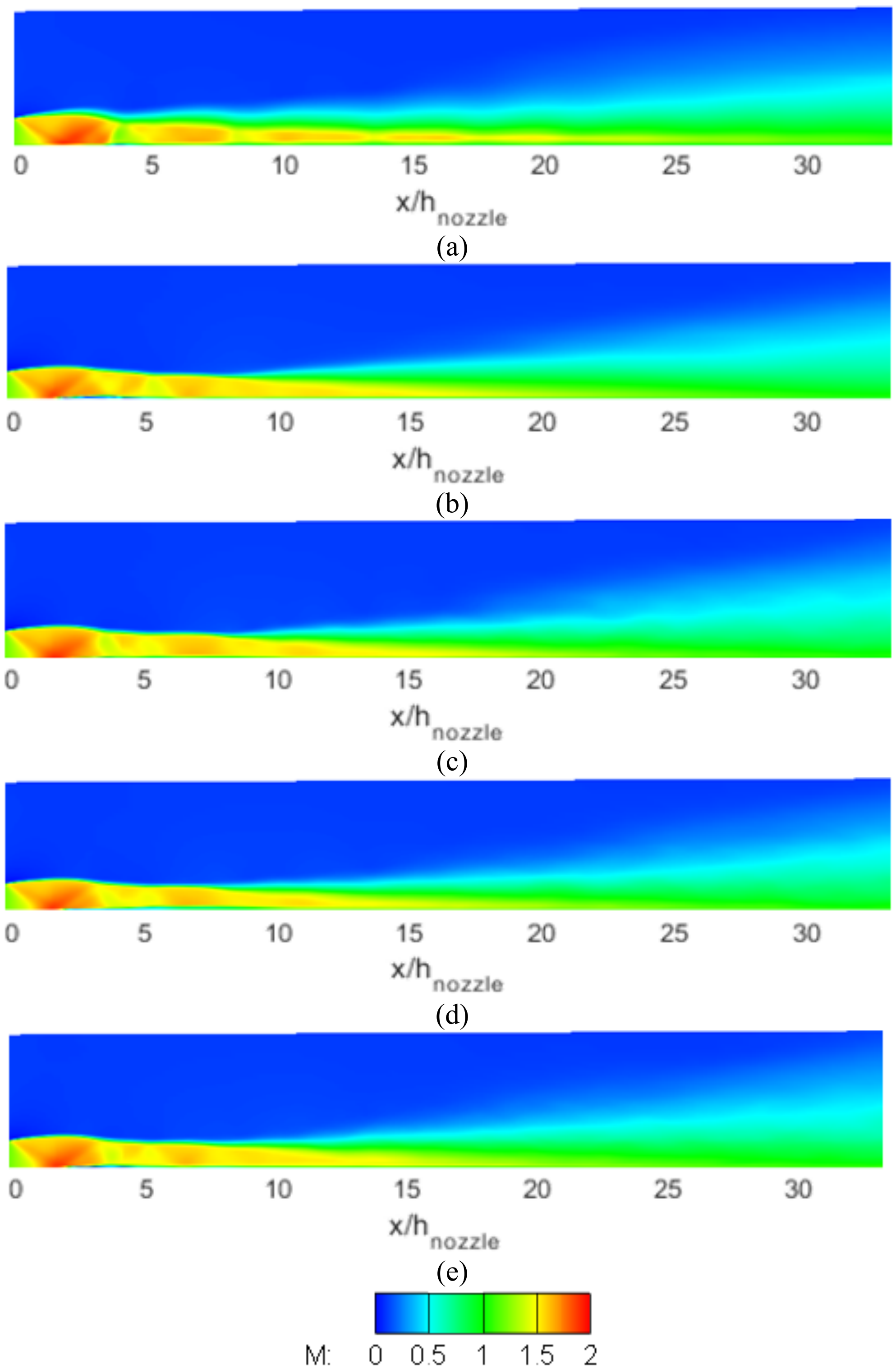

Figure 3.6 Mean Mach number contours along the nozzle ¼ span for (a) SSRANS; (b) LESb Time-accurate; (c) $CFL_{max} = 9$; (d) $CFL_{max} = 5$; (e) $CFL_{max} = 3$.

From observations of the mean surface pressure along the nozzle centerline (Fig. 3.7), the shock intensity shows a strong dependence on the constant CFL threshold in the boundary layer. The simulations running with CFL_{max} predict higher pressure levels than the time accurate run between x/h_{nozzle} = 0 and x/h_{nozzle} = 15 while the solution from the SS-RANS simulation shows good agreement with the measured data (Fig. 3.8). Furthermore, the RANS model predicts substantially stronger shocks compared to the LESb model. This is likely due to the extra damping caused by the artificial dissipation of the LES model and the inability of the LES model to resolve the turbulent structures near the surface, resulting in a quasi-laminar boundary layer, especially at lower CFL_{max} values. Note that the time accurate run shows an increase in mean surface pressure at x/h_{nozzle} = 6.5 which is not predicted by the other numerical simulations.

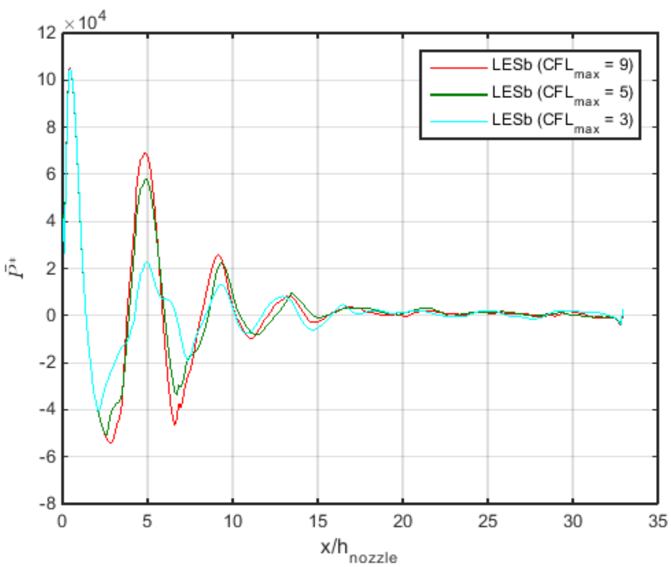

Figure 3.7 Mean surface pressure along the nozzle centerline

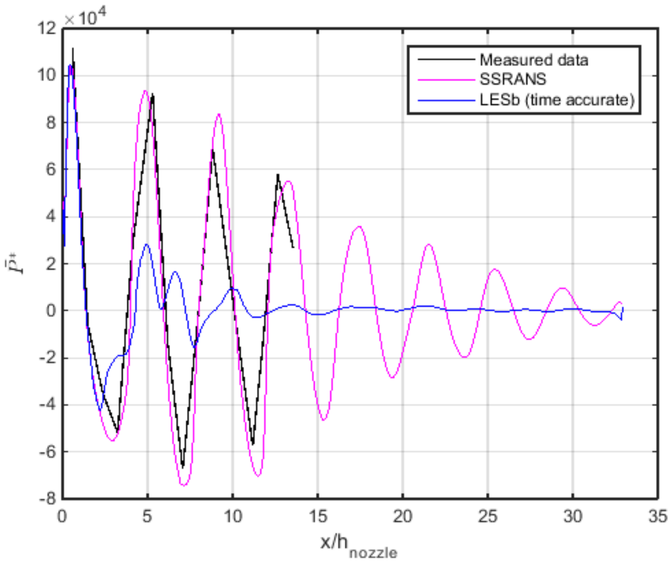

Figure 3.8 Mean surface pressure along the nozzle centerline.

Plots of the boundary layer profiles along the nozzle centerline are shown in Figure 3.9. The profiles upstream of the first shock-boundary layer interaction ($x/h_{nozzle} = 1$) are very similar between all of the LESb runs. The steady-state RANS consistently predicts a thinner boundary layer as a result of the larger turbulent shear stress computed by the RANS model. The LESb solutions show significantly different stream-wise velocity profiles downstream of the second shock-boundary layer interaction ($x/h_{nozzle} = 5$). Note that the wall shear stress grows with increasing CFL_{max}, thus producing a steeper gradient of velocity while the simulations running with a lower CFL_{max} predict a velocity profile typical of a laminar boundary layer. The difference between the predicted profiles may be also attributed to the introduction of artificial instabilities by the constant CFL region in the boundary layer. A detailed analysis of the numerical artifacts from the constant CFL solutions is shown below.

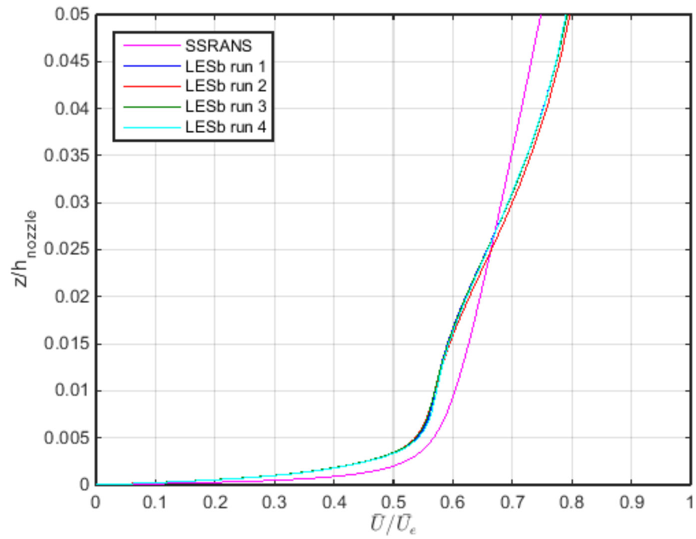

(a)

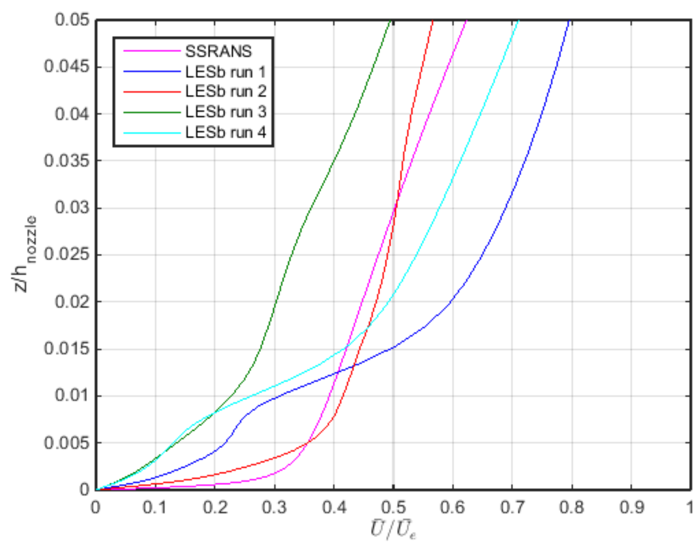

(b)

Figure 3.9 Mean stream-wise velocity along the nozzle centerline at (a) $x/h_{nozzle} = 1$; (b) $x/h_{nozzle} = 5$. Velocity levels are normalized by the mean jet exit velocity

A proper orthogonal decomposition (POD) of the fluctuating pressure field is used to analyze the flow structures and the numerical errors introduced by the constant CFL method in the boundary layer. The POD process computes a set of orthogonal modes from snapshots of the instantaneous CFD solutions. The POD decomposition is optimal in the sense that a snapshot may be reconstructed satisfactorily using only a few of the most energetic modes. The analysis is performed over a period of 100 time steps and the first 5 POD modes are used to reconstruct each snapshot of the pressure along the nozzle ¼-span. The reconstructions of the first 4 individual modes for each of the numerical solutions are shown in Appendix C. Figure 3.10 shows that the first 5 modes contain over 90% of the total energy in the system.

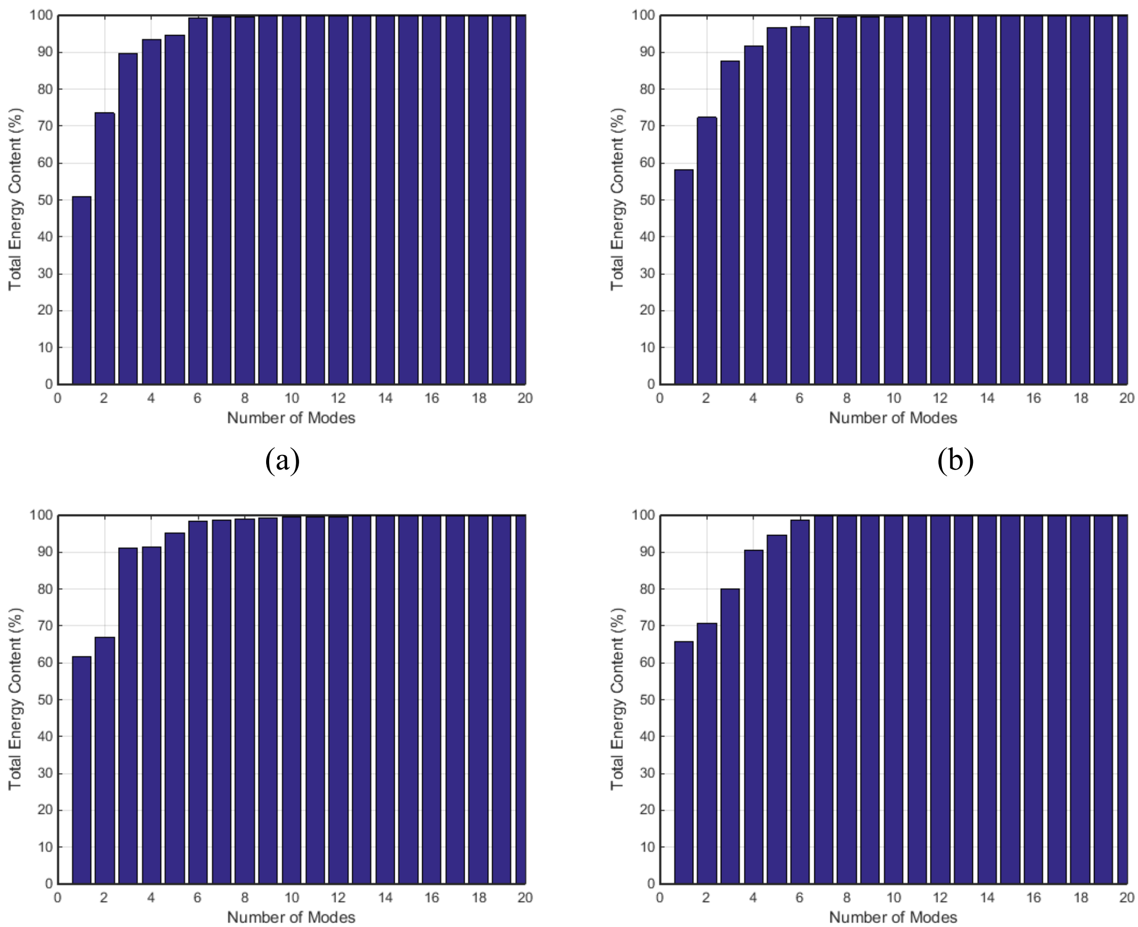

(a) (b)

(c) (d)

Figure 3.10 modal energy content for (a) Time-accurate; (b) $CFL_{max} = 9$; (c) $CFL_{max} = 5$; (d) $CFL_{max} = 3$

Figures 3.11 – 3.12 show instantaneous contour plots of the reconstructed total and fluctuating pressure fields along the nozzle ¼ span over a period of 30 μs. Note that the color scales of these modes have been omitted from this thesis. The dark blue indicates regions of low pressure while the dark red represents regions of high pressure. The time-accurate simulation shows strong activity in the shear layer region starting at $x/h_{nozzle} = 4$. These modes may be generated by the interaction between the shocks and the jet shear layer. The strength and size grow as the fluctuations in the shear layer travel downstream.

Figure 3.11 shows that the stretched-time cases increase the strength of the artificial structures introduced by the LESb model. The modes travel downstream and appear to be originating at approximately x/h_{nozzle} = 3.5, where the flow separation from the laminar shock-boundary layer interaction (SBLI) drastically changes the pressures at the wall. This phenomenon is shown clearly in the CFL_{max} = 3.0 case, where the most energetic POD modes are the artificial oscillations near the deck surface. The overall energy content of the reconstructed POD modes increases with decreasing CFL_{max} as a result of the expansion of the stretched-time domain. Figures 3.12b – 3.12c show that for simulations running with a CFL_{max} limit larger than 3.0, the artificial oscillations are confined to a very small domain and do not interfere with the remainder of the flow field. The frequencies of the periodic fluctuations coincide with the absolute frequency peaks observed in the PSD plots (Fig. 3.3).

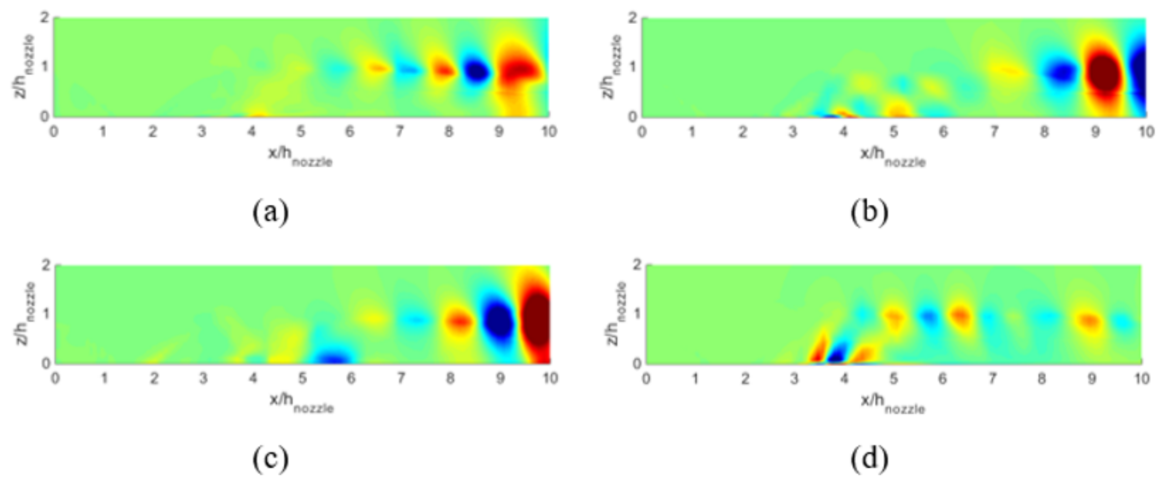

Figure 3.11 Snapshots of the reconstructed fluctuating pressure along the nozzle ¼ span at t = 0.0385 s. (a) Time-accurate; (b) $CFL_{max} = 9$; (c) $CFL_{max} = 5$; (d) $CFL_{max} = 3$.

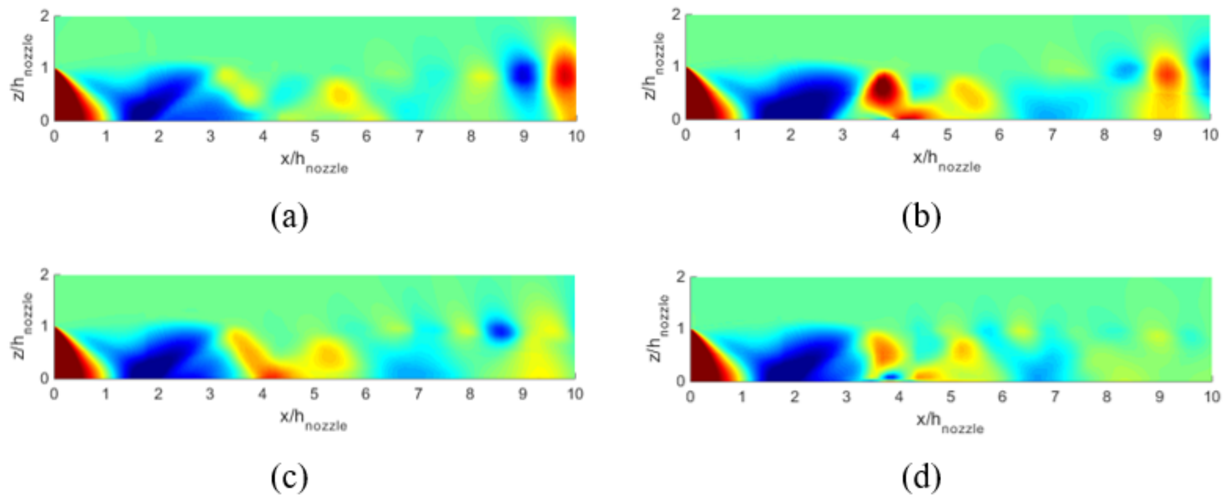

Figure 3.12 Snapshots of the reconstructed total pressure along the nozzle ¼-span at t = 0.0385 s. (a) Time-accurate; (b) $CFL_{max} = 9$; (c) $CFL_{max} = 5$; (d) $CFL_{max} = 3$.

The two-point cross-correlation coefficients R_{ij} of the unsteady wall pressures are shown in Figures 3.14 – 3.17. The sampling locations used to generate the normalized cross-correlation plots are shown in Fig. 3.13. The pairs of points in the axial direction, AB and AC, are separated by $x/h_{nozzle} = 0.9$ while the pairs DE and DF are separated by $x/h_{nozzle} = 2.7$. The span-wise cross correlations BG, BH, EI and EJ are generated using a separation distance of $x/h_{nozzle} = 0.9$. When the correlation coefficient is zero, two signals are considered uncorrelated with each other while a coefficient of unity indicates that the two signals are perfectly correlated. The A, B, C, G and H sensor location will be referred as "upstream" while the locations for D, E, F, I and J sensors will be referred as "downstream".

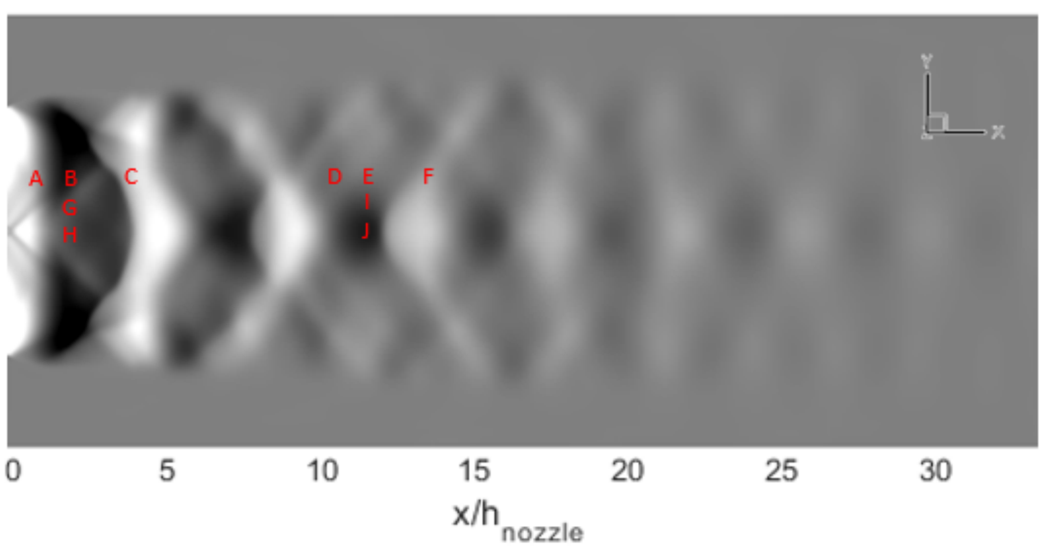

Figure 3.13 Surface sensor locations used to analyze the wall-pressure cross-correlations

The axial convective velocities at the downstream locations are computed from the lag of the correlation peak and are shown in Table 3.4. The convection speed is often assumed to be 60% of the experimental jet exit velocity. A comparison between the experimental and numerical data shows that the LESb model over-predicts the convection velocity by 35%.

Table 3.4 Convection axial velocities

	V_{DE} (ft/s)	V_{DF} (ft/s)
Measured data (60% U_e)	893	893
Time-accurate	1488	1136
$CFL_{max} = 9$	1389	1025
$CFL_{max} = 5$	1389	1042
$CFL_{max} = 3$	1389	1025

Figure 3.14a shows good upstream correlation when the sensors on the deck are separated by x/h_{nozzle} = 0.9, yet by x/h_{nozzle} = 2.7 the signals become nearly uncorrelated. The correlation strength and the correlation length from the measured data grow when the sensors are moved further downstream because the characteristic scales grow with increasing downstream distance. A similar behavior is observed in the stretched-time LESb results, although the computed cross-correlation peaks are much higher. The overall trend in the plots shows that the LESb models predicts cross-correlations that are four times the peak values of the measured data for the upstream sensors and nearly perfect cross-correlations for the downstream locations.

The quasi-periodic nature of the cross-correlation function in the numerical predictions is the result of strong, narrow-band flow oscillations in the boundary layer. It is believed that these are numerical artifacts introduced by the LESb hybrid model as they are present even when the CFL_{max} subroutine is disabled. Moreover, the strength and frequency of the oscillations changes based on how far the LES model extends within the boundary layer. Figure 3.14 illustrates that the constant CFL in the boundary layer alters the coherent nature of unsteady pressures on the deck, where the period between the correlation peaks decreases with increasing CFL_{max}. In the time-accurate simulation, the stream-wise cross-correlation peaks between sensors A and B repeat at a frequency of 786 Hz. Instead, the simulations running with $CFL_{max} = 9$, $CFL_{max} = 5$ and $CFL_{max} = 3$ show frequencies equal to 706 Hz, 553 Hz and 464 Hz, respectively. However, the impact of the constant CFL in the boundary layer on the cross-correlation functions is much less severe at $x/h_{nozzle} = 10$, where the jet shear layer begins to dominate the unsteadiness at the wall (Fig. 3.15). Note that the alignment of the cross-stream correlation peaks in Figures 3.16 and 3.17 indicates that the convected turbulent structures near the wall are nearly two-dimensional.

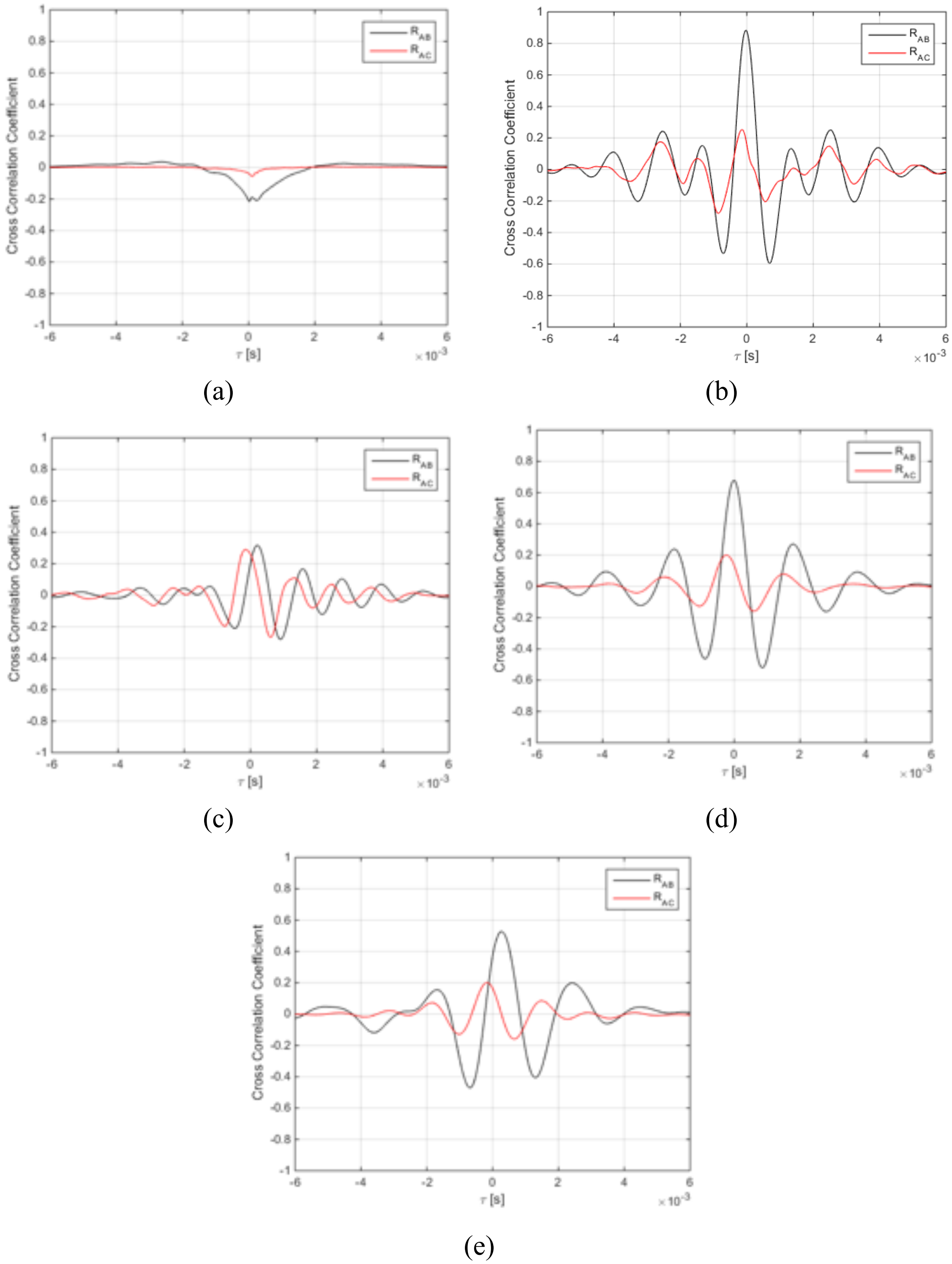

Figure 3.14 Upstream axial pressure correlations from the NPR = 4.0 data. (a) Measured; (b) Time-accurate; (c) CFL_{max} = 9; (d) CFL_{max} = 5, (e) CFL_{max} = 3.

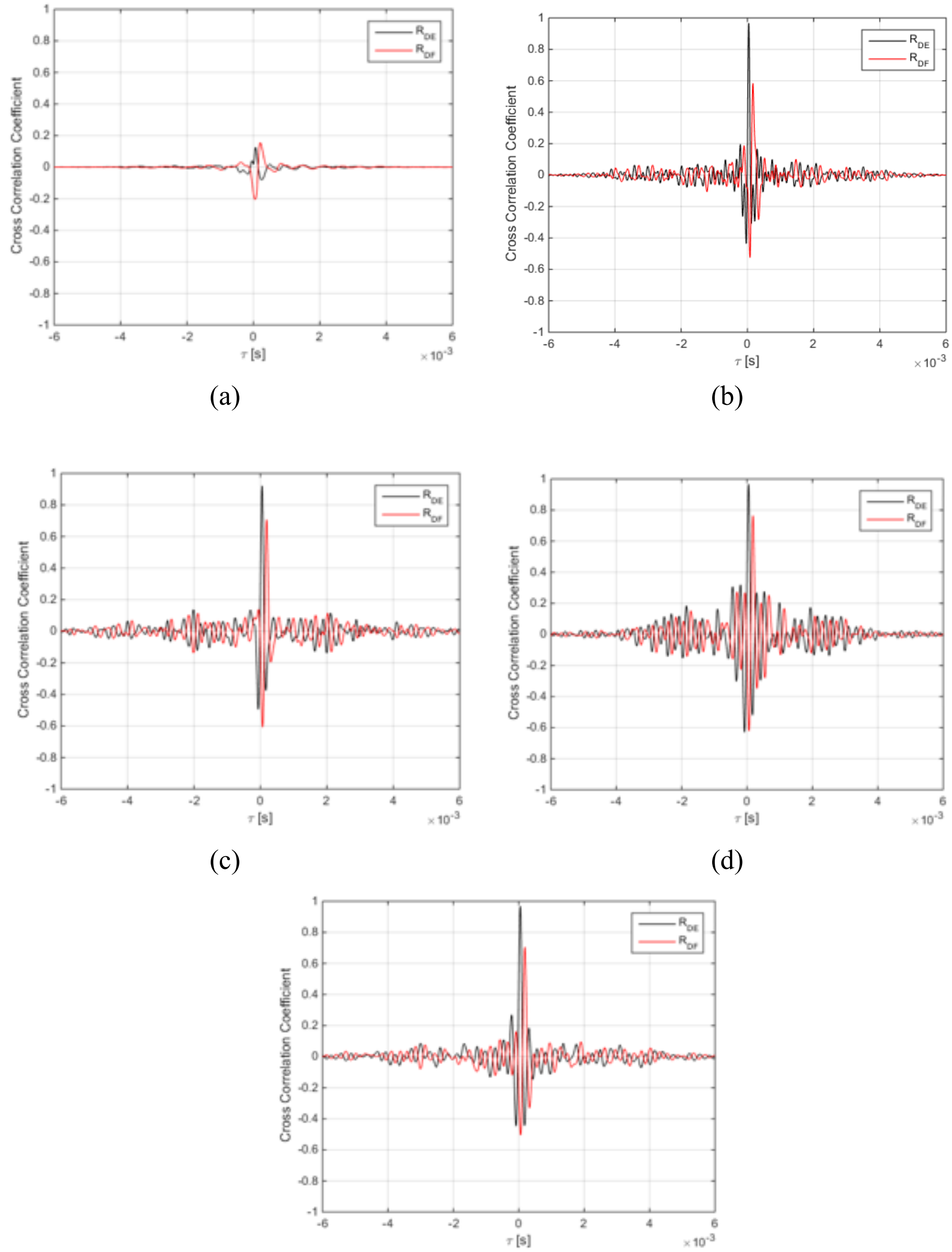

Figure 3.15 Downstream axial pressure correlations from the NPR = 4.0 data. (a) Measured; (b) Time-accurate; (c) $CFL_{max} = 9$; (d) $CFL_{max} = 5$; (e) $CFL_{max} = 3$.

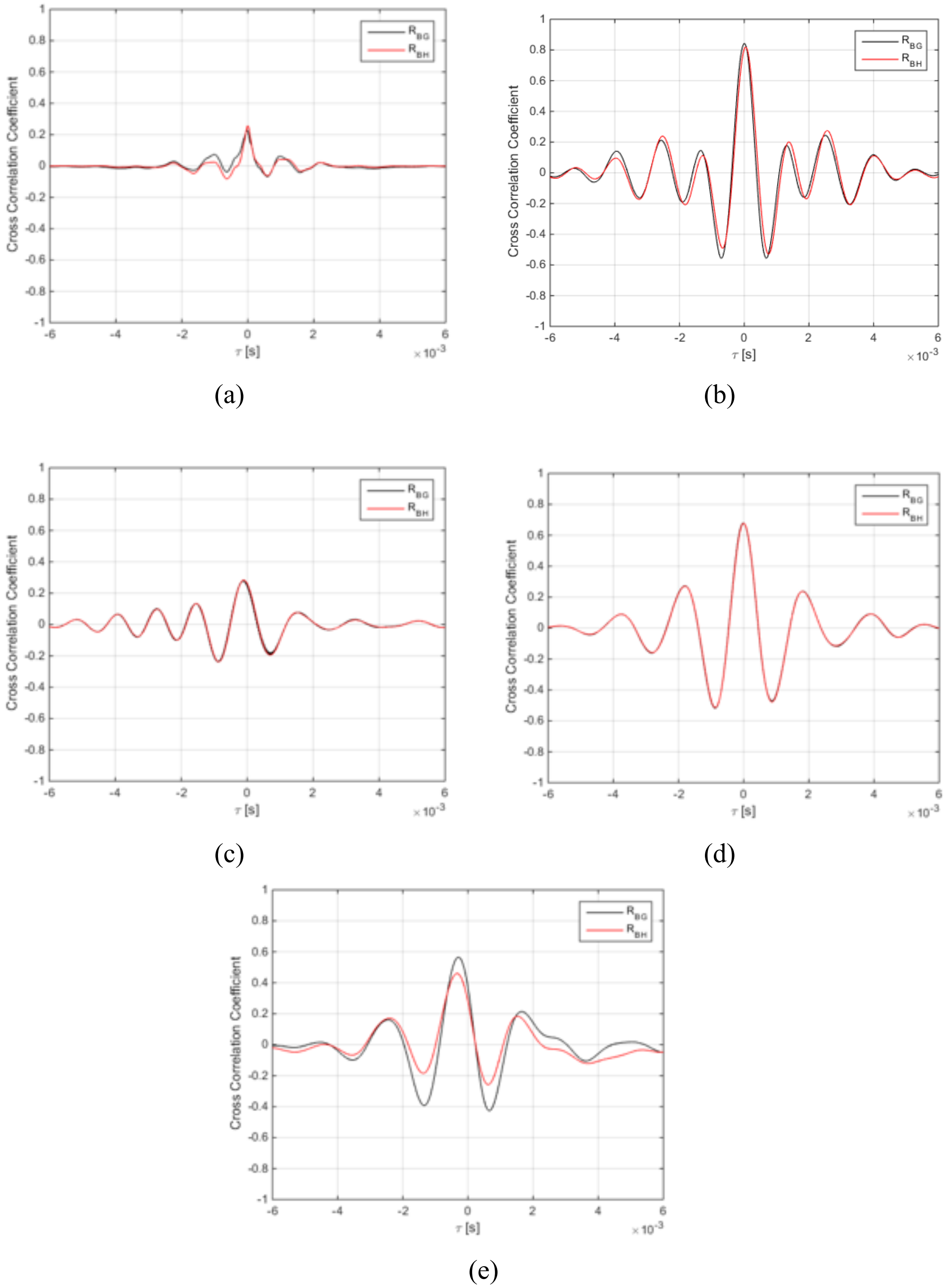

Figure 3.16 Upstream cross-stream pressure correlations from the NPR = 4.0 data. (a) Measured; (b) Time-accurate; (c) $CFL_{max} = 9$; (d) $CFL_{max} = 5$; (e) $CFL_{max} = 3$

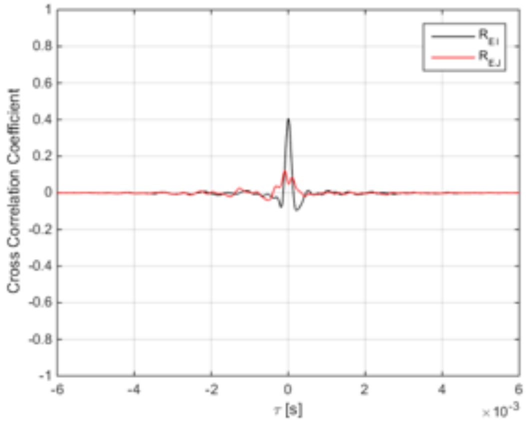

(a)

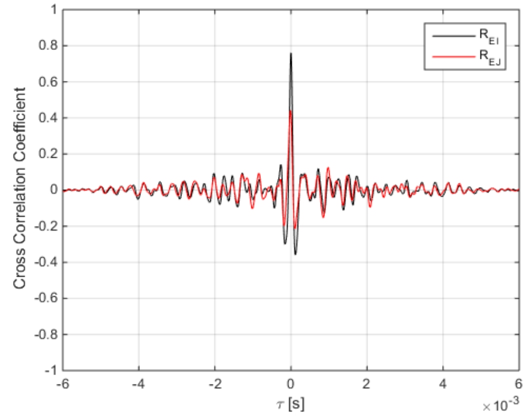

(b)

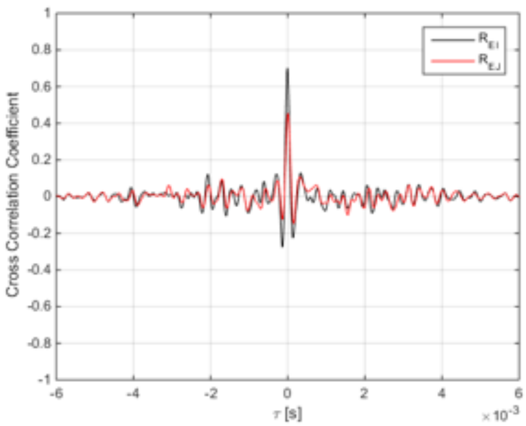

(c)

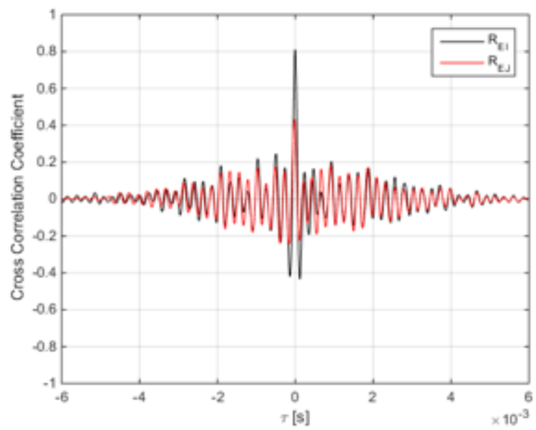

(d)

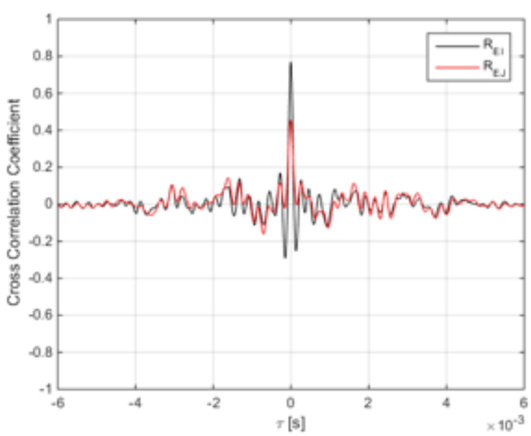

(e)

Figure 3.17 Downstream cross-stream pressure correlations from the NPR = 4.0 data. (a) Measured; (b) Time-accurate; (c) $CFL_{max} = 9$; (d) $CFL_{max} = 5$; (e) $CFL_{max} = 3$.

3.2 Turbulence Dissipation

This section outlines the effects of the turbulence dissipation on the computed jet flow. The length scale coefficient C_b is used to model the turbulence viscosity and to impose a limit on the turbulent kinetic energy dissipation as described in Chapter 2. Increasing C_b favors the growth of the region where the hybrid LESb model reduces to a RANS-based turbulence model and accelerates the rate at which turbulent kinetic energy is converted into thermal internal energy.

A numerical study has been conducted on the NPR = 4.0 case using the LESb solver with a constant CFL in the boundary layer. The input conditions are shown in Table 3.5. The analysis begins with an inspection of the power spectral density estimates along the nozzle ¼-span (Fig. 3.18). The sensors locations are identical to those used in section 3.1.

Table 3.5 Input conditions used for the turbulence dissipation parametric study.

Run	NPR	M	T (R)	P (psi)	Δt (μs)	CFL_{max}	C_b
5	4.0	0.5	777	58.8	5	5.0	1.0
6	4.0	0.5	777	58.8	5	5.0	0.1
7	4.0	0.5	777	58.8	5	5.0	0.01

Figure 3.18a shows that the amount of turbulent energy dissipation does not have a significant impact on the upstream wall-pressure spectra, where the unsteadiness is dominated by the shock-boundary layer interactions. Further downstream, the added viscosity overdamps the unsteadiness of the boundary layer and the shear layer, thus generating different spectral contents. Again, the numerical solutions show an over-prediction of the low frequency unsteadiness at the upstream locations while for the $C_b = 0.1$ case the model agrees very well with the measured data (Figure 3.18c). Contrarily, the solution of the $C_b = 1$ case shows a significantly lower power spectral density content, as a result of the excessive turbulence damping.

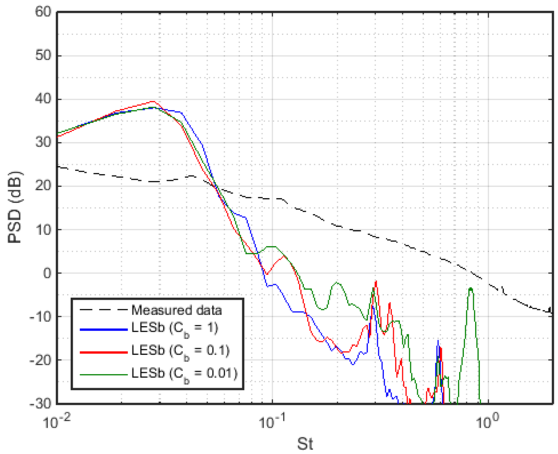

(a)

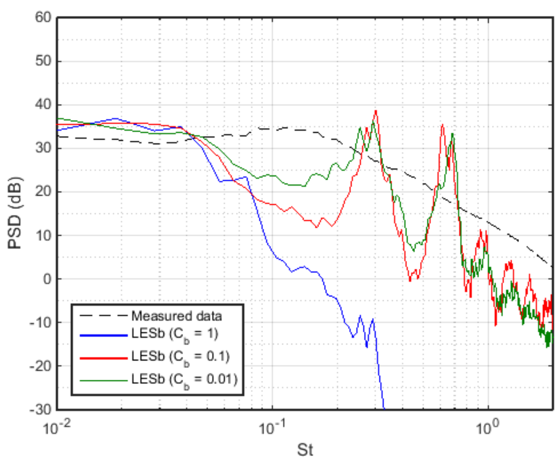

(b)

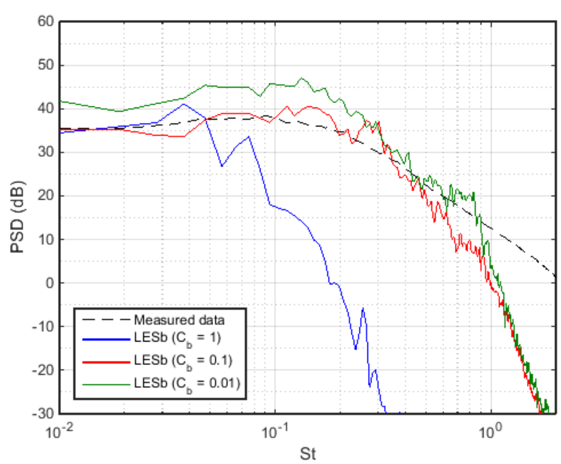

(c)

Figure 3.18 Welch power spectral densities of surface pressure fluctuations along the nozzle ¼-span at (a) $x/h_{nozzle} = 2.4$; (b) $x/h_{nozzle} = 7.1$; (c) $x/h_{nozzle} = 11.8$.

The mean Mach number contours along the nozzle centerline (Fig. 3.19) show that the shock train profile approaches the RANS solution when $C_b \geq 1$. This is due to an over-damping of the unsteadiness in the boundary layer and in the shear layer which reduces the growth rate of the shear layer and increases the shock strength. A similar behavior can be seen in the accumulated Mach number contours along the nozzle ¼ span in Figure 3.20.

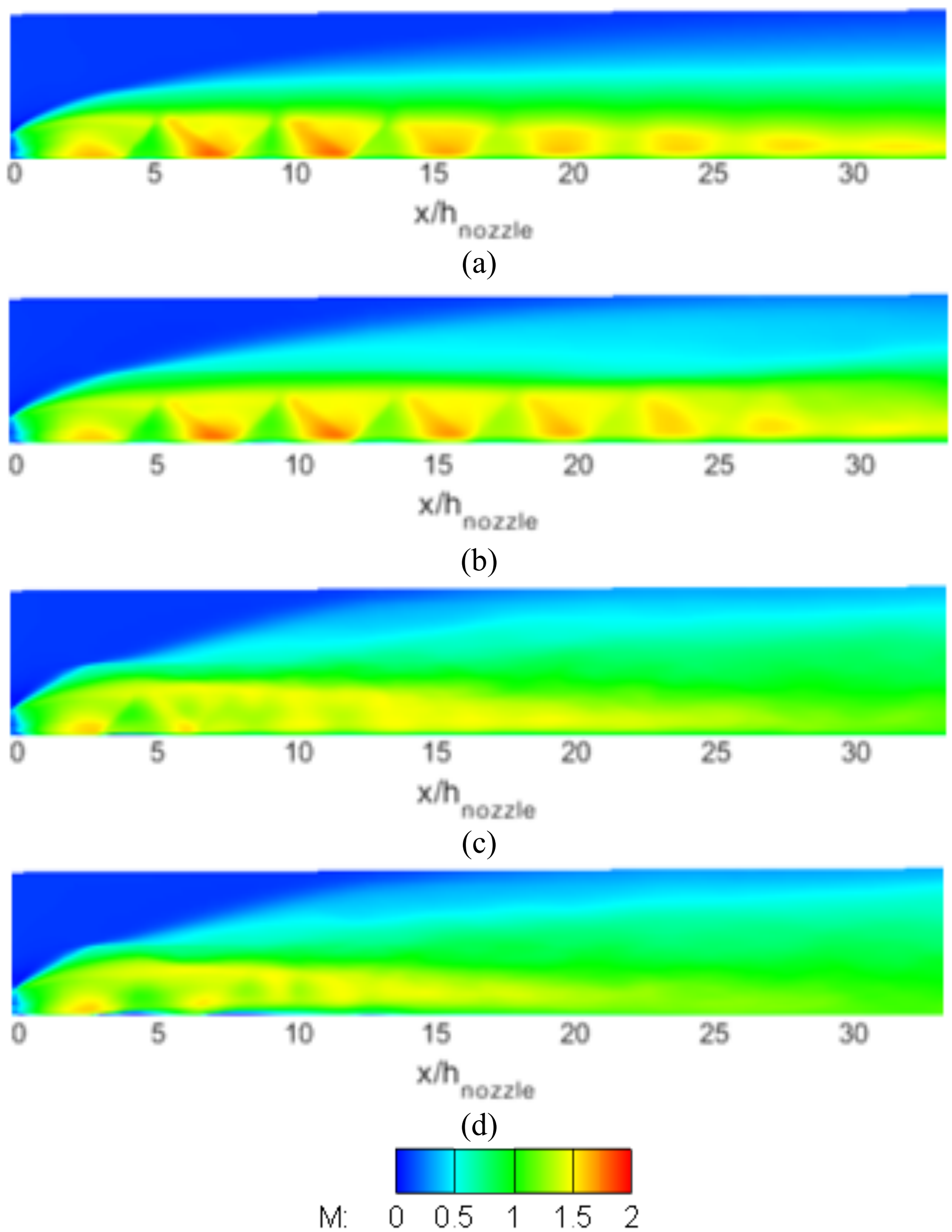

Figure 3.19 Mean Mach number contours along the nozzle centerline for (a) SSRANS; (b) $C_b = 1.0$ (c) $C_b = 0.1$; (d) $C_b = 0.01$.

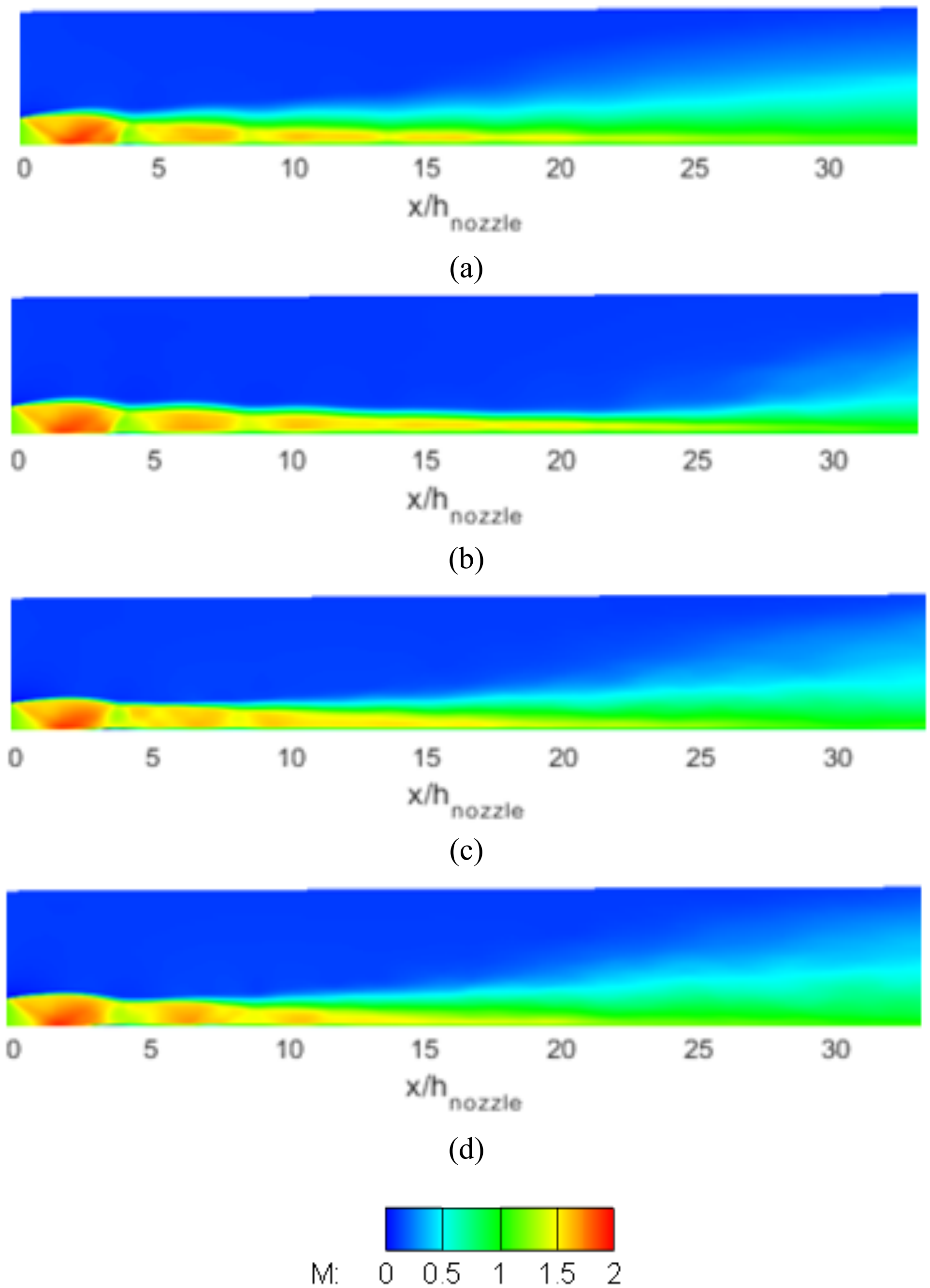

Figure 3.20 Mean Mach number contours along the nozzle ¼-span for (a) SSRANS; (b) $C_b = 1.0$ (c) $C_b = 0.1$; (d) $C_b = 0.01$.

The mean pressure along the nozzle centerline shows that increasing C_b improves the shock strength estimates and delays the axial damping of the shock cells (Fig. 3.21). When C_b is lower than 1.0, the time-averaged results obtained from the LESb models match poorly against the solution from the SS-RANS model. This is caused by the existence of large flow separations that drastically change the mean flow due to the lower turbulent viscosity in the boundary layer resolved by the LESb model.

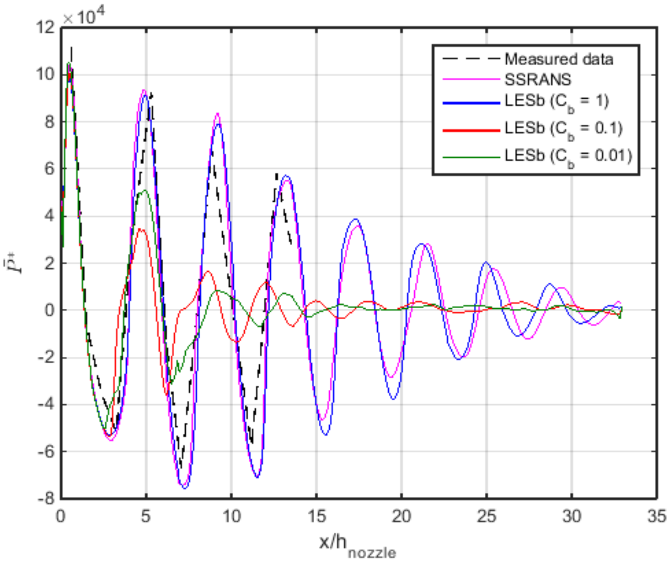

Figure 3.21 Mean surface pressure along the nozzle centerline.

As C_b approaches a value of zero, the solution approximates a fully laminar case. This can be observed by plotting the boundary layer profiles along the nozzle centerline against each other (Fig. 3.22). The simulation running with a turbulence dissipation coefficient of 0.01 shows a delay in the initial shear layer growth and an increase in size of the separation bubble behind the first shock. This behavior is caused by the strong laminar shock-boundary layer interactions generated by the lack of viscous damping. The upstream boundary layer profiles from the LESb simulations are relatively similar to each other, suggesting that the amount of viscous dissipation does not have a significant impact on the upstream flow in the near-wall region.

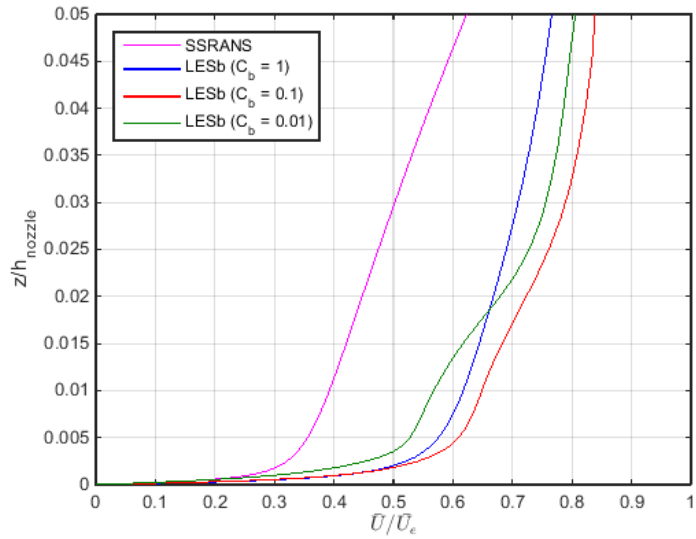

(a)

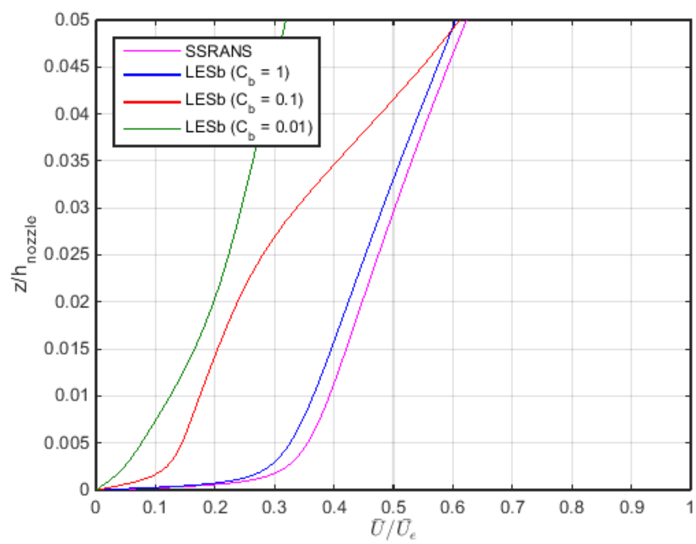

(b)

Figure 3.22 Mean stream-wise velocity along the nozzle centerline at (a) x/h_{nozzle} = 1; (b) x/h_{nozzle} = 5. Velocity levels are normalized by the mean jet exit velocity

In order to better understand the impact of the viscous dissipation on the computed turbulent field, a fully inviscid LES case has been run using the same flow conditions shown in Table 3.5. The inviscid case solves the Euler equations where the fluid is assumed to have zero viscosity, therefore bypassing the diffusion terms present in the Navier-Stokes equations. Figure 3.23 shows the instantaneous Mach number contours along the nozzle centerline and the ¼-span. The shear layer remains steady up to x/h_{nozzle} = 10, after which the flow becomes unsteady. The LES sub-grid model is not suppressing the unsteadiness because the current grid resolution is not fine enough to support the shear layer becoming unsteady even in the absence of the added sub-grid turbulence dissipation. Since the impact of the shear layer and boundary layer on the aft deck are a major cause of the unsteady loading, it is important to be able to accurately predict their development and flow characteristics.

This problem can be mitigated with the use of a boundary layer shield which prevents the LES model from affecting the flow in regions where the grid resolution is insufficient to properly resolve the turbulence near the boundary layer. A parametric study on the impact of the boundary layer shield on the flow field is presented in Section 3.8.

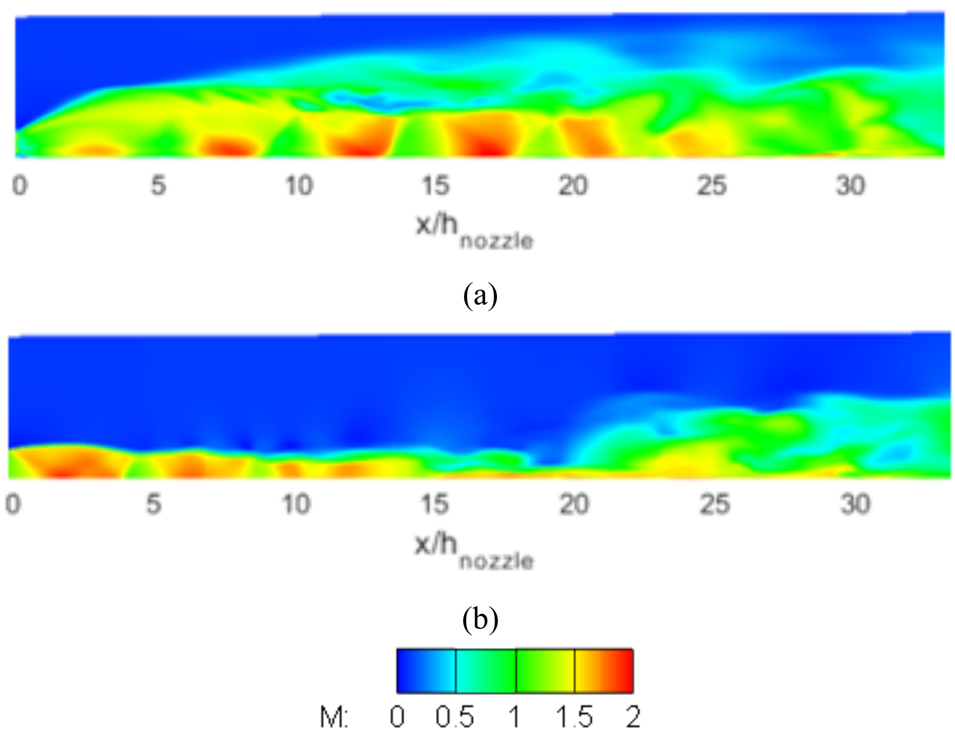

Figure 3.23 Instantaneous Mach number contours for inviscid LES run. (a) Nozzle centerline; (b) nozzle ¼-span.

Table 3.6 shows a comparison of the predicted convection velocities with the average value from the experiments. The LESb simulations running with C_b = 0.1 and C_b = 0.01 overestimate the axial convection speeds by 43% with marginally higher values predicted by the simulation running with C_b = 0.01. The axial convection velocities for the C_b = 1 case indicate the existence of flow structures traveling upstream. It is believed that these structures are not part of the physics of the problem, thus they are considered numerical artifacts of the overdamped solution.

Table 3.6 Convective axial velocities

	C_b	V_{DE} (ft/s)	V_{DF} (ft/s)
Measured data		893	893
$C_b = 1$	1.0	-2083	-475
$C_b = 0.1$	0.1	1562	987
C_b 0.01	0.01	1389	1071

Figures 3.24 – 3.27 show the predicted two-point cross-correlation coefficients R_{ij} of the unsteady wall-pressure fluctuations. The sampling locations used to generate the cross-correlation plots are shown in Fig. 3.13. The plots show a strong dependence on the value of the turbulence dissipation coefficient C_b. When the two-point separation distance is 2.7 nozzle heights, the Wind-US solver predicts nearly perfect correlation for the $C_b = 1.0$ (Fig. 3.24b) while the other two runs show peak values that are 20% and 10 % of the correlation predicted by the simulation running with $C_b = 1$. At the downstream locations (Fig. 3.25), run 1 shows cross-correlation peaks that are quasi-periodic in nature. The simulations running with $C_b = 0.1$ and $C_b = 0.01$ show trends similar to those observed in the boundary layer preservation study. This suggests that the strength of the numerical artifacts observed in section 3.1 grows as the turbulent kinetic energy dissipation is increased. The overdamping of the unsteadiness at the downstream locations allows the propagation of these large coherent structures which are not considered part of the physics of the problem. Additionally, the alignment of the cross-stream correlation peaks indicates that the convected wall-pressure fluctuations are nearly two-dimensional in nature (Fig. 3.26 – 2.37).

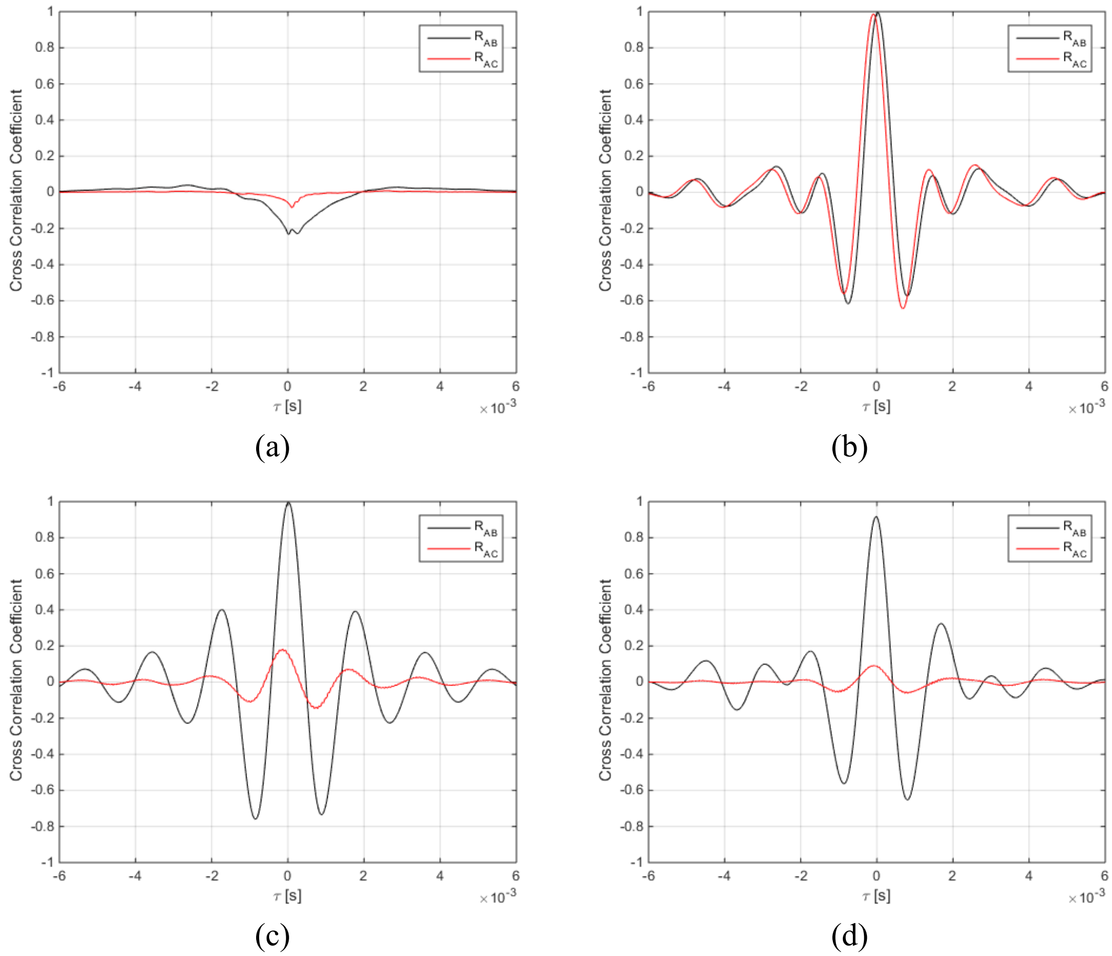

Figure 3.24 Upstream axial pressure correlations from the NPR = 4.0 data. (a) Measured; (b) C_b = 1; (c) C_b = 0.1; (d) C_b = 0.01.

.

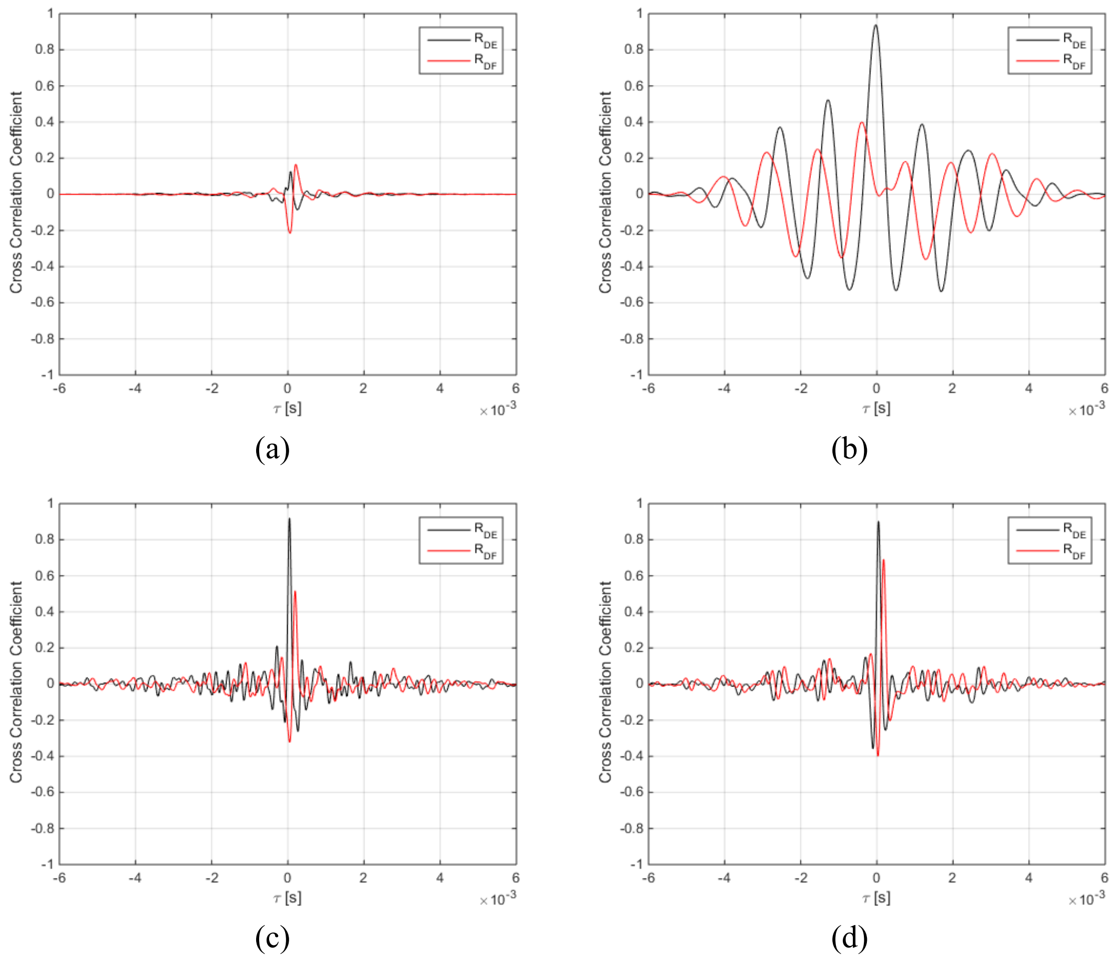

Figure 3.25 Downstream axial pressure correlations from the NPR = 4.0 data. (a) Measured; (b) C_b = 1; (c) C_b = 0.1; (d) C_b = 0.01.

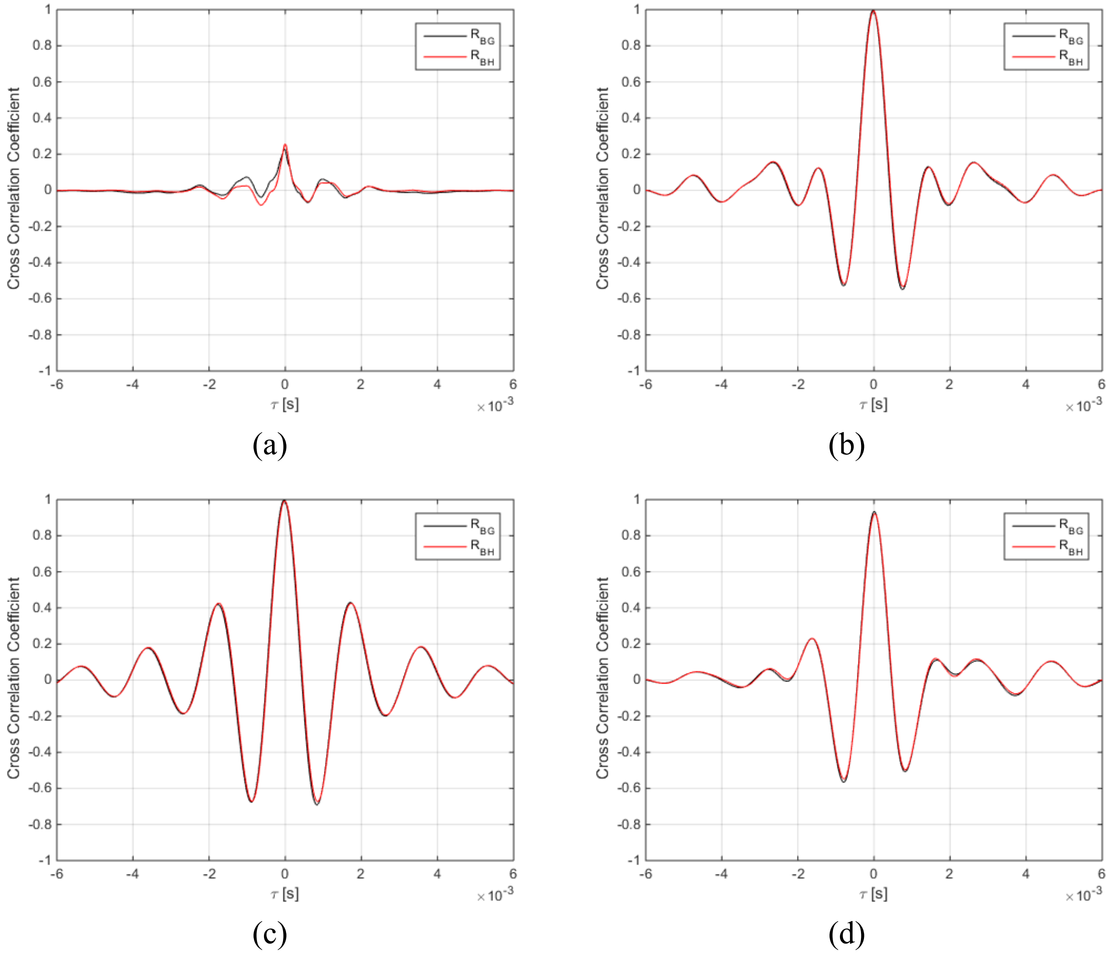

Figure 3.26 Upstream cross-stream pressure correlations from the NPR = 4.0 data. (a) Measured; (b) $C_b = 1$; (c) $C_b = 0.1$; (d) $C_b = 0.01$.

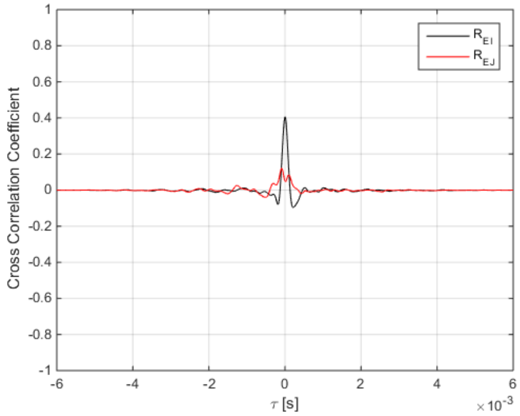

(a)

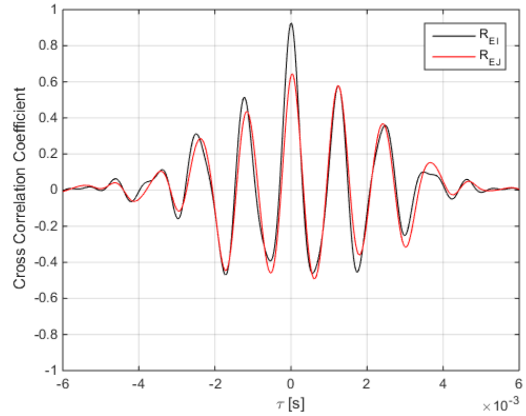

(b)

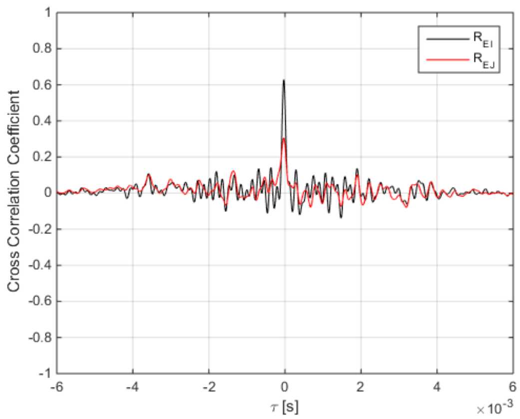

(c)

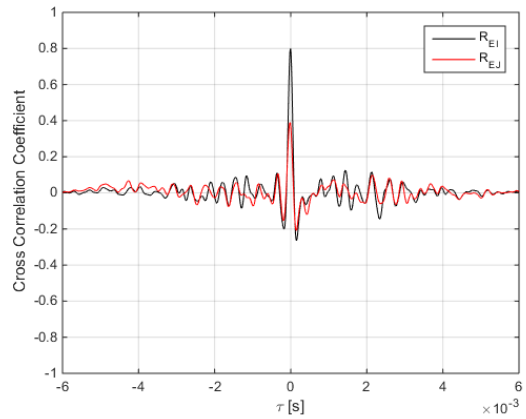

(d)

Figure 3.27 Downstream cross-stream pressure correlations from the NPR = 4.0 data. (a) Measured; (b) $C_b = 1$; (c) $C_b = 0.1$; (d) $C_b = 0.01$.

.

3.3 Physical Time Step

A parametric study has been performed to gain a deeper understanding of the impact of the physical time step on the numerical solutions. In CFD calculations, the time step size is one of the most important parameters as it determines the resolution of the smallest turbulent structures and the amount of time needed to run the simulation. Longer time steps are often used to reach faster convergence to a steady state solution or to accumulate more time history data.

The Wind-US code uses an implicit time step solver which does not require the use of global sub-iterations to synchronize the interior boundaries. For unsteady problems, the time step in seconds is specified directly in the input file. The present LESb simulations are carried out using the default Runge-Kutta time marching scheme while the time step size is increased logarithmically between each run. Note that the CFL limit in the boundary layer CFL_{max} and the turbulence viscosity coefficient C_b are kept constant to isolate the effects of the physical time step on the flow field.

Table 3.7 shows the initial conditions for each run. Each simulation has been run for a total run time of 0.04 seconds and the total elapsed times are listed in Table 3.8.

Table 3.7 Input conditions used for physical time step parametric study.

Run	NPR	M	T (R)	P (psi)	Δt (μs)	CFL_{max}	C_b
8	4.0	0.5	777	58.8	0.5	5.0	0.1
9	4.0	0.5	777	58.8	5	5.0	0.1
10	4.0	0.5	777	58.8	50	5.0	0.1

Table 3.8 Total elapsed times and non-dimensional Nyquist frequencies.

Run	Δt (μs)	$St_{nyquist}$	Total elapsed time (hrs)
8	0.5	48.3	126
9	5	4.83	11
10	50	0.483	1

The wall-pressure power spectral density estimates (Fig. 3.28) show that decreasing the time step size leads to a growth of the unsteady energy content across all frequencies. The simulations running with $\Delta t = 0.5$ μs and $\Delta t = 5$ μs over-predict the unsteadiness at the upstream locations while, at the downstream location, the low-frequency estimates from runs 1 and 2 are in good agreement with the experiments (Figure 2.38c). The simulation running with $\Delta t = 50$ μs instead under-predicts the amount of unsteadiness at the high-frequencies as a result of the inadequate temporal resolution. Note the maximum resolved frequency of $\Delta t = 50$ is consistent with the prediction based on the sampling rate of the CFD solutions (Table 3.8).

Figure 3.28a illustrates that the frequency peaks generated by the numerical artifacts from the constant CFL region are inversely proportional to the physical time step size. The simulation running with $\Delta t = 5$ μs shows a peak in the PSD estimate near $St = 0.3$ while the $\Delta t = 50$ μs run shows a peak at $St = 0.07$. The PSD peak of the simulation running with $dt = 0.5$ μs is not shown here because it falls beyond $St = 2$. For unsteady LES simulations running with a constant CFL in the boundary layer, the size of the stretched time domain increases with the physical time step size. Therefore, it can be concluded that the peak frequencies shown in Fig. 3.28 are proportional to the size of the stretched-time region.

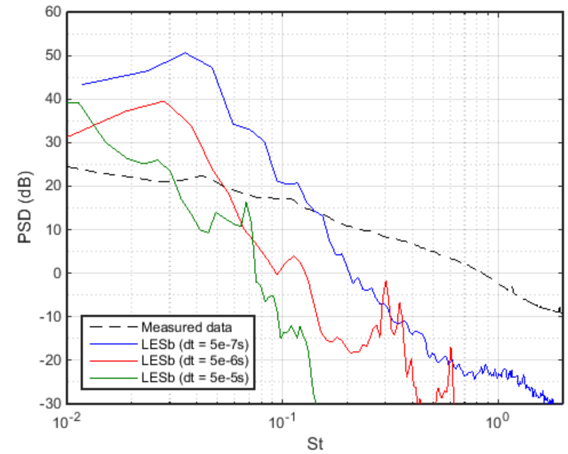

(a)

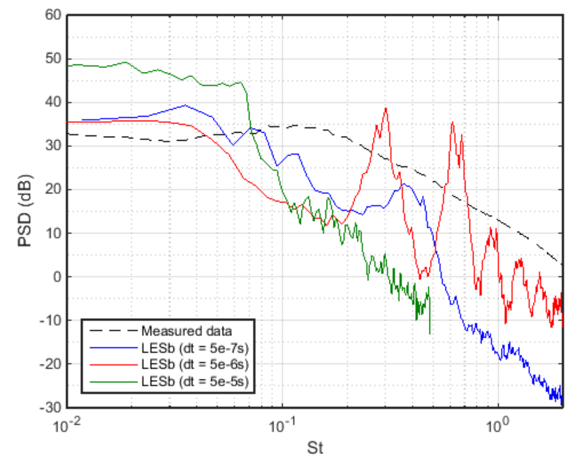

(b)

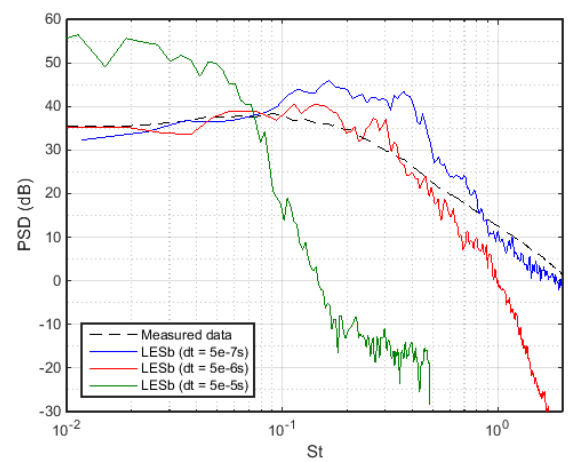

(c)

Figure 3.28 Welch power spectral densities of surface pressure fluctuations along the nozzle ¼-span at (a) $x/h_{nozzle} = 2.4$; (b) $x/h_{nozzle} = 7.1$; (c) $x/h_{nozzle} = 11.8$.

A cutting plane normal to the deck surface is used to generate the accumulated mean Mach number contours of the flow exiting the nozzle for the steady-state RANS and the LESb solutions. Figures 3.29 and 3.30 show the results along the nozzle centerline and the ¼ span.

The LESb model with the largest time step (Δt = 50 μs) predicts a mean pressure field that closely resembles the SS-RANS solution. A similar behavior can be observed in section 3.2, where the simulation with the added turbulence viscosity predicted lower unsteadiness and a weaker damping of the shock train. The mean Mach number contours of Δt = 50 μs show the shear layer becoming unsteady. This could be explained by the lack of run time necessary to reach a steady state solution as the time step is increased. The ¼-span Mach number contours of Δt = 0.5 μs and Δt = 5 μs reveal a slower growth of the shear layer which further suggests that the grid resolution downstream of the of nozzle exit is not fine enough to resolve the initial growth of the shear layer. Furthermore, the simulation running with Δt = 0.5 μs also shows a large separation bubble in the SBLI region as a result of the laminar boundary layer predicted by the LESb model.

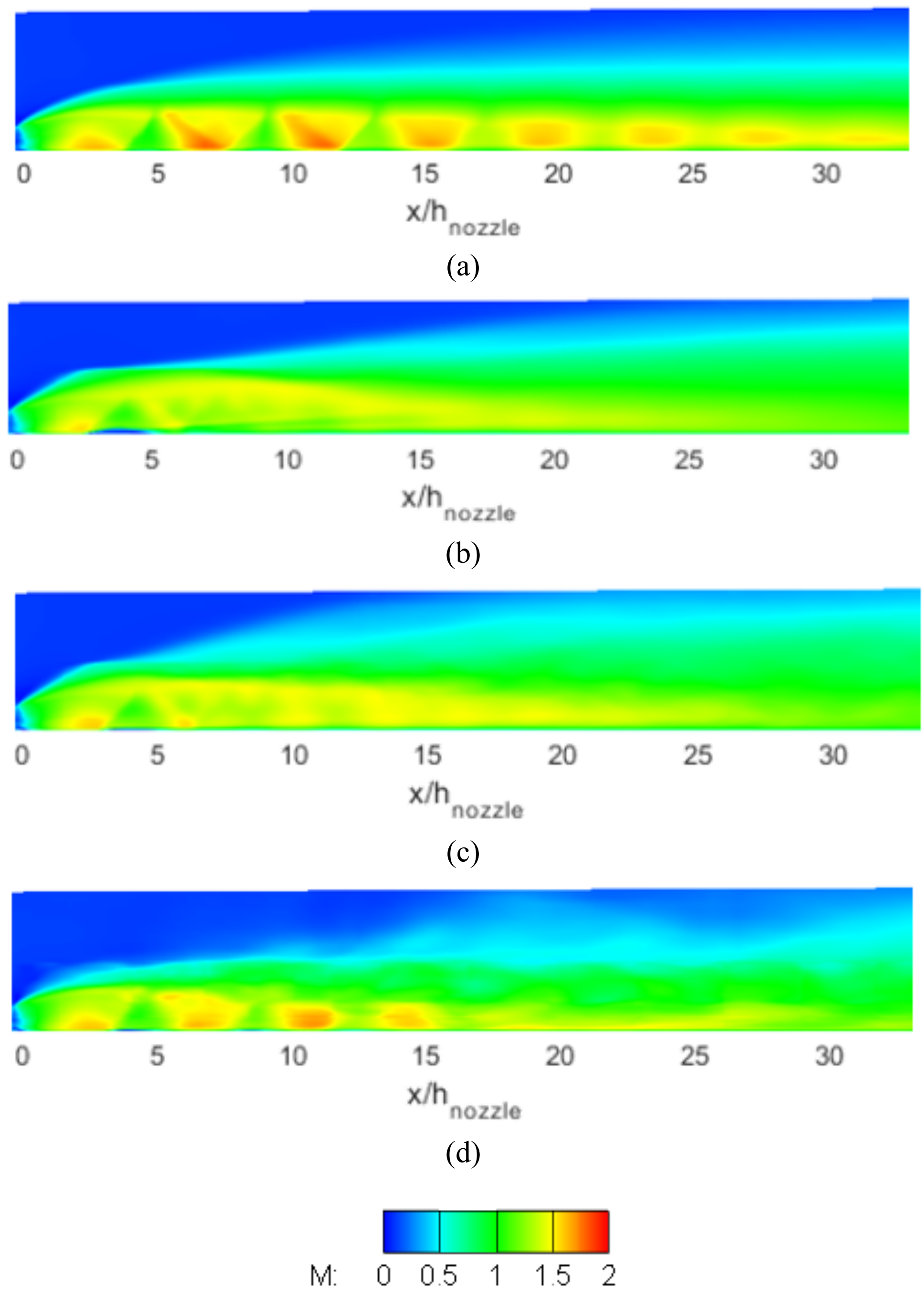

Figure 3.29 Mean Mach number contours along the nozzle centerline for (a) SSRANS; (b) Δt = 0.5 μs (c) Δt = 5 μs; (d) Δt = 50 μs.

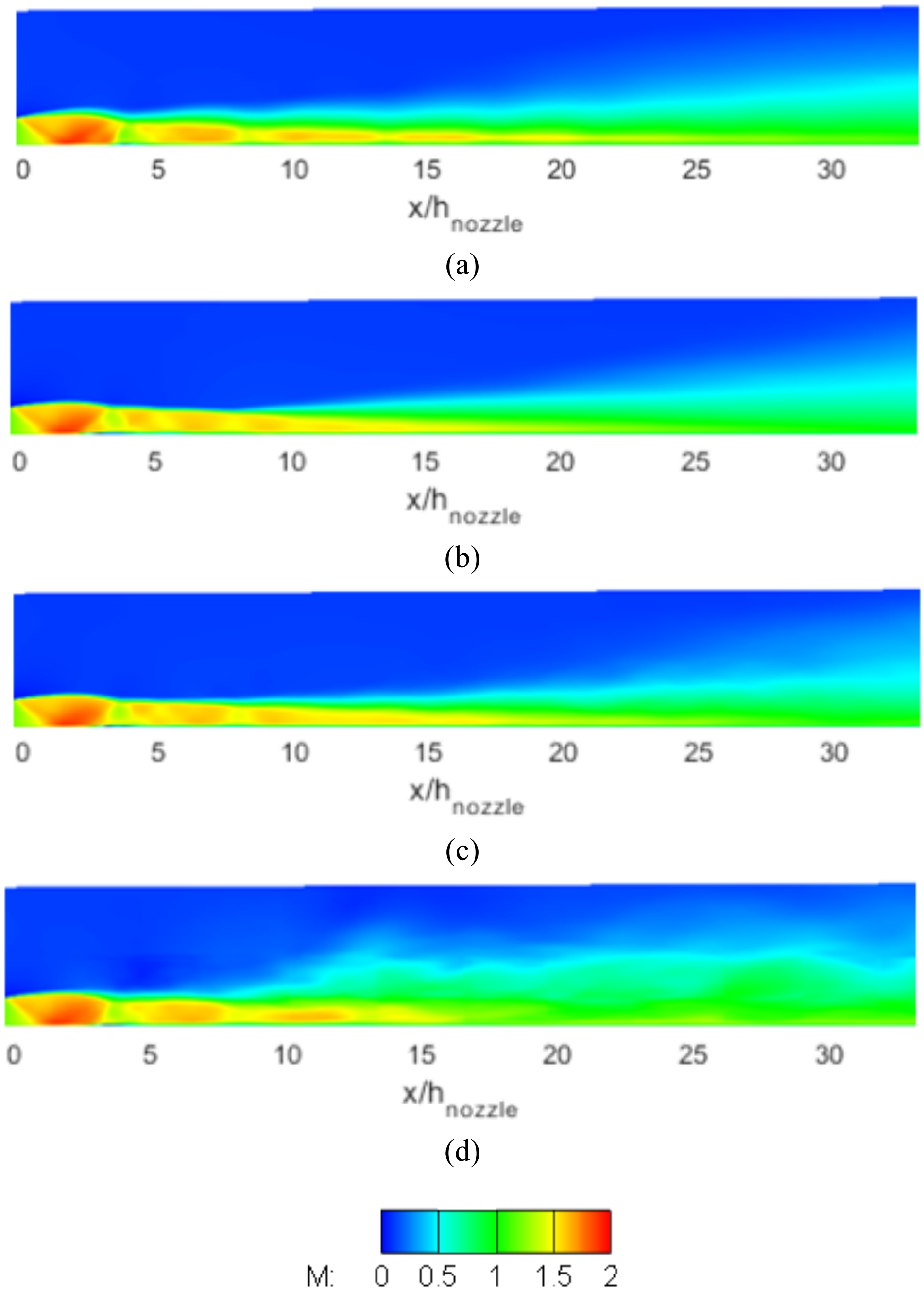

Figure 3.30 Mean Mach number contours along the nozzle ¼-span for (a) SSRANS; (b) Δt = 0.5 μs (c) Δt = 5 μs; (d) Δt = 50 μs.

Figure 3.31 shows the non-dimensional mean surface pressure along the nozzle centerline. It is thought that the under-prediction of the mean wall pressure profile for the LESb running with Δt = 0.5 μs and Δt = 5 μs is a result of the overextension of the LES model to the boundary layer region. The variation in the downstream shock spacing is likely due to the difference in the shear layer growth rate.

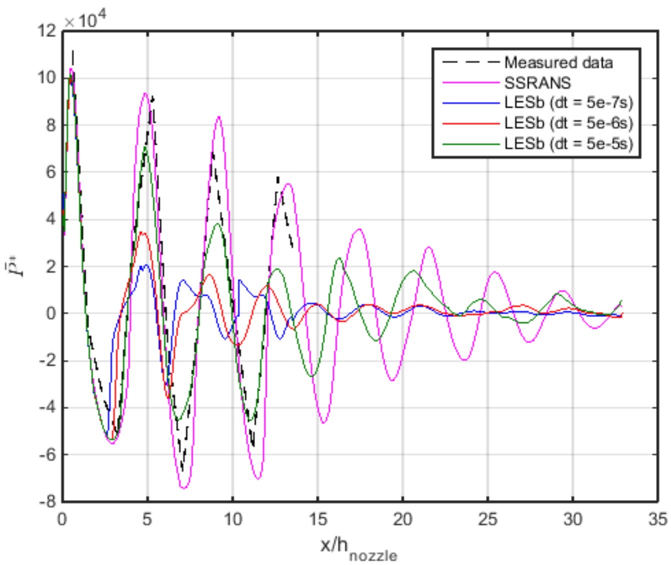

Figure 3.31 Mean surface pressure along the nozzle centerline.

Plots of the boundary layer profiles along the nozzle centerline are shown in Figure 3.32. The profiles upstream of the first shock-boundary layer interaction ($x/h_{nozzle} = 1$) show moderate variation between the LESb runs mainly because the amount of unsteadiness in the upstream boundary layer varies with the time step size. Downstream of the first shock structure, the velocity profile of the simulation running with dt = 0.5 μs shows the existence of a separated laminar region as observed in the mean Mach number contours (Fig. 3.29) while at the upstream location, the steady state RANS consistently predicts a thinner boundary layer as a result of the smaller turbulent shear stress computed by the RANS model.

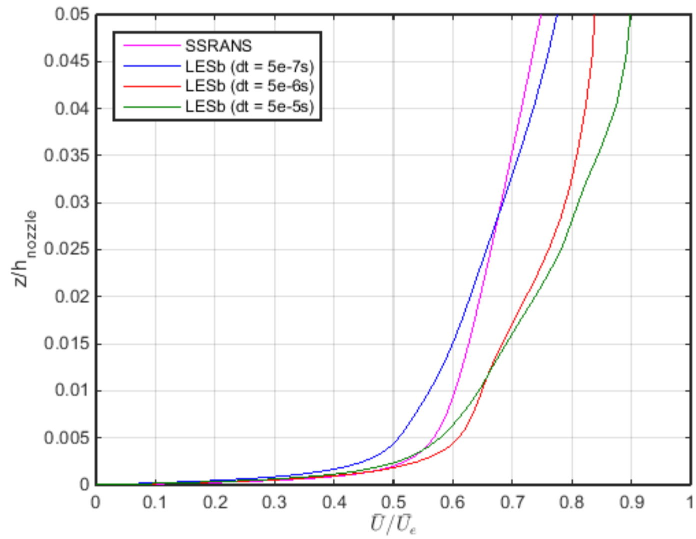

(a)

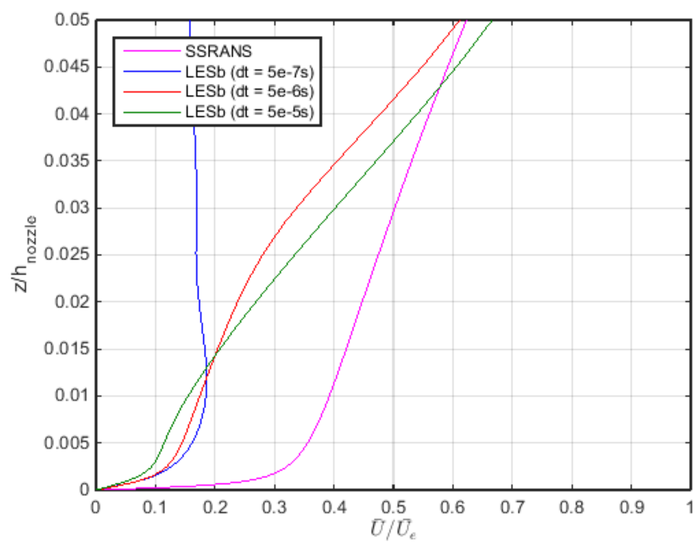

(b)

Figure 3.32 Mean stream-wise velocity along the nozzle centerline at (a) $x/h_{nozzle} = 1$; (b) $x/h_{nozzle} = 5$. Velocity levels are normalized by the mean jet exit velocity

The general trend shown in Table 3.9 is that the downstream convection velocity decreases as the global time step is increased. Comparison between the measured data and the CFD simulations shows that $\Delta t = 0.5$ μs and $\Delta t = 5$ μs overpredict the mean axial convection velocity by approximately 45% whereas Δt = 50 μs largely underpredicts the experimental results.

Figure 3.33 shows that the frequency at which the upstream cross-correlation peaks occur is inversely proportional to the time step size. These strong, periodic features are believed to be caused by the artificial modes generated by the constant CFL in the boundary layer. As the physical time step is increased, the overall size of the constant CFL region also grows, generating strong coherent structures that extend all the way to 14 nozzle heights downstream of the nozzle exit. The normalized correlation fields of the downstream wall pressure fluctuations are clearly influenced by the size of the physical time step and the presence of these numerical artifacts as shown in Figure 3.34. The simulations running with Δt = 0.5 μs and Δt = 5 μs show that the spurious oscillations may have dissipated by the time they reach a downstream distance of 10 nozzle heights.

Table 3.9 Axial convection velocities

	V_{DE} (ft/s)	V_{DF} (ft/s)
Measured data	893	893
Δt = 0.5 μs	1506	1123
Δt = 5 μs	1563	987
Δt = 50 μs	417	289

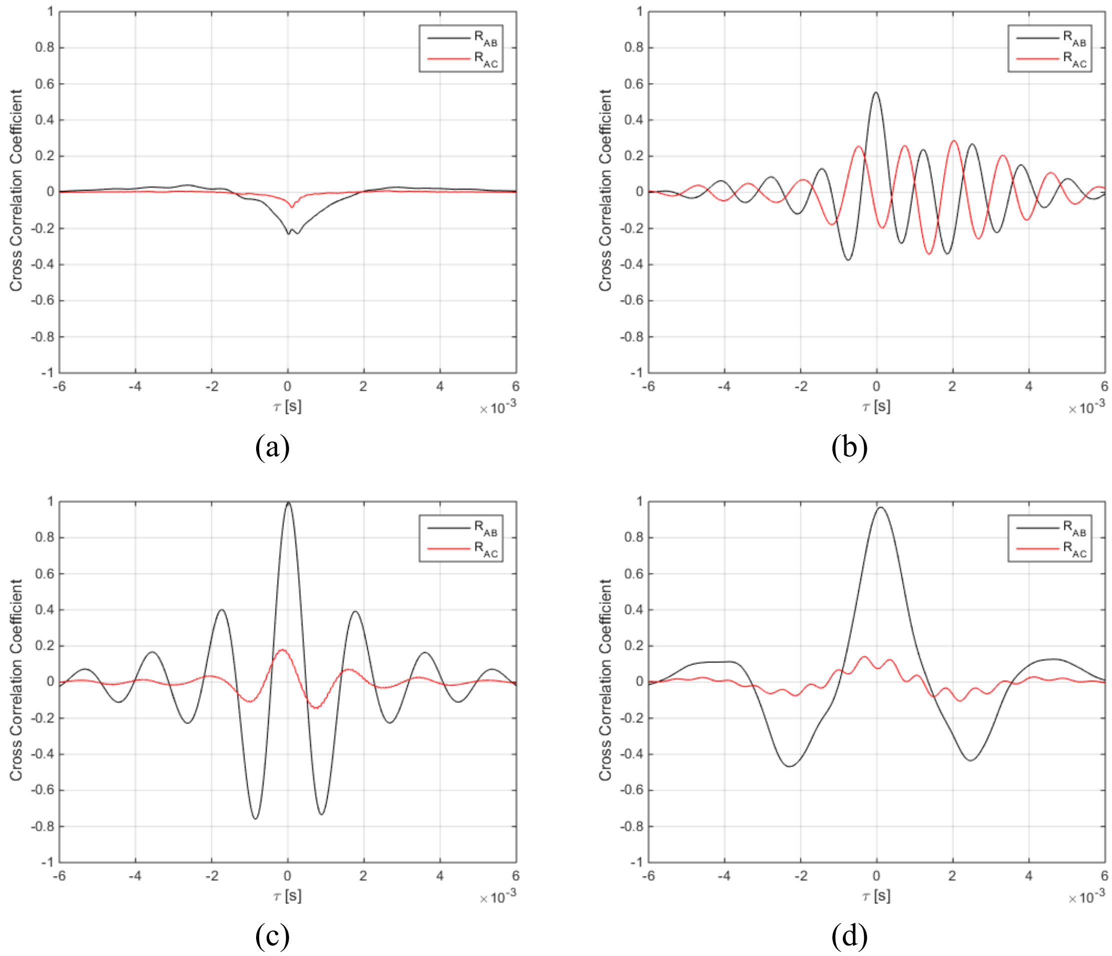

Figure 3.33 Upstream axial pressure correlations from the NPR = 4.0 data. (a) Measured; (b) Δt = 0.5 μs (c) Δt = 5 μs; (d) Δt = 50 μs.

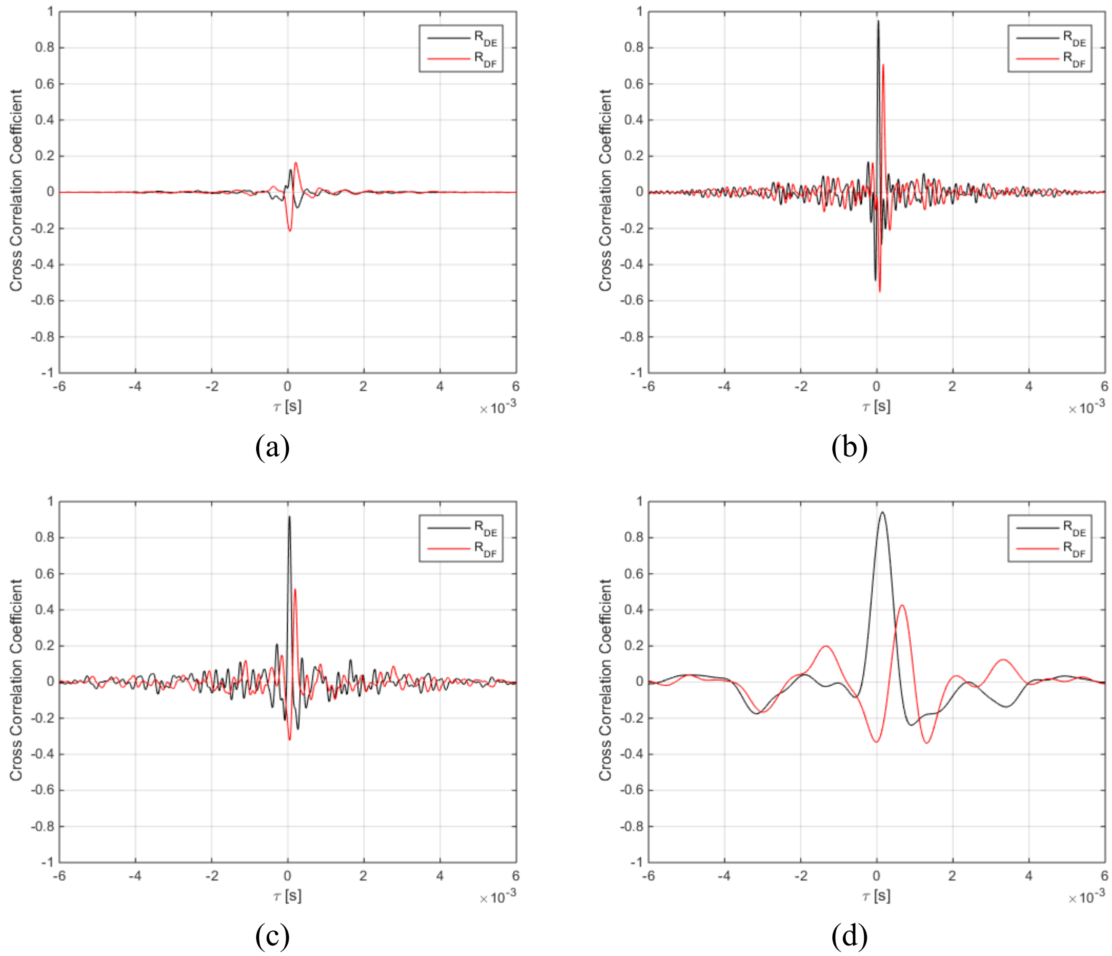

Figure 3.34 Downstream axial pressure correlations from the NPR = 4.0 data. (a) Measured; (b) Δt = 0.5 μs (c) Δt = 5 μs; (d) Δt = 50 μs.

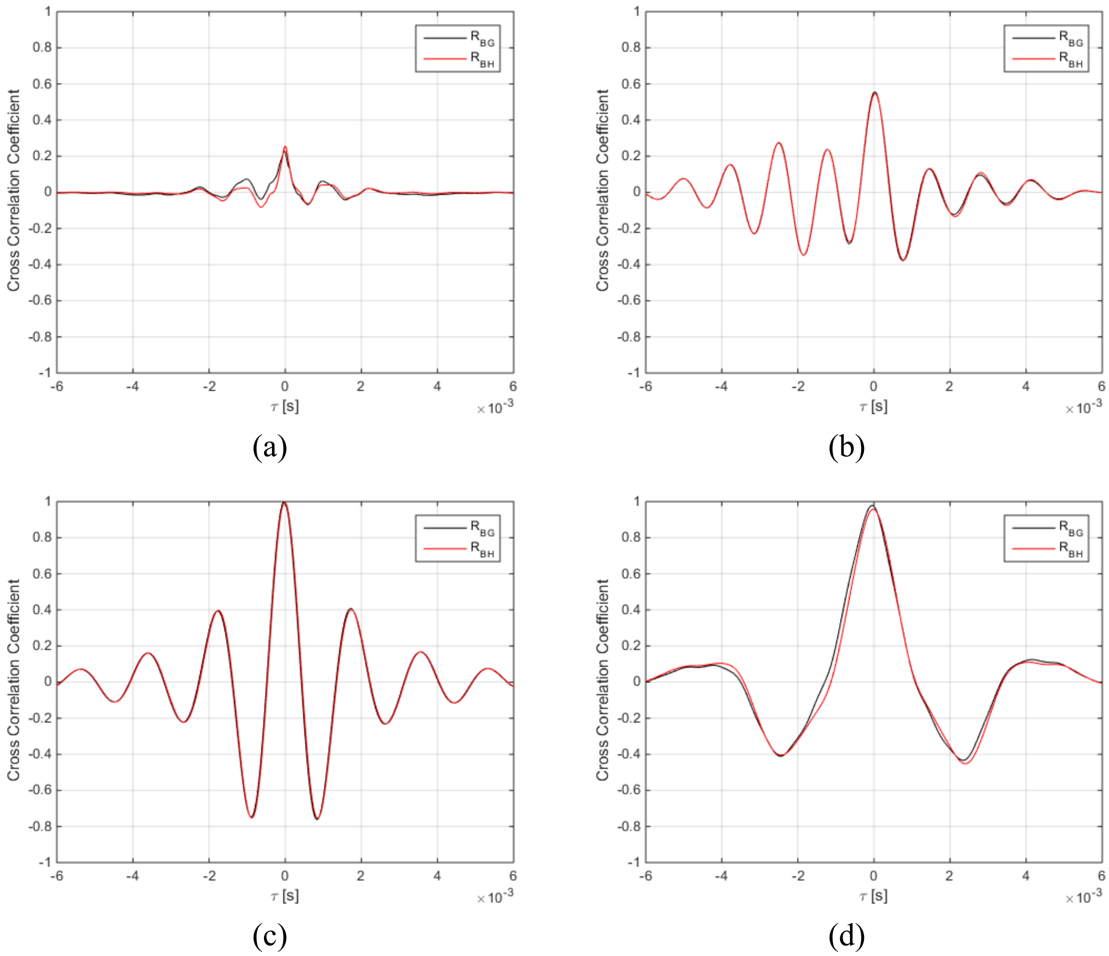

Figure 3.35 Upstream cross-stream pressure correlations from the NPR = 4.0 data. (a) Measured; (b) $\Delta t = 0.5$ μs (c) $\Delta t = 5$ μs; (d) $\Delta t = 50$ μs.

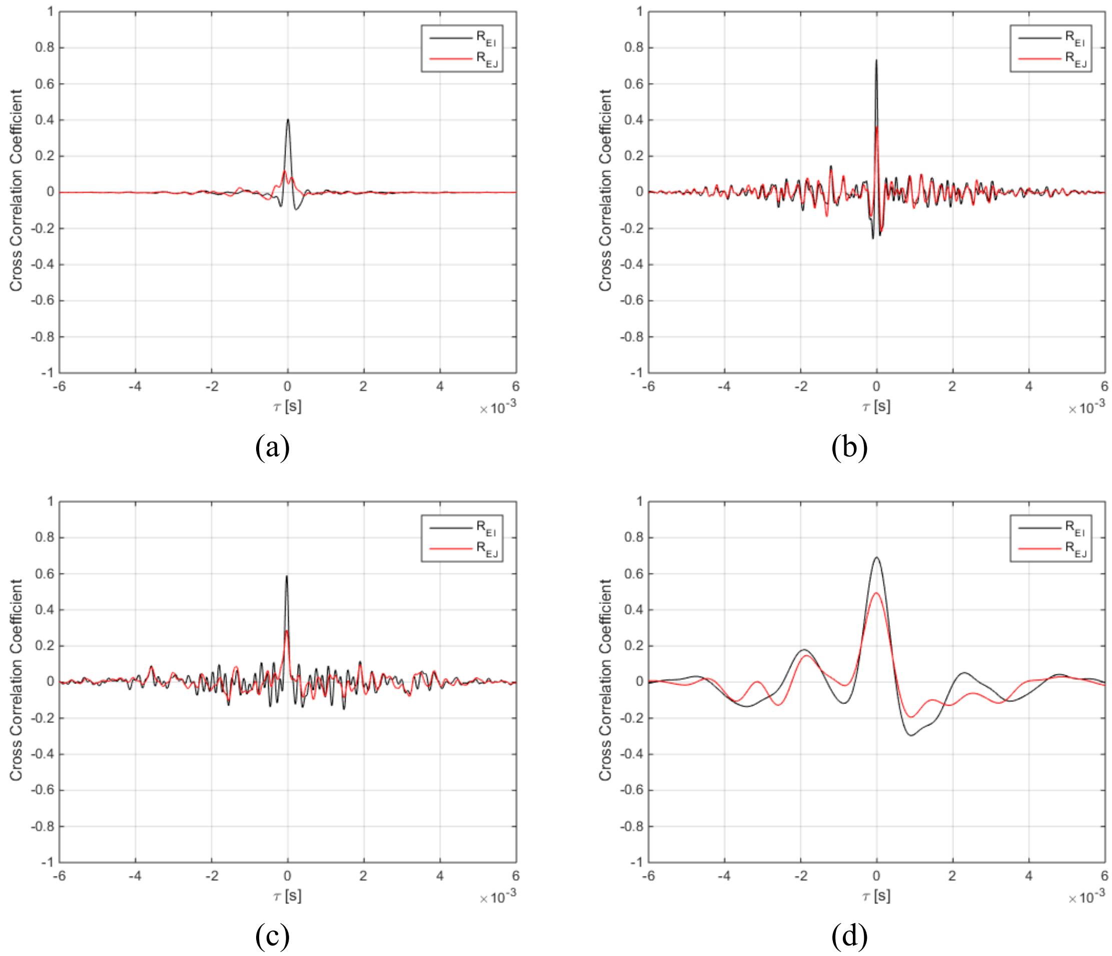

Figure 3.36 Downstream cross-stream pressure correlations from the NPR = 4.0 data. (a) Measured; (b) Δt = 0.5 μs (c) Δt = 5 μs; (d) Δt = 50 μs.

3.4 Selecting the Baseline Numerical Model

In this section, results from multiple Large-Eddy Simulations have been examined and compared to the wall pressure data measured by UTRC in order to select a baseline model for the subsequent numerical studies.

Table 3.10 shows the initial conditions for each of the LESb runs. Runs 2, 3 and 4 are running at the maximum allowable CFL_{max} limit in order to minimize the extent of the stretched time region. Each of the following simulations has been run for a total simulated time of t = 0.04 seconds. The elapsed run time estimates in hours for a total period of 1.0 seconds are listed in Table 3.11. Comparisons with the fully time-accurate simulation show that the implementation of the boundary layer preservation model leads to a substantial decrease in execution time by allowing the solver to run using larger time steps. Note that the simulations running with the constant CFL in the boundary layer become more unstable with increasing time step size. This pattern can be observed in the simulations running with CFL_{max} = 10 and CFL_{max} = 3, where the CFL_{max} limit decreases with increasing time step size. The simulation running with CFL_{max} = 11 shows that it is possible to maintain numerical stability at higher a CFL_{max} by increasing the turbulence dissipation coefficient C_b. The numerical instability at high CFL_{max} values is likely due to the insufficient turbulence dissipation introduced by the growing LES region near the deck surface and in the shear layer.

Table 3.10 Initial flow conditions and LESb parameters

Run	NPR	M	T (R)	P (psi)	Δt (μs)	CFL_{max}	C_b
11	4.0	0.5	777	58.8	0.3	---	0.01
12	4.0	0.5	777	58.8	1	10	0.01
13	4.0	0.5	777	58.8	6	3.0	0.01
14	4.0	0.5	777	58.8	6	11	0.10

Table 3.11 Elapsed times

Run	Δt (μs)	Total elapsed time (t = 0.04s)	Elapsed time estimate (t = 1.0s)
11	0.3	160 hrs	4,000 hrs
12	1	47 hrs	1,175 hrs
13	6	8 hrs	200 hrs
14	6	8 hrs	200 hrs

Comparisons between the LESb runs and the measured data are shown in Figure 3.37. The slow development of the initial shear layer results in the inaccurate prediction of the wall power spectral density near the nozzle exit (Fig. 3.37a). Figures 3.37b – 3.37c show good agreement between the simulation running with CFL_{max} = 11 and the fully time-accurate solution, indicating that it is possible to achieve a 20-fold decrease in CPU time and preserve the spectral accuracy of the unsteadiness of interest by using the CFL_{max} limiter. Note that the CFL_{max} = 3 run under-predicts the high frequency content at the downstream locations as a result of the extended stretched-time layer. A similar behavior was observed in section 3.1.

Figures 3.38-3.39 present the accumulated Mach number contours along the nozzle centerline and the nozzle ¼-span. The CFL_{max} = 10 and CFL_{max} = 3 simulations show a slower growth of the shear layer at x/h_{nozzle} = 5 when compared to the other CFD results. Additionally, the LESb simulations running with C_b = 0.01 predict a weaker shock train and a shorter potential core than the steady-state RANS. The RANS model predicts a potential core that extends well beyond 30 nozzle heights downstream of the nozzle exit, whereas the LESb models estimate a potential core length of approximately 25 nozzle heights. When the turbulent kinetic energy dissipation limiter is lower than 0.1, the LES model approaches the viscous wall region, where the grid resolution is not fine enough to properly resolve the boundary layer, resulting in a series of laminar shock-boundary layer interactions. These interactions over-damp the mean shock structures and increase the size of the separation bubble as shown in Figures 3.40 – 3.41. The CFL_{max} = 11 case shows a significant improvement of the upstream mean shock strength while still predicting an overly-damped shock train further downstream.

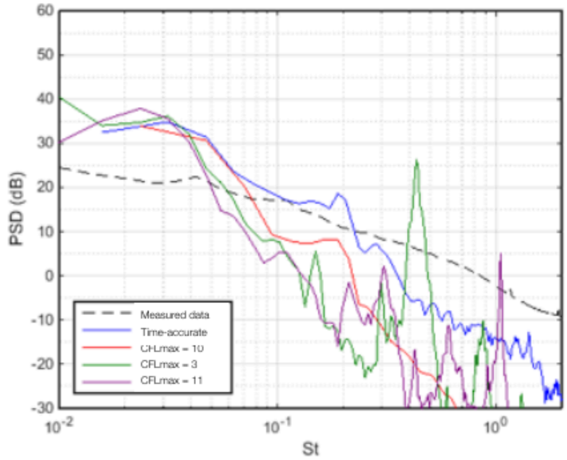

(a)

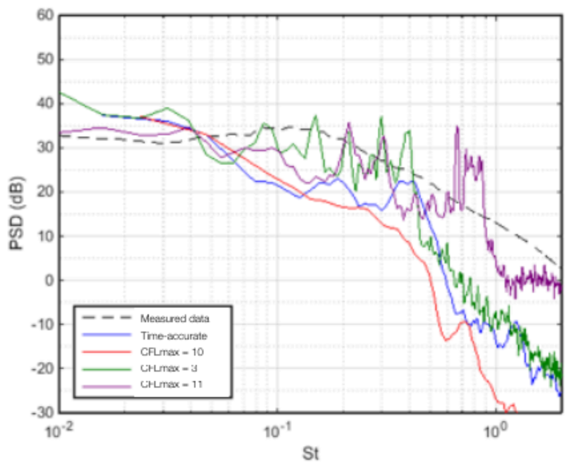

(b)

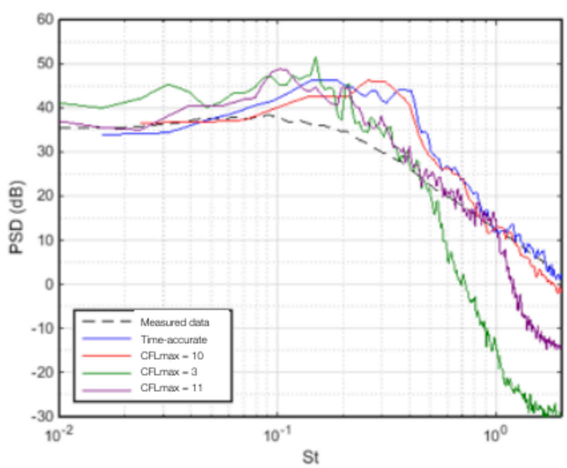

(c)

Figure 3.37 Welch power spectral densities of surface pressure fluctuations along the nozzle ¼-span at (a) $x/h_{nozzle} = 2.4$; (b) $x/h_{nozzle} = 7.1$; (c) $x/h_{nozzle} = 11.8$.

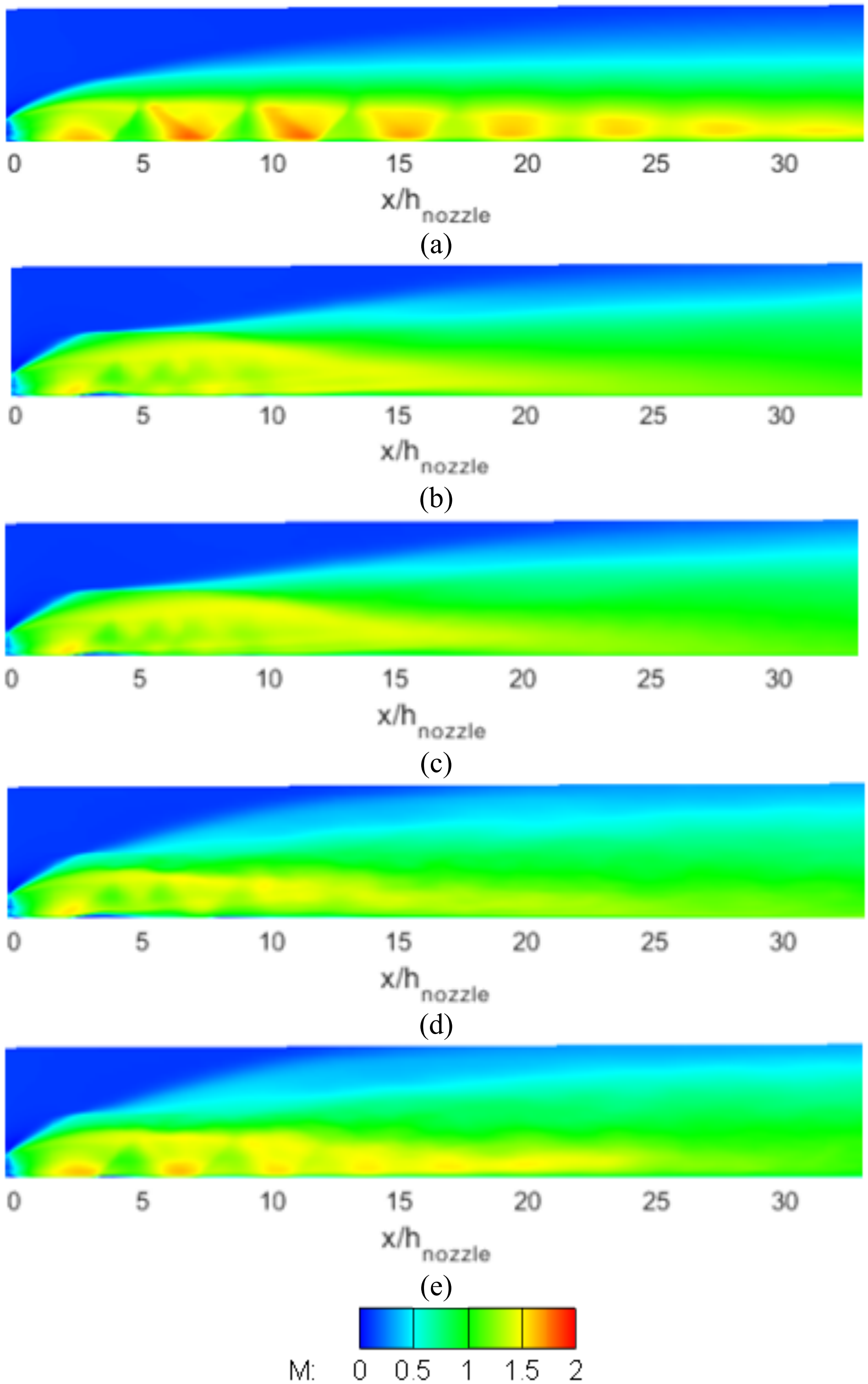

Figure 3.38 Mean Mach number contours along the nozzle centerline for (a) SSRANS; (b) Time-accurate (c) $CFL_{max} = 10$; (d) $CFL_{max} = 3$; (e) $CFL_{max} = 11$.

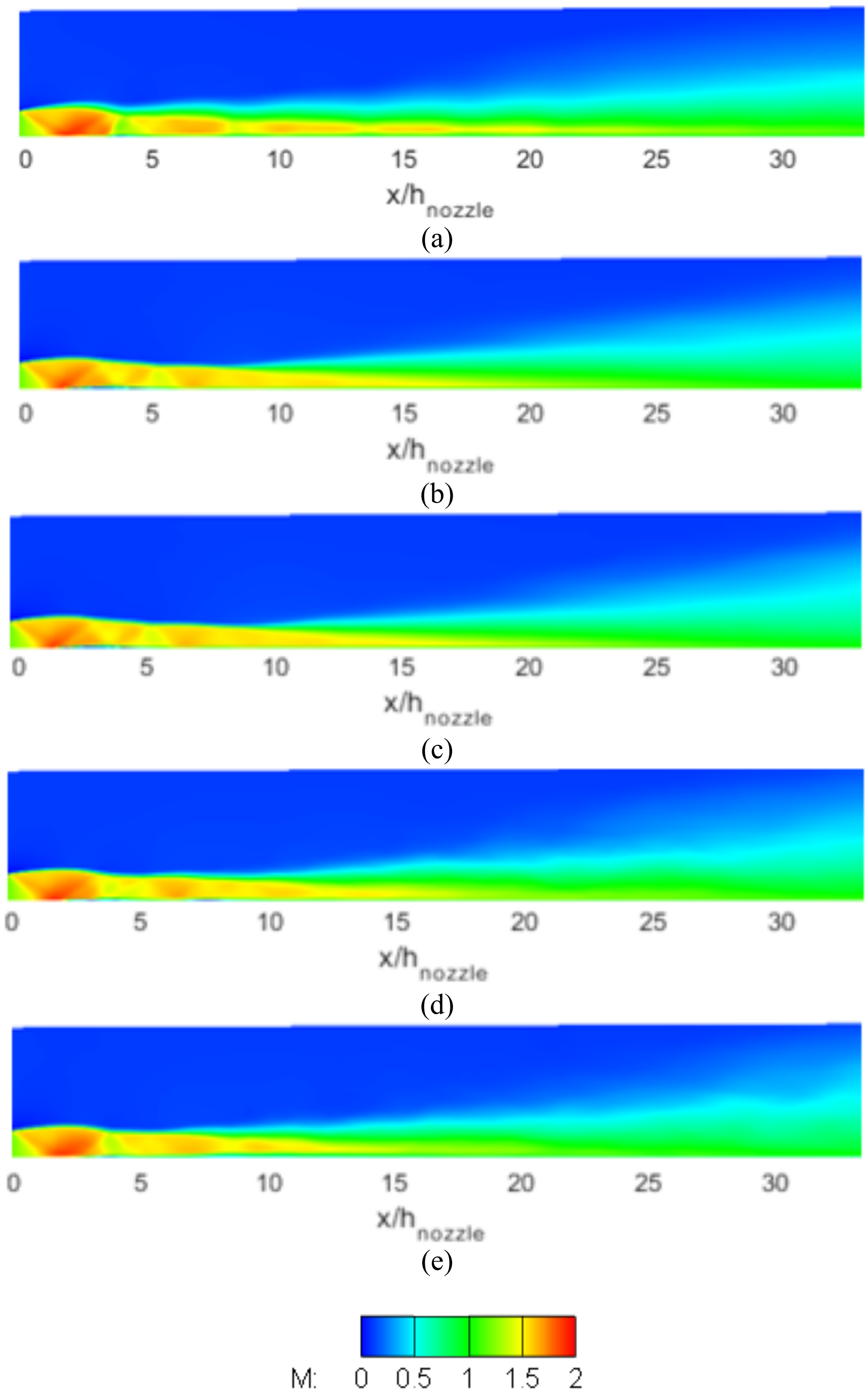

Figure 3.39 Mean Mach number contours along the nozzle ¼-span for (a) SSRANS; (b) Time-accurate (c) CFL_{max} = 10; (d) CFL_{max} = 3; (e) CFL_{max} = 11.

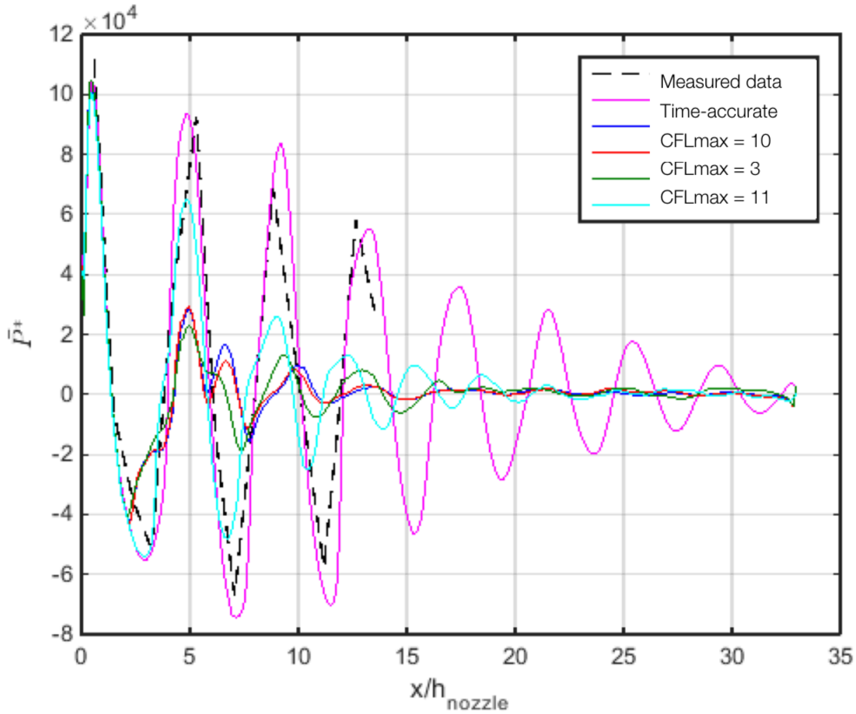

Figure 3.40 Mean surface pressure along the nozzle centerline.

Figure 3.41 shows the normalized velocity profile near the deck surface at 1 and 5 nozzle heights downstream of the nozzle exit. The time step size does not appear to have a significant impact on the upstream boundary layer profiles. However, Figure 3.41a shows a clear difference between the velocity profiles in the near-wall region from z/h_{nozzle} = 0 to z/h_{nozzle} = 0.005. Between z/h_{nozzle} = 0 and z/h_{nozzle} = 0.005, the LESb simulations running with C_b = 0.01 overlap with each other while the CFL_{max} = 11 run aligns with the solution given by the SS-RANS simulation. The difference between the boundary layer profiles up to z/h_{nozzle} = 0.005 changes the downstream interaction between the shocks and the boundary layer. The variations in the mean stream-wise velocity profiles may be caused by the different turbulent kinetic energy coefficients. In fact, increasing C_b also increases the size of the region in which the combined LESb model reduces to the standard RANS SST model.

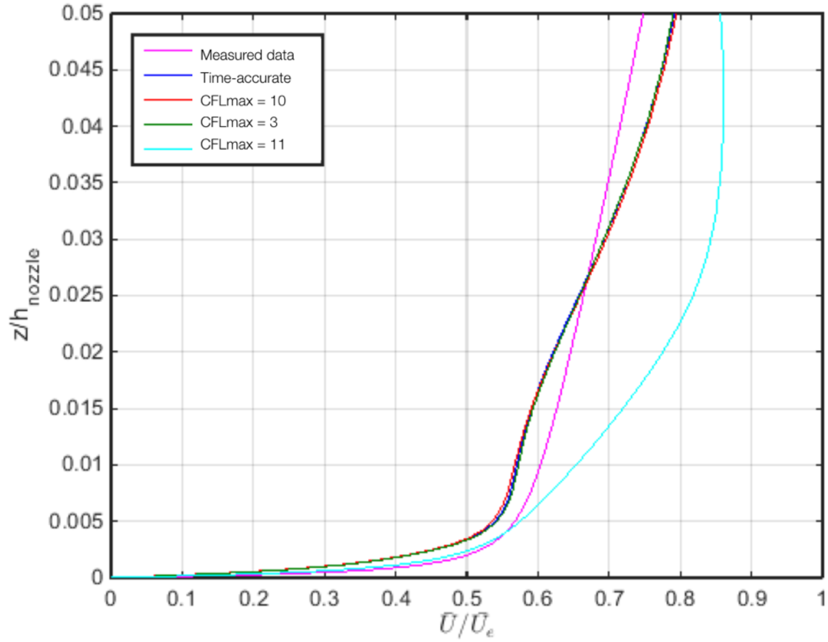

(a)

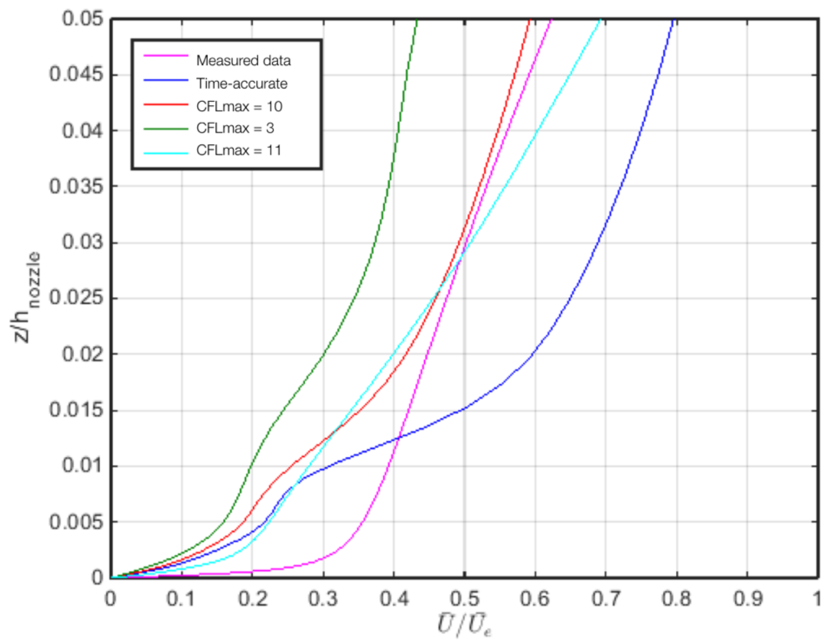

(b)

Figure 3.41 Mean stream-wise velocity along the nozzle centerline at (a) $x/h_{nozzle} = 1$; (b) $x/h_{nozzle} = 5$. Velocity levels are normalized by the mean jet exit velocity

Table 3.12 shows that the stretched-time simulation with the increased turbulence dissipation gives a more accurate estimate of the convective axial velocity compared to the other simulations. Based on the findings presented in this chapter (i.e. mean pressure profiles, elapsed time and PSD estimates), the simulation running with CFL_{max} = 11 will be used as the baseline case for all of the subsequent parametric studies. Although the power spectral density estimates of the numerical simulations show fair agreement with the measured data for the downstream sensors, the CFD simulations are not able to accurately predict the unsteadiness at the upstream locations. Further improvement in the spectral accuracy of the unsteady results is necessary, but outside the scope of this thesis.

Table 3.12 Axial convection velocities

	V_{DE} (ft/s)	V_{DF} (ft/s)
Measured data	893	893
Time-accurate	1488	1136
CFL_{max} = 10	226	167
CFL_{max} = 3	1488	977
CFL_{max} = 11	1302	947

A stability map has been created based on the numerical results from the Large Eddy Simulations. The horizontal axis represents the physical time step used in the time accurate regions non-dimensionalized by the inverse of the characteristic jet frequency, U_{jet}/h_{nozzle}. For reference, the physical time step used in the simulation running with CFL_{max} = 11 corresponds to a $CFL_{characteristic}$ of 0.125. Three criteria have been imposed to define a region for optimal numerical efficiency. The computational expense limit is based on the wall-clock times estimates (Table 3.11) and ensures performance improvements of at least an order of magnitude with respect to the time- accurate simulation. Imposing a minimum threshold on the CFL_{max} prevents the constant CFL region to extend too far into the jet potential core and the shear layer, limiting the impact of the numerical artifacts on the computed solution. The colored lines show a map of the maximum allowable CFL_{max} for a given time step and turbulence energy dissipation limiter. For the unsteady calculations, a limit of $CFL_{characteristic} > 0.2$ has been imposed to allow the detection of high-frequency pressure fluctuations and resulting flow structures.

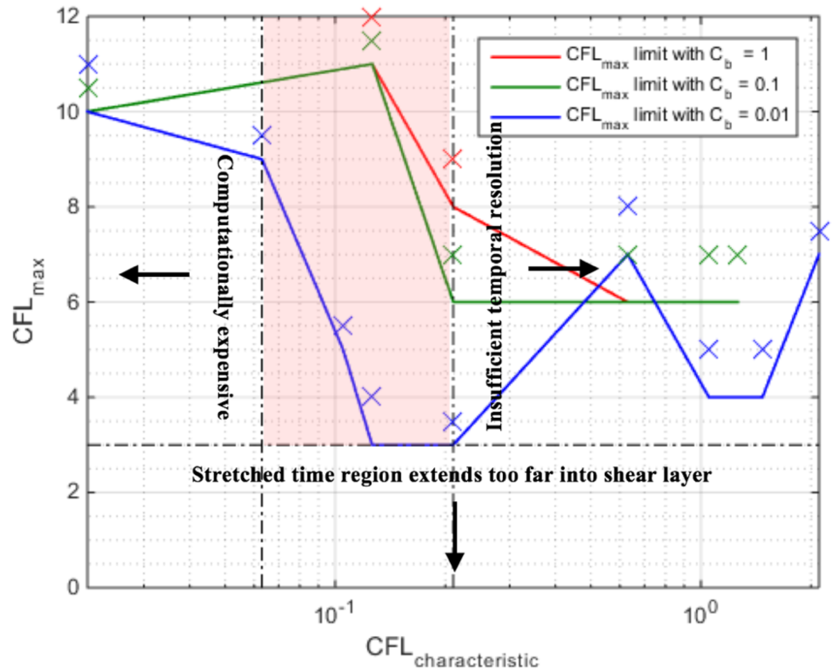

Figure 3.42 Numerical stability map. The × markers represent failed LESb runs.

3.5 Grid Sequencing

A parametric study is conducted on the impact of the grid resolution on the computed wall pressure field. For structured grids, Wind-US allows the user to thin the computational grid using a sequencing algorithm, which results in reduced CPU requirements. A different sequencing level can be specified for each direction (x, y, z). For every sequencing level, every other grid point is used in the calculation. For instance, the sequence 0 2 0 uses only every other fourth grid point in the y direction while retaining the full grid resolution in x and z directions. At the end of each time step, the solution is interpolated back onto the original grid in order to provide a continuous field for post-processing.

The sequencing parameters used in the LESb runs are shown in Table 3.13. The sequencing levels have been chosen to achieve a decrease in CPU time by a factor of 2, 2 and 4, respectively. Note that the CPU cost of indirect I/O operations generates high overhead levels, resulting in speedup times that are significantly lower than the theoretical values (Table 3.14). Turning off the data gathering in Wind-US prevents the solver from having to interpolate the solution back onto the full grid at every time step, thus achieving the speedup times expected from the grid coarsening.

Table 3.13 Initial conditions and sequencing parameters

Run	NPR	M	T (K)	P (psi)	Δt (μs)	CFL_{max}	C_b	Sequence (xyz)
15	4.0	0.5	777	58.8	6	11	0.1	0 0 0
16	4.0	0.5	777	58.8	6	11	0.1	0 2 0
17	4.0	0.5	777	58.8	6	11	0.1	1 1 1
18	4.0	0.5	777	58.8	6	11	0.1	2 2 2

Table 3.14 Speedup times with data gathering turned ON and with data gathering turned OFF

Run	Sequence (xyz)	Total elapsed time (data gathering ON)	Total elapsed time (data gathering OFF)
15	0 0 0	8 hrs	0.4 hrs
16	0 2 0	12 hrs	0.2 hrs
17	1 1 1	9 hrs	0.2 hrs
18	2 2 2	7 hrs	0.1 hrs

The power spectral density estimates (Fig. 3.43) show that all of the sequenced grids poorly predict the majority of the unsteadiness as a result of the insufficient spatial resolution. Additionally, the coarsening of the grid in the span-wise direction should not have a significant impact on the computed power spectral densities as the shocks are believed to be nearly two-dimensional. However, there exists a large difference in the PSD estimates between the simulations running with a grid sequencing of 0 0 0 and 0 2 0, suggesting that the shock systems should not be treated as two-dimensional.

The mean Mach number contours along the nozzle centerline show that the grid sequencing introduces a boundary zone discontinuity at the upper shear layer (Fig. 3.44). This discontinuity is believed to be an artifact generated when the solver is interpolating the data onto the full grid. Figure 3.44e illustrates that the CFD model running with the coarser grid is largely under-resolving the unsteadiness, thus inducing a zero-growth shear layer. An attempt has been made to eliminate the discontinuity at the boundary zone using test option 188, a subroutine of Wind-US which disables the interpolation of turbulence transport variables when the flow passes through a zone boundary. However, results from the CFD simulation running with the disabled interpolation at the boundary zone still show the presence of a discontinuity at the nozzle centerline.

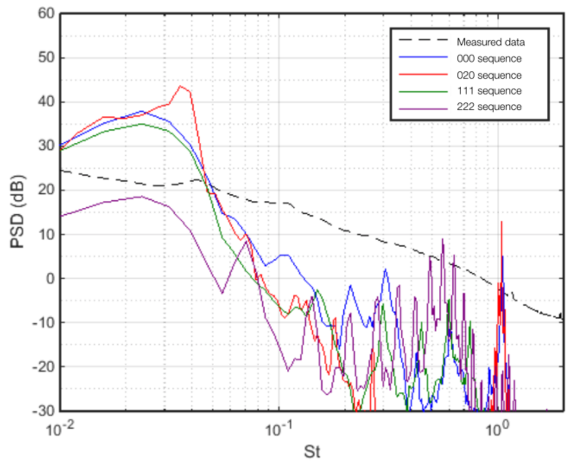

(a)

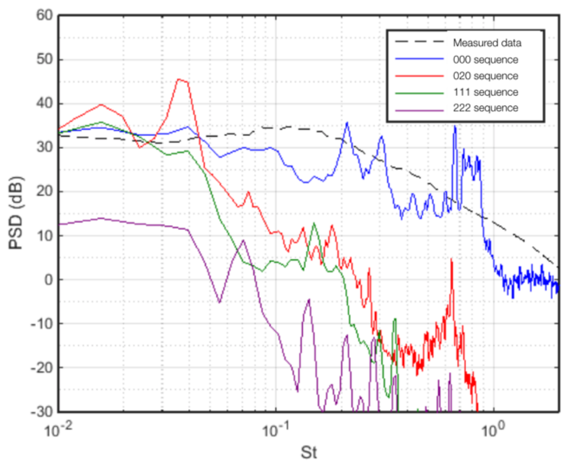

(b)

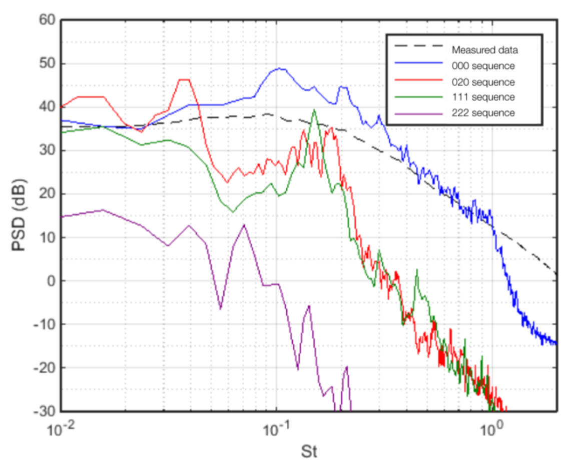

(c)

Figure 3.43 Welch power spectral densities of surface pressure fluctuations along the nozzle ¼-span at (a) $x/h_{nozzle} = 2.4$; (b) $x/h_{nozzle} = 7.1$; (c) $x/h_{nozzle} = 11.8$.

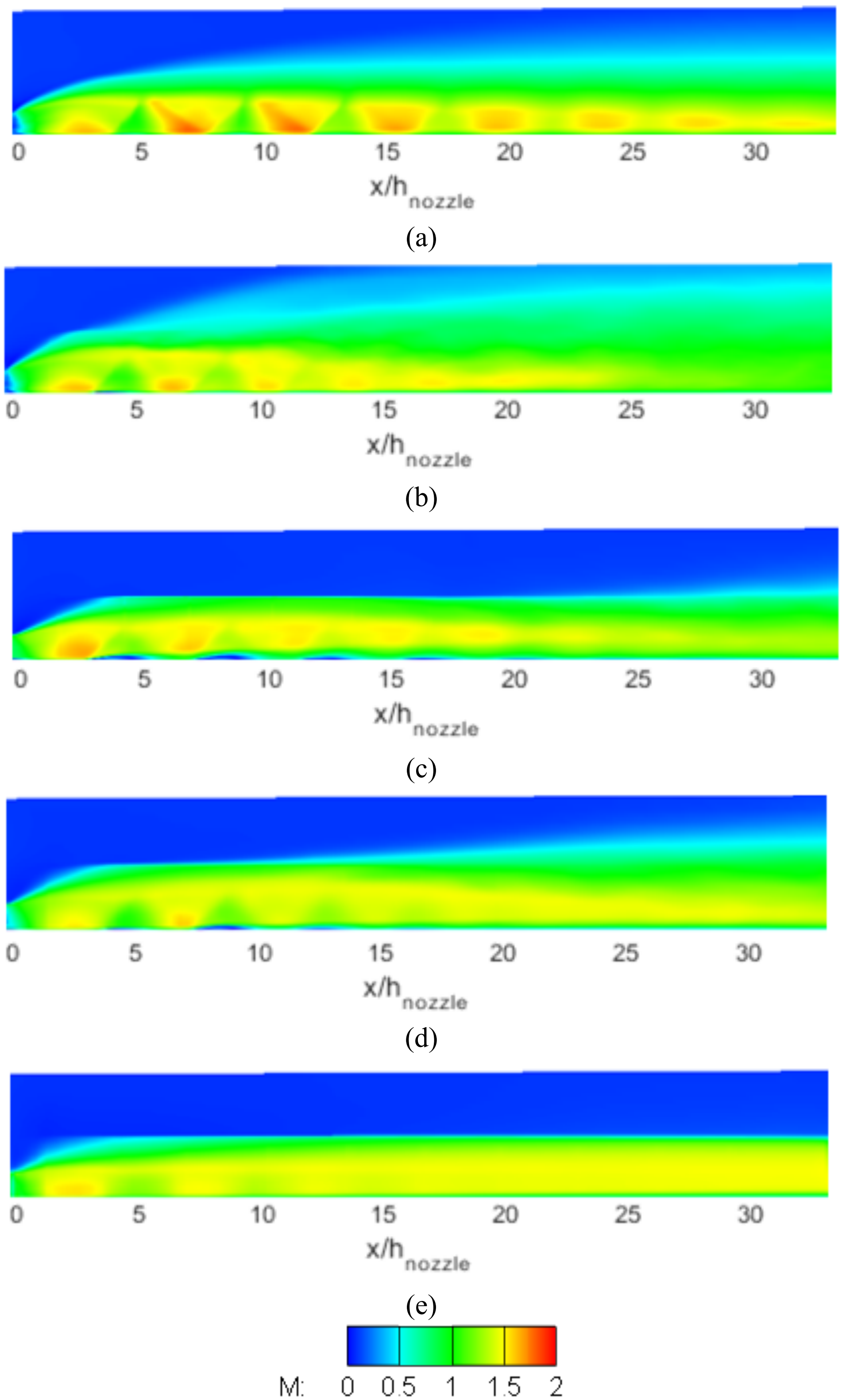

Figure 3.44 Mean Mach number contours along the nozzle centerline for (a) SSRANS; (b) 000 sequence; (c) 020 sequence; (d) 111 sequence; (e) 222 sequence.

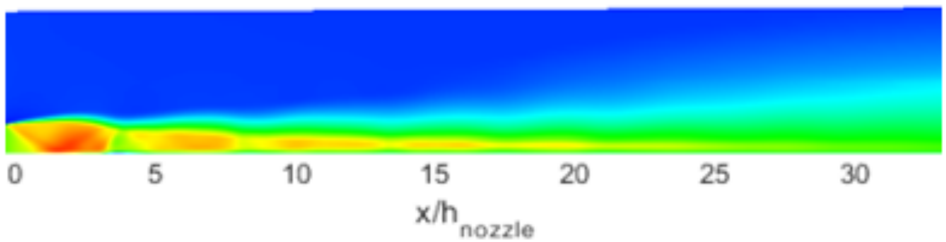

(a)

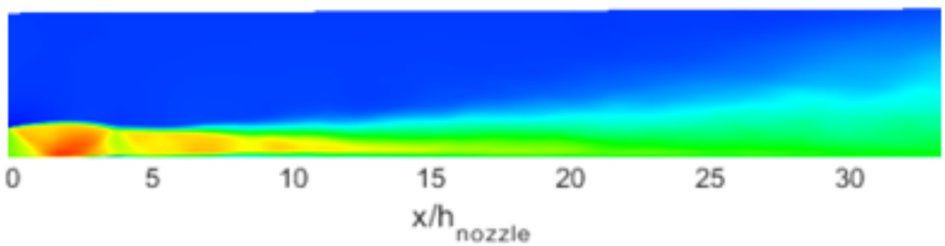

(b)

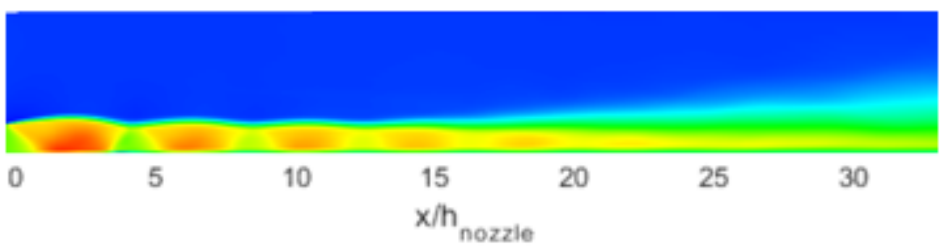

(c)

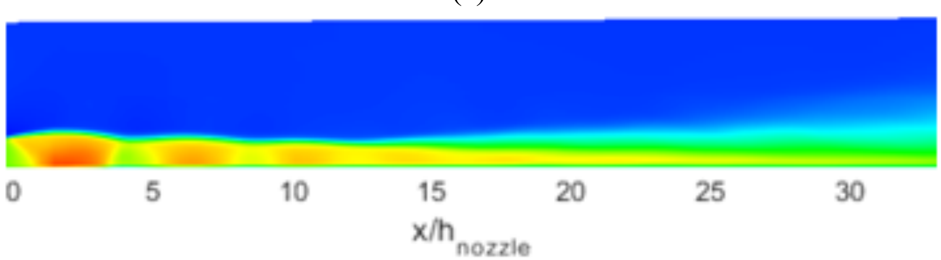

(d)

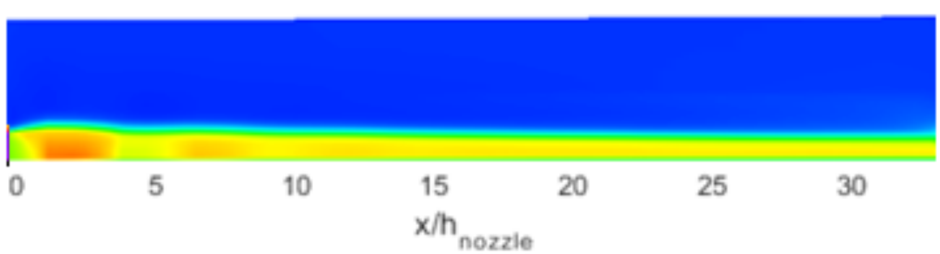

(e)

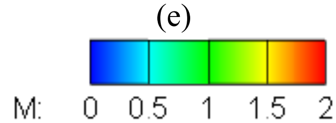

Figure 3.45 Mean Mach number contours along the nozzle ¼-span for (a) SSRANS; (b) 000 sequence; (c) 020 sequence; (d) 111 sequence; (e) 222 sequence.

As the coarseness of the grid resolution in the boundary layer increases, so does the shock spacing and the axial damping of the shock train as shown in Fig. 3.46. The mean stream-wise velocity at $x/h_{nozzle} = 1$ shows similar profiles between all LES runs; the only exception being the simulation running with the coarser grid. This indicates that coarsening the grid up to a factor of 2 does not significantly impact the boundary layer at the nozzle exit. However, the line plots of the 020 and 111 sequences show the presence of strong flow separation near the downstream SBLI region as a result of the under-resolved turbulent boundary-layer shock interactions.

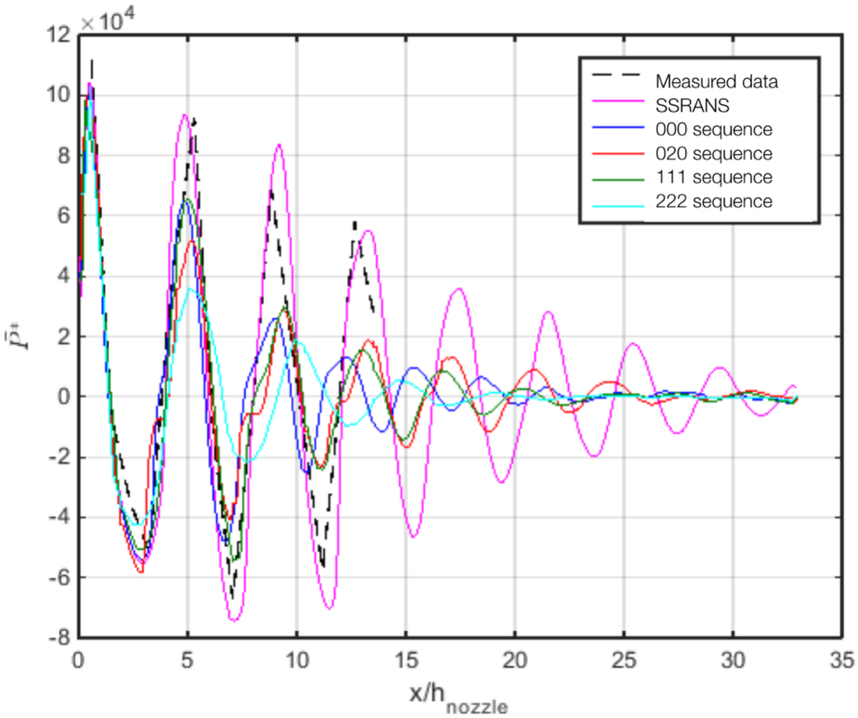

Figure 3.46 Mean surface pressure along the nozzle centerline.

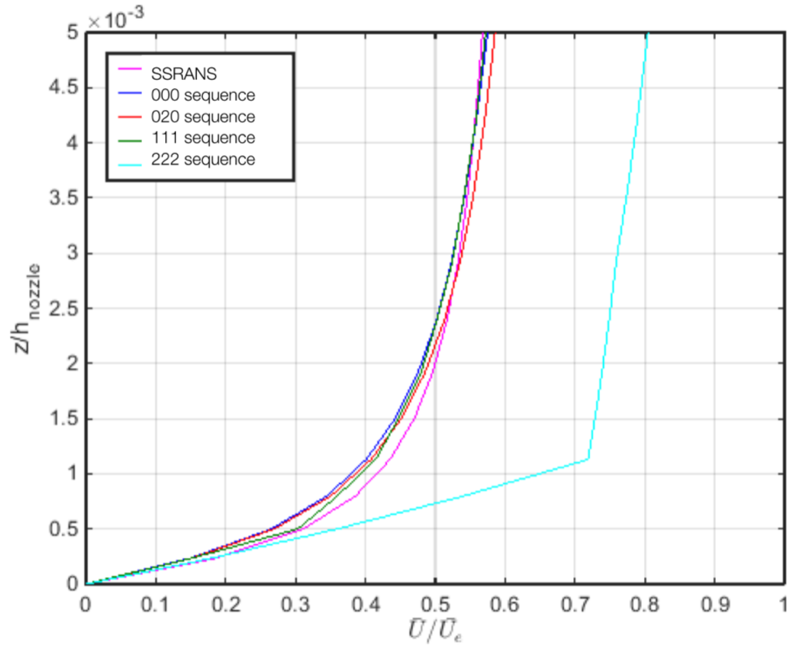

(a)

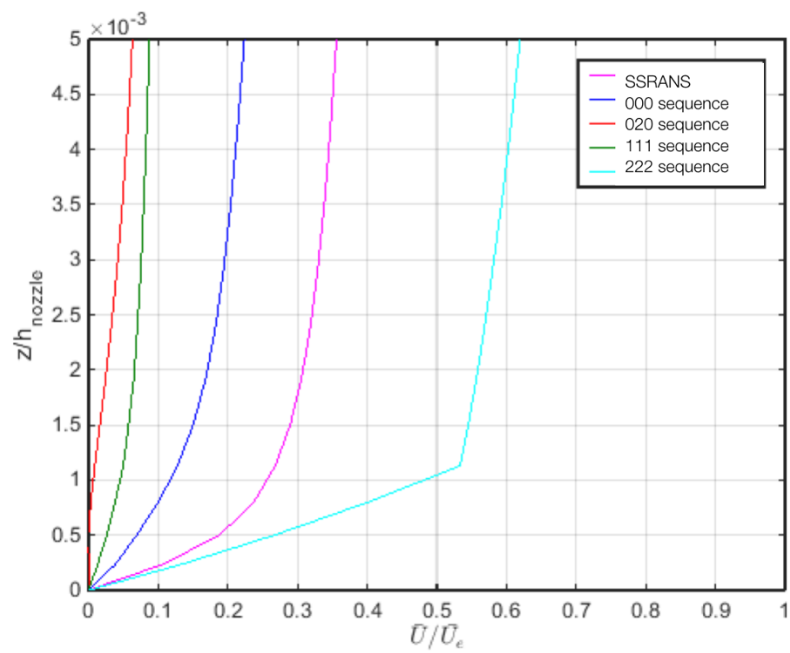

(b)

Figure 3.47 Mean stream-wise velocity along the nozzle centerline at (a) $x/h_{nozzle} = 1$; (b) $x/h_{nozzle} = 5$. Velocity levels are normalized by the mean jet exit velocity

3.6 Numerical Scheme

The choice of the finite difference scheme used to discretize the convective terms of the Navier-Stokes equations can have significant consequences on the accuracy and stability of the CFD solver. This section provides details on the numerical methods available in Wind-US and their impact on the computed turbulent jet flow.

A parametric study is performed using four different spatial schemes. The first case uses the default Wind-US scheme, a 2nd order Roe upwind-biased algorithm, modified for stretched grids. This scheme partially uses upwind information, while retaining the simplicity and efficiency of a centered scheme. The upwind bias forces the discrete approximation to directly simulate the signal propagation properties of hyperbolic systems, resulting in an essentially oscillation-free solution. The second and third cases run with 1st and 2nd order Roe fully-upwind schemes, respectively. Generally, fully-upwind schemes are more stable than upwind-biased formulations, even though they are more complex and computationally intensive. The fourth case uses a 3rd order Roe upwind-biased algorithm, modified for stretched grids. Table 3.15 shows the elapsed real time and the input parameters used for each numerical case. Note that each simulation has been run for simulated time of t = 0.04 seconds.

Table 3.15 Initial flow conditions and LESb parameters

Run	NPR	Δt (μs)	CFL_{max}	C_b	Numerical Scheme	Total elapsed time (t = 0.04 s)
19	4.0	6	11	0.1	2nd order upwind-biased	8 hrs
20	4.0	6	11	0.1	1st order fully upwind	14 hrs
21	4.0	6	11	0.1	2nd order fully upwind	18 hrs
22	4.0	6	11	0.1	3rd order upwind-biased	17 hrs

Figure 3.48 shows that by changing the default scheme from 2nd order to 1st order the amount of unsteadiness predicted by the solver is greatly reduced as a result of the severe numerical dissipation introduced by the lower-order scheme. The 2nd order fully-upwind and 3rd order upwind-biased schemes provide power spectral density levels nearly identical to those predicted by the default 2nd order scheme. This result indicates that, in this particular case, using a higher-order formulation or a fully-upwind scheme does not improve the accuracy of the solver.

Pure upwind-based methods tend to be more stable near the shocks due to their higher levels of inherent dissipation. Total variation diminishing (TVD) limiters can be used to reduce the pressure fluctuations on either side of the shock. Applying these fixes near discontinuities is a greater challenge in Large-Eddy Simulations than in RANS because any additional damping will act to weaken the resolved turbulent structures. Therefore, care must be taken to only apply enough dissipation to keep the scheme stable in the shock region. The total variation diminishing flux limiter (TVD) is set to a compression value of 1.0 to improve numerical stability when using high-order schemes (2^{nd} order or higher). The TVD limits the local maxima and minima to acceptable values based on the data used by the discretization scheme during the interpolation and extrapolation of flux quantities.

The 1st-order schemes only use single point interpolation; therefore, the TVD limiter has no effect on such cases. Note that a TVD compression factor of 1.0 nearly reduces the 3^{rd} order upwind-biased scheme to the default 2^{nd} order scheme. Further studies using higher TVD factors are necessary to fully understand the impact of high-order discretization schemes on the computed wall-pressure spectra.

The mean Mach number contours show that the impact of the numerical schemes on the accumulated LESb solutions is negligible (Fig. 3.49 – 3.50). Additionally, the mean wall-pressure and stream-wise velocity fields (Fig. 3.51 – 3.52) show nearly identical profiles between all LESb runs. The conclusion is that the default spatial scheme running with a TVD of 1.0 provides the shortest run time while retaining the spectral accuracy of the high-order fully-upwind scheme.

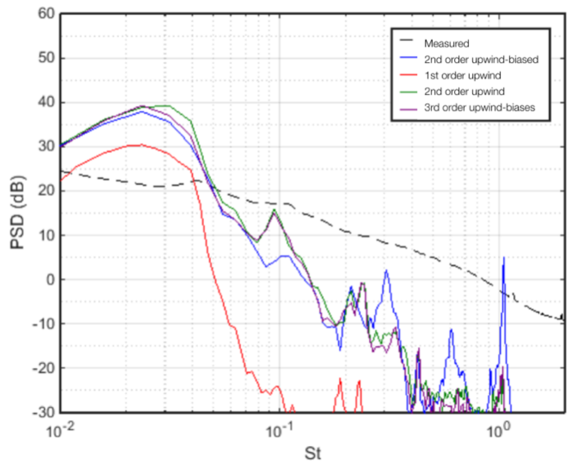

(a)

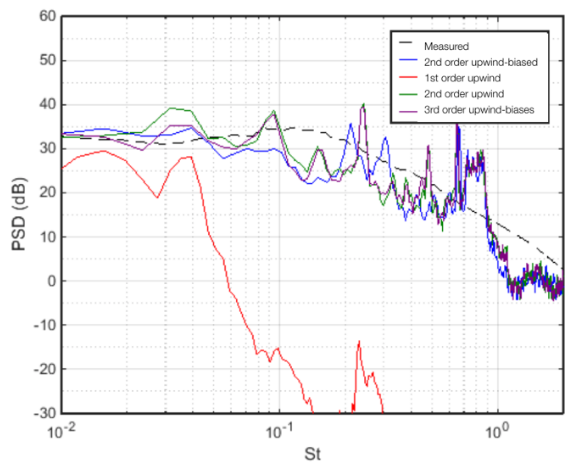

(b)

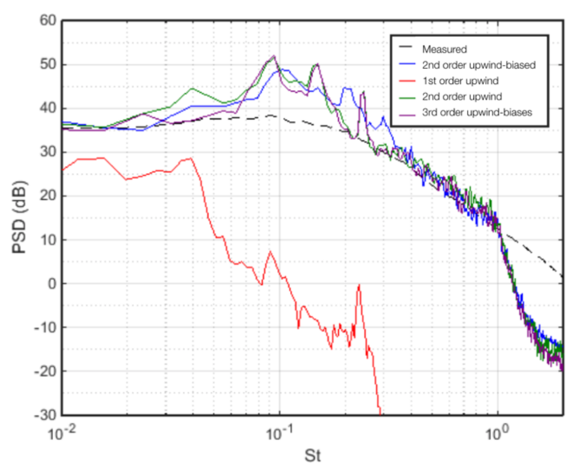

(c)

Figure 3.48 Welch power spectral densities of surface pressure fluctuations along the nozzle ¼-span at (a) $x/h_{nozzle} = 2.4$; (b) $x/h_{nozzle} = 7.1$; (c) $x/h_{nozzle} = 11.8$.

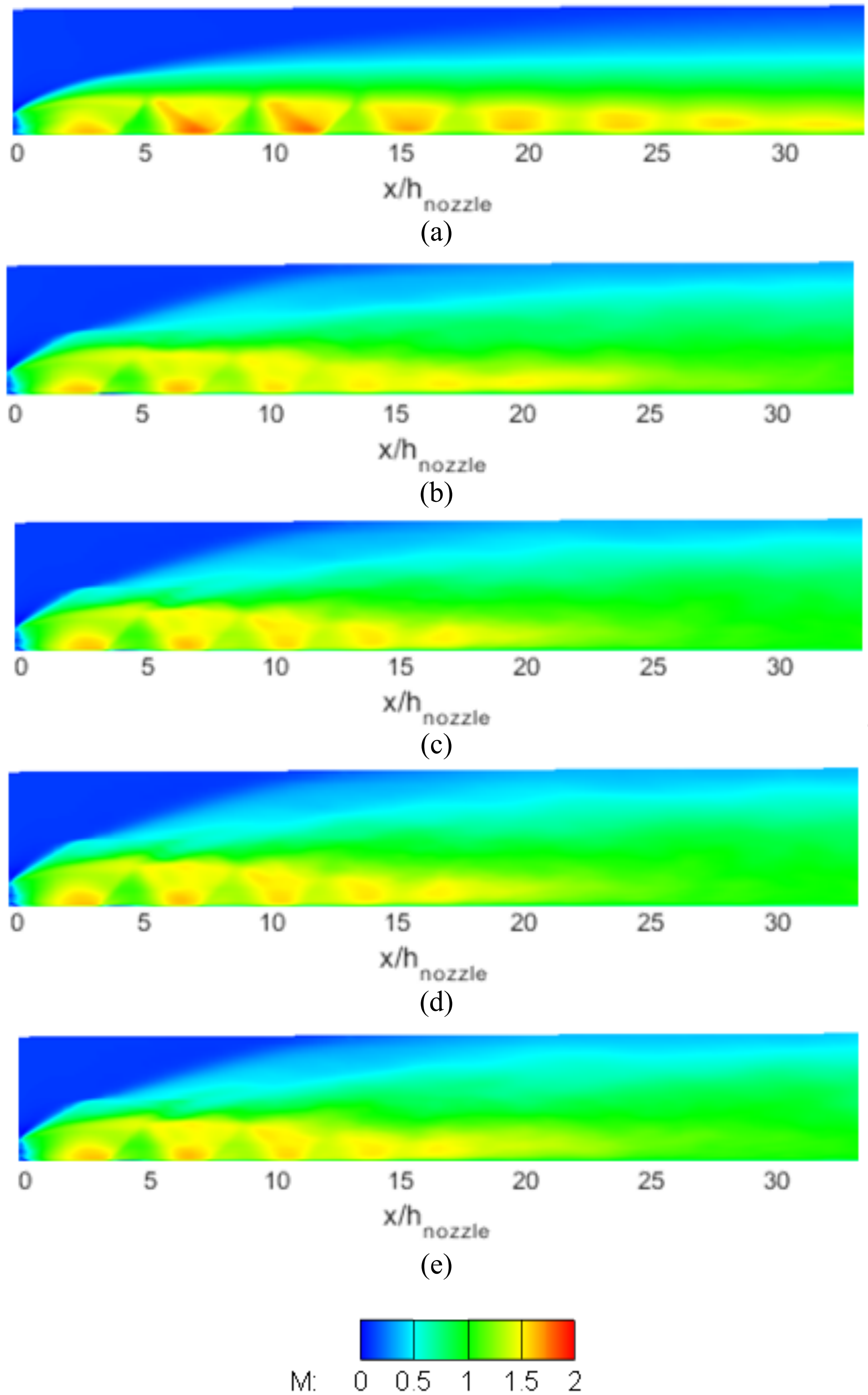

Figure 3.49 Mean Mach number contours along the nozzle centerline for (a) SSRANS; (b) 2nd order upwind-biased; (c) 1st order upwind; (d) 2nd order upwind; (e) 3rd order upwind-biased.

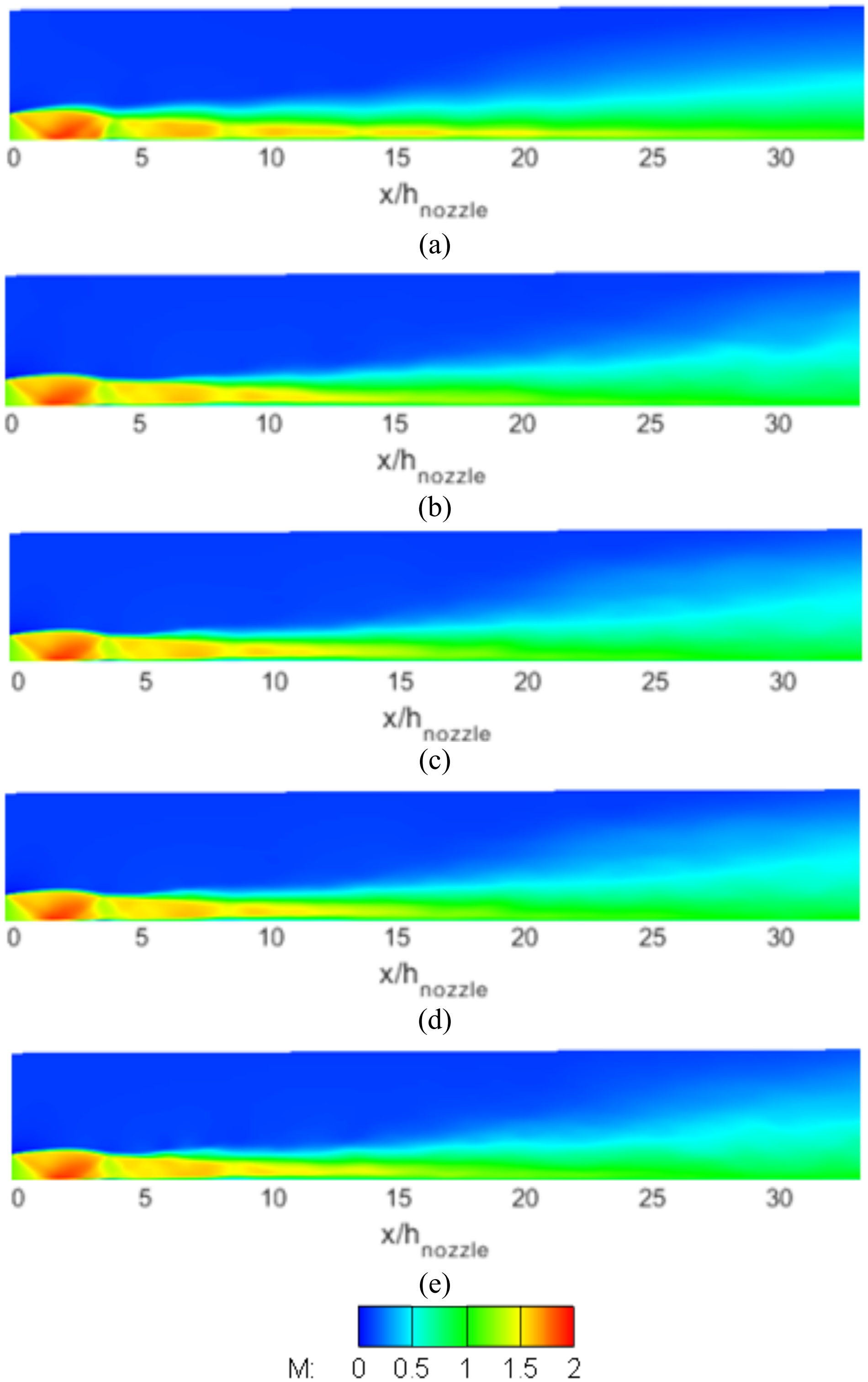

Figure 3.50 Mean Mach number contours along the nozzle ¼-span for (a) SSRANS; (b) 2^{nd} order upwind-biased; (c) 1^{st} order upwind; (d) 2^{nd} order upwind; (e) 3^{rd} order upwind-biased.

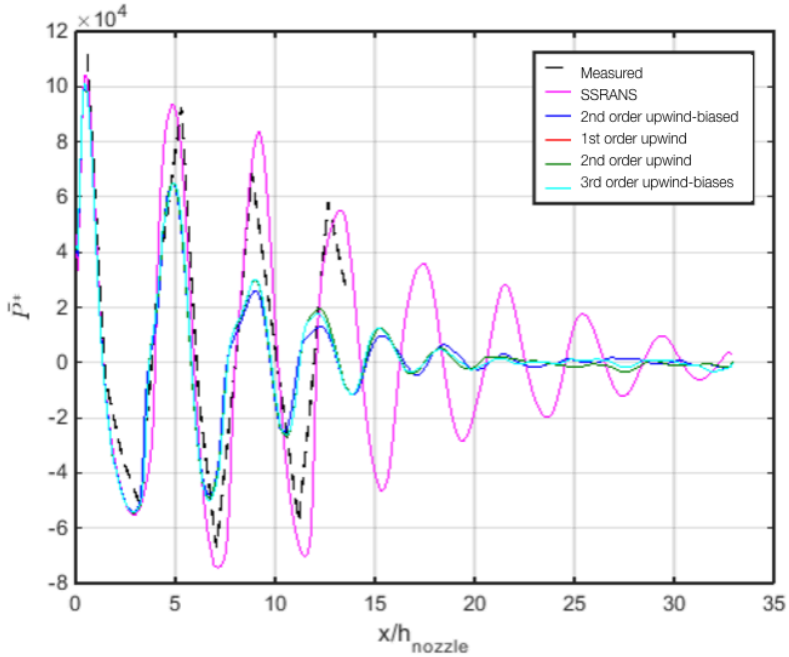

Figure 3.51 Mean surface pressure along the nozzle centerline.

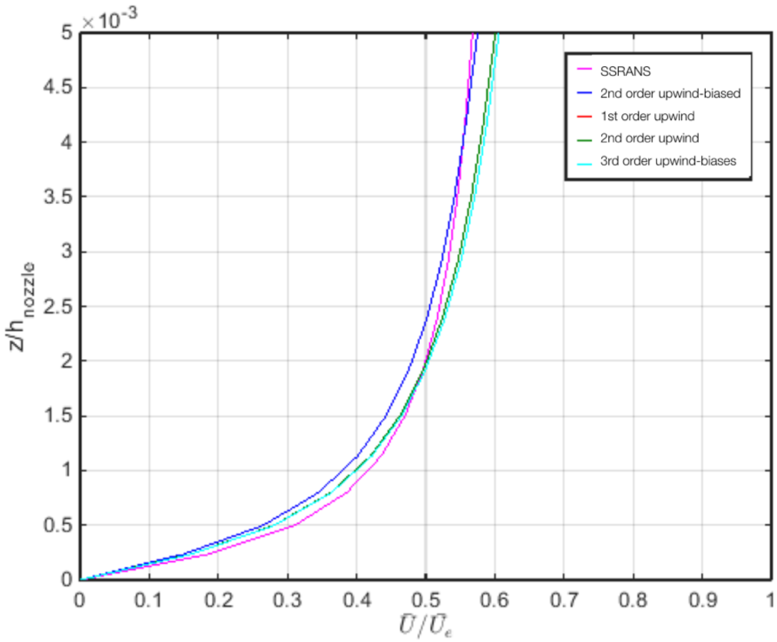

(a)

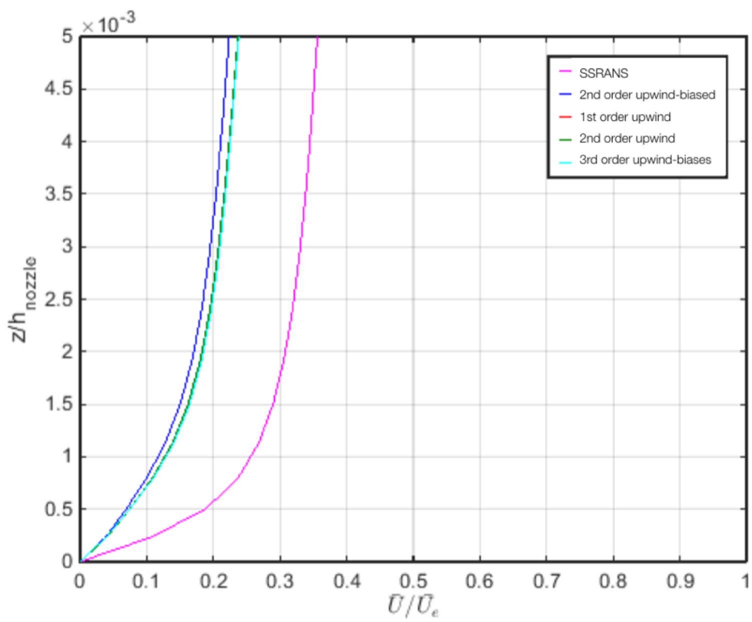

(b)

Figure 3.52 Mean stream-wise velocity along the nozzle centerline at (a) x/h_{nozzle} = 1; (b) x/h_{nozzle} = 5. Velocity levels are normalized by the mean jet exit velocity

The convective axial velocities at the downstream locations are computed from the lag of the correlation peak and are shown in Table 3.16. Runs 19, 21 and 22 predict very similar convective velocities, while the 1st order spatial scheme shows the existence of upstream traveling waves. A similar result was observed in Section 2. It is believed that the added dissipation from the low-order scheme increases the strength of the periodic artifacts near the deck surface, altering the coherent nature of wall pressure fluctuations.

The normalized cross-correlation functions for the 2nd order fully-upwind and 3rd order upwind-biased schemes do not show any significant difference with respect to the baseline LESb model. Figure 3.53 shows that the 1st order scheme predicts upstream wall-pressure fluctuations that are perfectly correlated at $x/h_{nozzle} = 2.7$ while the other runs show a decrease in the axial-correlation of 80%.

Table 3.16 Axial convection velocities

Run	Δt (μs)	Numerical Scheme	V_{DE} (ft/s)	V_{DF} (ft/s)
19	6	2nd order upwind-biased	1302	947
20	6	1st order fully upwind	-3472	-1250
21	6	2nd order fully upwind	1302	919
22	6	3rd order upwind-biased	1302	919

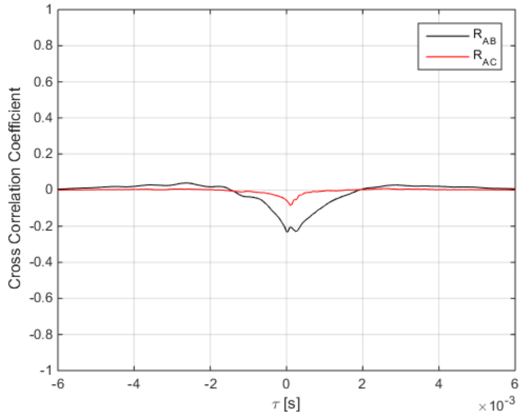

(a)

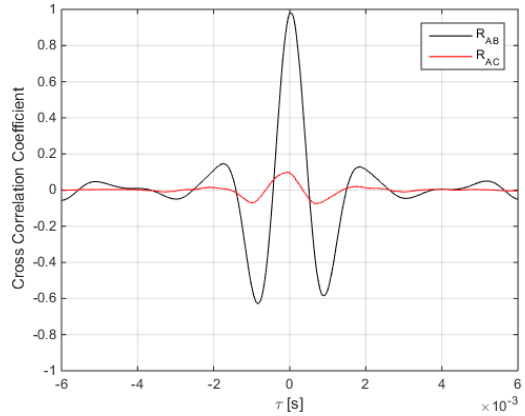

(b)

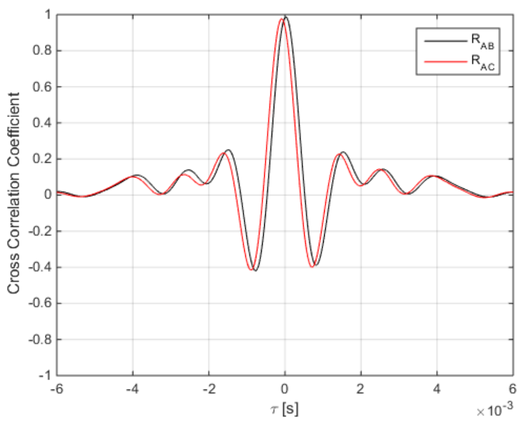

(c)

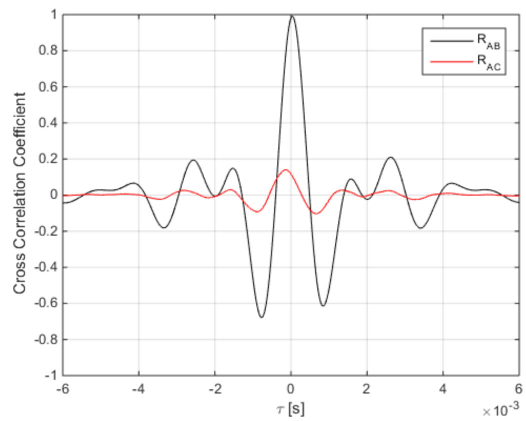

(d)

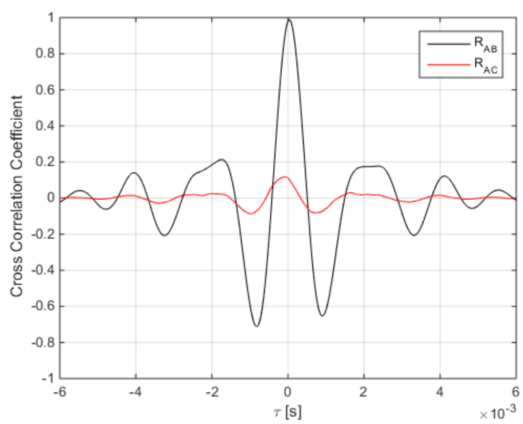

(e)

Figure 3.53 Upstream axial pressure correlations from the NPR = 4.0 data. (a) Measured; (b) 2nd order upwind-biased; (c) 1st order upwind; (d) 2nd order upwind; (e) 3rd order upwind-biased.

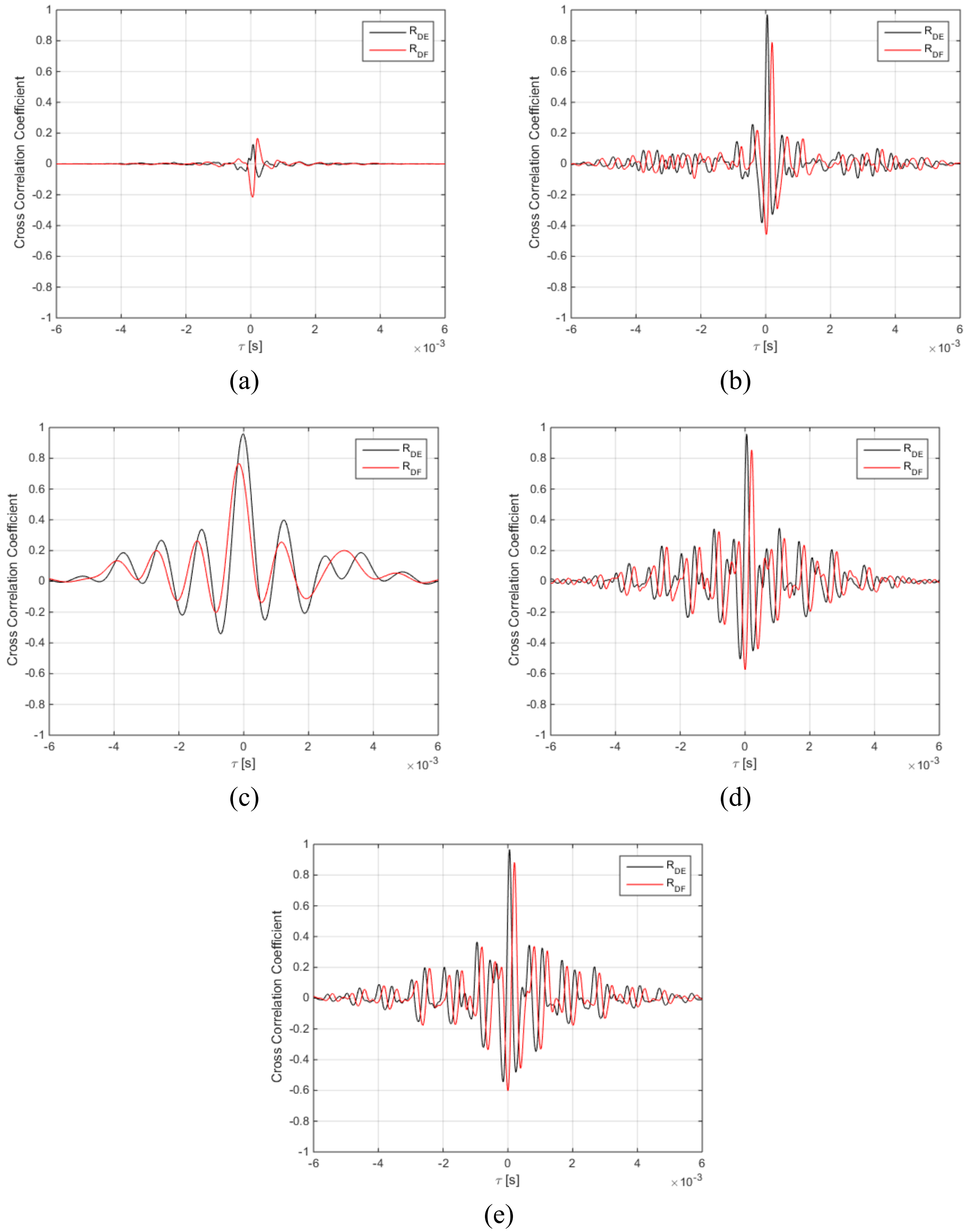

Figure 3.54 Downstream axial pressure correlations from the NPR = 4.0 data. (a) Measured; (b) 2nd order upwind-biased; (c) 1st order upwind; (d) 2nd order upwind; (e) 3rd order upwind-biased.

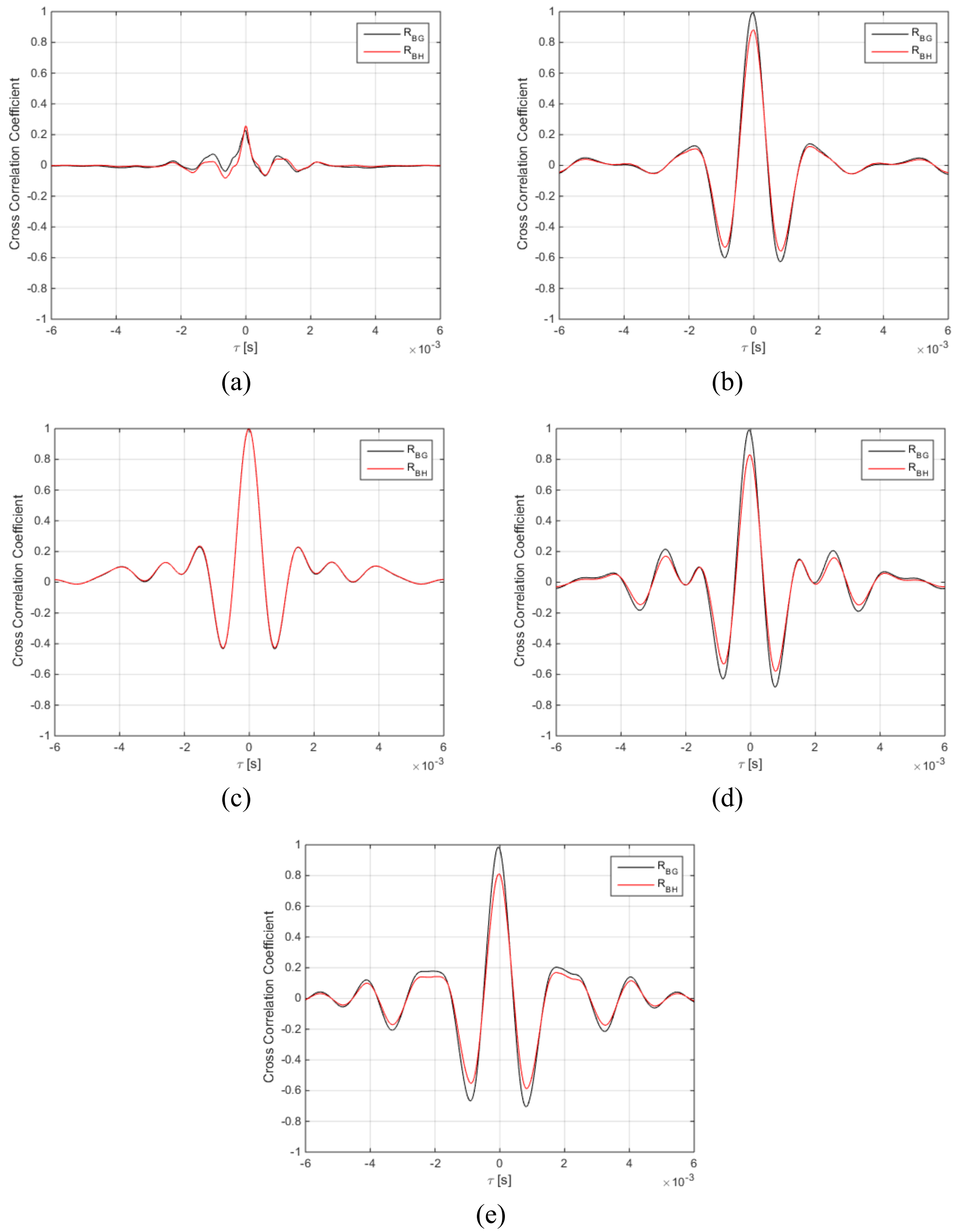

Figure 3.55 Upstream cross-stream pressure correlations from the NPR = 4.0 data. (a) Measured; (b) 2nd order upwind-biased; (c) 1st order upwind; (d) 2nd order upwind; (e) 3rd order upwind-biased.

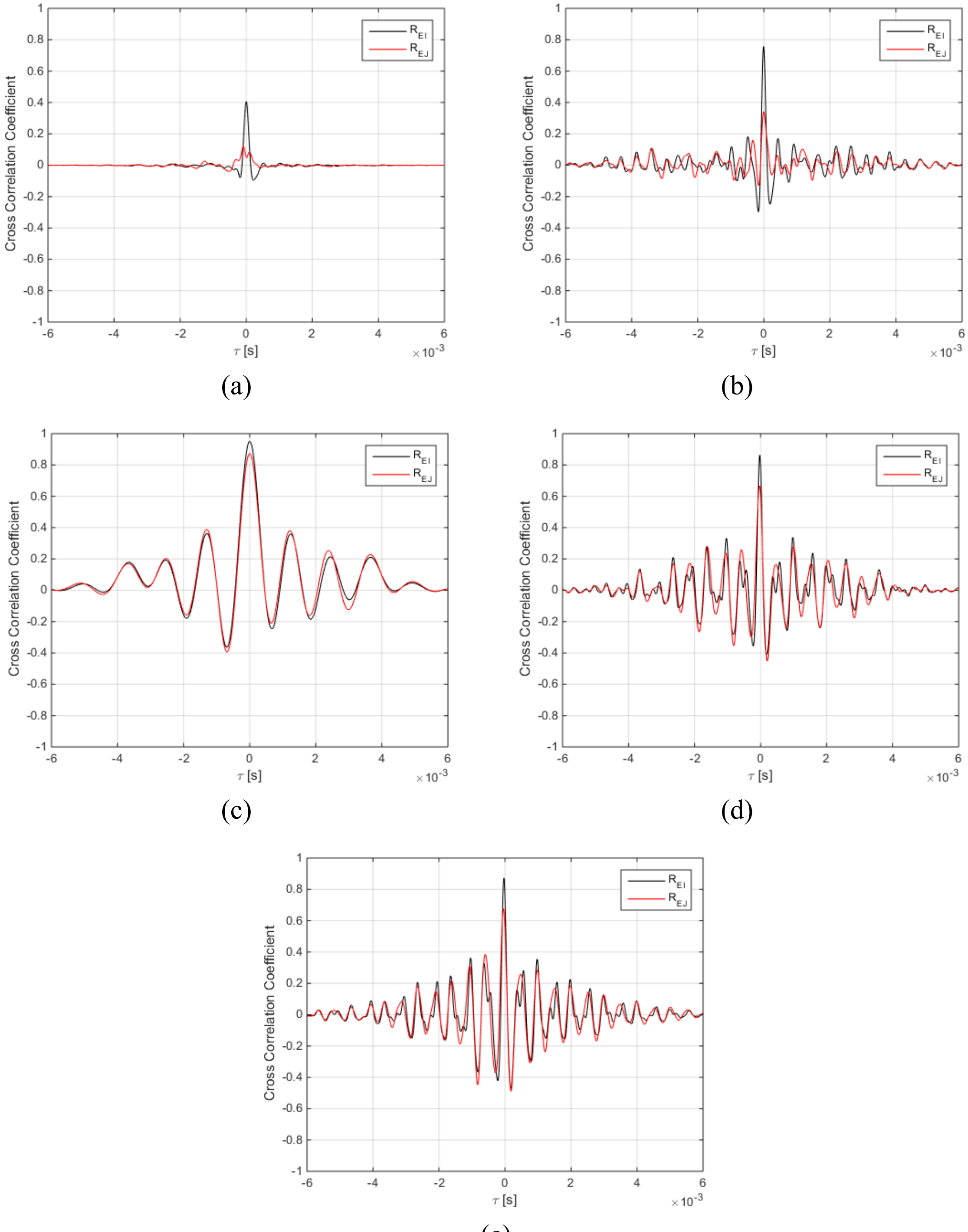

Figure 3.56 Downstream cross-stream pressure correlations from the NPR = 4.0 data. (a) Measured; (b) 2nd order upwind-biased; (c) 1st order upwind; (d) 2nd order upwind; (e) 3rd order upwind-biased.

3.7 *Upstream Forcing*

A numerical study is conducted on a wall-bounded turbulent jet whose boundary layers are tripped inside the nozzle. The main purpose of this study is to investigate the impact of the unsteady upstream forcing on the shock-boundary layer interactions and the development of the jet shear layer. The boundary layers are tripped by the injection of random velocity disturbances at the upper and lower walls of the nozzle. Fig. 3.57 presents a visualization of the instantaneous transverse velocity contours in the (x,z) and (x,y) planes. The figure shows that the injection layers are located at x/h_{nozzle} = -0.1 upstream of the nozzle exit. The close distance to the nozzle exit provides enough downstream distance to analyze the effects of the tripped boundary layer on the wall-pressure field.

Bogey and Marsden [34] suggest that the injected disturbances should have a peak velocity magnitude of at least 9% of the jet exit velocity to ensure that the disturbances are aggressive enough to trip the upstream boundary layers. The injection parameters have been adjusted so that the peak turbulence intensities are 10% of the jet exit velocity with an injection angle of $\emptyset_{inj} = 90°$ normal to the wall. Furthermore, the unsteady excitations are partially random and not strongly correlated so that the jet can develop in a natural way. The quasi-random nature of the injected disturbances minimizes the production of spurious acoustic waves by the forcing. Wind-US allows the superposition of up to ten different perturbations to generate an unsteady velocity field. A list of the individual disturbances used to construct the upstream excitations is shown in Table 3.17.

Figure 3.58 shows a representation of the excitation signal. The simulation without upstream forcing is identical to the baseline LESb case described in section 3.4. The mean mass-flow rates at the nozzle exit of the runs with and without the upstream forcing are 2.7265 kg/s and 2.7287 kg/s, respectively.

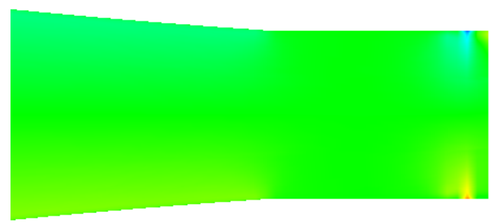

(a)

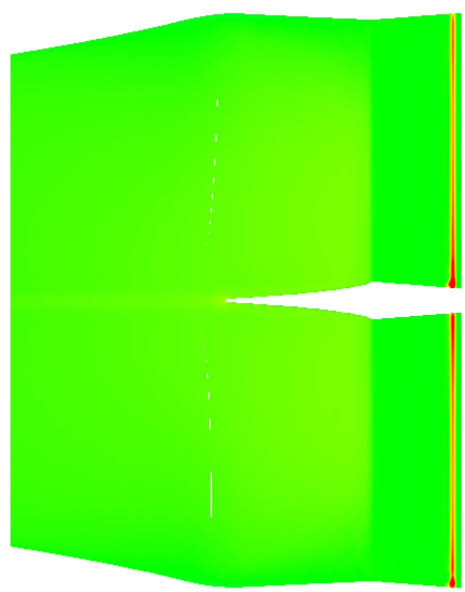

(b)

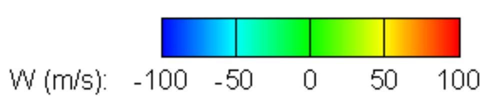

Figure 3.57 Instantaneous normal velocity contours upstream of the nozzle exit. (a) y = $1.85h_{nozzle}$ cutting plane; (b) z = $0h_{nozzle}$ cutting plane.

Table 3.17 Unsteady arbitrary inflow parameters. The frequency components of the individual excitations are non-dimensionalized by the jet characteristic frequency.

Forcing signal	T_{inj} (R)	$\emptyset_{\mathrm{inj}}$ (°)	U_{peak} (ft/s)	Frequency (St)	Phase (°)
1	777	90	30	0.02	0
2	777	90	30	0.04	180
3	777	90	30	0.05	15
4	777	90	30	0.15	200
5	777	90	30	0.19	30
6	777	90	30	0.33	250
7	777	90	30	0.47	50
8	777	90	30	0.57	75
9	777	90	30	0.71	90
10	777	90	30	0.95	125

Table 3.18 Input conditions.

Run	NPR	Upstream Forcing
23	4.0	No
24	4.0	Yes

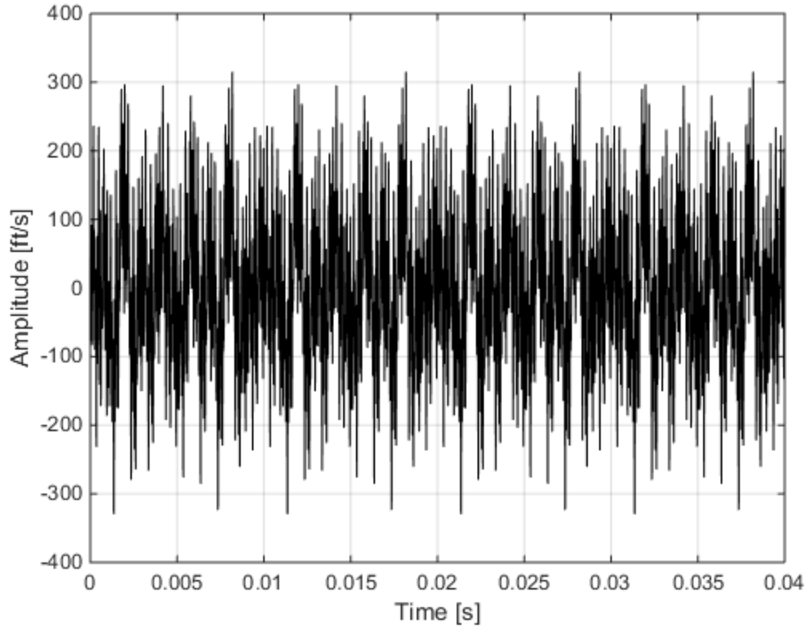

Figure 3.58 Upstream forcing signal

The impact of the tripped boundary layer on the wall pressure spectra is shown in Figure 3.59. The upstream forcing generates more broadband unsteadiness near the nozzle exit compared to the case without forcing (Fig. 3.59a). The figures indicate that the baseline case is over-damping the boundary layer unsteadiness, possibly due to the artificial dissipation introduced by the LES. The PSD data from the simulation with the upstream forcing shows better correlation with the measured data for all three sensor locations, indicating that the introduction of upstream forcing can be used to improve the prediction of pressure fluctuations on the deck surface.

A direct comparison of the mean flow illustrates some of the differences between the two solutions. In the simulation with the upstream forcing, the shear layer on the nozzle centerline shows very little growth up to a downstream distance of ten nozzle heights (Fig 3.60). The ¼-span flow visualization of the upstream forcing results shows a rapid acceleration of the shear layer growth at approximately five nozzle heights downstream of the nozzle exit. Additionally, a large bubble of flow separation can be observed at $x/h_{nozzle} = 3$ as a result of the shock interacting with the more unsteady boundary layer. The higher power spectral density levels at the low frequencies provide further evidence of intense the SBLIs present in the case with the tripped upstream boundary layer.

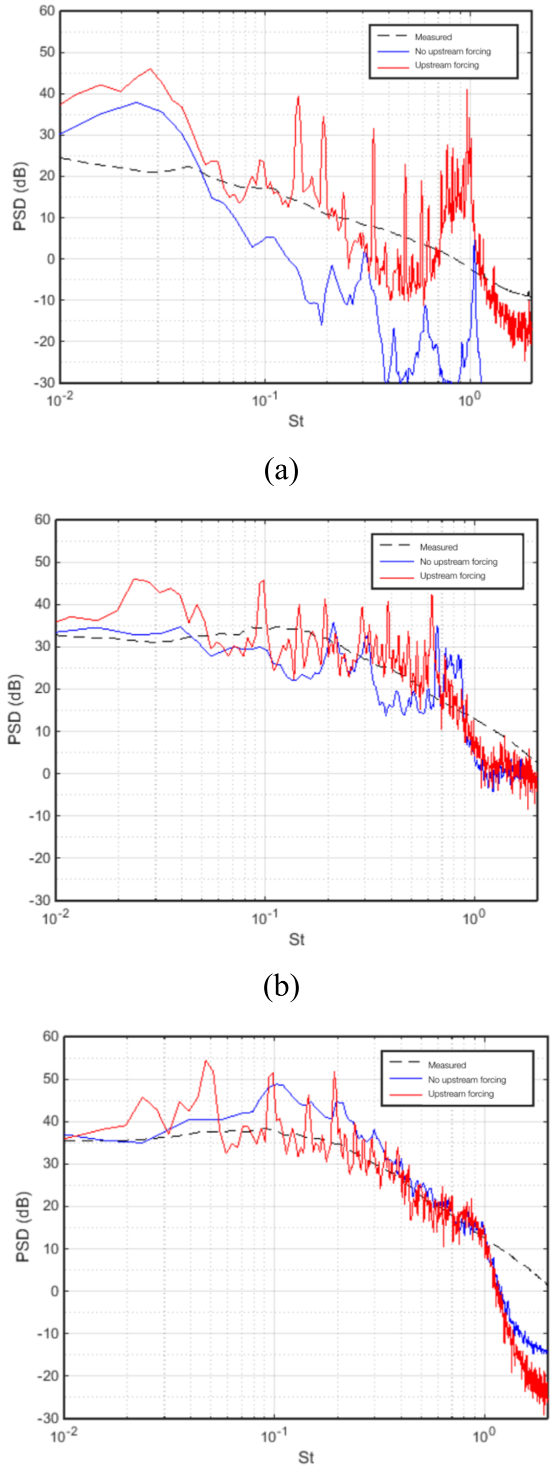

(a)

(b)

(c)

Figure 3.59 Welch power spectral densities of surface pressure fluctuations along the nozzle ¼-span at (a) $x/h_{nozzle} = 2.4$; (b) $x/h_{nozzle} = 7.1$; (c) $x/h_{nozzle} = 11.8$.

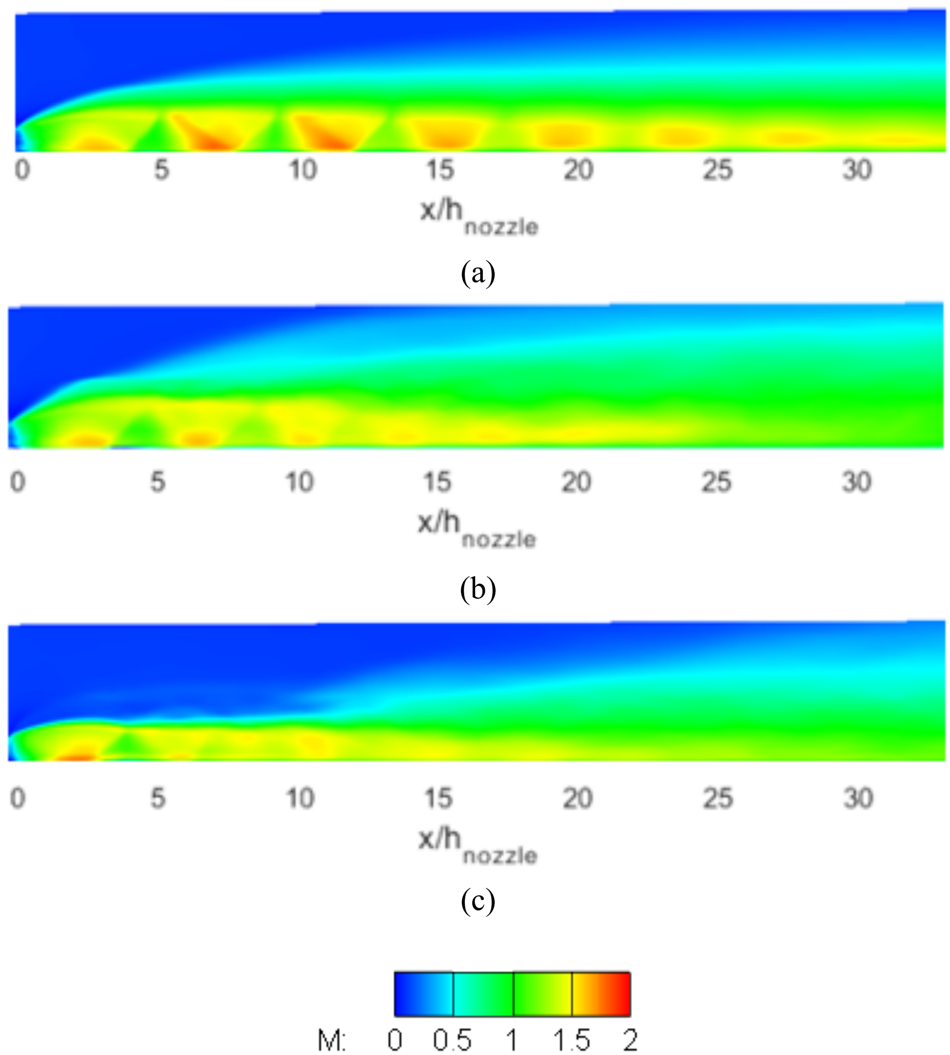

Figure 3.60 Mean Mach number contours along the nozzle centerline for (a) SSRANS; (b) No upstream forcing (c) Upstream forcing.

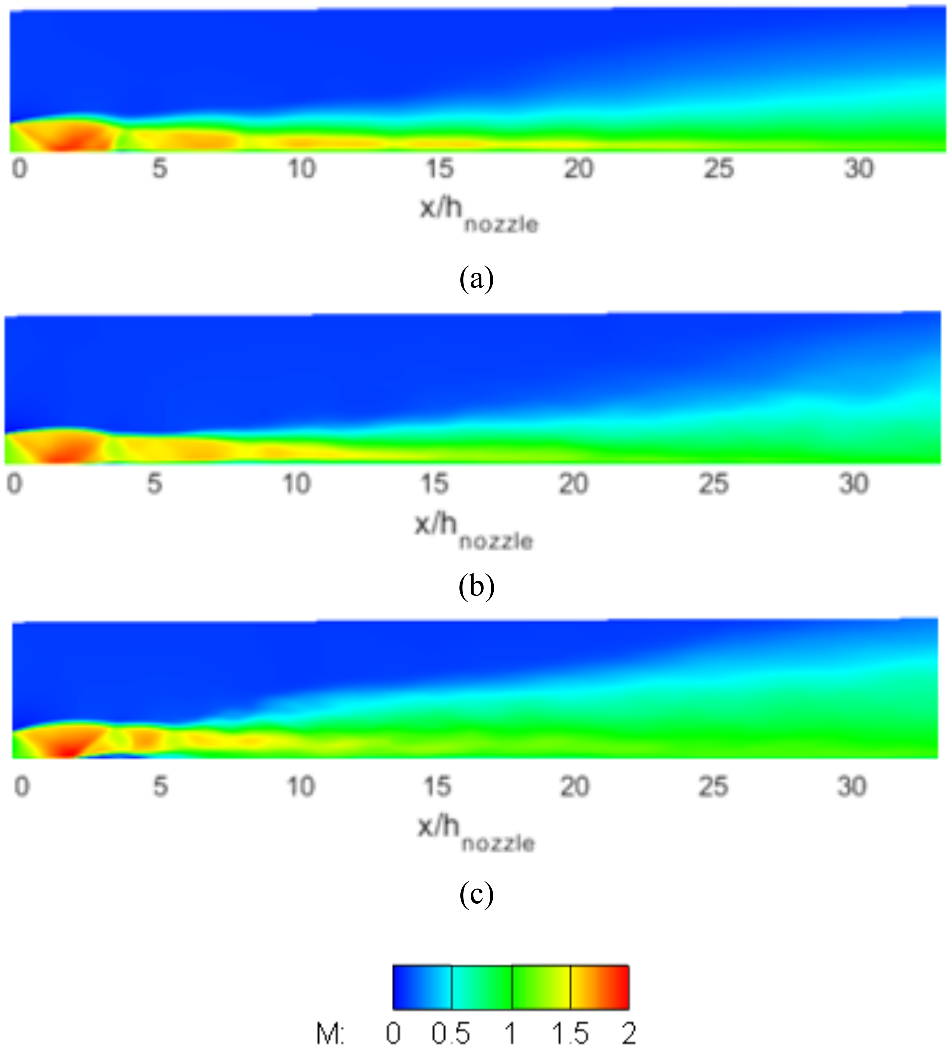

Figure 3.61 Mean Mach number contours along the nozzle ¼-span for (a) SSRANS; (b) No upstream forcing (c) Upstream forcing.

The upstream forcing does not show a significant difference in the mean shock strength, with the exception of the first shock cell which shows a particularly high pressure level (Fig. 3.62). The shock spacing on the nozzle centerline shows a small difference between the two LESb runs. A marginal increase in the shock spacing is observable in Figure 3.62. Nonetheless, the downstream shocks are still overdamped compared to the SS-RANS solution.

Figure 3.63 shows very similar boundary layer profiles between the two LESb cases, indicating that the upstream forcing has mostly impacted the development of the shear layer.

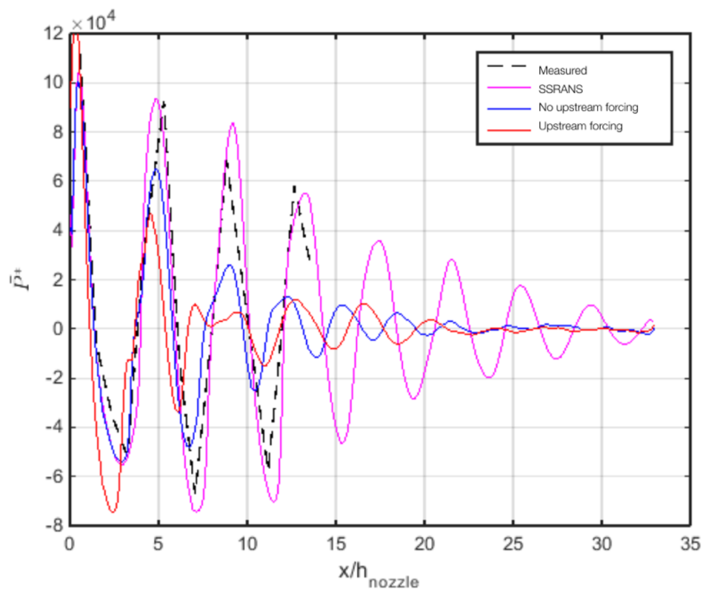

Figure 3.62 Mean surface pressure along nozzle centerline

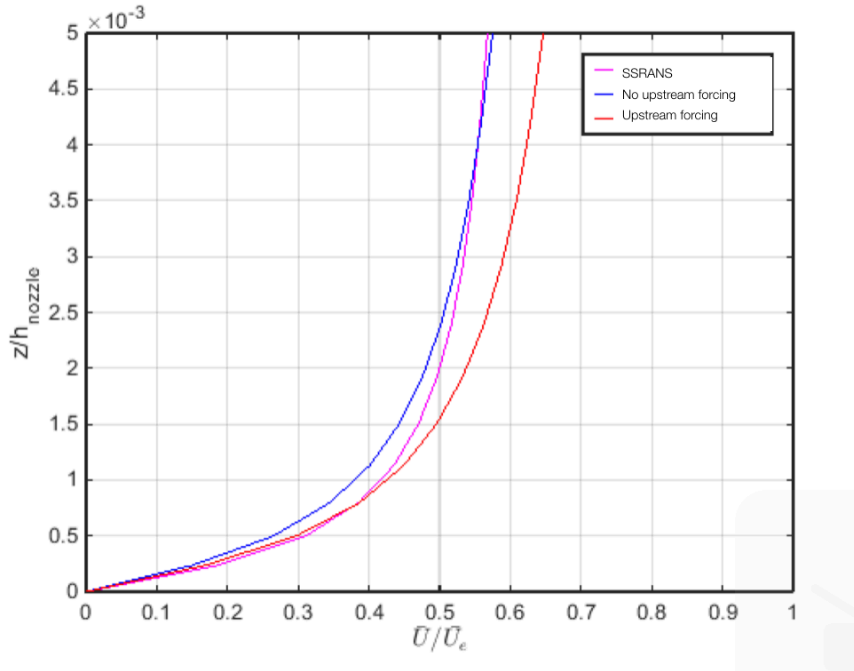

(a)

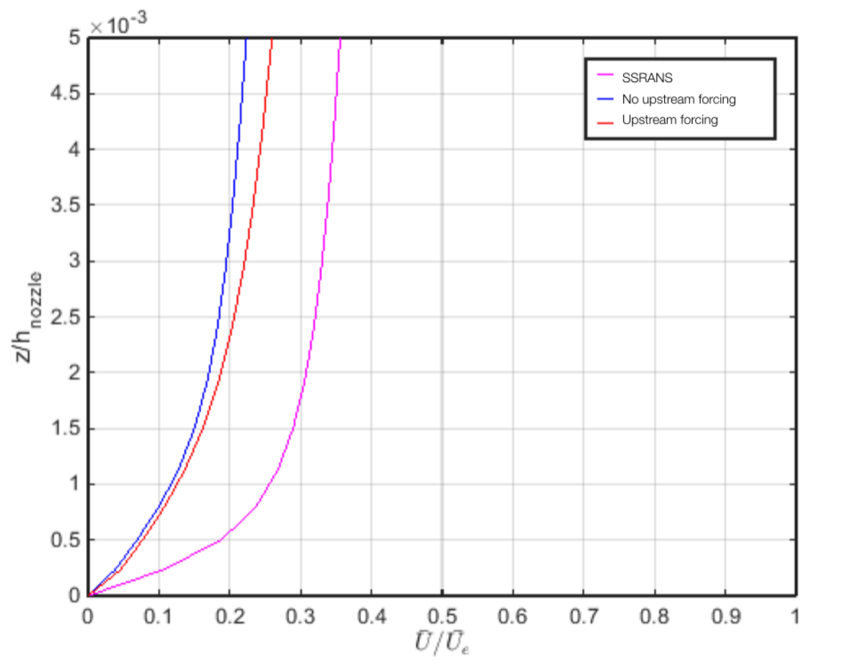

(b)

Figure 3.63 Mean stream-wise velocity along the nozzle centerline at (a) x/h_{nozzle} = 1; (b) x/h_{nozzle} = 5. Velocity levels are normalized by the mean jet exit velocity

The injection of unsteady velocity fluctuations does not affect the axial convection velocity of the downstream structures (Table 3.19). However, the upstream forcing appears to have a severe impact on the coherent nature of the wall-pressure field as shown in the wall-pressure cross-correlation plots below.

The sampling locations used to generate the cross-correlation coefficients are shown in Figure 3.13. The normalized cross-correlation coefficients show weaker cross-correlations for the LESb run with the upstream forcing. Additionally, figures 3.64b – 3.67b show that the upstream forcing introduces a periodic component with a frequency of St = 0.96, corresponding to the frequency peak observed in the upstream power spectral density plot (Fig. 3.59a). The points of maximum cross-correlation computed from the downstream sensors repeat with a frequency of St = 0.048, which corresponds to the frequency peak observed in the downstream power spectral density plot (Fig 3.59c). This suggests that the coherent nature of the upstream turbulent structures is largely dominated by the high frequency components of the forcing function. The dominant frequency affecting the coherence of the wall pressure field decreases with increasing downstream distance. Figure 3.64 shows that the impact of the upstream forcing on the coherence of the axial wall-pressure field is still present at $x/h_{nozzle} = 10$.

Table 3.19 Axial convection velocities.

Run	Δt (μs)	Upstream forcing	V_{DE} (ft/s)	V_{DF} (ft/s)
23	6	No	1302	947
24	6	Yes	1488	947

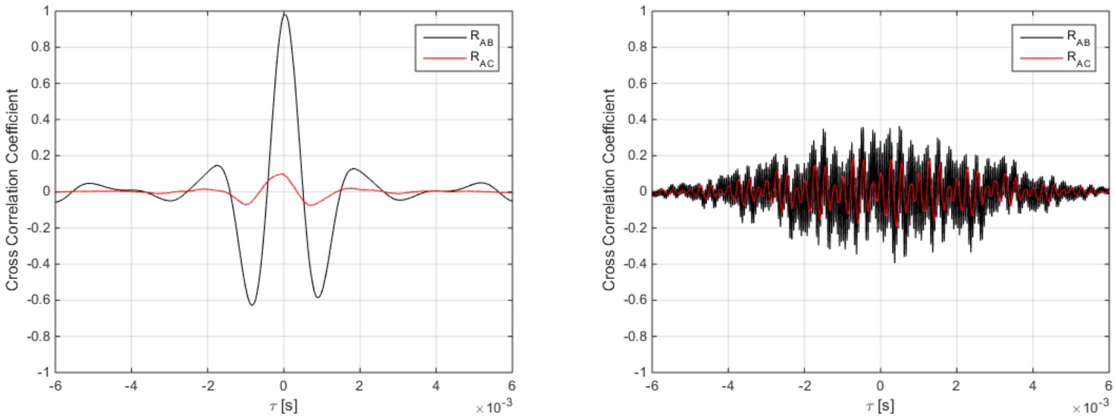

(a) (b)

Figure 3.64 Upstream axial pressure correlations from the NPR = 4.0 data. (a) No upstream forcing; (b) Upstream forcing.

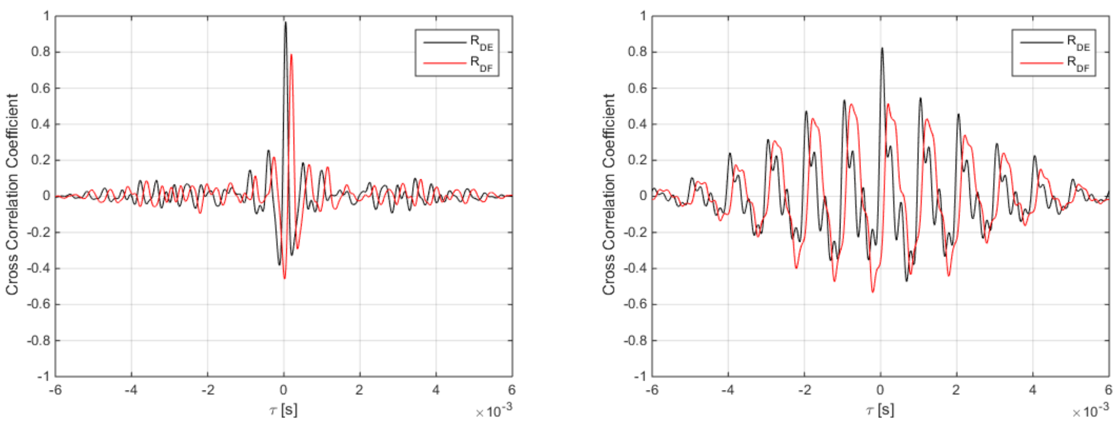

(a) (b)

Figure 3.65 Downstream axial pressure correlations from the NPR = 4.0 data. (a) No upstream forcing; (b) Upstream forcing.

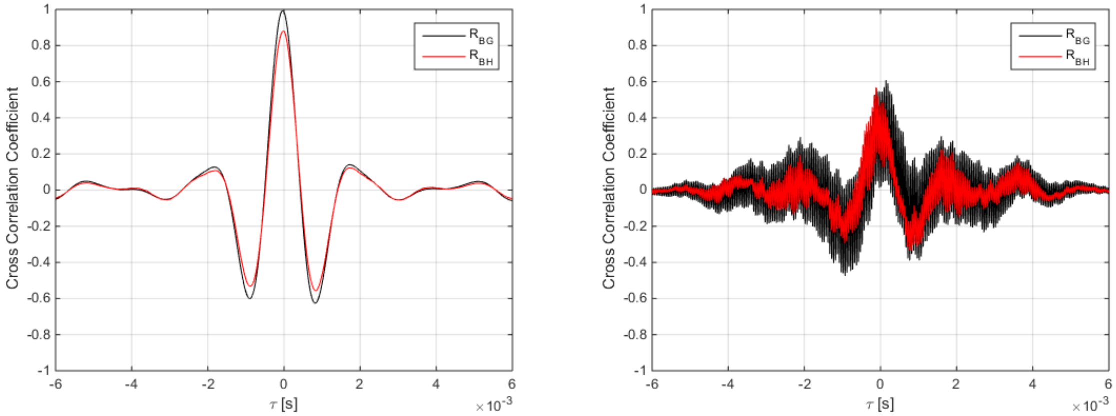

(a) (b)

Figure 3.66 Upstream cross-stream pressure correlations from the NPR = 4.0 data. (a) LESb run 1; (b) LESb run 2.

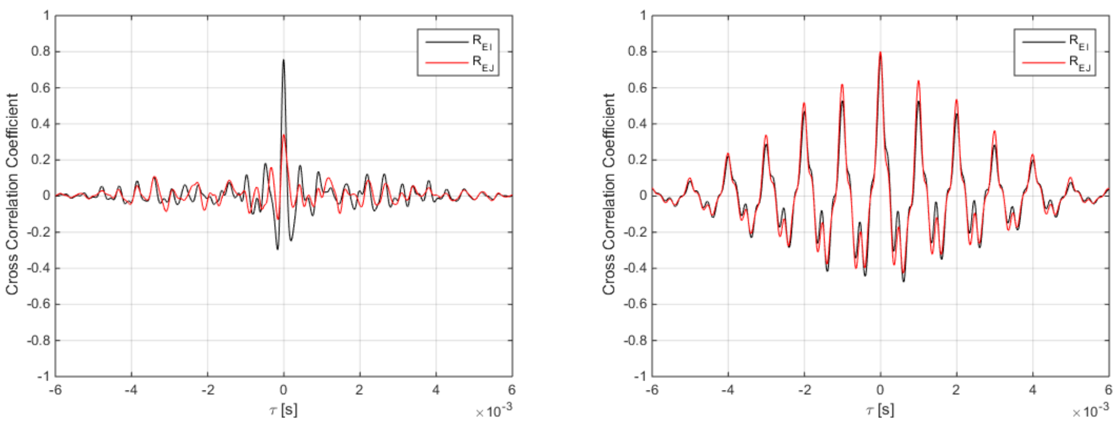

(a) (b)

Figure 3.67 Downstream cross-stream pressure correlations from the NPR = 4.0 data. (a) No upstream forcing; (b) Upstream forcing.

3.8 LES Shield

It has been observed that the time-averaged results obtained from the LESb simulations do not match the RANS results, particularly when $C_b < 1$. This is because the LES model is under-predicting the turbulence viscosity levels in the near-wall regions, resulting in a mean velocity profile similar to that of a laminar boundary layer.

A boundary layer shield formulation has been developed for Wind-US in order to properly resolve the turbulence in the boundary layer and limit the LES model to a region far enough from any viscous boundary, where the grid resolution is sufficient for the LES model to accurately resolve the turbulent quantities. The boundary layer shield (BLS) is based on a modified Menter F_2 function [35]. The new formulation ensures that the shield is active to the boundary layer thickness plus the LES grid length scale (Δ_{LES}). The multiplier C_{bls}, which adjusts the BLS edge offset based on the LES grid length scale, has been set to the default value of 1.0 to ensure that the boundary layer is computed with the RANS model. The LES shield is tested on the baseline LESb case to determine its impact on the mean flow solution.

Table 3.20 Input conditions.

Run	NPR	BLS
25	4.0	No
26	4.0	Yes

The power spectral density estimates show no improvement with respect to the baseline LESb model. These results indicate that the lack of high-frequency unsteadiness in the boundary layer may not be related to the artificial damping introduced by the LES model. Also, it is important to note that the spectra between the two simulations collapse at the sensor locations further downstream. This is the region where the majority of the unsteadiness is dominated by the shear layer which is unaffected by the current shield formulation. A comparison of the RMS wall-pressure fluctuations along the nozzle centerline shows that the shield considerably reduces the unsteady surface pressure generated by the LES model near the laminar SBLI region ($x/h_{nozzle} = 4$). This results in a significant improvement of the predicted aeroacoustic loading near the first shock (Fig. 3.69).

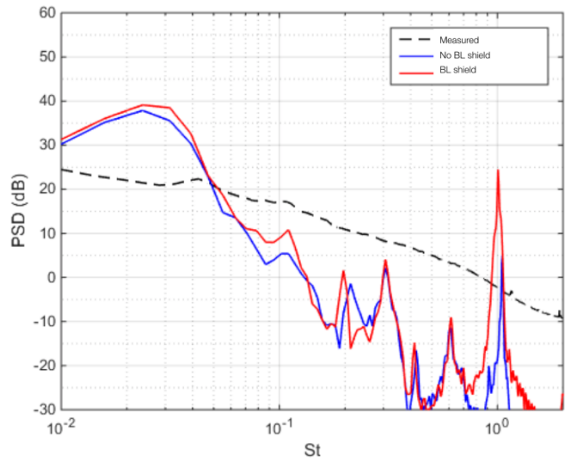

(a)

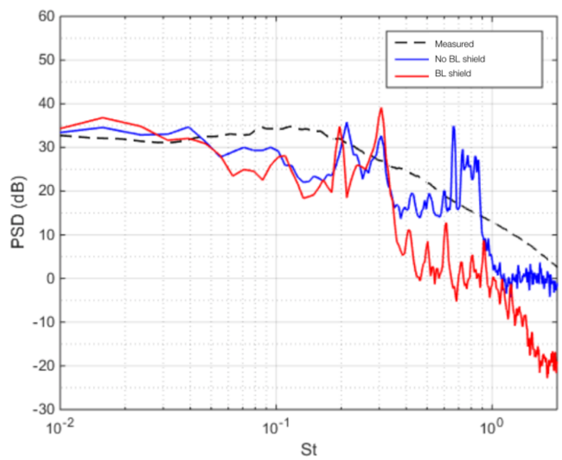

(b)

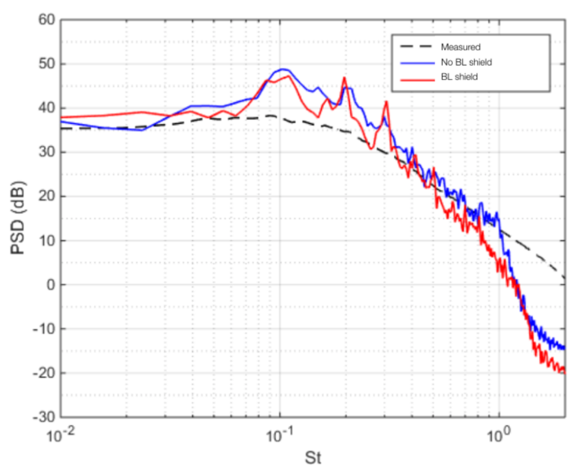

(c)

Figure 3.68 Welch power spectral densities of surface pressure fluctuations along the nozzle ¼-span at (a) x/h_{nozzle} = 2.4; (b) x/h_{nozzle} =7.1; (c) x/h_{nozzle} =11.8.

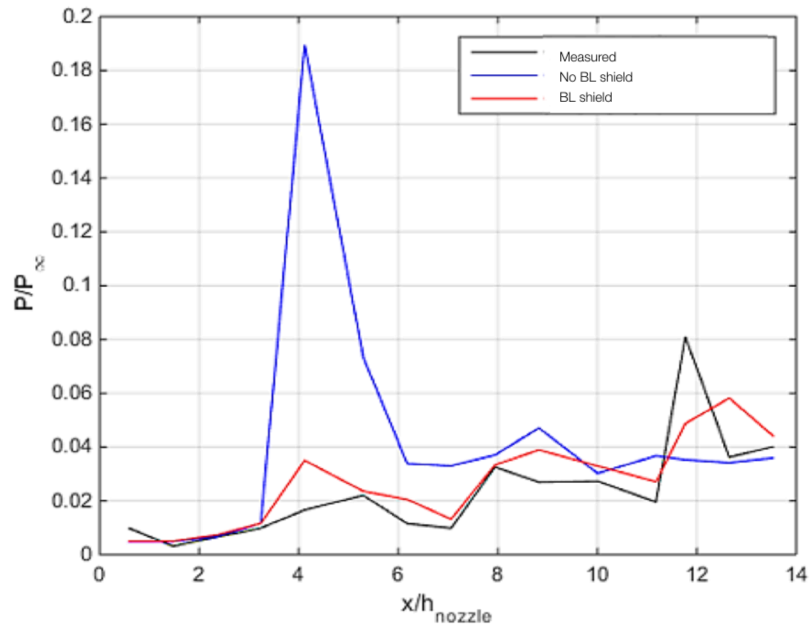

Figure 3.69 RMS of surface pressure fluctuations on the nozzle centerline. Pressure levels are normalized by the freestream pressure.

The production of turbulent fluctuations in the boundary layer occurs at turbulent scales that are under resolved by the LES model. The unresolved turbulent dissipation is related to $\Delta_{LES.}$ Increasing the step size of the grid increases the LES grid length scale and the dissipation of the model. Then turbulence production is not resolved anymore whereas dissipation is largely over predicted, resulting in a quasi-laminar SBLI which damps out the shock train. Figure 3.70 shows excellent matching of the upstream shock strength between the SSRANS and LESb BLS solutions. This is because the boundary layer shield is preventing the unresolved LES from entering the boundary layer. The upstream mean velocity profiles (Fig. 3.71) from the RANS and BLS solutions collapse on top of each other because the solver is reverting from LES to RANS in the near-wall region. Additionally, the accumulated Mach number profiles show that the LESb model with the BLS formulation computes a separation bubble downstream of the first shock that looks very similar to that predicted by the SS-RANS solution. At $x/h_{nozzle} = 20$, the RANS model predicts a jet shear layer 30% thinner than the LESb solutions, resulting in larger mean shock spacing and strength on the rear half of the deck.

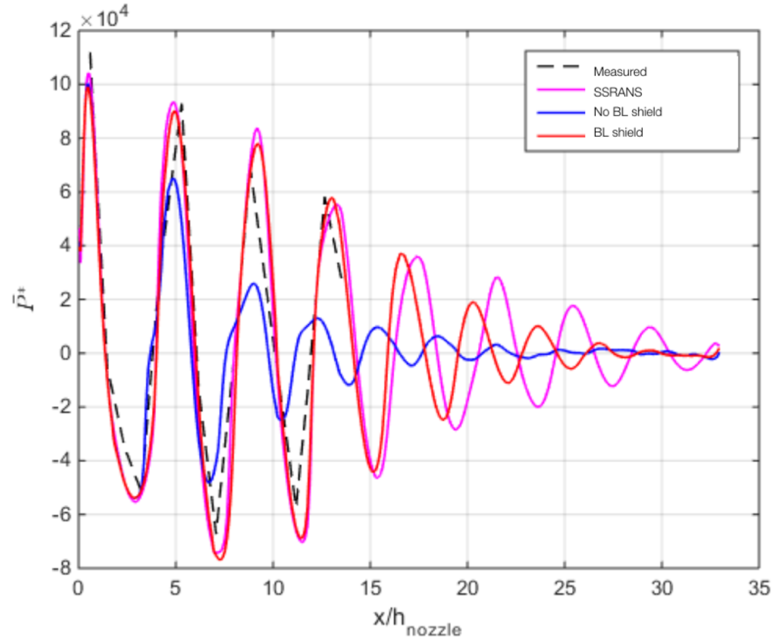

Figure 3.70 Mean surface pressure along nozzle centerline

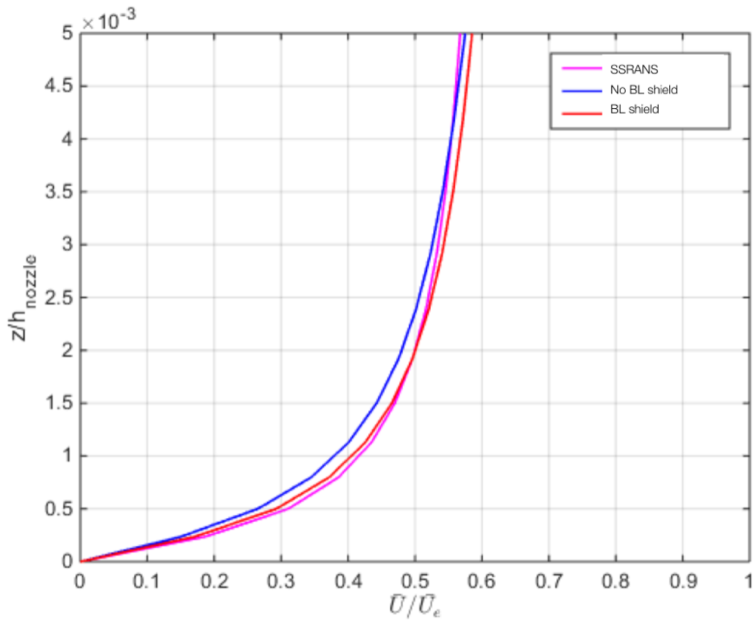

(a)

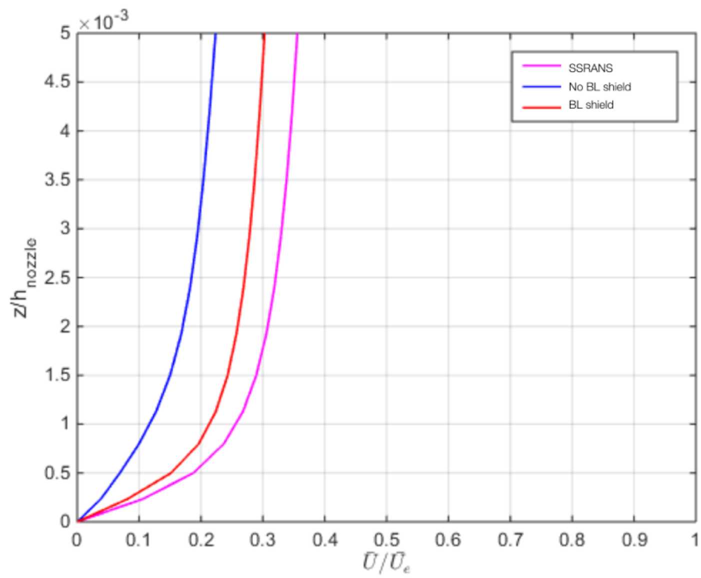

(b)

Figure 3.71 Mean stream-wise velocity along the nozzle centerline at (a) $x/h_{nozzle} = 1$; (b) $x/h_{nozzle} = 5$. Velocity levels are normalized by the mean jet exit velocity

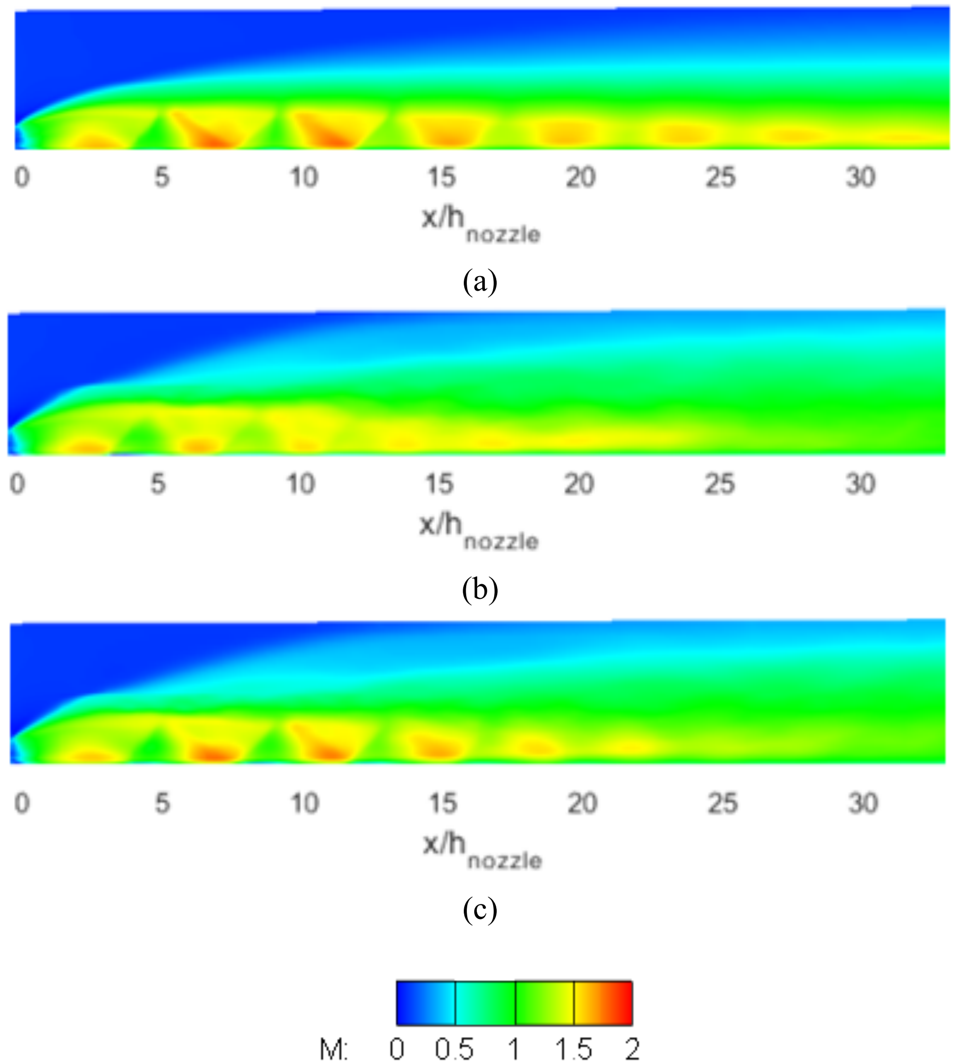

Figure 3.72 Mean Mach number contours along the nozzle centerline for (a) SSRANS; (b) No BL shield; (c) BL shield.

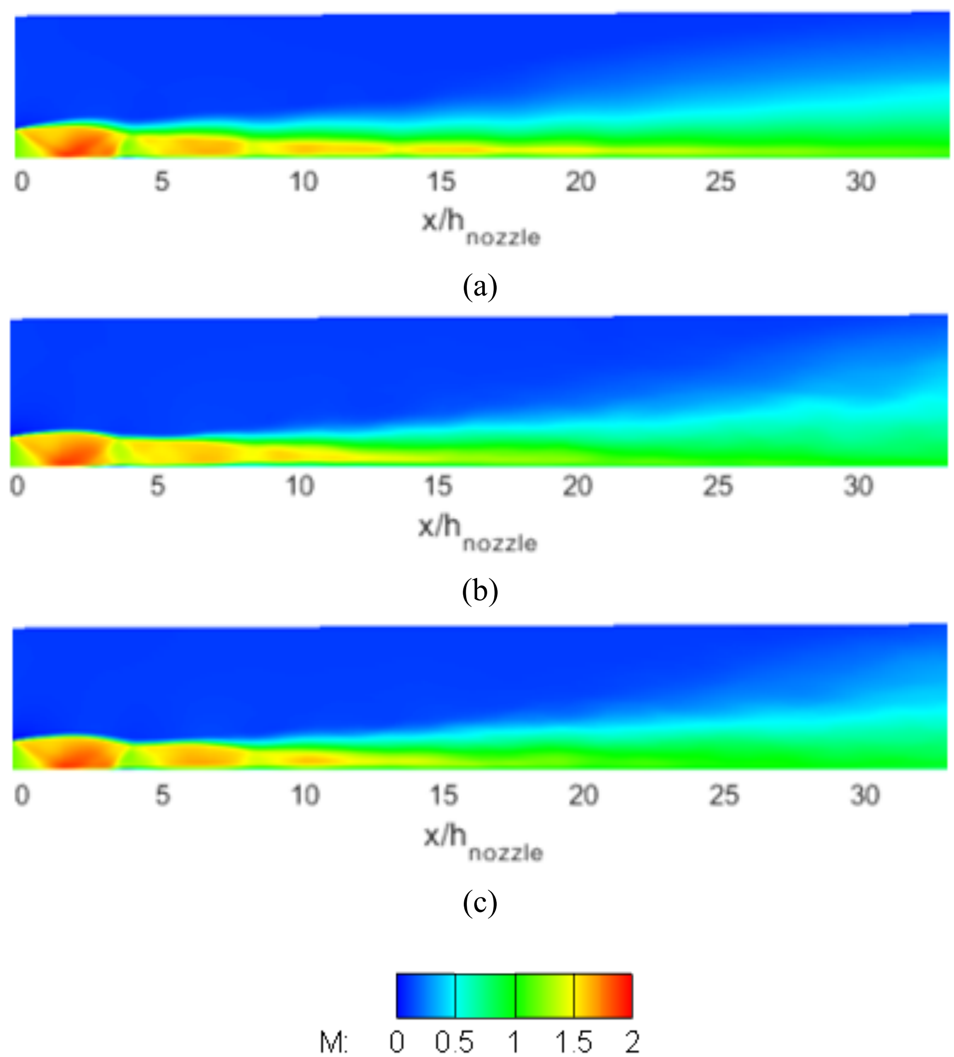

Figure 3.73 Mean Mach number contours along the nozzle ¼-span for (a) SSRANS; (b) No BL shield; (c) BL shield.

Both LESb runs over predict the measured convection velocity by more than 20% (Table 3.20), indicating that the boundary layer shield formulation does not provide a more accurate means of predicting the downstream convection velocity. Visualizations of the cross-correlation coefficients are shown in Figures 3.74 – 3.77. The simulation running with the BLS predicts axial correlation coefficients similar to those predicted by the baseline LESb solution. At a two-point separation distance of x/h_{nozzle} = 2.7, the upstream sensors show a peak correlation coefficient of 0.15 for the baseline run while the simulation with the boundary layer shield predicts nearly perfect correlation. The stronger SBLI predicted by the baseline LESb simulation likely weakens the wall-pressure correlation between the sensors located upstream and downstream of the first shock.

Table 3.21 Axial convection velocities

Run	Δt (s)	BLS	V_{DE} (ft/s)	V_{DF} (ft/s)
25	6	No	1302	947
26	6	Yes	1488	1008

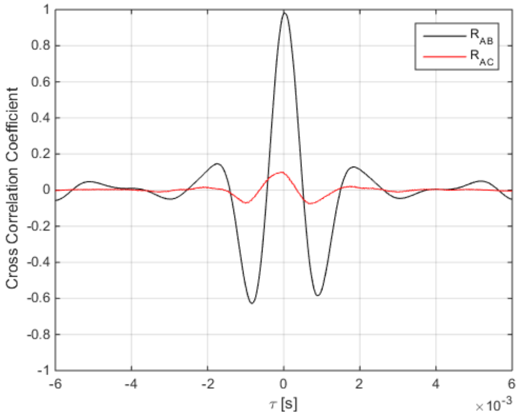

(a)

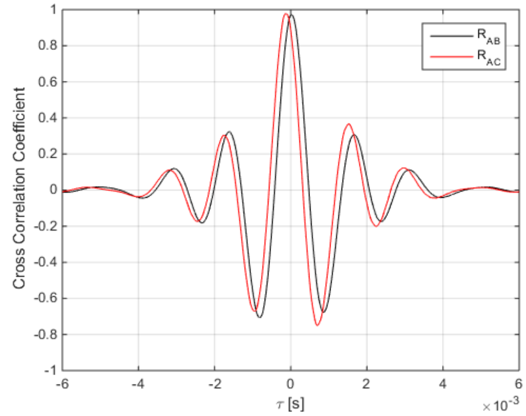

(b)

Figure 3.74 Upstream axial pressure correlations from the NPR = 4.0 data. (a) No BL shield; (b) BL shield.

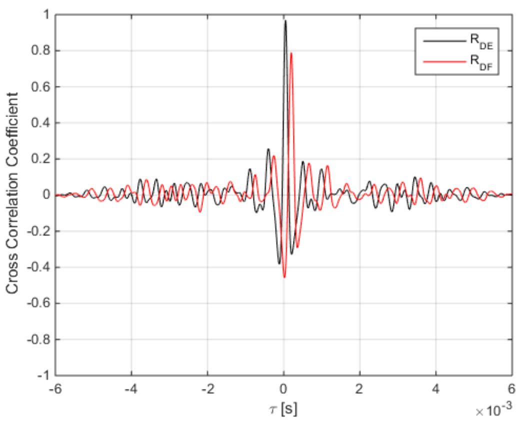

(b)

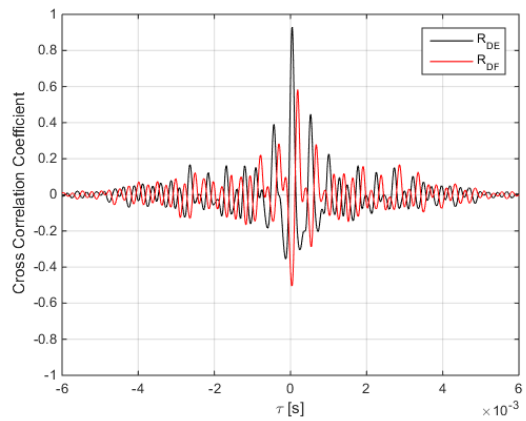

(b

Figure 3.75 Downstream axial pressure correlations from the NPR = 4.0 data. (a) No BL shield; (b) BL shield.

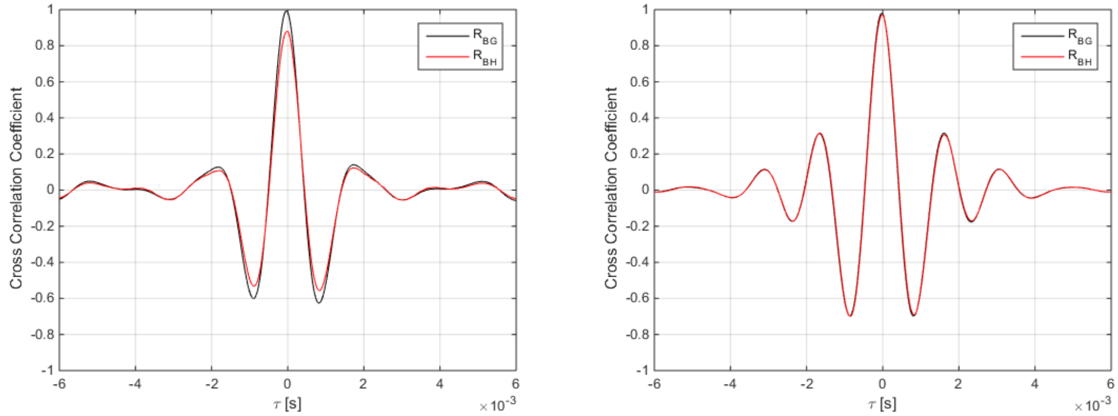

(a) (b)

Figure 3.76 Upstream cross-stream pressure correlations from the NPR = 4.0 data. (a) No BL shield; (b) BL shield.

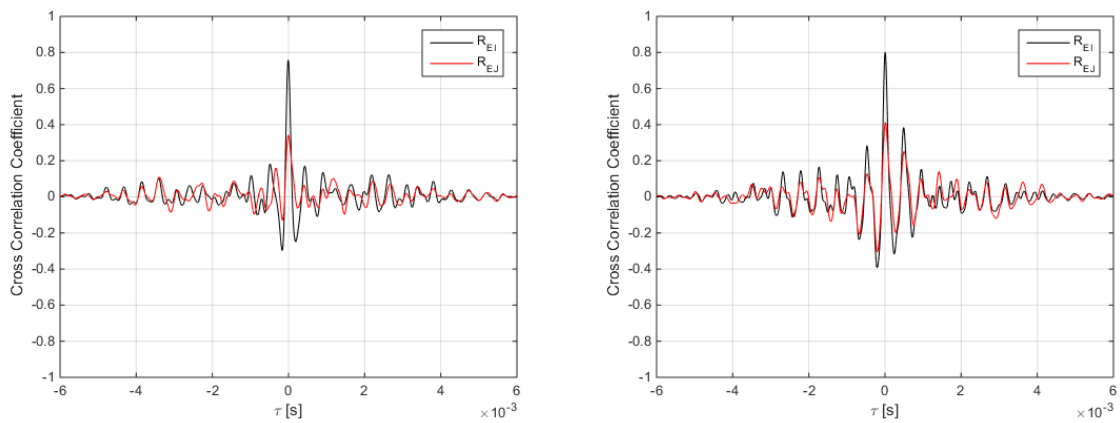

(a) (b)

Figure 3.77 Downstream cross-stream pressure correlations from the NPR = 4.0 data. (a) No BL shield; (b) BL shield.

Unheated Jet Experiments

Sub-scale experiments of wall bounded jets have been designed and run in the Penn State high-speed jet noise facility to further understand the unsteady surface pressures generated by aeroacoustic loading over a flat plate. The experiments are performed on two rectangular nozzles at four different operating conditions. A patch-and-scan near-field acoustic holography technique is proposed to reconstruct the cross-spectra and cross-correlations from the uncorrelated wall pressure measurements.

This chapter will describe the design of the nozzles and flat plate, the pressure transducers used to measure the unsteady pressures, the signal processing procedure used in the data analysis and the results of the sub-scale experiments.

4.1 Experimental Setup

Two different nozzles are tested at five different operating conditions. The two geometries include one with a 4:1 aspect ratio (AR4), and one with an 8:1 aspect ratio (AR8). The nozzles are mounted flush to a flat plate instrumented with Endevco pressure transducers designed to measure the acoustic pressure on the plate surface. The CAD drawings for the two experimental nozzles are shown in Figure 4.1. Both nozzles converge to an exit area of 0.785 in^2. This is equivalent to a 1-inch diameter round nozzle. The exit dimensions for the AR4 nozzle are 0.443 x 1.773 inches, and 0.313 x 2.507 inches for the AR8 nozzle.

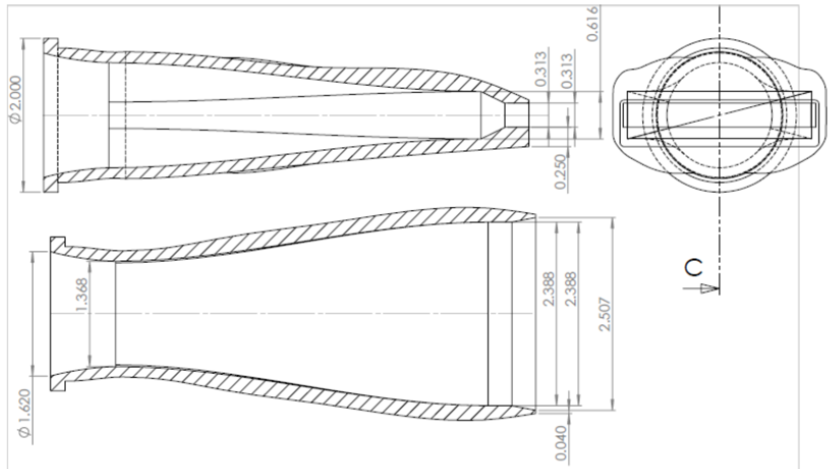

(a)

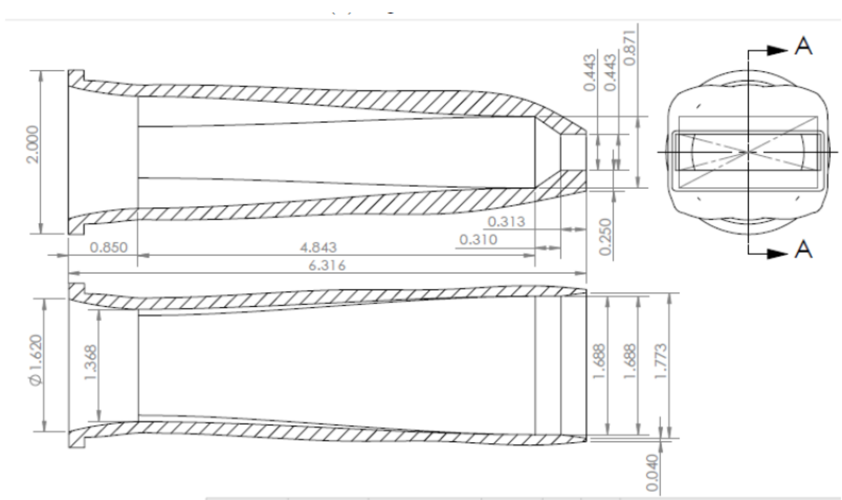

(b)

Figure 3.78 Dimensions in inches of the two experimental nozzle designs [27]. (a) 8:1 aspect ratio; (b) 4:1 aspect ratio.

The data acquisition instrumentation is comprised of fourteen far-field 1/8" GRAS microphones type 40DP, ten near-field 1/8" GRAS microphones type 40DP, three 5-psi Endevco transducers model 8510-B and two 5-psi Endevco transducers model 8507-C. Figure 4.2 shows photographs of the experimental setup. The near-field microphones are suspended 11 inches above the deck with a grazing angle of incidence to the aluminum plates. The microphones are aligned along the diagonal of the deck with a separation distance of 1.5 inches between each microphone while the near-field boom is covered by 1" thick acoustic foam to suppress unwanted reflections. The surface pressure transducers are mounted flush with the deck surface. Note that the Endevco model 8510-B is designed to be flush mounted to the deck by screwing the transducer through the bottom of the plate using a 10-32 mounting thread while the Endevco model 8507-C is installed by inserting the transducer inside a flexible plastic tube which is then secured to the flat plate with a layer of epoxy.

Because of the limited number of surface pressure transducers available for the experiment, the deck is broken up into several sections, including two sections instrumented with the pressure transducers (Fig. 4.3). In order to map out the entire wall pressure field, the sections are shuffled around to different locations. The plates that make up the deck can be rotated by 180 degrees, shifted sideways and moved downstream. Three of the pressure transducers (sensors 1, 2 and 3) are arranged diagonally to achieve better downstream resolution while the other two sensors are stacked in the downstream direction in order to perform the cross-spectral analysis of the unsteady wall-pressure field. One of the 8510-B units (sensor 1) was found defective. Therefore, the data from that sensor has been omitted from this thesis.

(a)

(b)

Figure 3.79 Experimental setup of the aft-deck experiment. (a) Back view; (b) front view.

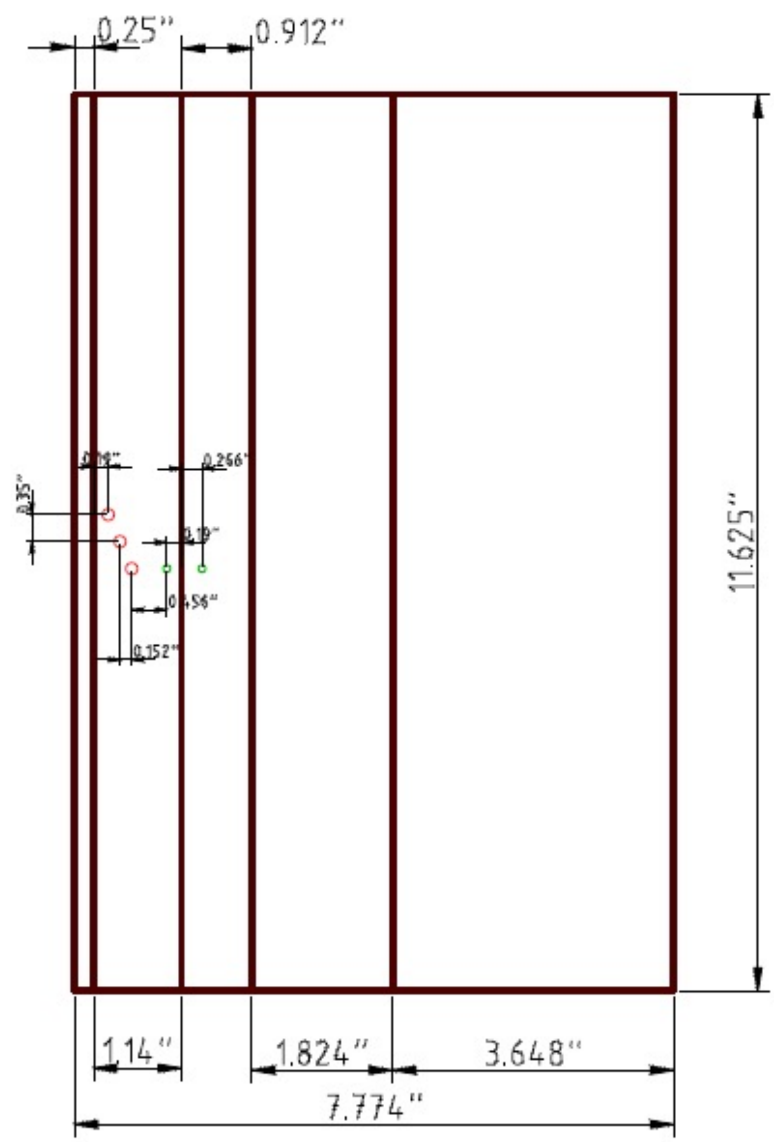

Figure 3.80 CAD drawing of the aft-deck. Endevcos model 8510-B are shown in red while Endevcos model 8507-C are shown in green. The dimensions are in inches.

The far-field boom is designed to hold individual microphones with a grazing angle of incidence to the jet. The microphones are typically distributed between 20˚ and 120˚ from the jet axis with a radial distance to the nozzle exit of 70-80 inches for all microphones. For the current experiments, the far-field measurements are performed at 14 different polar angles. The far-field microphones are distributed between 20.5 ˚ and 110.5 ˚ from the jet axis. Though data was gathered, the data analysis from the far-field microphones has not been included in this thesis.

Figures 4.4 and 4.5 show schematics of the resulting full sensor grids after shifting and rotating all of the plates. For each nozzle geometry, the transverse distance between each row of measurement positions is 0.35 inches. The axial offset between each sensor along the nozzle centerline is 0.152 inches up to a downstream distance of 11 nozzle heights for the AR4 geometry, and 16 nozzle heights for the AR8 geometry. The y-axes are normalized by their respective nozzle widths. Three different sensor locations are used to compare the measured spectral densities with the subscale experiments perfomed by Lurie [27]. Lurie's experiments used the same nozzle geometries, but 50-psi Endevco transducers to study the unsteady pressure fields on the deck.

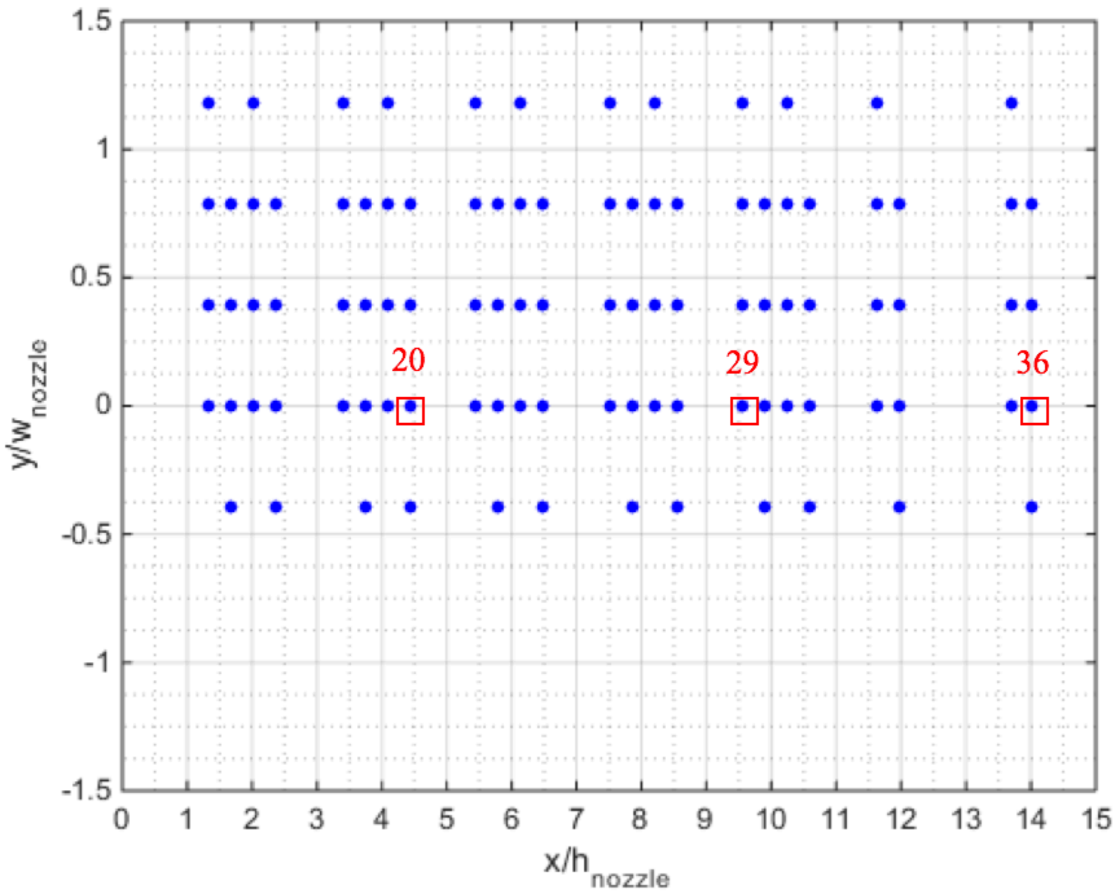

Figure 3.81 Full sensor grid for the AR4 nozzle geometry. The sensors used to compute the power spectral density estimates are highlighted in red.

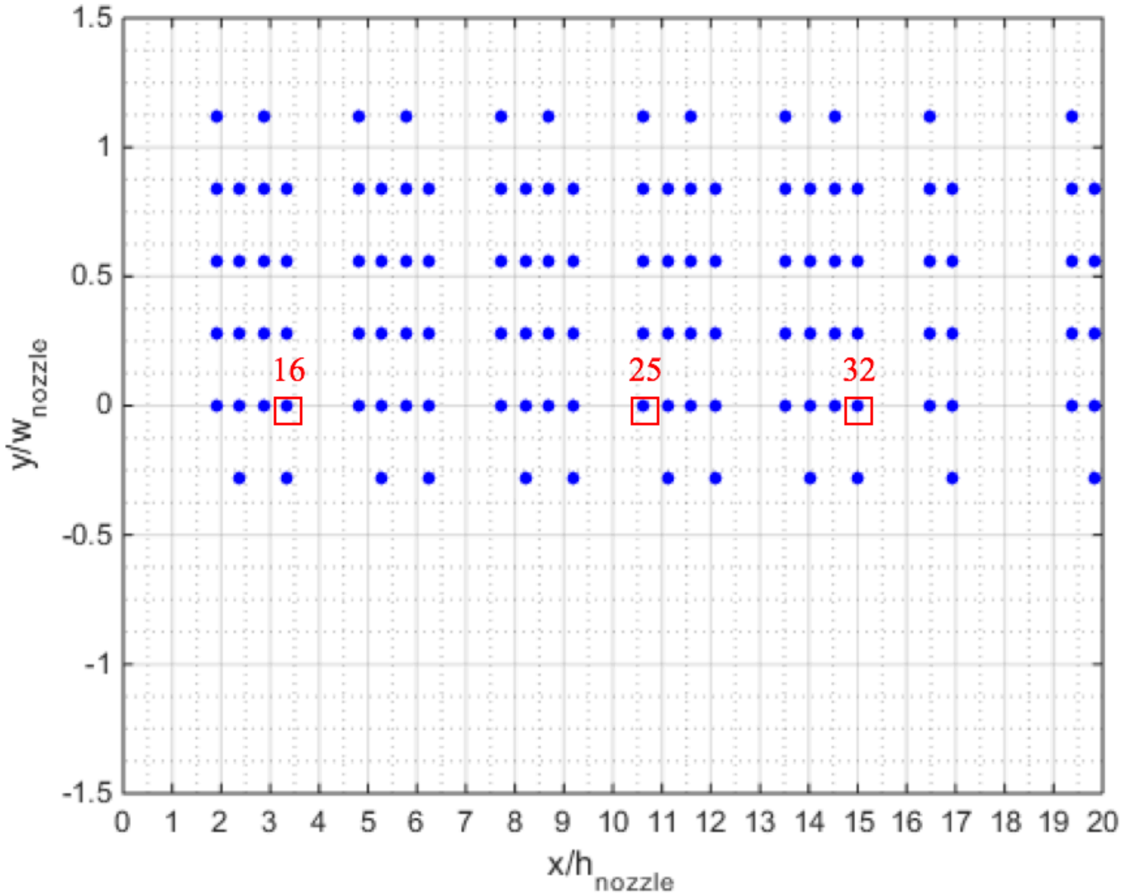

Figure 3.82 Full sensor grid for the AR8 nozzle geometry. The sensors used to compute the power spectral density estimates are highlighted in red.

The unheated jet experiments are performed using a total temperature ratio of 1.0 and four different nozzle pressure ratios: NPR = 1.5 (subsonic), NPR = 2.3 (over-expanded), NPR = 2.62 (on-design) and NPR = 3.5 (under-expanded). Figures 4.6 and 4.7 show shadowgraphs for the two nozzle geometries for each of the unheated conditions. The flow visualizations reveal how the initial shear layer angle is affected by the run condition. In the subsonic and supersonic on-design cases, the initial jet shear layer exhausts almost horizontally out from the nozzle. For the over-expanded case, the shear layer angles down towards the plate while for the under-expanded flow, the shear layer angles up away from the deck. The shadowgraphs also show that the shock spacing and strength increase with higher nozzle pressure ratios. The main shock structure originates from the top of the nozzle exit, impacts the deck, and reflects up towards the shear layer before impacting the plate a second time.

Previous experiments by Lurie et. al [27] had shown the existence of shock structures originating from the bottom of the nozzle exit in each of the supersonic cases. Lurie argued that these structures might have been a result of the flow separation generatced by a small lip between the end of the nozzle and the beginning of the deck. A 0.25” aluminum plate has been placed between the nozzle exit and the deck to ensure a smoother transition between the two surfaces. However, the shadowgraphs shown in figures 4.6 and 4.7 show that the structures are still present during the current experiments. Figure 4.8 shows the shadowgraphs of the nozzle oriented vertically, with no deck. The shock that originates from the bottom lip of the nozzle is still visible during the runs without the deck. It is still unclear if these structures are indeed shocks, or if they are Mach waves caused by an irregularity inside the nozzles. However, the impact they have on the flow variables is likely to be small.

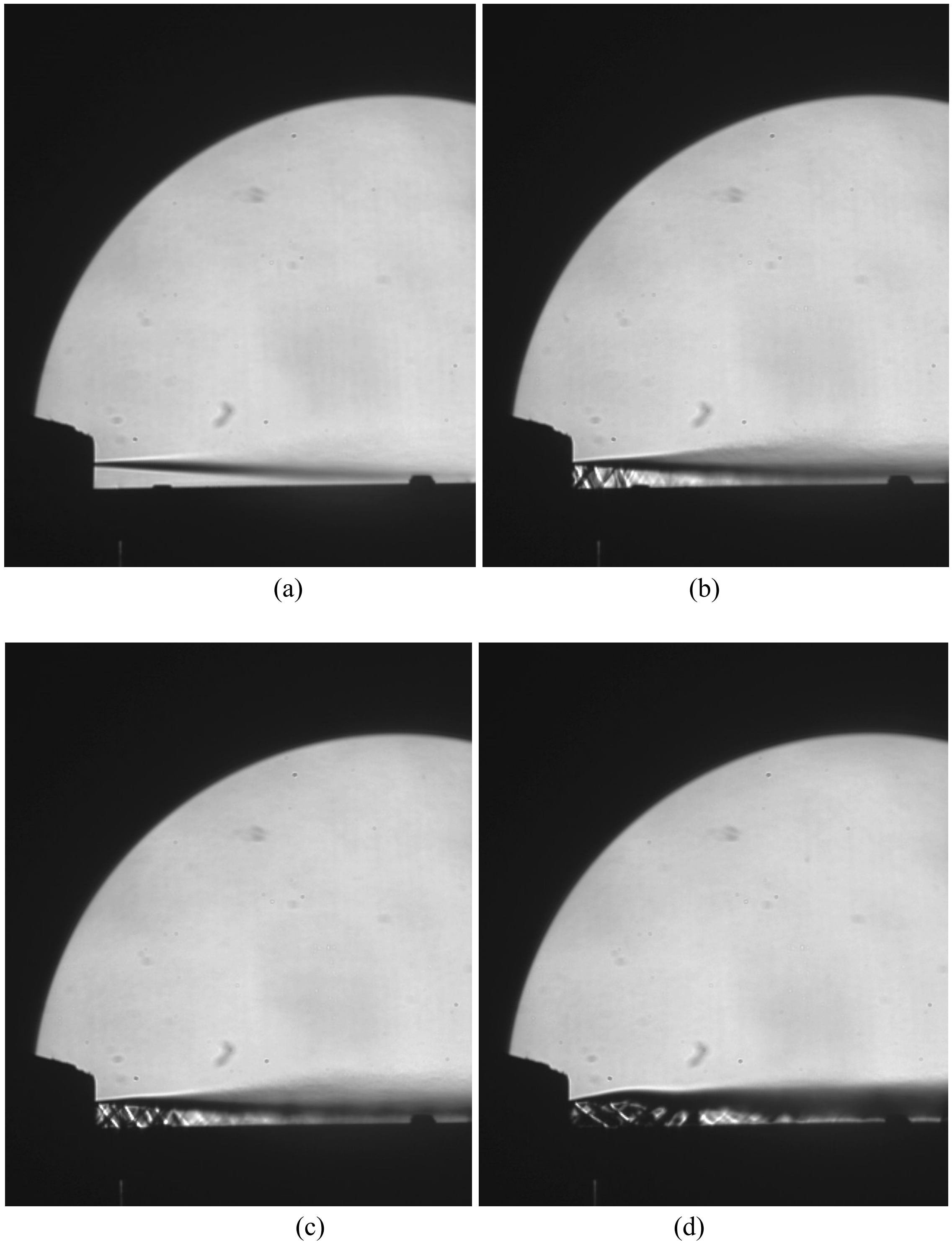

Figure 3.83 Shadowgraphs of the aft-deck experiments using the AR8 nozzle. (a) NPR = 1.5; (b) NPR = 2.3; (c) NPR = 2.62; (d) NPR = 3.5.

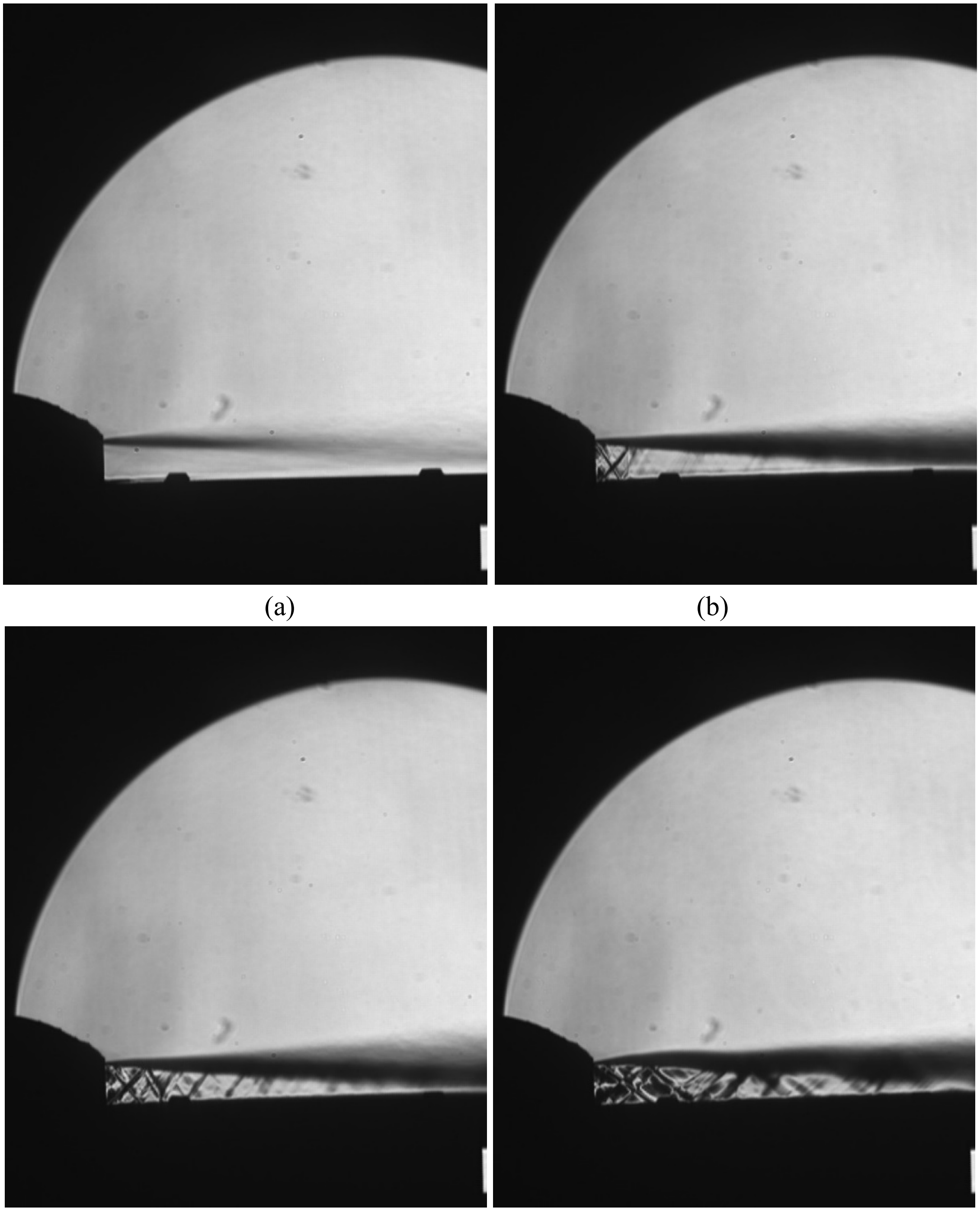

(a) (b)

(c) (d)

Figure 3.84 Shadowgraphs of the aft-deck experiments using the AR4 nozzle. (a) NPR = 1.5; (b) NPR = 2.3; (c) NPR = 2.62; (d) NPR = 3.5.

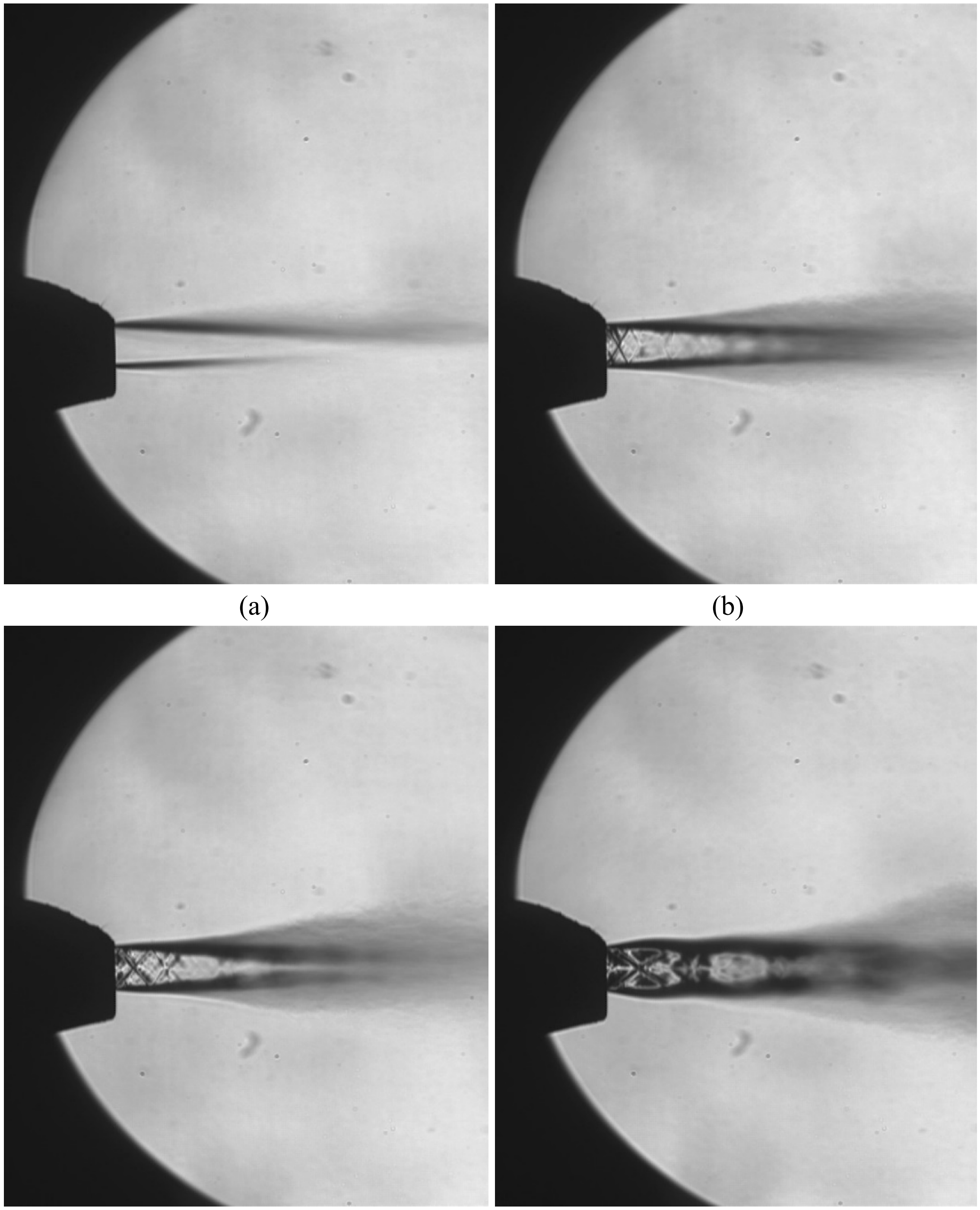

(a) (b) (c) (d)

Figure 3.85 Shadowgraphs of the AR4 nozzle with no deck. (a) NPR = 1.5; (b) NPR = 2.3; (c) NPR = 2.62; (d) NPR = 3.5.

4.2 Experimental Results

Figures 4.9 and 4.10 show the Welch power spectral density estimates of the background noise for the AR4 and AR8 experiments. Note that the average noise floor of the near-field microphones and the pressure transducers is approximately 70 dB/Hz below the measured signals. For all subsequent analysis, a low-pass filter with a cut-off frequency of 30 kHz is applied to the surface presssure data to remove the 35 kHz resonance peak of the Endevco transducers from the data post-processing.

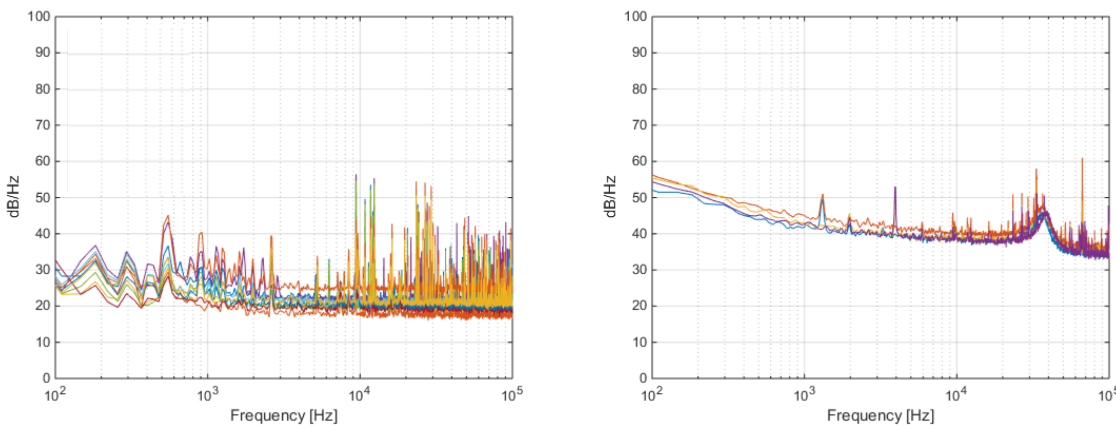

(a) (b)

Figure 3.86 PSD estimate of the background noise for the AR4 experiment. (a) Near-field microphones; (b) Endevco pressure transducers.

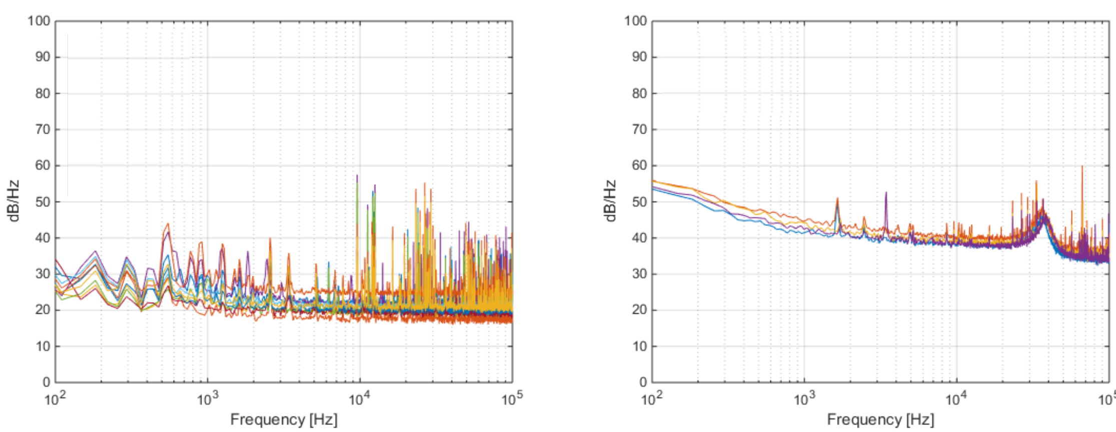

(a) (b)

Figure 3.87 PSD estimate of the background noise for the AR8 experiment. (a) Near-field microphones; (b) Endevco pressure transducers.

Figure 4.11 and 4.12 show comparisons of the RMS and mean pressures along the nozzle centerline between the two experiments. The RMS pressure is converted from pascals to dB using Eq. 4.1, where the reference pressure is taken to be 20 μPa.

$$dB = 20\log_{10}\left(\frac{P_{rms}}{P_{ref}}\right) \tag{4.1}$$

The shock spacing and amplitude in the mean pressure plots are in good agreement with the measurements perfomed by Lurie. Note that the subsonic cases do not show any shocks or expansion waves, as expected. The spacing and strength of the shocks increases with the higher exit Mach numbers. Furthermore, the peak shock strength weakens with increasing downstream distance.

The RMS pressure plots show that the RMS pressure increases with downstream distance and nozzle pressure ratio. The difference in RMS pressure observed at $x/h_{nozzle} = 3$ is due to the presence of screech noise in Lurie's measurements, particularly in the NPR = 2.3 and NPR = 2.62 runs.

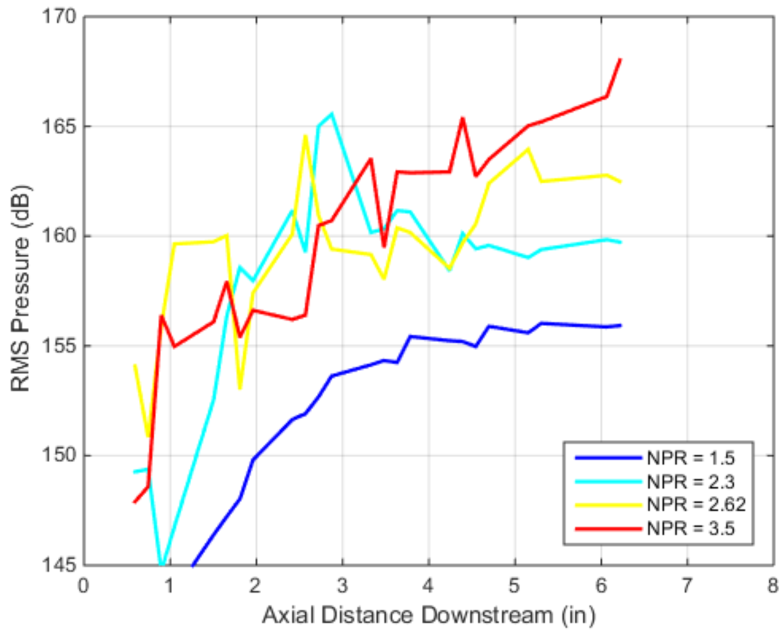

(a)

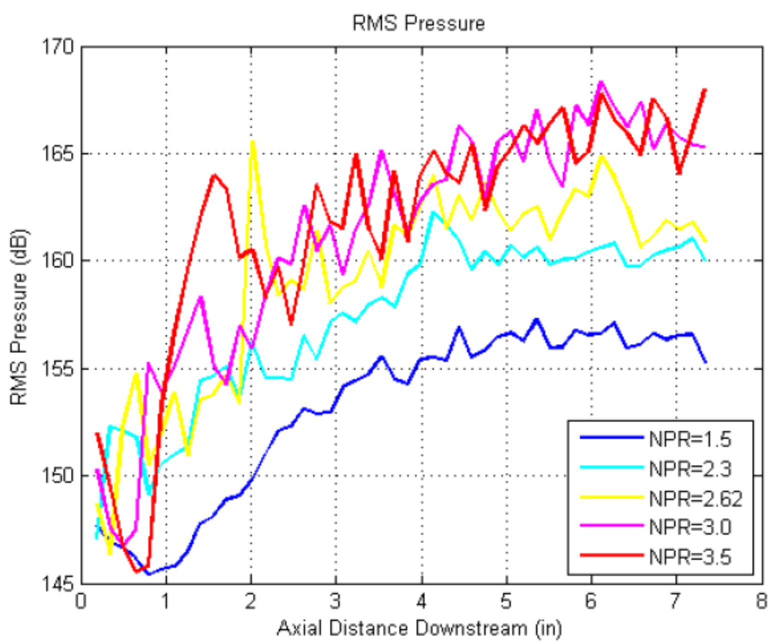

(b)

Figure 3.88 RMS pressure on the centerline of the AR4 nozzle. (a) Measured data; (b) Lurie's experiments [27].

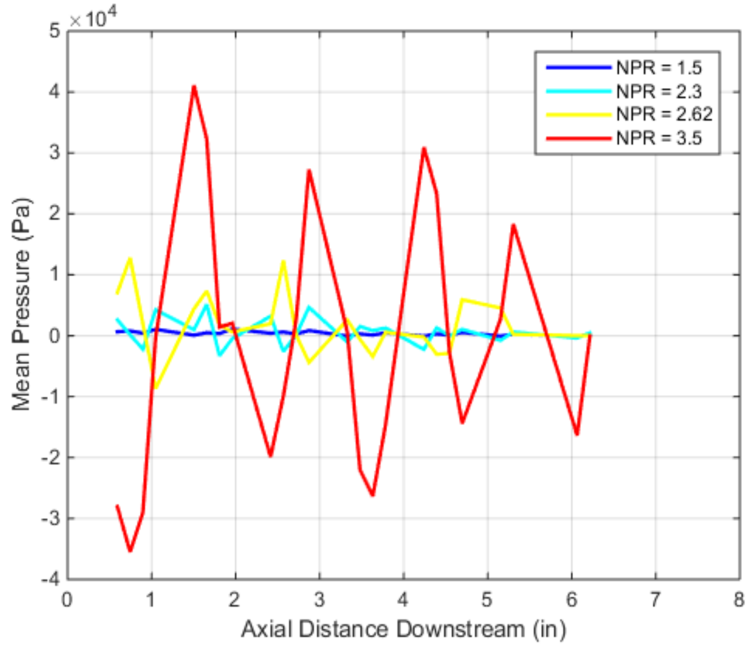

(a)

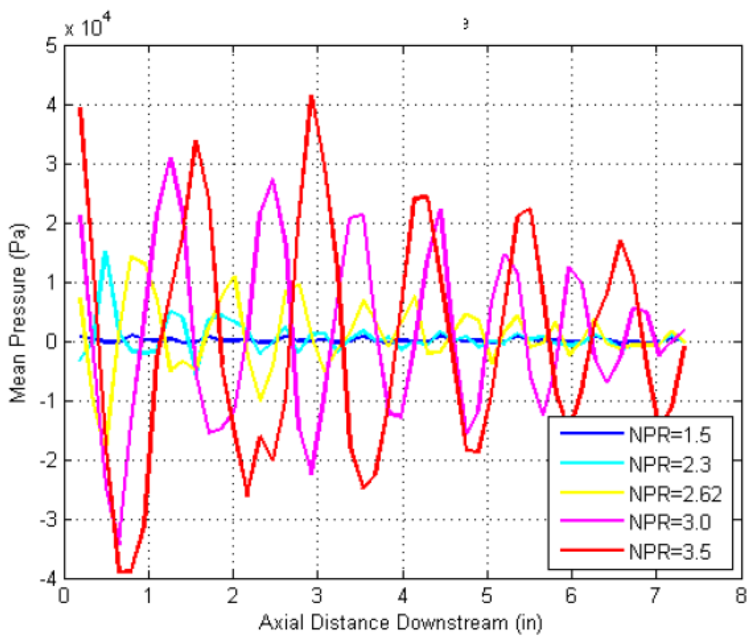

(b)

Figure 3.89 Mean pressure on the centerline of the AR4 nozzle. (a) Measured data; (b) Lurie's experiments [27].

Welch power spectral densities for the AR4 nozzle geometries are shown in Figures 4.13 – 4.16. The sensor locations used to calculate the power spectral densities are shown in Figure 4.4. The computed PSDs correlate well with Lurie's findings, indicating that the 50-psi sensors have enough sensitivty to capture most of the unsteadiness in t he flow. In figure 4.13, sensor 20 shows that the NPR = 1.5 case has an amplitude of 100 dB/Hz at the lower frequencies while the three other run conditions have an amplitude of near 120 dB/Hz. This difference is caused by the shock-boundary layer interactions that occur in the supersonic cases that generate more low-frequency unsteadiness.

Figure 4.15 shows that the NPR = 1.5, NPR = 2.3 and NPR = 2.62 cases have similar low-frequency contents at approximately x/h_{nozzle} = 14 because the downstream wall pressure field is largely dominated by the interactions between the shear layer and the plates. The NPR = 3.5 case instead shows higher energy content at frequencies below 3 kHz as a result of strong shock structures that are still present in the jet core.

For practically all sensor locations, the high-frequency content is primarely dominated by the unsteadiness of the shear layer. The NPR = 1.5 run stands out from the other three conditions as containing much lower activity at the high frequencies due to a less active shear layer. At the upstream location, the growth rate of the shear layer is highly dependent on the nozzle pressure ratio. The differences in the shock strength, shock spacing and shear layer thickness all lead to different spectral shape. This is particularly observable in Figure 4.13, where the comparison between the NPR = 1.5 and the other runs shows a difference of at least 10 dB/Hz at the frequencies below 1000 Hz and above 10 kHz. At the downstream locations, the high frequency contents for all supersonic cases collapse as a result of the expanded shear layer being the primary source of unsteadiness. The underexpanded cases in Figure 4.13a show the presence of severe pressure flucuations, or screech tones, for the NPR = 2.3 and NPR = 2.62 cases with peak frequencies of 8.5 kHz and 10 kHz, respectively.

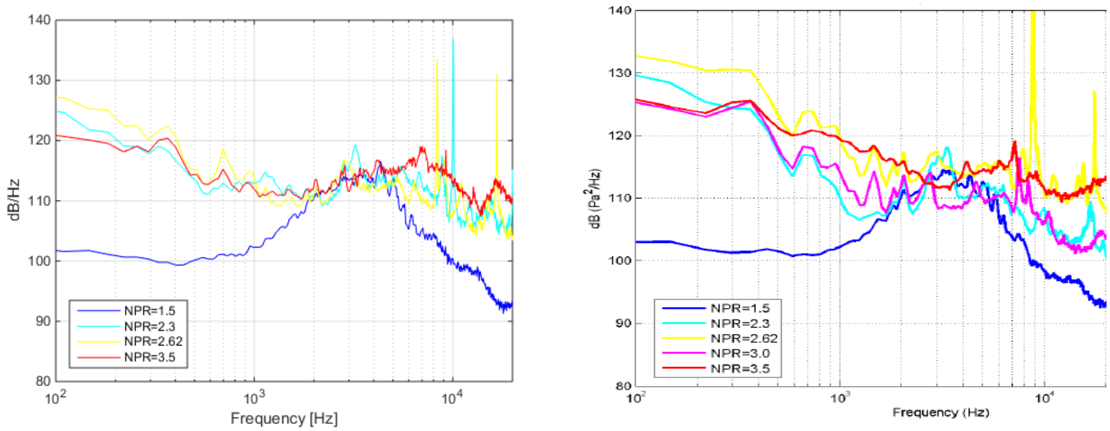

(a) (b)

Figure 3.90 Welch PSD estimate for sensor 20 of the AR4 nozzle. (a) Measured data; (b) Lurie's experiments [27].

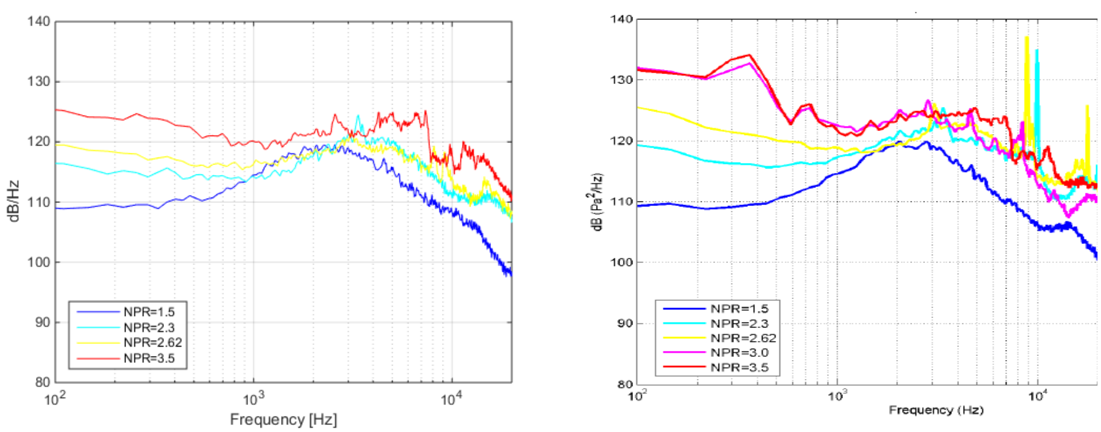

(a) (b)

Figure 3.91 Welch PSD estimate for sensor 29 of the AR4 nozzle. (a) Measured data; (b) Lurie's experiments [27].

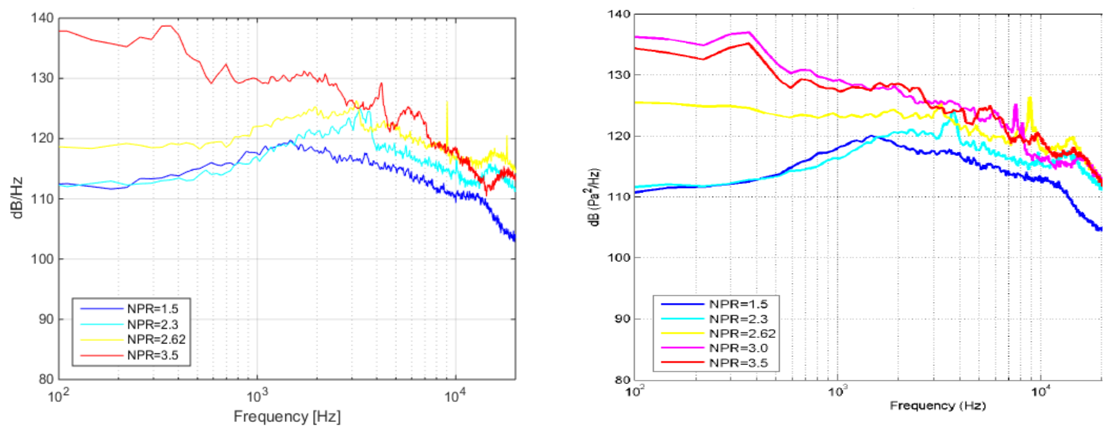

(a) (b)

Figure 3.92 Welch PSD estimate for sensor 36 of the AR4 nozzle. (a) Measured data; (b) Lurie's experiments [27].

Figures 4.16 and 4.17 show comparisons of the mean and RMS pressures along the nozzle centerline for the AR8 nozzle experiments. The RMS data at 1.5 and 2.5 inches downstream of the nozzle exit shows high pressure peaks that are not seen in Lurie's experiments (Fig. 4.16). The higher RMS levels could be a result of result of the flow separation occurring between the plates which can significantly increase the unsteadiness near the wall. The measurements show trends similar to those observed in the AR4 nozzle. Comparisons of the shock spacings and amplitudes with the experiments performed by Lurie [27] show good correlation with the exception of the first shock which shows a lower pressure peak. This discrepancy is pheraphs caused by the spatial undersampling of the pressure field in the downstream direction. The subsonic case does not show any shocks or expansion waves, as expected. Furthermore, the spacing and strength of the shocks increases with higher exit Mach numbers.

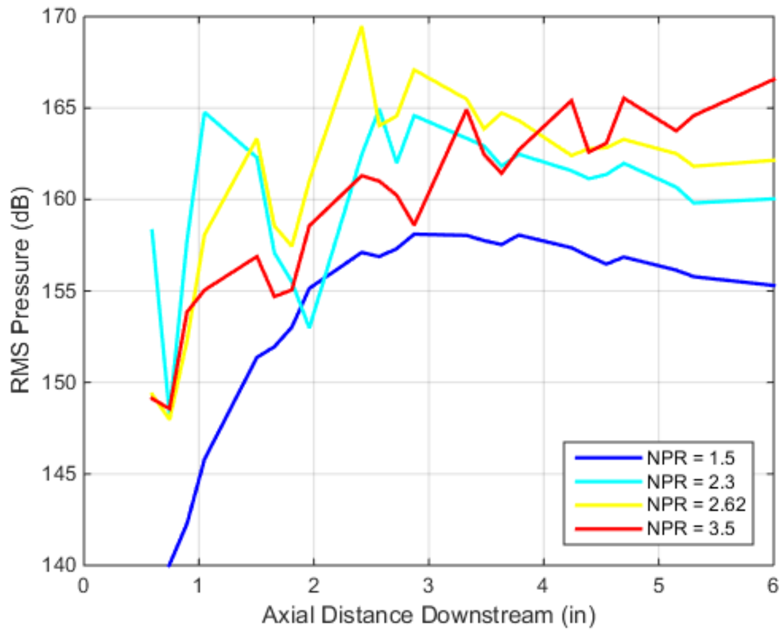

(a)

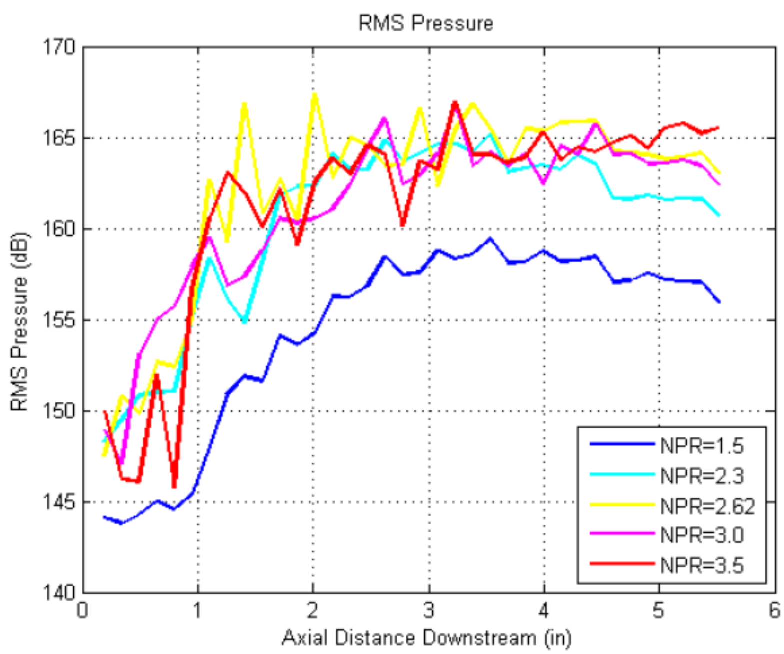

(b)

Figure 3.93 RMS pressure on the centerline of the AR8 nozzle. (a) Measured data; (b) Lurie's experiments [27].

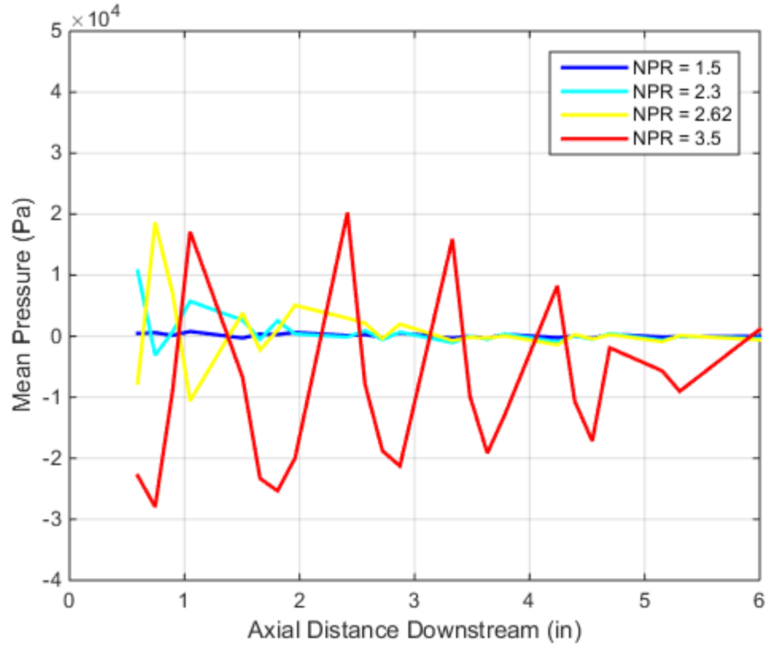

(a)

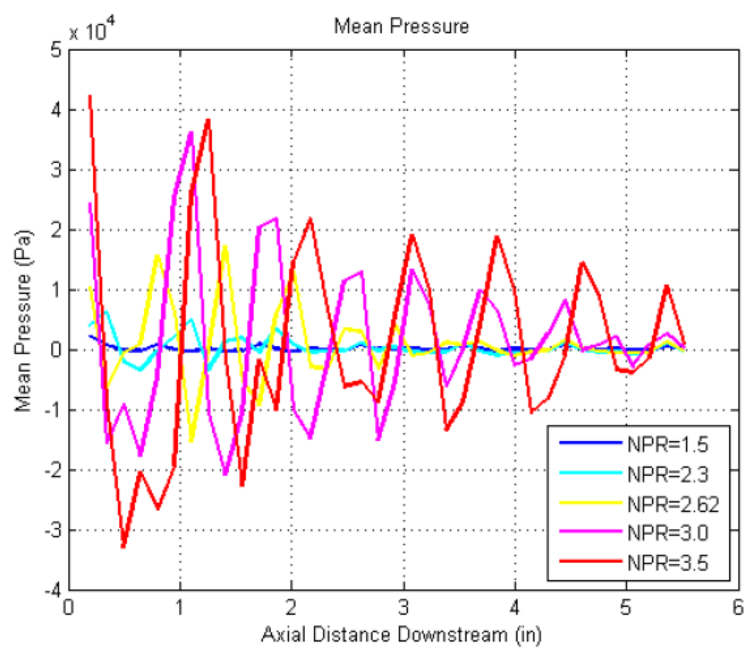

(b)

Figure 3.94 Mean pressure on the centerline of the AR8 nozzle. (a) Measured data; (b) Lurie's experiments [27].

Welch power spectral densities for all run conditions are shown in Figures 4.18 – 4.20. The sensors' locations used to extract the PSD data are shown in Figure 4.5. The general trends are very similar to those observed in the AR4 experiments. The supersonic runs show a distinct difference in acoustic energy below 1 kHz compared to the subsonic run as a result of the unsteady pressure fluctuations generated by the shock-boundary layer interactions (SBLI), as described by Dupont [6]. Figure 4.20 indicates that the contributions from the shocks are still present in the unsteady wall pressure field at x/h_{nozzle} = 14. The same phenomenon can be observed in the AR4 nozzle experiments (Fig. 4.15). From observations of the Welch PSD estimates in Figures 3.15, the over-expanded case (NPR = 2.3) nearly collapses with the subsonic case, indicating that most of the energy in the shock train has been dissipated by x/h_{nozzle} = 14. This trend differs in the AR8 experiments, where the over-expanded run shows a difference of 6 dB/Hz at 100 Hz compared to the NPR = 1.5 case, thus indicating some contributions from the shocks even at the furthest downstream location.

Another important oservation is that the AR8 nozzle geometry generates more screech tones than the AR4 nozzle, as a result of the thicker nozzle lip. These tones are observable in the NPR = 2.3 and NPR = 2.62 runs. Overall, the results from the AR4 and AR 8 experiments show a very good match with the trends captured by Lurie [27].

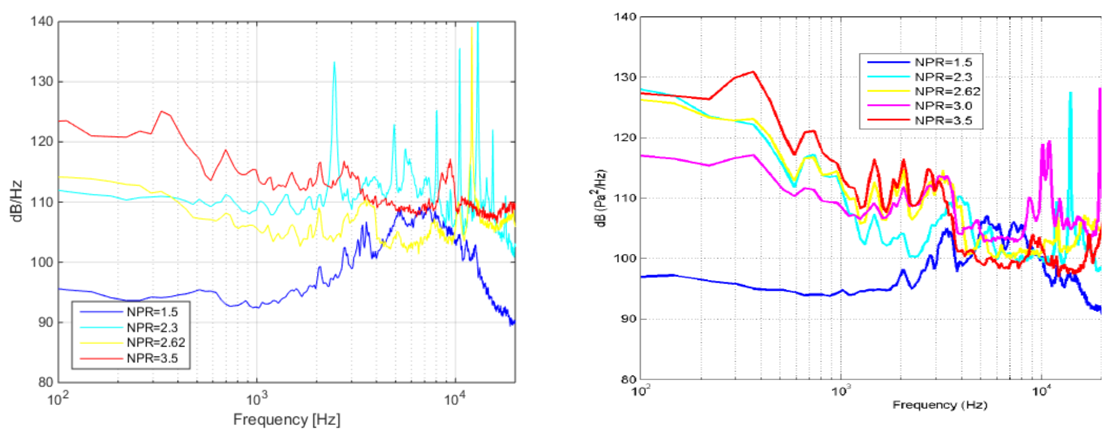

(a) (b)

Figure 3.95 Welch PSD estimate for sensor 16 of the AR8 nozzle. (a) Measured data; (b) Lurie's experiments [27].

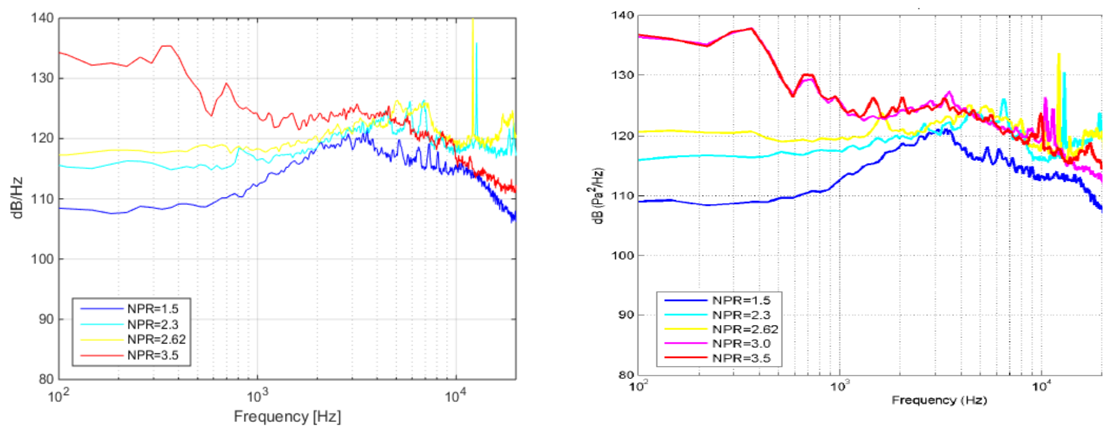

(a) (b)

Figure 3.96 Welch PSD estimate for sensor 25 of the AR8 nozzle. (a) Measured data; (b) Lurie's experiments [27].

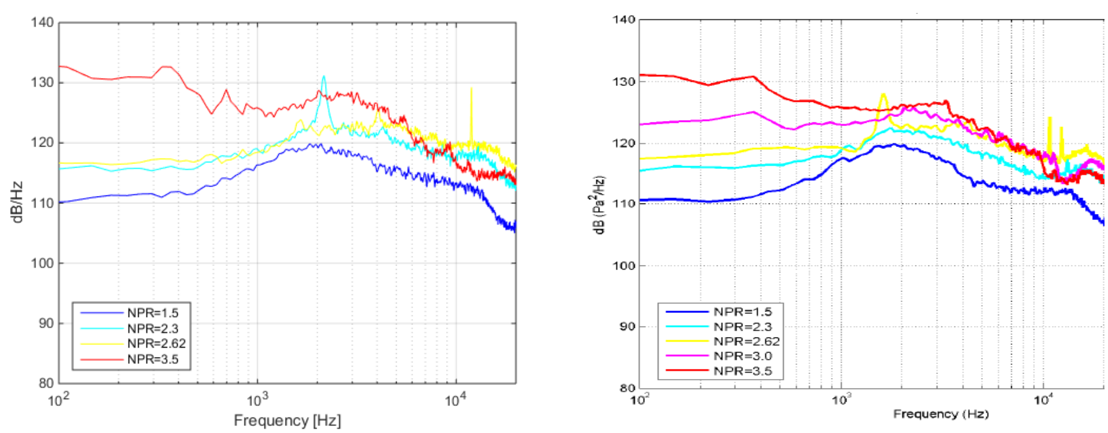

(a) (b)

Figure 3.97 Welch PSD estimate for sensor 32 of the AR8 nozzle. (a) Measured data; (b) Lurie's experiments [27].

4.3 Cross-spectral Matrix Reconstruction using NAH

A patch-and-scan based near-field acoustic holography (NAH) technique has been used to recover the full hologram cross-spectral matrix of the surface pressures using the cross-spectrum between a limited number of surface pressure transducers and an array of near-field reference microphones. The derivation of the cross-spectral matrix reconstruction was worked out by Morris [36]. The experimental setup is shown in Figure 4.2.

Acoustic holography is a method that is often used to estimate the sound field near a source by measuring the acoustic pressure at points located on a surface, called a hologram. The equation used to extract the cross-spectral matrix of the pressure field on the deck surface (G_{YZ}) is shown by Eq. 4.2. The hologram G_{YZ} can be reconstructed from the cross-spectra of the near-field microphones (G_{XX}) and the cross-spectra between the pressure transducers and the near-field references (C_Δ). S_1 and D_1 represent the orthonormal matrix of right eigenvectors and the diagonal matrix of real non-negative eigenvalues. Both matrices can then be obtained from the singular value decomposition of G_{XX}.

$$[G_{YZ}] = \left\{[C_\Delta^*]^T S_1^* [D_1^*]^{-\frac{1}{2}}\right\}\left\{[C_\Delta]^T S_1^T \left[D_1^{-\frac{1}{2}}\right]^T\right\} \tag{4.2}$$

The cross-spectral reconstruction is performed using the wall pressure data along the nozzle centerline at different downstream locations. The positions of the upstream and downstream sensors used to reconstruct the two-point cross-spectra for both nozzle geometries are shown below in Figures 4.21 and 4.22.

Note that some of the wall-pressure signals used in the cross-spectral reconstruction are not recorded simultaneously, thus the phase information between the wall-pressure measurements is lost. This problem can be overcome with the addition of a set of reference microphones, assuming that the surface mounted transducers and the reference microphones are sensing fluctuations from the same noise source and that the cross-spectral field can be split into a limited number of coherent and uncorrelated partial fields. The cross-spectral matrix G_{xx} is obtained by averaging the cross-spectra of the near-field reference microphones. The two-point separation distance used to compute the cross-spectral field of the surface pressures is 1.3 nozzle heights for the AR4 experiment and 2.9 nozzle heights for the AR8 experiment. The reconstructed cross-spectra holograms are compared to the true cross-spectra obtained from the simultaneous measurements of the wall-pressures using sensors 3 and 5. A 20 kHz low-pass filter is applied to the measured data to remove the resonance peaks of the Endevco transducers.

A copy of the MATLAB program used to reconstruct the cross-spectra hologram is included in Appendix D.

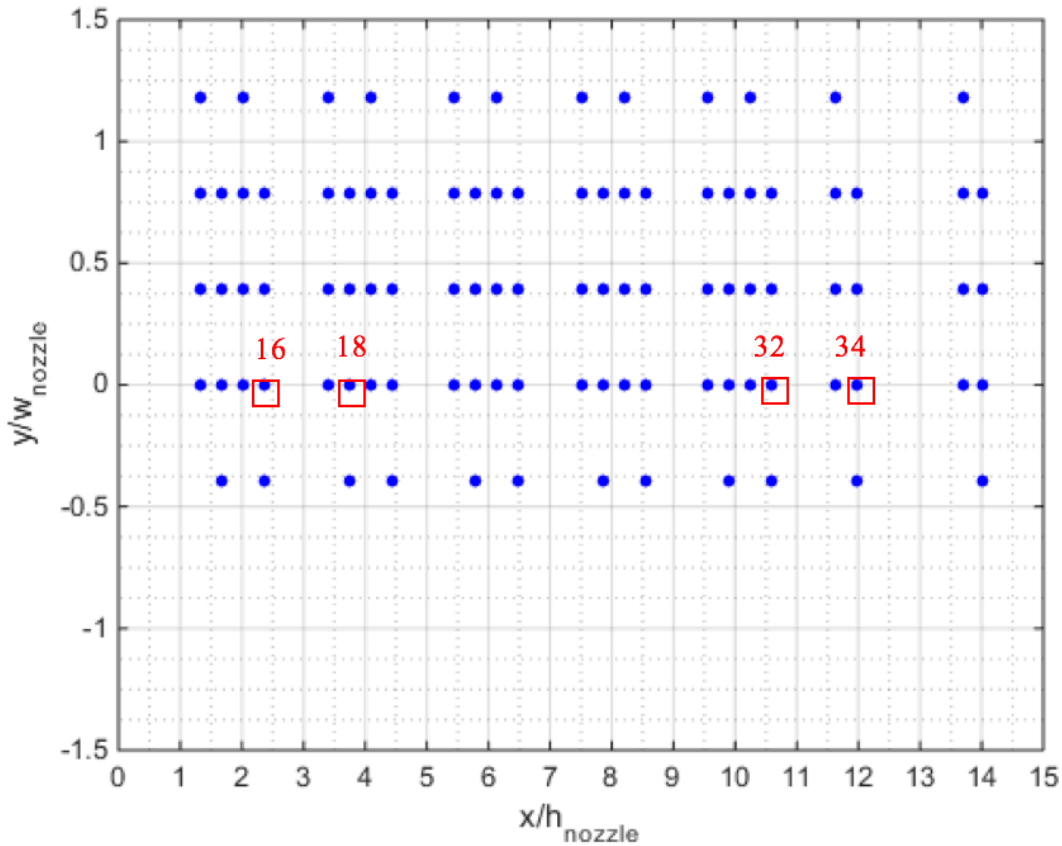

Figure 3.98 Full sensor grid for the AR4 nozzle geometry. The sensors used to compute the cross-spectral density estimates are highlighted in red.

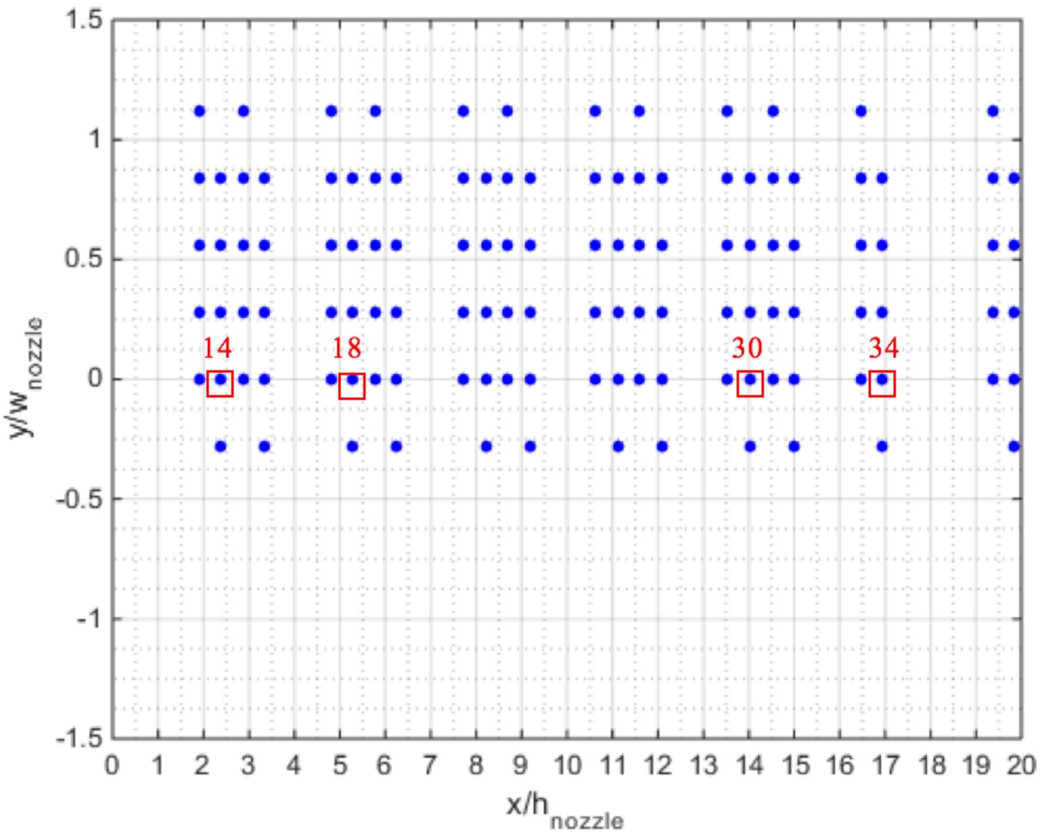

Figure 3.99 Full sensor grid for the AR8 nozzle geometry. The sensors used to compute the cross-spectral density estimates are highlighted in red.

Figures 4.23 – 4.26 show the phase and magnitude of the true and the reconstructed surface pressure cross-spectra for the AR4 nozzle geometry. Figures 4.27 – 4.30 show the phase and magnitude of the reconstructed pressure cross-spectra for the AR8 experiments. For the analysis presented in this section, the acoustic data from the NPR = 1.5 and NPR = 3.5 runs are used to reconstruct the acoustic pressure field on the deck surface.

The cross-spectra visualizations show that the proposed NAH technique can succesfully reconstruct the cross-spectra magnitude for frequencies above 1 kHz. Note that the NAH method does a better job at reconstructing the cross-spectral density between points located near the jet exit, where the average difference between the reconstructed and exact magnitudes is less than 1 dB/Hz. Unfortunately, the algorithm is not able to fully reproduce the phase information, limiting its ability to predict the coherence between any two pressure points on the deck surface. It is suggested that a shorter separation distance between the reference microphones would be more appropriate to better retrieve the phase correlation.

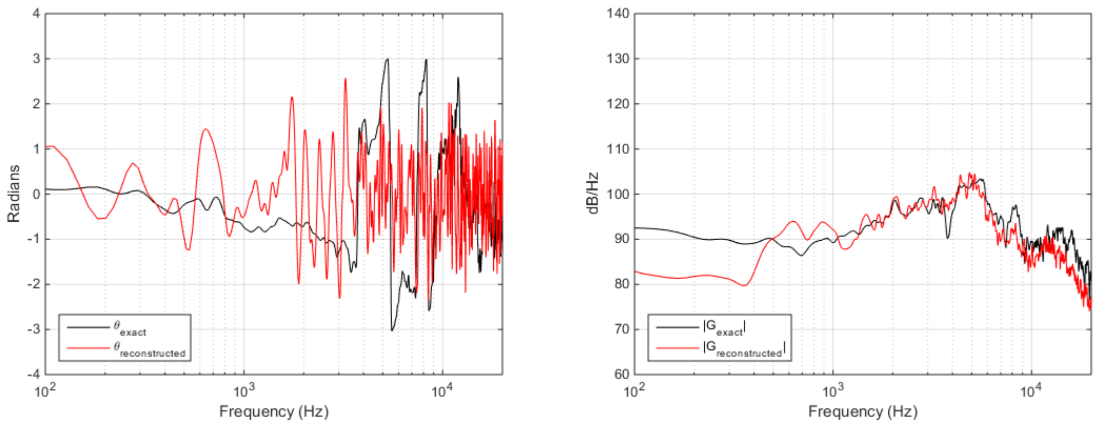

(a) (b)

Figure 3.100 AR4 Cross-spectra reconstruction between sensors 16 and 18 for NPR = 1.5. (a) Cross-spectral density phase; (b) cross-spectral density magnitude.

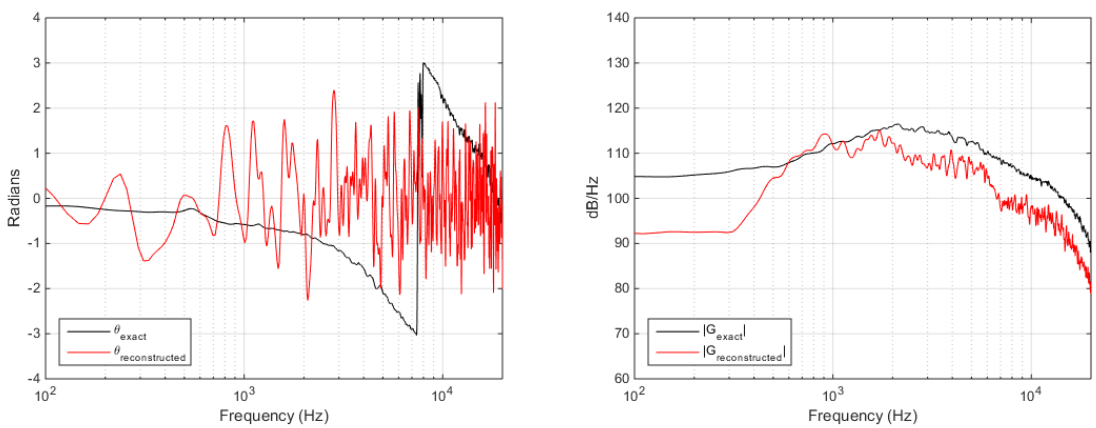

(a) (b)

Figure 3.101 AR4 Cross-spectra reconstruction between sensors 32 and 34 for NPR = 1.5. (a) Cross-spectral density phase; (b) cross-spectral density magnitude.

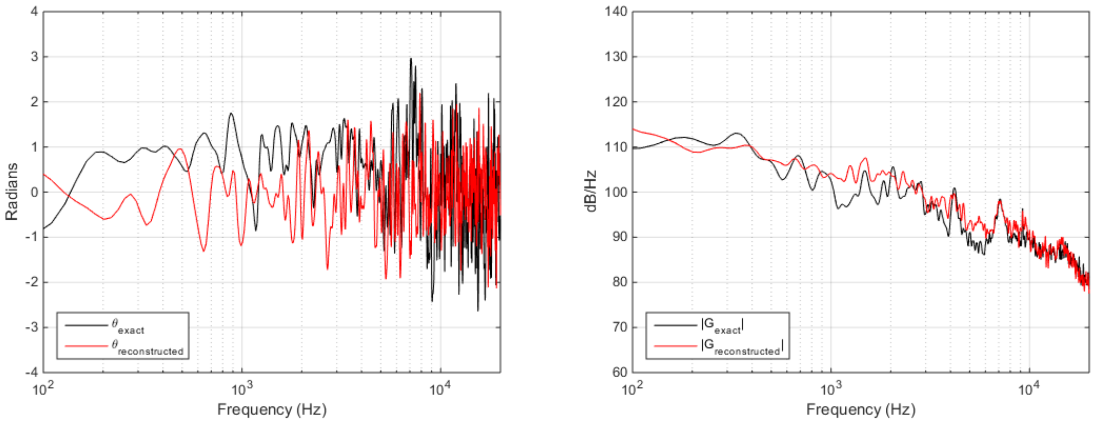

(a) (b)

Figure 3.102 AR4 Cross-spectra reconstruction between sensors 16 and 18 for NPR = 3.5. (a) Cross-spectral density phase; (b) cross-spectral density magnitude.

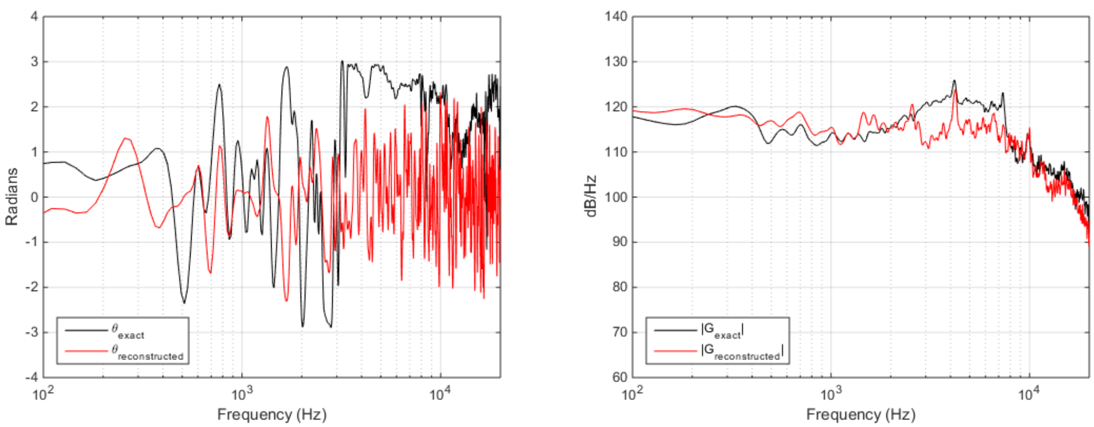

(a) (b)

Figure 3.103 AR4 Cross-spectra reconstruction between sensors 32 and 34 for NPR = 3.5. (a) Cross-spectral density phase; (b) cross-spectral density magnitude.

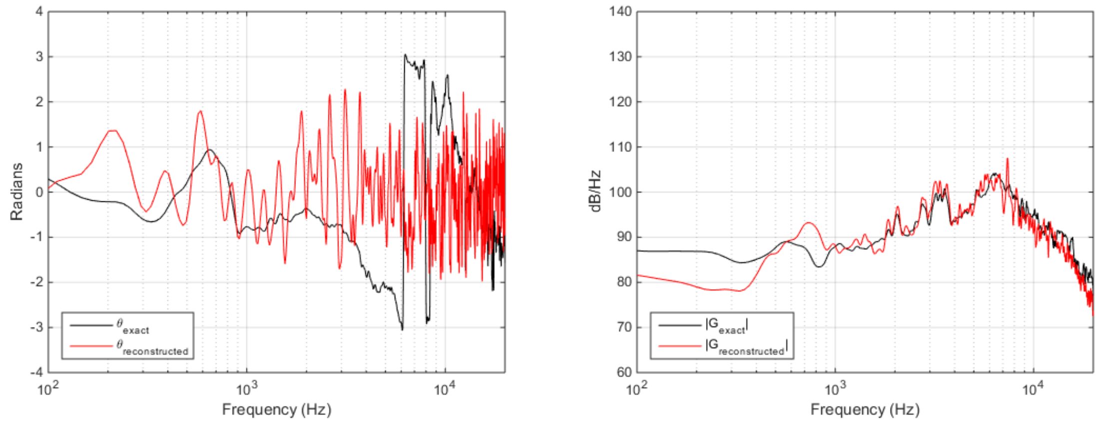

(a) (b)

Figure 3.104 AR8 Cross-spectra reconstruction between sensors 14 and 18 for NPR = 1.5. (a) Cross-spectral density phase; (b) cross-spectral density magnitude.

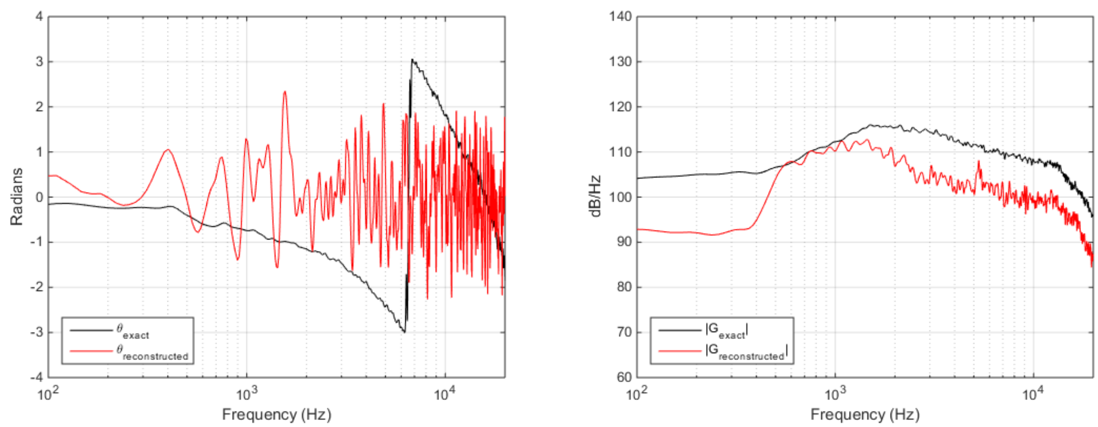

(a) (b)

Figure 3.105 AR8 Cross-spectra reconstruction between sensors 30 and 34 for NPR = 1.5. (a) Cross-spectral density phase; (b) cross-spectral density magnitude.

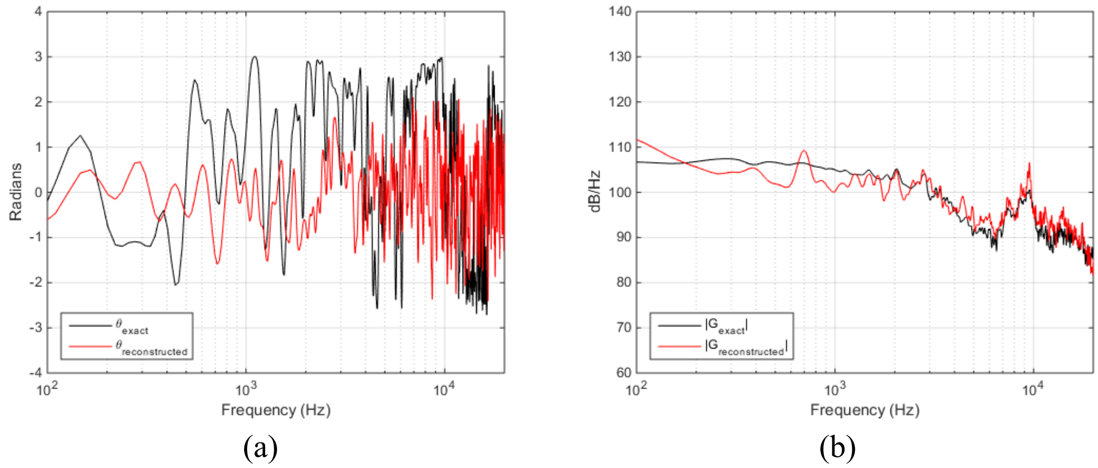

Figure 3.106 AR8 Cross-spectra reconstruction between sensors 14 and 18 for NPR = 3.5. (a) Cross-spectral density phase; (b) cross-spectral density magnitude.

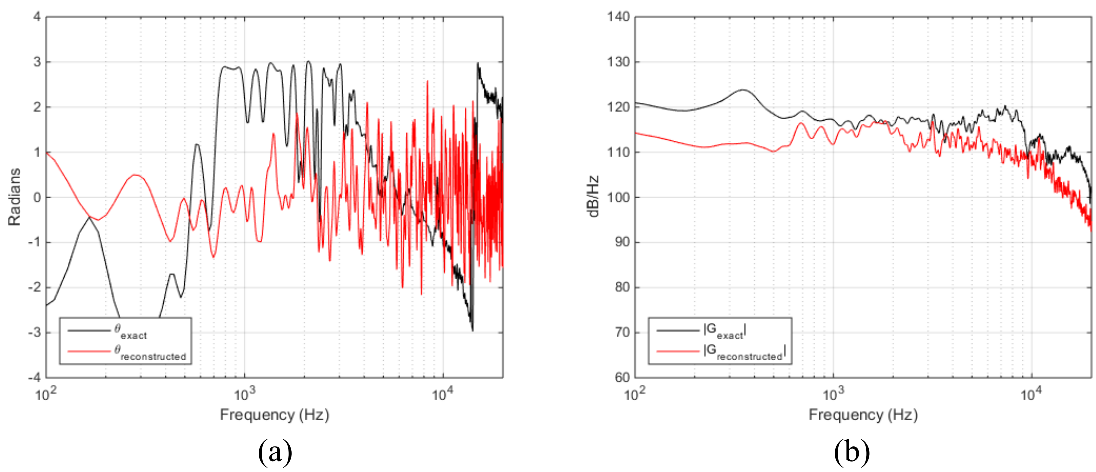

Figure 3.107 AR8 Cross-spectra reconstruction between sensors 30 and 34 for NPR = 3.5. (a) Cross-spectral density phase; (b) cross-spectral density magnitude.

Chapter 5
Summary and Future Work

This chapter provides a summary of the experimental and computational studies described in this thesis. The chapter is divided into three sections. Section 5.1 is a summary of the CFD results. Section 5.2 presents a discussion of the unheated jet experiments. Section 5.3 discusses the findings and limitations of the current work, and also outlines directions for future research.

5.1 Summary of the Numerical Simulations

Wind-US is a computational platform that is used for the computations shown in this study. The CFD code uses a second-order-accurate finite difference scheme to solve the Euler or the compressible Reynolds-averaged form of the Navier-Stokes equations using a Runge-Kutta time matching scheme and 2nd order Roe upwind-biased algorithm that has been modified for stretched grids. The numerical calculations were started from a steady-state simulation (RANS) in order to minimize the transient period. The unsteady runs were then performed using a hybrid RANS/LES model with a constant CFL number method. In the hybrid model, the standard RANS solver is used in regions near the boundaries while a sub-grid scale formulation is used in regions where the grid resolution is fine enough to support the LES solver. The constant CFL subroutine sets a CFL limiter near the viscous boundaries for time accurate calculations, allowing the local time step to vary based on a selected CFL number threshold (CFL_{max}). The size of the computational domain that is affected by the CFL limiter scales with the global time step and the inverse of the CFL limiting value.

The computational domain is split into 135 individual zones to allow for parallel computation. The geometry consists of a rectangular nozzle with an aspect ratio of 8:1 and flat plate which extends horizontally downstream of the nozzle exit for a total of 33 nozzle heights. A multi-block structured grid is used to mesh the aft-deck geometry and the surrounding domain. The inflow conditions are held constant for all zones inside the nozzle. In addition, freestream conditions are applied to the outflow and freestream boundaries during the course of the simulation. Numerical calculations of an under-expanded flow have been performed at a nozzle pressure ratio (NPR) of 4.0 and a total temperature ratio (TTR) of 1.0 to match the supersonic experiment performed by UTRC. The impact of several numerical parameters is studied using flow visualizations of the mean Mach number and mean surface pressure fields.

The hybrid model running with the CFL limiter achieved a 20-fold reduction in computational time with respect to the fully time-accurate simulation while preserving the spectral resolution of the unsteadiness of interest. However, it was observed that the hybrid LES model introduces artificial oscillations in the flow field. A proper orthogonal decomposition (POD) analysis was performed on several of the simulations. The POD revealed that this phenomenon was localized in regions where strong shock-boundary layer interactions occur. Additionally, it was observed that the most energetic modes contribute to an artificial downstream traveling wave. The strength of these artifacts scaled with the inverse of the CFL limiter and the turbulent kinetic energy dissipation, while the peak frequency of the oscillations increased with smaller time step sizes. The strength and frequency of the artifacts also scaled with the size of the stretched-time region affected by the constant CFL method. It is suggested to use a CFL limiter (CFL_{max}) higher than 3.0 to limit the impact of the numerical artifacts on the flow solution and a turbulent dissipation coefficient (C_b) lower than 1.0 to prevent over-damping of the unsteadiness near the viscous layers.

The LESb model generally under-predicted the initial shear layer growth and the potential core length as a result of the artificial damping and filtering introduced by the LES model. Furthermore, solutions from the inviscid run have shown that the grid resolution near the viscous walls is not fine enough to support the LES sub-grid model. As a result, the hybrid LES model predicted strong laminar shock boundary layer interactions that drastically altered the aeroacoustic loading on the deck. Since the impact of the shear layer and boundary layer on the aft deck are a major cause of the unsteady loading, a boundary layer shield formulation was introduced to prevent the LES model from affecting the flow in regions where the grid resolution was insufficient to properly resolve the turbulence in the viscous sub-layers.

Comparison of the power spectral densities between the numerical results from the CFD simulations with the BL shield and the measured data showed fair agreement for sensors that are located $x/h_{nozzle} \geq 12$. However, the power spectral density estimates for the upstream sensor locations showed poor agreement with the measured data. The addition of the boundary layer shield showed no improvement for the upstream PSD estimates with respect to the baseline LESb model. The RMS and mean pressure levels on the deck surface predicted by the RANS/LES model also showed a favorable comparison to the RMS and mean pressure fields measured in the experiments.

5.2 Summary of the Unheated Jet Experiments

Sub-scale experiments of wall bounded jets were designed and run at the Pennsylvania State high-speed jet noise facility. Two different nozzles with an 8:1 and a 4:1 aspect ratio were tested at four operating conditions, including a subsonic case (NPR = 1.5), an over-expanded case (NPR = 2.3), an on-design case (NPR = 2.62) and an under-expanded case (NPR = 3.5). The nozzles were mounted flush to a flat plate instrumented with four Endevco pressure transducers designed to measure the acoustic pressure on the plate surface.

In addition to the pressure transducers, an array of ten reference near-field microphones was suspended 11 inches above the deck. Shadowgraphs of the jet flow provided evidence that each run condition was achieved successfully.

The power density spectra of the surface pressures along the nozzle centerline were measured by the Endevco transducers and showed very good agreement with the experiments performed by Lurie [27]. The spectrum in the NPR = 1.5 run was broadband with a peak at 3 kHz and a gradual roll-off at the higher frequencies. The supersonic cases showed higher energy content below 1 kHz as a result of the shock-boundary layer interactions. In the AR4 experiment, the NPR = 2.3 data showed a collapse of the low-frequency energy with the NPR = 1.5 case after a downstream distance of 16 nozzle heights, indicating that the effects of the shocks had dissipated. The PSD peaks measured above 10 kHz are believed to be screech tones caused by the interaction between a standing system of shock waves and disturbances convecting in the shear layer. These tones were more prominent in the AR8 nozzle as a result of the thicker nozzle lip.

The pressure transducers also provided a clear picture of the RMS pressures on the deck surface. Comparisons of the RMS pressures along the nozzle centerline showed good correlation between the measurements and the experiments performed by Lurie [27]. The subsonic case showed the lowest RMS levels with a steady increase in pressure fluctuations up to 4 nozzle heights downstream of the nozzle exit. For both nozzle configurations, the RMS pressure increased with increasing NPR.

The mean pressure plots showed no shock activity for the NPR = 1.5 run (subsonic), as expected. A shock train started developing when the flow reached an over-expanded flow condition. Another important observation is that the size and strength of the shock diamonds scaled with higher exit Mach numbers. These shock structures dissipated as they propagated throughout the length of the deck. For the AR8 nozzle, the first shock showed a lower pressure peak than that measured by Lurie. This discrepancy was caused by the spatial undersampling of the pressure field in the downstream direction.

Finally, a patch-and-scan near-field acoustic holography technique was proposed to reconstruct the cross-spectra and cross-correlations from the uncorrelated wall-pressure measurements. The cross-spectra visualizations showed that the NAH technique successfully reconstructed the cross-spectra magnitudes for frequencies above 10 kHz. However, the algorithm was not able to fully reproduce the phase information, limiting its ability to predict the coherence between any two pressure points on the deck surface.

5.3 Future Work

While the LESb model has shown significant improvement in reducing the computational costs, a number of open problems must be overcome to allow the development of a reliable and accurate platform for the prediction of the unsteady aeroacoustic loading caused by a turbulent jet. The current simulations generally show an over-prediction of the low frequency spectral energy with respect to the measured data. The implementation of a Spalart DES model, which is intended to improve the results for unsteady and massively separated flows, combined with a higher grid resolution, could help achieve better resolution of the unsteady pressure field on the deck. Additional post-processing techniques such as turbulence budget and Koopman mode analysis and should be performed to further study the impact of the different numerical models on the computed flow field. Finally, a full fluid-structure interaction model needs to be developed to assist in the design of the aft-deck.

Experimentally, instrumenting the plate with more pressure transducers would allow better downstream resolution and eliminate the potential errors caused by the need to reset the plates in between each run. It is also suggested that using a shorter separation distance between the reference microphones would allow the phase information to be retrieved from the nearfield acoustic holography. Additional work can be also performed to study the effects of upstream boundary layer tripping on the measured aeroacoustic loadings and to compare the results with the numerical data.

Appendix A

Cross-Correlation MATLAB Code

```
% This code calculates and plots the cross-correlation coefficient
(corr_c) between the surface pressure signals (a,b) extracted from the
WindUS simulations.

%Import acoustic data

basename5='G:\runs\NAH_4\E';
gen='.GEN';
kulite=[33 34]; %select two wall pressure points

%assemble data

for ll=1:length(kulite)
    ii=kulite(ll);
    filename5=[basename5,(num2str(ii)),gen];
    fid = fopen([filename5]);
    y5=textscan(fid,'%f %f %*[^\n]','headerlines',7);
    t5=y5{1};
    p5=y5{2};
    Fs=1/(t5(2)-t5(1));
    r(ll,:)=p5(floor(0.002*Fs):end);
end

W=floor(0.01*Fs);
w_h=hann(W).'; %set up Hanning window

Nrecs = floor((length(r(1,:)) - W)/(W/2) + 1); %find number of bins

%compute cross-correlation coefficient

for jj=1:length(kulite)-1
b=r(1,:);
a=r(jj+1,:);
for kk=1:Nrecs
    c=a(1+W/2*(kk-1):W+W/2*(kk-1))-mean(a(1+W/2*(kk-1):W+W/2*(kk-1)));
    d=b(1+W/2*(kk-1):W+W/2*(kk-1))-mean(b(1+W/2*(kk-1):W+W/2*(kk-1)));
    [A(kk,:),B(kk,:)]=xcorr(w_h.*c,w_h.*d,'coeff');
```

```
end

corr_c(jj,:)=mean(A,1); %normalized cross-correlation coefficients
lagg(jj,:)=mean(B,1); %cross-correlation delays
end
%plot cross-correlation

figure()
plot(lagg(1,:)./Fs,corr_c(1,:),'k');
xlabel('\tau [s]')
ylabel('Cross-correlation coefficient, R_i_j')
title('Cross Correlations Coefficients')
xlim([-4e-3 4e-3])
ylim([-1 1])
grid on
h=legend('R_Y_Z [Exact]');
set(h, 'Location', 'SouthEast')
```

Appendix B

POD MATLAB Code

```
%This code is used to perform the proper orthogonal decomposition of
the acoustic pressure field (P_fluct) from the unsteady Wind-US
calculations. The code calculates the energy contributions of each mode
(menergy) and outputs a .gif animation of the selected POD mode groups
(P_mode).


%Import and assemble the WindUS pressure data

fid =
fopen(['C:\Users\Claudio\Desktop\Research\prog_report_May13\timehistory
\3e-7_0.01\36POD.GEN']);%%(',sprintf('%d',i),')
p36=textscan(fid,'%f %f %f %f %f %*[^\n]','headerlines',1356);
fclose(fid);
p36=[p36{1} p36{2} p36{3} p36{4} p36{5}];
fid =
fopen(['C:\Users\Claudio\Desktop\Research\prog_report_May13\timehistory
\3e-7_0.01\39POD.GEN']);%%(',sprintf('%d',i),')
p39=textscan(fid,'%f %f %f %f %f %*[^\n]','headerlines',1356);
fclose(fid);
p39=[p39{1} p39{2} p39{3} p39{4} p39{5}];

fid =
fopen(['C:\Users\Claudio\Desktop\Research\prog_report_May13\timehistory
\3e-7_0.01\37POD.GEN']);%%(',sprintf('%d',i),')
p37=textscan(fid,'%f %f %f %f %f %*[^\n]','headerlines',1302);
fclose(fid);
p37=[p37{1} p37{2} p37{3} p37{4} p37{5}];
fid =
fopen(['C:\Users\Claudio\Desktop\Research\prog_report_May13\timehistory
\3e-7_0.01\40POD.GEN']);%%(',sprintf('%d',i),')
p40=textscan(fid,'%f %f %f %f %f %*[^\n]','headerlines',1302);
fclose(fid);
p40=[p40{1} p40{2} p40{3} p40{4} p40{5}];
```

```
fid =
fopen(['C:\Users\Claudio\Desktop\Research\prog_report_May13\timehistory
\3e-7_0.01\38POD.GEN']);%%(',sprintf('%d',i),')
p38=textscan(fid,'%f %f %f %f %f %*[^\n]','headerlines',1302);
fclose(fid);
p38=[p38{1} p38{2} p38{3} p38{4} p38{5}];
fid =
fopen(['C:\Users\Claudio\Desktop\Research\prog_report_May13\timehistory
\3e-7_0.01\41POD.GEN']);%%(',sprintf('%d',i),')
p41=textscan(fid,'%f %f %f %f %f %*[^\n]','headerlines',1302);
fclose(fid);
p41=[p41{1} p41{2} p41{3} p41{4} p41{5}];

fid =
fopen(['C:\Users\Claudio\Desktop\Research\prog_report_May13\timehistory
\3e-7_0.01\46POD.GEN']);%%(',sprintf('%d',i),')
p46=textscan(fid,'%f %f %f %f %f %*[^\n]','headerlines',1626);
fclose(fid);
p46=[p46{1} p46{2} p46{3} p46{4} p46{5}];
fid =
fopen(['C:\Users\Claudio\Desktop\Research\prog_report_May13\timehistory
\3e-7_0.01\48POD.GEN']);%%(',sprintf('%d',i),')
p48=textscan(fid,'%f %f %f %f %f %*[^\n]','headerlines',1626);
fclose(fid);
p48=[p48{1} p48{2} p48{3} p48{4} p48{5}];

fid =
fopen(['C:\Users\Claudio\Desktop\Research\prog_report_May13\timehistory
\3e-7_0.01\47POD.GEN']);%%(',sprintf('%d',i),')
p47=textscan(fid,'%f %f %f %f %f %*[^\n]','headerlines',1626);
fclose(fid);
p47=[p47{1} p47{2} p47{3} p47{4} p47{5}];
fid =
fopen(['C:\Users\Claudio\Desktop\Research\prog_report_May13\timehistory
\3e-7_0.01\49POD.GEN']);%%(',sprintf('%d',i),')
p49=textscan(fid,'%f %f %f %f %f %*[^\n]','headerlines',1626);
fclose(fid);
p49=[p49{1} p49{2} p49{3} p49{4} p49{5}];

N=100; %number of snapshots

%POD modes range

mode1=1;
mode2=5;
```

```
%load and assemble grid information from WindUS

load('G:\runs\grid\x36')
load('G:\runs\grid\x37')
load('G:\runs\grid\x38')
load('G:\runs\grid\x39')
load('G:\runs\grid\x40')
load('G:\runs\grid\x41')
load('G:\runs\grid\x46')
load('G:\runs\grid\x47')
load('G:\runs\grid\x48')
load('G:\runs\grid\x49')

load('G:\runs\grid\z36')
load('G:\runs\grid\z37')
load('G:\runs\grid\z38')
load('G:\runs\grid\z39')
load('G:\runs\grid\z40')
load('G:\runs\grid\z41')
load('G:\runs\grid\z46')
load('G:\runs\grid\z47')
load('G:\runs\grid\z48')
load('G:\runs\grid\z49')
x=[x36 x39;x37 x40;x38 x41;x46 x48;x47 x49].';
x=(x-0.222631007000000)./0.0215798;
z=[z36 z39;z37 z40;z38 z41;z46 z48;z47 z49].';
z=(z+0.010790558500000)./0.0215798;

for ii=1:N;
    pp36(:,ii) = reshape(p36(271*(ii-1)+1:271*ii,1:5).',[],1);
    pp39(:,ii) = reshape(p39(271*(ii-1)+1:271*ii,1:5).',[],1);
    pp37(:,ii) = reshape(p37(260*(ii-1)+1:260*ii,1:5).',[],1);
    pp40(:,ii) = reshape(p40(260*(ii-1)+1:260*ii,1:5).',[],1);
    pp38(:,ii) = reshape(p38(260*(ii-1)+1:260*ii,1:5).',[],1);
    pp41(:,ii) = reshape(p41(260*(ii-1)+1:260*ii,1:5).',[],1);
    pp46(:,ii) = reshape(p46(325*(ii-1)+1:325*ii,1:5).',[],1);
    pp48(:,ii) = reshape(p48(325*(ii-1)+1:325*ii,1:5).',[],1);
    pp47(:,ii) = reshape(p47(325*(ii-1)+1:325*ii,1:5).',[],1);
    pp49(:,ii) = reshape(p49(325*(ii-1)+1:325*ii,1:5).',[],1);
end

pp36=pp36(2:1351,1:N);
pp39=pp39(2:1351,1:N);
pp37=pp37(2:1297,1:N);
pp40=pp40(2:1297,1:N);
```

```
pp38=pp38(2:1297,1:N);
pp41=pp41(2:1297,1:N);
pp46=pp46(2:1621,1:N);
pp48=pp48(2:1621,1:N);
pp47=pp47(2:1621,1:N);
pp49=pp49(2:1621,1:N);

p1=[];
for i=1:(length(pp36)/54)
    p1=[p1;pp36(54*(i-1)+1:54*i,:)];
    p1=[p1;pp39(54*(i-1)+1:54*i,:)];
end

p2=[];
p3=[];
for i=1:(length(pp37)/54)
    p2=[p2;pp37(54*(i-1)+1:54*i,:)];
    p2=[p2;pp40(54*(i-1)+1:54*i,:)];
    p3=[p3;pp38(54*(i-1)+1:54*i,:)];
    p3=[p3;pp41(54*(i-1)+1:54*i,:)];
end
p4=[];
p5=[];
for i=1:(length(pp46)/54)
    p4=[p4;pp46(54*(i-1)+1:54*i,:)];
    p4=[p4;pp48(54*(i-1)+1:54*i,:)];
    p5=[p5;pp47(54*(i-1)+1:54*i,:)];
    p5=[p5;pp49(54*(i-1)+1:54*i,:)];
end

P=[p1;p2;p3;p4;p5];
P_mean=mean(P,2); %mean pressure
P_fluct=bsxfun(@minus,P,P_mean); %fluctuating pressure
R=P_fluct'*P_fluct; %autocovariance matrix
[eV,D]=eig(R);
[L,I]=sort(diag(D));
for i=1:length(D)
        eValue(length(D)+1-i)=L(i); %sorted eigenvalues
        eVec(:,length(D)+1-i)=eV(:,I(i)); %sorted eigenvectors
end
eValue(length(eValue))=0;
menergy=eValue/sum(eValue); %mode energy
for k=1:N
        tmp=P_fluct*eVec(:,k);
        phi(:,k)=tmp/norm(tmp); %POD modes
```

```
end
time=linspace(0.035,0.0362,N);

%plot POD mode groups

gifname='3e-7, 1-2 mode.gif';
l=figure('color','w')
hold on
for t=1:N
        a=phi(:,mode1:mode2)'*P_fluct(:,t); %POD coefficient
        P_recon=phi(:,mode1:mode2)*a; %POD reconstruction
        P_mode(:,:,t)=reshape(P_fluct(:,t),[108,133]); %project
pressure on grid coordinates

        pcolor(x,z,P_mode(:,:,t)); %plot
        title(['Fluctuating pressure along 1/4 span - [dt = 3e-7s  t ='
num2str(time(t)) 's]'])
        xlabel({'x/h_n_o_z_z_l_e';''})
        ylabel('z/h_n_o_z_z_l_e')
        shading interp
        colormap jet
        caxis([-2 2])
        ylim([0 1])
        xlim([0 6])
        %axis equal
        %axis tight
         if t==1
        h=colorbar('Location','SouthOutside')

        v = get(h,'title');
       set(v,'string','Fluctuating pressure [psi]');
         end
        F=getframe(l);
        im = frame2im(F);
        [imind,cm] = rgb2ind(im,256);
        if t == 1;
        imwrite(imind,cm,gifname,'gif','DelayTime',0,'Loopcount',inf);
        else
imwrite(imind,cm,gifname,'gif','DelayTime',0,'WriteMode','append');
        end
end
```

Appendix C

Individual POD Modes: 1 - 4

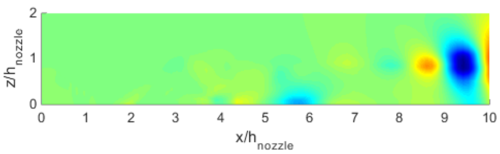

(a)

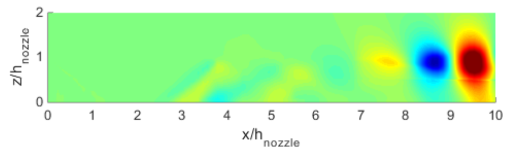

(b)

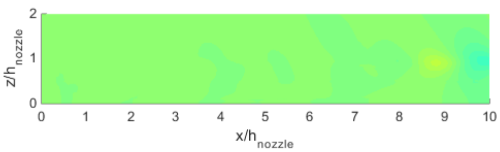

(c)

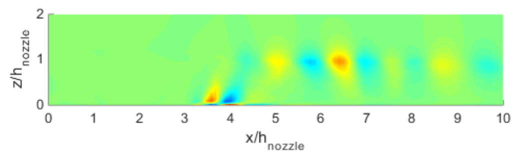

(d)

Figure C. 1 1st mode of the reconstructed fluctuating pressure along the nozzle ¼ span at t = 0.0385 s. (a) LESb run 1; (b) LESb run 2; (c) LESb run 3; (d) LESb run 4.

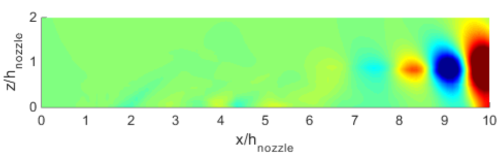

(a)

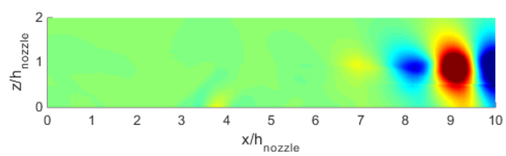

(b)

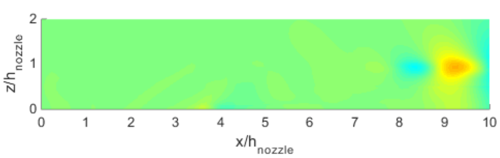

(c)

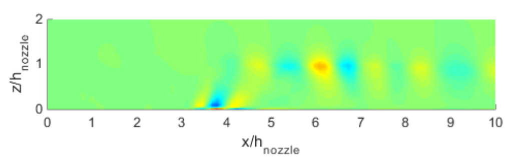

(d)

Figure C. 2 2nd mode of the reconstructed fluctuating pressure along the nozzle ¼ span at t = 0.0385 s. (a) LESb run 1; (b) LESb run 2; (c) LESb run 3; (d) LESb run 4.

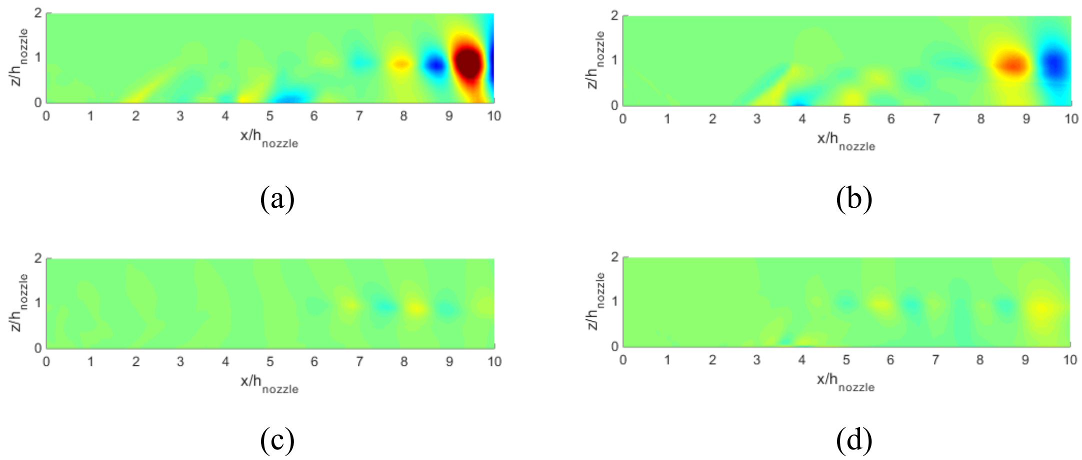

Figure C. 3 3rd mode of the reconstructed fluctuating pressure along the nozzle ¼ span at t = 0.0385 s. (a) LESb run 1; (b) LESb run 2; (c) LESb run 3; (d) LESb run 4.

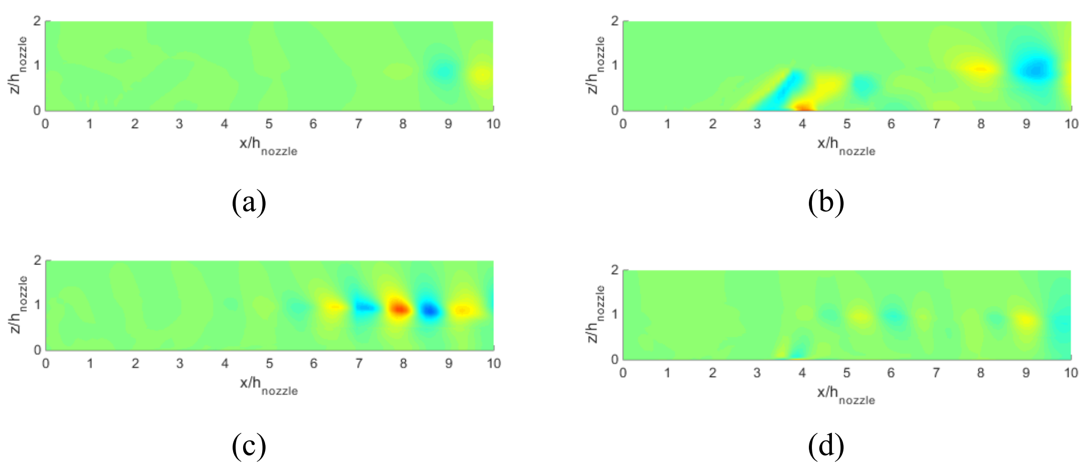

Figure C. 4 4th mode of the reconstructed fluctuating pressure along the nozzle ¼ span at t = 0.0385 s. (a) LESb run 1; (b) LESb run 2; (c) LESb run 3; (d) LESb run 4.

Appendix D

NAH MATLAB Code

```
% This code reconstructs the Welch complex cross-spectrum (Gyz) using a
set of reference microphones and a limited number of surface pressure
transducers. The results are compared to the exact Welch complex cross-
spectrum (Pyz) from the axially aligned sensors. The code outputs the
magnitude and phase of the exact and reconstructed cross-spectra. The
code also computes the exact and reconstructed cross-correlation
coefficients from the cross-spectral data.

run=[168 168]; %runs used to compute the exact cross-spectrum
run2=[168 208]; %runs used in the cross-spectral reconstruction
Ne = [12 14]; %channels used to compute the exact cross-spectrum
Ne2=[12 12]; %channels used in the cross-spectral reconstruction
Nnf = [1 2 3 4 5 6 7 8 9 10]; %near-field microphones
gg=10; %number of partial fields used

Fs=1/3.32999999999996E-06; %sampling frequency
Pref = 0.00002; %reference Pressure
cal_ff=[4.34 10.13 8.06 5.25 5.03 9.75 7.62 7.67 8.40 7.65 8.09 8.23
9.36 7.01]; %far-field microphones calibration values
cal_nf=[6.9415 11.8501 9.2692 7.5204 9.2249 7.9037 9.7199 8.9624 4.8041
8.1496]; %near-field microphones calibration values
cal_e=[21938.03526           27648.88889      24396.07843
      22217.85714]; %Endevco sensors calibration values

W=8192; %Hanning window size
w_h=1;

%Construct up 20kHz low-pass filter

n=100;
wp2=(2/Fs)*20000;
b6=fir1(n,wp2,'low',kaiser(101,10));

%Set up acoustic data import

for ss=1:length(Ne)
tt=run(ss);
```

```
name='G:\Aft Deck\Data Acquisition\Raw
Data\07Dec15\Raw_Data\JNA_07Dec15_#';
gen='a.mat';
filename=[name,(num2str(tt)),gen];
load(filename)
basename2='UntitledPXIeBlade34ai';
kk=Ne(ss)+11;
var_name2=eval([basename2,num2str(kk)]);
e_data(ss,:)=filter(b6,1,var_name2.Data)*(cal_e(Ne(ss)));
Nrecs = floor((length(e_data(ss,:)) - W)/(W/2) + 1);
End

%Apply filter and calibration on near-field mic data from measurement
run2(1)

for ii=1:length(Nnf)
name='G:\Aft Deck\Data Acquisition\Raw
Data\07Dec15\Raw_Data\JNA_07Dec15_#';
gen='a.mat';
filename=[name,(num2str(run2(1))),gen];
load(filename)
basename2='UntitledPXIeBlade34ai';
kk=Nnf(ii)+1;
var_name2=eval([basename2,num2str(kk)]);
nf_data1(ii,:)=filter(b6,1,var_name2.Data)*(sqrt((0.00002^2)*10^(94/10)
))/(cal_nf(ii)/1000);
nf_data2(ii,:)=filter(b6,1,var_name2.Data)*(sqrt((0.00002^2)*10^(94/10)
))/(cal_nf(ii)/1000);
end

%Apply filter and calibration on near-field mic data from measurement
run2(2)

for ii=1:length(Nnf)
name='G:\Aft Deck\Data Acquisition\Raw
Data\07Dec15\Raw_Data\JNA_07Dec15_#';
gen='a.mat';
filename=[name,(num2str(run2(2))),gen];
load(filename)
basename2='UntitledPXIeBlade34ai';
kk=Nnf(ii)+1;
var_name2=eval([basename2,num2str(kk)]);
nf_data2(ii,:)=filter(b6,1,var_name2.Data)*(sqrt((0.00002^2)*10^(94/10)
))/(cal_nf(ii)/1000);
end
```

```
%Apply filter and calibration on Endevco data

for ss=1:length(Ne2)
tt=run2(ss);
name='G:\Aft Deck\Data Acquisition\Raw
Data\07Dec15\Raw_Data\JNA_07Dec15_#';
gen='a.mat';
filename=[name,(num2str(tt)),gen];
load(filename)
basename2='UntitledPXIeBlade34ai';
kk=Ne(ss)+11;
var_name2=eval([basename2,num2str(kk)]);
e_data2(ss,:)=filter(b6,1,var_name2.Data)*(cal_e(Ne(ss)));
end
%calculate exact complex cross-spectral density

for kk=1:Nrecs
    c=e_data(1,1+W/2*(kk-1):W+W/2*(kk-1))-mean(e_data(1,1+W/2*(kk-
1):W+W/2*(kk-1)));
    d=e_data(2,1+W/2*(kk-1):W+W/2*(kk-1))-mean(e_data(2,1+W/2*(kk-
1):W+W/2*(kk-1)));
    corrLength=length(c)+length(d)-1;
    pyz(kk,:)=fft(d.*w_h,corrLength).*conj(fft(c.*w_h,corrLength));
    Jj(kk,:)=(sqrt(sum(abs(w_h.*c).^2)*sum(abs(w_h.*d).^2)));
end
YZ_rms(:,:,:)=mean(Jj,1);
Pyz(:,:,:)=mean(pyz,1); %exact complex cross-spectral density

F=Fs*(0:(size(Pyz,2)-1))/size(Pyz,2); %array of frequency points

%calculate the average complex cross-spectra between all the nearfield
microphones

for ww=1:length(Nnf)
    for mm=1:length(Nnf)
        for kk=1:Nrecs
        c=nf_data1(ww,1+W/2*(kk-1):W+W/2*(kk-1))-
mean(nf_data1(ww,1+W/2*(kk-1):W+W/2*(kk-1)));
        d=nf_data1(mm,1+W/2*(kk-1):W+W/2*(kk-1))-
mean(nf_data1(mm,1+W/2*(kk-1):W+W/2*(kk-1)));
        Z(kk,:)=fft(d.*w_h,corrLength).*conj(fft(c.*w_h,corrLength));
        end
        Cr1(ww,mm,:)=mean(Z,1); %complex cross-spectra between all
nearfield microphones from run2(1)
```

```
    end
end
for ww=1:length(Nnf)
    for mm=1:length(Nnf)
        for kk=1:Nrecs
        c=nf_data2(ww,1+W/2*(kk-1):W+W/2*(kk-1))-
mean(nf_data2(ww,1+W/2*(kk-1):W+W/2*(kk-1)));
        d=nf_data2(mm,1+W/2*(kk-1):W+W/2*(kk-1))-
mean(nf_data2(mm,1+W/2*(kk-1):W+W/2*(kk-1)));
        Z(kk,:)=fft(d.*w_h,corrLength).*conj(fft(c.*w_h,corrLength));
        end
        Cr2(ww,mm,:)=mean(Z,1); %complex cross-spectra between all
nearfield microphones from run2(2)

    end
end
Gxx(:,:,:)=(Cr1+Cr2)./2; %average complex cross-spectra between all
nearfield microphones

%calculate complex cross-spectra between Endevco sensors and all near-
field microphones

for ww=1:length(Nnf)
    for mm=1:2
        for kk=1:Nrecs
        e=e_data2(mm,1+W/2*(kk-1):W+W/2*(kk-1))-
mean(e_data2(mm,1+W/2*(kk-1):W+W/2*(kk-1)));
        if mm==1
        f=nf_data1(ww,1+W/2*(kk-1):W+W/2*(kk-1))-
mean(nf_data1(ww,1+W/2*(kk-1):W+W/2*(kk-1)));
        else
        f=nf_data2(ww,1+W/2*(kk-1):W+W/2*(kk-1))-
mean(nf_data2(ww,1+W/2*(kk-1):W+W/2*(kk-1)));
        end
        H(kk,:)=fft(f.*w_h,corrLength).*conj(fft(e.*w_h,corrLength));
        end
        Cd(ww,mm,:)=mean(H,1); %complex cross-spectra between Endevco
sensors and all near-field microphones
    end
end

%perform NAH and reconstruct complex cross-spectral density


for oo=1:length(Nnf)
```

```
        for kk=1:Nrecs
        c1=e_data2(1,1+W/2*(kk-1):W+W/2*(kk-1))-
mean(e_data2(1,1+W/2*(kk-1):W+W/2*(kk-1)));
        d1=nf_data1(oo,1+W/2*(kk-1):W+W/2*(kk-1))-
mean(nf_data1(oo,1+W/2*(kk-1):W+W/2*(kk-1)));
        d2=nf_data2(oo,1+W/2*(kk-1):W+W/2*(kk-1))-
mean(nf_data2(oo,1+W/2*(kk-1):W+W/2*(kk-1)));
        c2=e_data2(2,1+W/2*(kk-1):W+W/2*(kk-1))-
mean2(e_data(2,1+W/2*(kk-1):W+W/2*(kk-1)));
        V(kk,:)=fft(d1.*w_h,corrLength).*conj(fft(c1.*w_h,corrLength));
        N(kk,:)=fft(d2.*w_h,corrLength).*conj(fft(c2.*w_h,corrLength));
        end
    Gyx(1,oo,:)=mean(V,1);
    Gxz(oo,1,:)=mean(N,1);
end
for hh=1:size(Gxx,3)
    ll(:,:,hh)=Gyx(:,:,hh)*pinv(Gxx(:,:,hh))*Gxz(:,:,hh);
end
Gyz2=reshape((ll),[length(ll),1]); %reconstructed complex cross-
spectral density

%calculate cross-spectral phase from exact and reconstructed arrays

g = gausswin(10);
g = g/sum(g);
Pyz_phase = conv(angle(Pyz*(1/(Fs*W))), g, 'same'); %exact
Gyz_phase = conv(angle(Gyz2*(1/(Fs*W))), g, 'same'); %reconstructed

%calculate cross-spectral magnitude from exact and reconstructed arrays


g = gausswin(10);
g = g/sum(g);
Pyz_abs = conv(abs(Pyz*(1/(Fs*W))), g, 'same'); %exact
Gyz_abs = conv(abs(Gyz2*(1/(Fs*W))), g, 'same'); %reconstructed

%plot comparison of exact and reconstructed cross-spectral phases

figure;
semilogx(F,Pyz_phase,'k');
hold on
semilogx(F,Gyz_phase,'r');
xlabel('Frequency (Hz)'); ylabel('Radians');
title('Cross-Spectral Density Phase (\theta_Y_Z)');
hold off
```

```
h=legend('\theta_e_x_a_c_t','\theta_r_e_c_o_n_s_t_r_u_c_t_e_d');
set(h, 'Location', 'southwest')
xlim([100 20000])
ylim([-4 4])
grid on

%plot comparison of exact and reconstructed cross-spectral magnitudes
figure;
semilogx(F,10*log10(Pyz_abs/(Pref^2)),'k');
hold on
semilogx(F,10*log10(Gyz_abs/(Pref^2)),'r');
xlabel('Frequency (Hz)'); ylabel('dB/Hz');
title('Cross-Spectral Density Magnitude(|G_Y_Z|)');
hold off
h=legend('|G_e_x_a_c_t|','|G_r_e_c_o_n_s_t_r_u_c_t_e_d|');
set(h, 'Location', 'southwest')
xlim([100 20000])
ylim([60 140])
grid on

%calculate cross-correlation coefficients from cross-spectral density
data

for jj=1:length(Ne)-1
b=e_data(1,:);
a=e_data(jj+1,:);
for kk=1:Nrecs
    u=a(floor(1+W/2*(kk-1)):floor(W+W/2*(kk-1)))-
mean(a(floor(1+W/2*(kk-1)):floor(W+W/2*(kk-1))));
    t=b(floor(1+W/2*(kk-1)):floor(W+W/2*(kk-1)))-
mean(b(floor(1+W/2*(kk-1)):floor(W+W/2*(kk-1))));
    [A2(kk,:),B2(kk,:)]=xcorr(w_h.*u,w_h.*t,'coeff');
end
corr_exact(jj,:)=mean(A2,1); %exact cross-correlation coefficient
lag(jj,:)=mean(B2,1); %frequency array
end

corr2 = fftshift(ifft(Gyz2*(1/(Fs*W))))/(YZ_rms*(1/(Fs*W)));
%reconstructed cross-correlation coefficient

%plot comparison of exact and reconstructed cross-correlation
coefficients

figure()
plot(lag(1,:)./Fs,corr_exact(1,:),'k');
```

```
xlabel('\tau [s]')
ylabel('Cross-Correlation Coefficient')
% hold on
% plot(lag(1,:)./Fs,corr2,'r');
xlim([-2e-3 2e-3])
ylim([-1 1])
grid on
grid minor
```

Bibliography

[1] Yahya, S. M. *Fundamentals of Compressible Flow: With Aircraft and Rocket Propulsion*. Tunbridge Wells, UK: New Age Science, 2010.

[2] Goldstein, M. E. *Aeroacoustics*. New York A.o: McGraw-Hill, 1976. Print.

[3] Abdellah Hadjadj. *Large-Eddy Simulation of Shock/Boundary-Layer Interaction*, AIAA Journal, Vol.50, No. 12 (2012), pp. 2919-2927

[4] Ganapathisubramani, B., Clemens, N.T. & Dolling, D.S. 2007, *Effects of upstream boundary layer on the unsteadiness of shock-induced separation*. J. Fluid Mech. 585, 369–394.

[5] Hou, Y.X., Unalmis, O.H & Bueno, P.C. 2004, *Effects of boundary-layer velocity fluctuations on unsteadiness of blunt-fin interactions*. AIAA J. 42(12), 2615–1219.

[6] Debieve, J.F. & Dupont, P. 2009. *Dependence between the shock and the separation bubble in a shock wave boundary layer interaction*. Shock Waves 19, 163–169.

[7] S. Priebe, M. Wu, and M. P. Martín. *Direct Numerical Simulation of a Reflected Shock-Wave Turbulent-Boundary-Layer Interaction*, AIAA Journal, Vol. 47, No. 5 (2009), pp. 1173-1185.

[8] Piponniau S, Dussauge JP, Debieve JF, Dupont P. 2009. *A simple model for low-frequency unsteadiness in shock-induced separation*. J. Fluid Mech. 629:87–108

[9] A. K. M. F. Hussain. *Coherent structures and turbulence*. Journal of Fluid Mechanics, 173:303–356, 1986.

[10] Kok, J. C. and H. van der Von (2009), *Destabilizing free shear layers in X-LES using a stochastic subgrid-scale model*, *NLR-TP-2009-327*, National Aerospace Laboratory NLR.

[11] J. M. Seiner, *Advances in high speed jet aeroacoustics*, AIAA paper 84-2275, 1984.

[12] M. Kandula, *Shock refracted acoustic wave model for screech amplitude in supersonic jets*, AlAA Journal, vol. 46, no. 3, pp. 682-689, 2008.

[13] Lighthill, M. J., *On Sound Generated Aerodynamically: I. General Theory*, Proceedings of the Royal Society of London, Series A, Vol. 211(1107), 1952, pp. 564 –587.

[14] Hu, Z. W., C. L. Morfey, and N. D. Sandham (2002), *Aeroacoustics of Wall-Bounded Turbulent Flows*, *AIAA Journal*, **40**(3), pp. 465–473.

[15] Shiyi Chen, Zhenhua Xia, Suyang Pei, Jianchun Wang, Yantao Yang, Zuoli Xiao and Yipeng Shi (2012). *Reynolds-stress-constrained large-eddy simulation of wall-bounded turbulent flows*. Journal of Fluid Mechanics, 703, pp 1-28.

[16] Ahlman, Daniel, Geert Brethouwer, and Arne V. Johansson. *Direct Numerical Simulation of a Plane Turbulent Wall-jet including Scalar Mixing*. Physics of Fluids Phys. Fluids 19.6 (2007): 065102.

[17] J. G. Eriksson, R. I. Karlsson, and J. Persson, *An experimental study of a two-dimensional plane turbulent wall jet*, Exp. Fluids 25, 50 1998.
[18] Northrop Grumman, *X-47B UCAS,* http://www.northropgrumman.com/Photos/pgL_UC-10028_026.jpg 10028_019%26rel%3D%2F%26name%3DPhotos.
[19] Gatski, T. B. and Bonnet, J.-P., *Compressibility, Turbulence and High Speed Flow*, 2009, Elsevier, Amsterdam
[20] *Wind-US 3.0 User's Guide*, The NPARC Alliance, 2012.
[21] Sandberg, R., Sandham, N., & Suponitsky, V. (2011). *DNS of fully turbulent jet flows in flight conditions including a canonical nozzle*. 17th AIAA/CEAS Aeroacoustics Conference (32nd AIAA Aeroacoustics Conference).
[22] D.C. Wilcox. *Reassessment of the scale-determining equation for advanced turbulence models*. AIAA journal, 26(11):1299–1310, 1988.
[23] G. Lindner, D. Markus and R. Model (2010). *Non-reactive free jet flow: Comparison of simulations using different turbulence models with reference measurements*. Proc. 5th Europ. Conf. on Comp. Fluid Dynamics
[24] Bush, R. H., and Mani, M. (2001). *A Two-Equation Large Eddy Stress Model for High Sub-Grid Shear*, AIAA Paper 2001-2561.
[25] Bardina, J. E. & Huang, P. G. & Coakley, T. J. & Ames Research Center. (1997). *Turbulence modeling validation, testing, and development*. National Aeronautics and Space Administration, Ames Research Center.
[26] Suzen, Y. B. and Hoffmann, K. A., *Investigation of Supersonic Jet Exhaust Flow by One- and Two-Equation Turbulence Models*, 36th AIAA Aerospace Sciences Meeting, Reno, Nevada, 1998, AIAA Paper 98-0322.
[27] Lurie M.B. (2015). *The prediction of Unsteady Aerodynamic Loading in High Aspect Ratio Wall Bounded Jets*. The Pennsylvania State University, Doctoral Dissertation
[28] MathWorks (2016), *Signal Processing Toolbox User's Guide*, MATLAB R2016a.
[29] Murakami, E., & Papamoschou, D. (2000). *Eddy convection in coaxial supersonic jets*. AIAA Journal, 38, 628-635.
[30] Uzun, A., and Hussaini, M.Y., *Investigation of high frequency noise generation in the near-nozzle region of a jet using large eddy simulation*, Theoretical and Computational Fluid Dynamics, Vol. 21, 2007, pp. 291–321.
[31] J. Delville. *La décomposition orthogonal aux valeurs propres et l'analyse de l'organisation tridimensionnelle de écoulements turbulents cisaillés libres*. PhD Thesis, Université de Poitiers, 1995.
[32] Sirovich, L., *Turbulence and the Dynamics of Coherent Structures. Part 1: Coherent Structures*, Quarterly of Applied Mathematics, Vol. 45, No. 3, October 1987, pp. 561–571
[33] K. E. Meyer, *Identify flow structures with Proper Orthogonal Decomposition (POD)*, DTU, Dansis seminar on visualization, 2008

[34] Bogey, C. and Marsden, O., *Large-eddy Simulation of the Flow and Acoustic Fields of a Reynolds Number 10^5 Subsonic Jet with Tripped Exit Boundary Layer*, Physics of Fluids, American Institute of Physics, 2011, 23, pp. 035104.
[35] Menter, F. R. *Two-equation eddy-viscosity turbulence models for engineering applications*. AIAA Journal, 32(8), 1984.
[36] Morris P.J., personal communication, August, 2015.
[37] Hald, J., *STSF – A Unique Technique for Scan-based Near-field Acoustic Holography without Restrictions on Coherence*, 1989.
[38] Mathworks, *XCORR Function*, www.mathworks.com/help/signal/ref/xcorr.html

Vita

Claudio Notarangelo received his B.S. from the University of Hartford in 2013, majoring in Mechanical Engineering and Music. Claudio enrolled at Penn State in the Fall of 2013 to pursue is M.S. in Acoustics. He currently works at Apple Inc. as a hardware design engineer.